Università degli Studi di Ferrara

UCA Universidad de Cádiz

INTERNATIONAL DOCTORAL COURSE IN
"EARTH AND MARINE SCIENCES (EMAS)"

CYCLE XXXIII

COORDINATOR Prof. COLTORTI MASSIMO

Chondrodonta (Bivalvia) proliferation in peri-Adriatic shallow-water carbonates: a bioevent preluding the Cretaceous OAE1a and OAE2

Scientific/Disciplinary Sector (SDS) GEO/02

Candidate
Dr. Gabriella Del Viscio

Supervisors
Prof. Michele Morsilli
Prof. Renato Posenato
Prof. Gianluca Frijia

Years 2017/2020

Table of contents

Chondrodonta (Bivalvia) proliferation in peri-Adriatic shallow-water carbonates: a bioevent preluding the Cretaceous OAE1a and OAE2

Abstract

The opportunistic, oyster-like bivalve *Chondrodonta*, common in Tethyan Cretaceous shallow-water carbonates, shows peaks of concentration during the Aptian – Cenomanian time interval. Despite this, neither a temporal nor a causal relationship between the flourishing of this bivalve and Oceanic Anoxic Events (OAEs) has emerged yet.

The stratigraphic distribution and the ecological significance of *Chondrodonta* have been analyzed to both define the timing between its accumulations and OAEs and infer OAE-related environmental perturbations triggering its proliferation.

The studied *Chondrodonta* accumulations occur in inner platform limestones of the lower Aptian Apulia Carbonate Platform straddling OAE1a, and of the upper Cenomanian Adriatic Carbonate Platform straddling OAE2. The stratigraphic framework around the *Chondrodonta* beds has been built using biostratigraphic and chemostratigraphic ($\delta^{13}C$, $\delta^{18}O$, $^{87}Sr/^{86}Sr$) data. Palaeoenvironmental changes associated with its proliferation have been inferred by coupling sedimentologic-lithostratigraphic analyses with the concentration of major, trace elements and REE.

Based on platform-to-basin stratigraphic correlations, the lower Aptian *Chondrodonta* beds occur right below the negative $\delta^{13}C$ excursion marking the onset of OAE1a and the upper Cenomanian beds occur below the $\delta^{13}C$ positive excursion of the OAE2 interval. In both cases, *Chondrodonta* appears in the stratigraphic succession associated with rudist limestones and then reaches a phase of maximum proliferation and predominance over rudists at the prelude of OAEs.

As emerged by stratigraphic and geochemical analyses, the *Chondrodonta* proliferation occurred in an interval of increasing nutrients and in low-energy seawaters with fluctuating oxygenation and intermittent terrigenous inputs. These environmental changes prevented the settlement of the less tolerant rudists while they promoted the thriving of *Chondrodonta* in monospecific (or quasi-) benthic communities close to the onset of OAEs.

The intervals of *Chondrodonta* proliferation also correlate to increasing fertility and environmental deterioration in the nearby basins. Further, the stratigraphic position of lower Aptian and upper Cenomanian *Chondrodonta* accumulations in worldwide carbonate platforms located at different palaeolatitudes and climates, generally predates the onset of OAEs and enables to consider the proliferation of this bivalve as a regional bioevent.

Accordingly, the flourishing of *Chondrodonta* is ascribable within an environmental "window", triggered by the changing climate preluding OAEs and mainly resulted in nutrient pulses on the platforms top. The opportunistic behavior of *Chondrodonta* was rather efficient in the transition from oligo- to mesotrophic conditions in shallow-water carbonate areas. This oyster-like bivalve benefitted from this environmental instability and occupied a short-lived environmental niche between more stable, stenotopic and eurytopic benthic communities.

The occurrence and duration of this environmental "window" were also controlled by local, quick fluctuations in other seawater parameters (*e.g.*, oxygenation, terrigenous inputs) and by limiting environmental factors related to palaeogeography and hydrodynamics.

However, further increase of inhospitable conditions leading to OAEs inhibited the proliferation of the bivalve, allowing fully mesotrophic taxa to dominate the benthic community. This is particularly demonstrated for the early Aptian *Chondrodonta*, abruptly outpaced by mesotrophic assemblages at the onset of OAE1a.

The proliferation of *Chondrodonta* can be, therefore, used as a regional stratigraphic marker for an early phase of environmental stress in shallow-water carbonate platforms. Its transitionary predominance within the benthic community represents the biotic response of the Cretaceous shallow-water carbonate systems to increasing environmental deterioration peaking with Oceanic Anoxic Events 1a and 2.

Proliferazione di *Chondrodonta* (Bivalvia) in carbonati di acque basse dell'area peri-Adriatica: bioevento a preludio degli Eventi Anossici Oceanici 1a e 2 del Cretaceo

Abstract

La *Chondrodonta*, un bivalve simil-ostreide e opportunista, è comunemente riportata nelle piattaforme carbonatiche Tetidee del Cretaceo, con una particolare concentrazione nel periodo Aptiano – Cenomaniano. Nonostante ciò, non è ancora emersa una chiara relazione né temporale né causale tra la proliferazione di questo bivalve e gli Eventi Anossici Oceanici (OAEs).

Per tali ragioni, la distribuzione stratigrafica e geografica e il significato paleoecologico della *Chondrodonta* sono stati analizzati ai fini di stabilire un preciso rapporto temporale tra i suoi accumuli e gli OAEs e di definire le possibili perturbazioni ambientali alla base della sua proliferazione.

Gli accumuli di *Chondrodonta* analizzati affiorano nelle successioni carbonatiche di piattaforma interna della Piattaforma Apula (Aptiano inferiore, a ridosso dell'OAE1a), e della Piattaforma Adriatica (Cenomaniano superiore, a ridosso dell'OAE2). Il contesto stratigrafico intorno agli accumuli è stato ricostruito attraverso analisi bio- e chemostratigrafiche ($\delta^{13}C$, $\delta^{18}O$, $^{87}Sr/^{86}Sr$). Analisi sedimentologico-litostratigrafiche e geochimiche (concentrazione di elementi maggiori, in traccia e di Terre Rare) hanno permesso di dedurre le variazioni paleo-ambientali associate alla proliferazione del bivalve.

Sulla base della correlazione dei record isotopici tra piattaforma e bacino, si è osservato come gli accumuli di *Chondrodonta* ricadano al di sotto delle tipiche escursioni nella curva del $\delta^{13}C$ che segnano, rispettivamente, l'inizio dell'OAE1a e dell'OAE2. In entrambe le successioni stratigrafiche studiate, la *Chondrodonta* appare subordinata all'interno dei calcari a rudiste e raggiunge una fase di massima proliferazione e predominanza sulle stesse rudiste in prossimità dell'inizio degli eventi anossici. Dalle analisi stratigrafiche e geochimiche è emerso come gli intervalli di proliferazione di *Chondrodonta* siano caratterizzati da un aumento di nutrienti oltre la soglia di tollerabilità per le rudiste, e da fluttuazioni nell'ossigenazione e nell'apporto terrigeno in acque di bassa energia.

Gli intervalli a *Chondrodonta* sono stati correlati anche ad una crescente fertilità e ad un progressivo deterioramento ambientale nelle vicine aree bacinali. Dall'analisi della letteratura è inoltre emerso come la posizione stratigrafica degli accumuli globali di *Chondrodonta* preceda l'inizio degli OAE1a e 2 in piattaforme carbonatiche poste a differenti latitudini e condizioni climatiche, permettendo di considerare la proliferazione di questo bivalve come un bioevento a scala regionale.

La proliferazione di *Chondrodonta* risulta quindi inseribile all'interno di una "finestra ambientale", innescata dai cambiamenti climatici che preludono gli OAEs e principalmente caratterizzata da un aumento di nutrienti sulle piattaforme carbonatiche. Il bivalve opportunista *Chondrodonta* beneficia, infatti, della transizione da condizioni oligotrofiche a mesotrofiche in piattaforma, occupando una nicchia ecologica posta al passaggio tra comunità stenotopiche ed euritopiche.

La presenza e la durata della "finestra ambientale" sono controllate anche da condizioni paleo-geografiche e idrodinamiche locali così come da locali fluttuazioni nell'ossigenazione delle acque e negli apporti terrigeni.

L'eccessivo deterioramento delle condizioni ambientali all'inizio degli OAEs inibisce, per contro, la proliferazione della *Chondrodonta* provocando la sua scomparsa dalla comunità bentonica in favore di specie propriamente mesotrofiche, come dimostrato per la *Chondrodonta* dell'Aptiano inferiore all'inizio dell'OAE1a.

La proliferazione della *Chondrodonta* rappresenta, quindi, un marker stratigrafico a scala regionale del crescente stress ambientale in piattaforma. La predominanza transitoria della *Chondrodonta* all'interno della comunità bentonica costituisce la risposta biologica dei sistemi carbonatici di acque basse al crescente deterioramento ambientale che culmina con gli Eventi Anossici Oceanici 1a e 2 del Cretaceo.

1. Introduction

1.1. The Cretaceous world, between greenhouse and anoxia

Earth's climate has changed continuously throughout the Phanerozoic, alternating between greenhouse and icehouse modes (Frakes *et al.*, 1992). In contrast to today's theoretic icehouse state, thwarted by global warming due to industrial activities (Randall *et al.*, 2007), the middle part of the Cretaceous period (Aptian to Turonian) represents an excellent example of greenhouse conditions (Jenkyns, 1999, 2003; Skelton *et al.*, 2003). This Cretaceous greenhouse mode was mainly induced by influxes of CO_2 into the atmosphere from volcanogenic and/or methanogenic sources (*e.g.,* Larson & Erba, 1999; Jenkyns, 2003), together with a plate-tectonic evolution (Miller *et al.*, 2005; Pucéat *et al.*, 2007) and a consequent reorganization of global oceanic circulation (*e.g.,* Weissert *et al.*, 1998; Poulsen *et al.*, 2003).

The major warming peak marking the middle part of the Cretaceous (Fig. 1.1) consists of exceptionally high atmosphere and seawater temperatures (Tarduno *et al.*, 1998; Erbacher *et al.*, 2001; Norris *et al.*, 2002; Jenkyns *et al*., 2004). During this time interval, polar regions were occupied by spacious forests (Francis & Frakes, 1993; O'Brien *et al.*, 2017) and permanent ice shields presumably lacked at the poles (Frakes *et al.*, 1992; Bice *et al.*, 2006). The seawater was characterized by the lowest Mg/Ca ratios of Phanerozoic times ("calcite sea"; *see* Steuber, 2002; Pomar & Hallock, 2008; Ries, 2009) and the sea-level was ~ 100 – 200 m higher than today (Miller *et al.*, 2005; Takashima *et al.*, 2006; Cloetingh & Haq, 2015). The resulting flooding of huge continental areas enabled the spread of tropical and subtropical carbonate factories (Höfling & Scott, 2002), with an exceptional extent (Skelton *et al.*, 2003).

The tropical shallow-water carbonate-producing biota during the Cretaceous included scleractinian corals, stromatoporoids, rudist bivalves, benthic foraminifers, micro-encrusters (*Bacinella-Lithocodium*), nerineid gastropods, dasycladal green algae and calcareous red algae (*e.g.,* Masse, 1992; Scott, 1995; Skelton *et al.*, 2003; Skelton & Gili, 2012). Particularly rudist bivalves, with aberrant shell morphologies ranging from club- to horn-like, experienced a great proliferation and an extraordinary adaptive radiation (Steuber *et al.*, 2016 and references therein), occupying several ecological niches of the level-bottom environment (Skelton, 2018).

However, the middle part of the Cretaceous is also characterized by disturbances in the global carbon cycle (Scholle & Arthur, 1980; Föllmi *et al.*, 2006), referred to as Oceanic Anoxic Events (OAEs; Schlanger & Jenkyns, 1976; Jenkyns, 2010) and mainly witnessed by the widespread deposition of

organic carbon-rich sediments (*i.e.,* "black shales"; Schlanger & Jenkyns, 1976) in pelagic and hemipelagic settings.

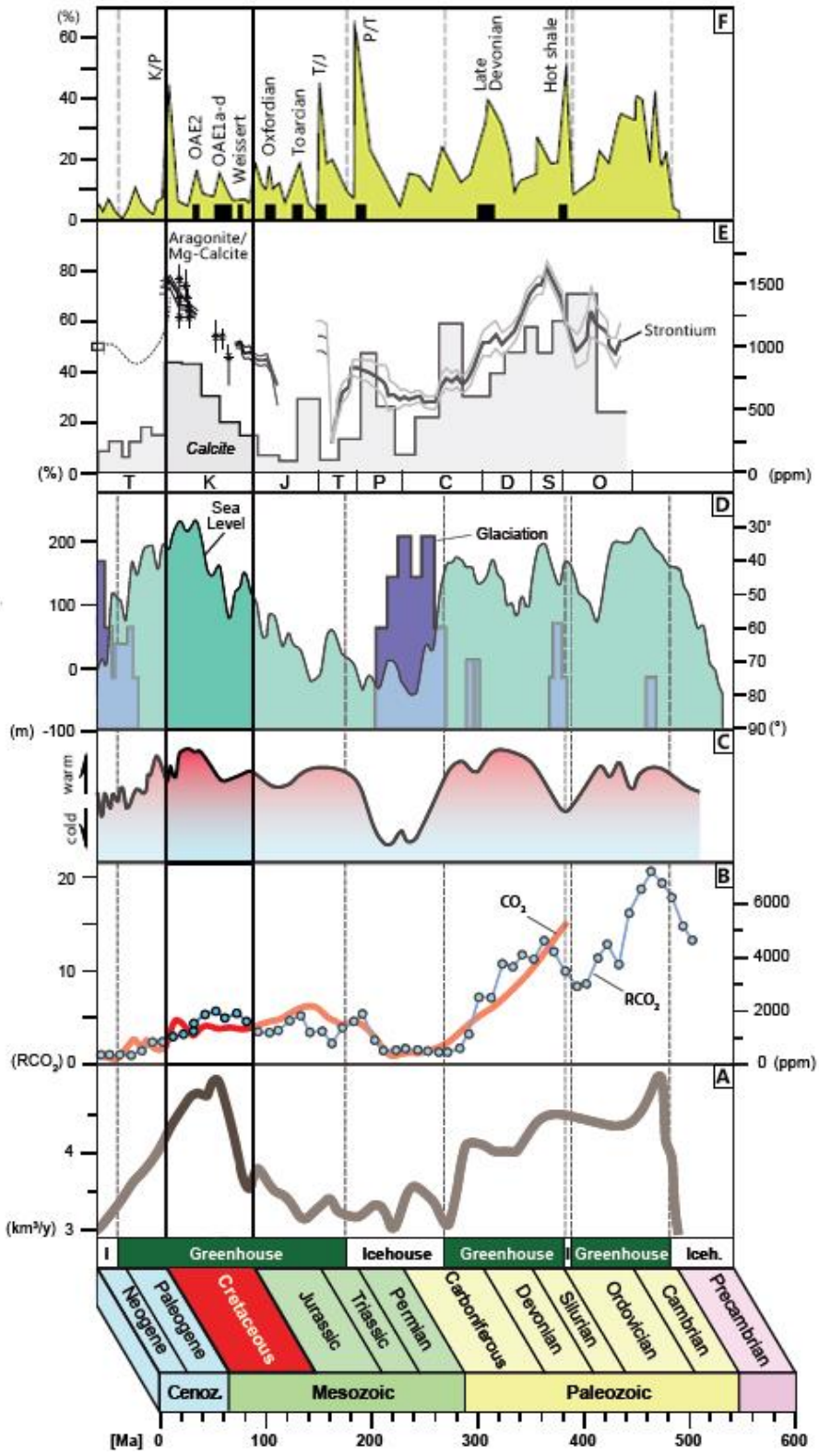

Fig. 1.1.

Major environmental - climate changes, geological and paleontological events throughout the Phanerozoic (Takashima *et al.*, 2006 and reference therein; Huck, 2011). The Cretaceous period is marked in red.

A) ocean crust and production rate.

B) atmospheric carbon dioxide: on the left, RCO_2 - ratio past/present and, on the right, smoothed CO_2 record.

C) atmospheric temperature.

D) sea-level changes (m) and palaeolatitudinal range of continental glaciation (°paleolatitude).

E) inferred skeletal mineralogy of main reef builders (left) and biocalcite strontium concentrations (right).

F) percentage extinction of marine genera and major OAEs.

OAEs were triggered by major and rapid influxes of atmospheric CO_2 into the atmosphere provoking an abrupt rise in the global temperature (*e.g.,* Larson & Erba, 1999; Jenkyns, 2003). This climate warming accelerated the hydrological cycle, increased the continental weathering, enhanced the nutrient discharge to oceans and lakes, and intensified the upwelling and the organic productivity (Jenkyns, 2003, 2010). All these perturbances during OAEs resulted in the development of thick and widespread oxygen-minimum zones in the world oceans, associated with high organic-carbon burial and subsequent drawdown of atmospheric CO_2 (Weissert *et al.*, 1998; Erbacher *et al.*, 2001; Heimhofer *et al.*, 2004).
Most OAEs can be traced worldwide as prominent excursions in the $\delta^{13}C_{carb}$ curve (Menegatti *et al.*, 1998; Jenkyns, 2003). Positive $\delta^{13}C_{carb}$ excursions are linked to the fixation of light carbon isotopes into the organic matter and to the relative enrichment of heavy isotopes in the remaining carbon isotope pool (Jenkyns, 2010).

Although still-pending debates on the importance of production *versus* preservation of organic carbon and the consequent widespread distribution of black shales in the basins (Schlanger & Jenkyns, 1976; Hochuli *et al.*, 1999; Erbacher *et al.*, 2001), primary productivity likely was the dominant mechanism driving the organic-carbon burial during OAEs (*e.g.,* Ohkouchi *et al.*, 2006; Browning & Watkins, 2008). Increased primary productivity reflected major changes in the nutrient supply (Jenkyns, 1999, 2003). The global nutrient budget around OAEs was, indeed, affected by the terrigenous nutrient input due to elevated hydrological cycling (Föllmi *et al.*, 2006), by the upwelling of nutrient-rich (NO_3, PO_4, Fe and Si) currents from intermediate and deep waters (Kuypers *et al.*, 2002; Poulsen *et al.*, 2003), as well as by hydrothermal nutrient-enriched brines provided by igneous activity (Leckie *et al.*, 2002; Kerr *et al.*, 2004; Snow *et al.*, 2005).

The climate instability associated with Cretaceous OAEs and the consequent major changes in the global nutrient budget inevitably affected the carbonate primary productivity, resulting in crises and in biotic turnovers both in the deep- and shallow-water domains. In deep-water settings, changes in the abundance, composition, and morphology of calcareous nannoplankton assemblages have been interpreted as the response of the pelagic ecosystems to palaeoenvironmental variations (*e.g.,* eutrophication) (Erba, 1994, 2004; Leckie *et al.*, 2002; Erba *et al.*, 1999, 2015).
In shallow-water settings (water depth < 100 m), the ecosystems highly depended on parameters like illumination, nutrient availability, salinity, or hydrodynamic levels. The worldwide Cretaceous carbonate platforms, in both the New (southern USA, Mexico, and Caribbean regions) and the Old (mainly around the Mediterranean and Middle East regions) World, were characterized by an episodic development (Skelton *et al.*, 2003). Their initially similar, overall pattern evolved differently from

the Aptian times onwards (Skelton *et al.*, 2003; Skelton & Gili, 2012) and showed demises of global extent, like during the early Aptian and at the Cenomanian – Turonian boundary (Fig. 1.2). The climate perturbations characterizing OAEs often resulted in the demise and drowning of carbonate platforms (*e.g.*, Wissler *et al.*, 2003; Millán *et al.*, 2011; Korbar *et al.*, 2012; Núñez-Useche *et al.*, 2020). In many other cases, platforms did not drown but experienced turnovers in the benthic communities and recorded, therefore, the biotic response of the carbonate systems to global climate crises (*e.g.,* Höfling & Scott, 2002; Huck *et al.*, 2010; Rameil *et al.*, 2010; Amodio & Weissert, 2017; Husinec & Read, 2018; Frijia *et al.*, 2019; Hueter *et al.*, 2019).

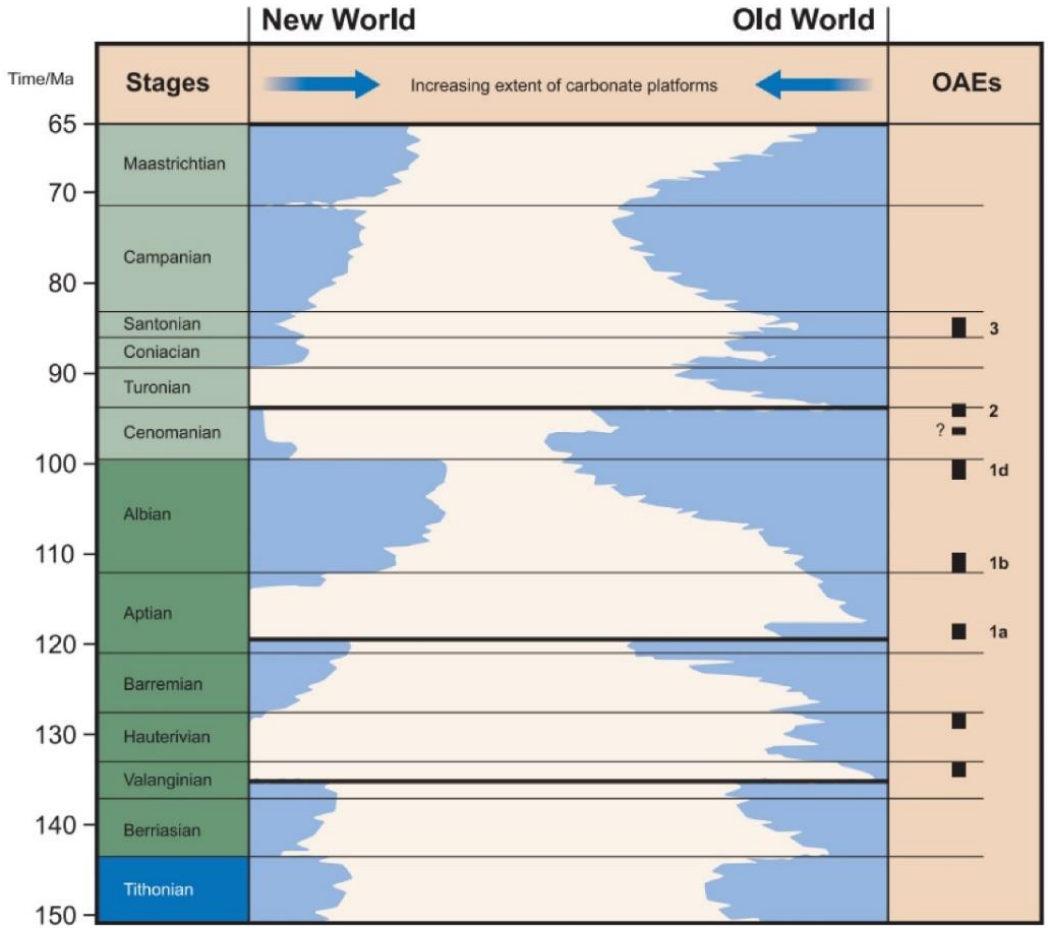

Fig. 1.2. Synoptic history of Tithonian and Cretaceous carbonate platform development (blue) in the New World and the Old World, with timings of major platform crises (bold horizontal lines) and oceanic anoxic events (OAEs) (Skelton *et al.*, 2003; Skelton & Gili, 2012).

The two major oceanic anoxic events of the Cretaceous, those of the late early Aptian (OAE1a, Selli Event) and of the Cenomanian–Turonian boundary (OAE2, Bonarelli Event) registered some of the highest temperatures reconstructed for the Cretaceous Period (Fig. 1.1; *see* Jenkyns, 2018 and references therein), promoting severe climate and environmental changes. Particularly, the vast congregation of rudist bivalves underwent two of its three major extinction events during the two

anoxic events (Ross & Skelton, 1993; Gili *et al.*, 1995; Skelton & Gili, 2002; Masse & Steuber, 2007; Steuber *et al.*, 2016; Skelton, 2018).

1.1.1. The early Aptian Oceanic Anoxic Event 1a

The late early Aptian OAE1a (*i.e.,* Selli Event – Schlanger & Jenkyns, 1976; Jenkyns, 2010) has an estimated duration of ~ 1.2 Ma (Erba, 2004) and represents the focus of much of the previous research on OAEs (Weissert *et al.*, 1985; Larson, 1991; Föllmi *et al.*, 1994; Menegatti *et al.*, 1998; Bralower *et al.*, 1999; Weissert & Erba, 2004; Skelton & Gili, 2012; Bottini *et al.*, 2015; Bottini & Erba, 2018 among many others).

The Barremian - Aptian climate warming was primarily linked to the emplacement of the Ontong Java Large Igneous Province (LIP) in the Pacific Ocean (Larson, 1991; Larson & Erba, 1999; Tejada *et al.*, 2009; Föllmi, 2012). The large amount of CO_2 released into the atmosphere and dissolved in seawater by submarine and subaerial volcanic activity (Föllmi, 2012; Erba *et al.*, 2015) and, secondly, by methane hydrate dissociation (Méhay *et al.*, 2009), triggered a sequence of climate disturbances that accelerated the hydrological cycle and increased precipitation rates, fluvial discharge, and continental runoff (Föllmi *et al.*, 2006; Najarro *et al.*, 2010).

The characteristic isotopic signature of OAE1a is a negative spike in both the $\delta^{13}C_{carb}$ (Fig. 1.3) and $\delta^{13}C_{org}$ curves followed by a positive excursion (Menegatti *et al.*, 1998; Leckie *et al.*, 2002; Jenkyns, 2003; Herrle *et al.*, 2004; Tejada *et al.*, 2009). The negative $\delta^{13}C_{carb}$ spike resulted from an input of isotopically light carbon in the carbon isotope pool, in contrast to the enhanced carbon burial driving the global $\delta^{13}C_{carb}$ to positive values. Possible processes supplying isotopically light carbon at the onset of OAE1a included large-scale venting of volcanogenic carbon dioxide and/or dissociation of gas hydrates and/or thermal metamorphism of coals, either singly or in combination (*e.g.,* Jenkyns, 2003, 2010). High resolution geochemical studies (*e.g.,* Jenkyns, 2018) also highlight at least three cooling episodes (*i.e.,* "cold snaps") of probable global distribution punctuating the long-term warmth recorded during OAE1a. These cold snaps represented transient falls in temperature and increased marine-dissolved oxygen levels. They correlated to increases in carbon-isotope values and positive $\delta^{13}C_{carb}$ shifts and were probably due to a rise in the quantities of organic matter being buried globally with consequent potential drawdown of atmospheric CO_2 (Jenkyns, 2018).

The onset of the negative $\delta^{13}C_{carb}$ excursion coincides with a widespread black shale deposition in basinal settings (Fig. 1.3; Menegatti *et al.*, 1998) as well as with increased open oceanic sea-surface temperatures (SST; *e.g.,* Dumitrescu *et al.*, 2006) and with photic-zone euxinia, the latter highlighted

by specific biomarkers (*i.e.,* chlorophyll and bacteriochlorophyll degradation products) marking the occurrence of green sulfur bacteria within black shales (*see* Pancost *et al.*, 2004).

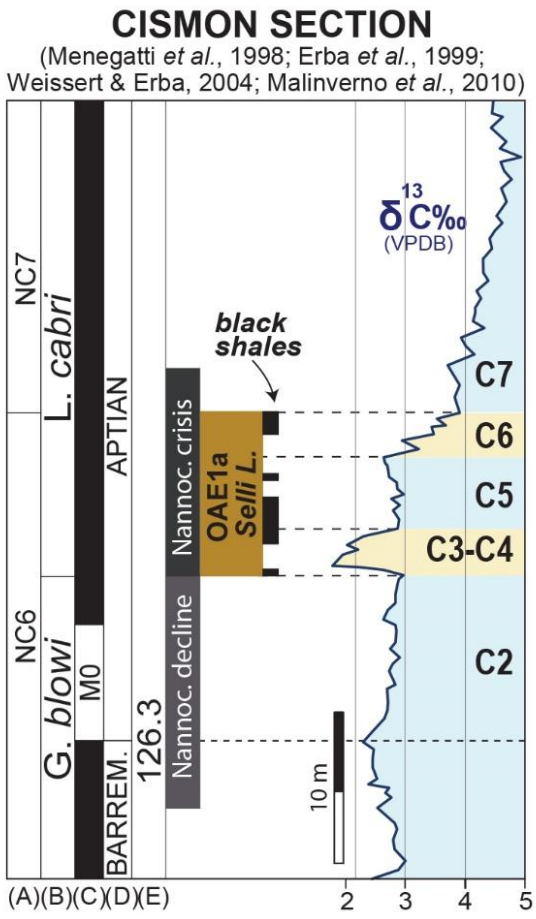

Fig. 1.3. The reference $\delta^{13}C_{carb}$ curve of the Cismon Apticore in southern Alps (Menegatti *et al.*, 1998; Erba *et al.*, 1999) showing the typical negative excursion in isotopic values (C3 – C4) preceding a positive shift. The nannofossil (A) and planktic foraminiferal (B) biostratigraphy is from Weissert & Erba (2004); the nomenclature of the C-isotope C2 – C7 segments and the black shale levels are from Menegatti *et al.* (1998) and the nannoconid decline and crisis intervals as well as the magnetic polarity (C) are from Malinverno *et al.* (2010); the numerical age of the Barremian – Aptian boundary (D, E) is after Ogg & Hinnov (2012).

The climate and environmental disturbances linked to OAE1a resulted in crises in both the pelagic and the neritic carbonate production (*e.g.,* Weissert *et al.*, 1998; Pancost *et al.*, 2004; Dumitrescu *et al.*, 2006; Föllmi *et al.*, 2006; Najarro *et al.*, 2010). The anoxic event is coeval with a sea-level rise and with a major change in nannofossil assemblages (Erba, 1994; Menegatti *et al.*, 1998; Bralower *et al.*, 1999; Erba *et al.*, 1999). The early Aptian decrease in nannoconids from the calcareous nannoplankton assemblages (*i.e.,* "nannoconid crisis" preceded by a decline; *see* Fig. 1.3 and Erba, 1994) immediately preceded the $\delta^{13}C_{carb}$ anomaly and the related black-shale deposition (Erba, 2004; Luciani *et al.*, 2001, 2006). The nannoconid crisis is interpreted as the response of the pelagic ecosystem to early palaeoenvironmental variations that culminated in the OAE1a-related high-productivity event (Erba, 2004; Weissert & Erba, 2004; Erba & Tremolada, 2004; Erba *et al.*, 1999, 2010, 2015). Such variations are likely related to ocean eutrophication and acidification (Erba *et al.*, 2010, 2015), despite the latter mechanism is still under debate (*see* Gibbs *et al.*, 2011; Naafs *et al.*, 2016).

In shallow-water settings, there is global evidence for a profound environmental change during OAE1a (Fig. 1.4). The warmer and more humid climate increased precipitations and continental weathering, which combined with a stronger upwelling near coastlines due to intensified atmospheric and oceanic circulation. As a result, the nutrient input (*e.g.,* phosphorous) to shallow-water areas increased (Föllmi, 1996, 2012), provoking carbonate platforms demise (Weissert *et al.*, 1998; Wissler

et al., 2003) and biotic turnovers from oligo- to meso- or even eutrophic benthic communities on the platform top (*e.g.,* Immenhauser *et al.*, 2005; Millán *et al.*, 2009; Skelton & Gili, 2012; Stein *et al.*, 2012; Huck *et al.*, 2014; Amodio & Weissert, 2017; Hueter *et al.*, 2019).

Carbonate platforms of the northern Tethys and the proto-North Atlantic drowned resulting in the deposition of condensed sequences and in the formation of hardgrounds, immediately before and during OAE1a (Weissert *et al.*, 1998, Wissler *et al.*, 2003; Föllmi *et al.*, 2006; Föllmi & Gainon, 2008; Bover-Arnal *et al.*, 2009; Millán *et al.*, 2011; Najarro *et al.*, 2011; Godet, 2013; Huck *et al.*, 2013, 2014; Núñez-Useche *et al.*, 2020 among others).

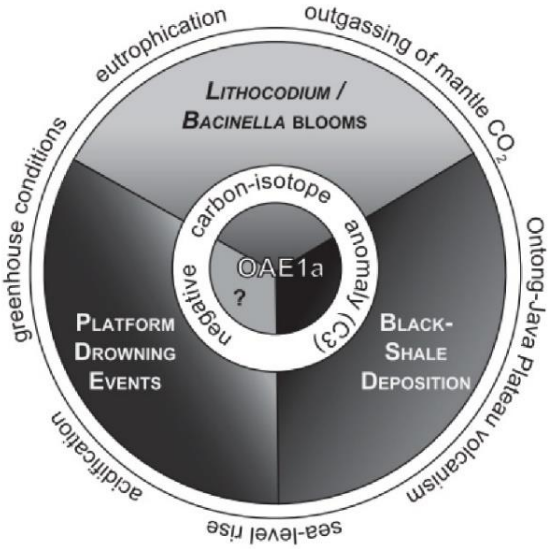

Fig. 1.4.
Simplified model of possible drivers of early Aptian environmental and palaeoceanographic changes at the turn of OAE1a, from Huck *et al.* (2012). The negative $\delta^{13}C$ anomaly (white circle) represents a defined stratigraphic interval in time, which is embedded in a time window comprising the neritic and the pelagic response modes of Tethyan carbonate systems (three grayish slices: micro-encruster blooms, platform drowning, and pelagic black-shale deposition) to environmental changes related to the anoxic event (increasingly darker colors signify increasing importance of the factor).

Conversely, carbonate platforms of the Central and Southern Tethys continued to grow under highly stressed conditions and with minor platform growth rates (Immenhauser *et al.*, 2004; D'Argenio *et al.*, 2004; Huck *et al.*, 2010; Amodio & Weissert, 2017; Husinec & Read, 2018). Shallow-water benthic communities adapted to changes in the nutrient input, resulting in turnovers from oligotrophic (*e.g.,* corals, partly rudists) to meso- and eutrophic (*e.g.,* orbitolinids, *Bacinella-Lithocodium*) associations (Pittet *et al.*, 2002; Huck *et al.*, 2010, 2014; Rameil *et al.*, 2010; Stein *et al.*, 2012; Graziano, 2013; Godet *et al.*, 2014; Amodio & Weissert, 2017; BouDagher-Fadel & Price, 2019; Hueter *et al.*, 2019, 2020).

1.1.2. The Cenomanian – Turonian Oceanic Anoxic Event 2

The Cenomanian/Turonian boundary event (*i.e.,* OAE2 or Bonarelli event) has an estimated duration of ~ 300 – 500 kyr (Kuypers *et al.*, 2002) and is considered to have caused the extinction of about

20% of marine genera (*see* Fig. 1.1) (Raup & Sepkoski, 1986). This event is characterized by anoxic conditions stretching from the photic zone to areas deeper than 3500 m (Pancost *et al.*, 2004), and by the worldwide deposition of black shales in basinal settings (Fig. 1.5). The Cenomanian/Turonian climate warming was mainly induced by large emissions of CO_2 into the atmosphere, due to an intense volcanic activity associated to the emplacement of the Carribean and High Artic Large Igneous Provinces (Snow *et al.*, 2005; Kuroda *et al.*, 2007; Jenkyns *et al.*, 2017). Such a great release of CO_2 increased temperatures and precipitation rates (Heimhofer *et al.*, 2018), enhanced terrestrial weathering and increased the nutrient load delivered to oceans which fueled, in turn, primary productivity (Leckie *et al.*, 2002; Jenkyns, 2003, 2010; Owens *et al.*, 2013; Jenkyns *et al.*, 2017). Other possible factors enhancing primary productivity are the nitrogen fixation (Junium & Arthur, 2007), the phosphorous regeneration from organic-rich sediments (Mort *et al.*, 2007; Monteiro *et al.*, 2012) and the release of great quantities of micro-nutrients like hydrothermal iron due to submarine volcanogenic activity (Adams *et al.*, 2010).

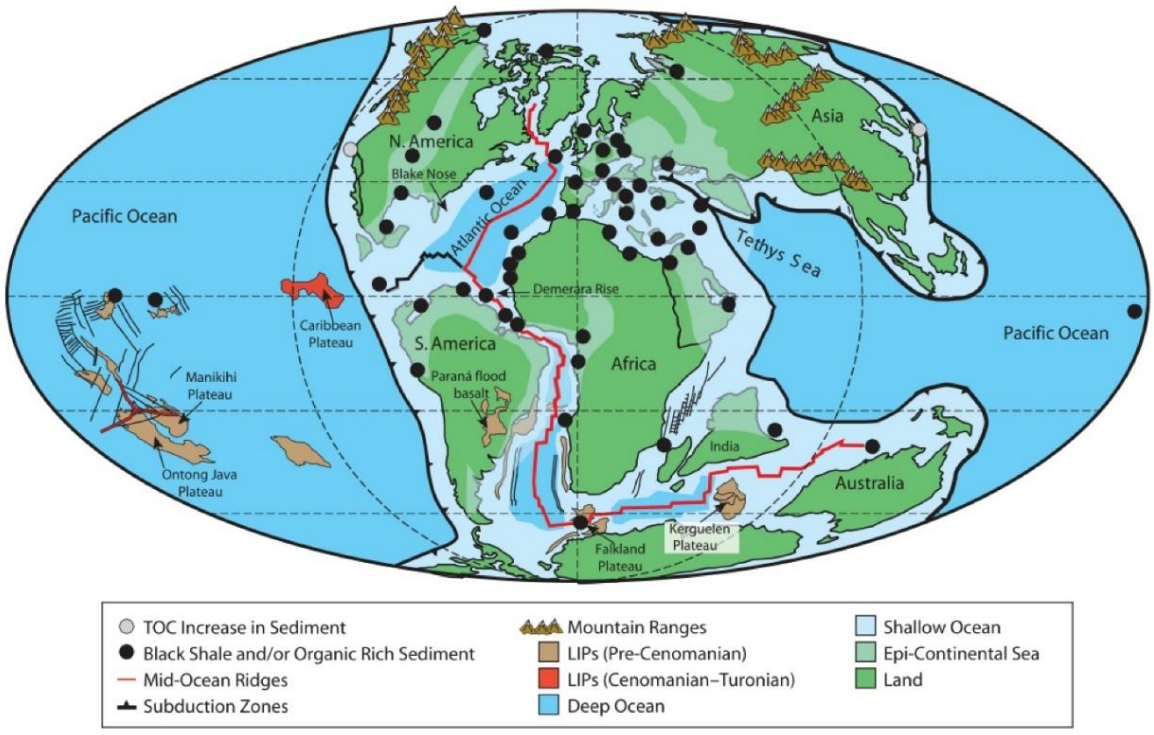

Fig. 1.5. Distribution of black shales and/or increased organic carbon sediments during OAE2 (from Takashima *et al.,* 2006).

OAE2 represents a major short-term perturbation of the global carbon cycle, reflected by a globally positive excursion in $\delta^{13}C$ (2‰ to 4‰) in both marine, terrestrial organic and inorganic carbon (*e.g.,* Schlanger & Jenkyns, 1976; Tsikos *et al.*, 2004; Jenkyns, 2010; Jarvis *et al.*, 2011). The long-term

warming during OAE2 is also interrupted by a transient fall in temperature (*i.e.,* the so-called Plenus Cold Event or Benthic Oxic Event; Jenkyns *et al.*, 2017; Jenkyns, 2018).

Global changes and extreme environmental conditions during OAE2 provoked extinctions followed by speciations in the calcareous nannoplankton (Erba, 2004). Changes in the planktic community are linked to the submarine volcanism, as supported by peaks in redox-sensitive trace metals in sediments and shells across OAE2 (Turgeon & Brumsack, 2006; Hetzel *et al.*, 2009). Furthermore, the loss of water column stratification at the end of the Cenomanian has been invoked for the extinction of deeper-dwelling foraminifers (*Rotalipora* sp., *Globigerinelloides bentonensis*) as well as for having facilitated the vertical advection of nutrients to fuel primary productivity (Leckie *et al.*, 1998, 2002; Huber *et al.*, 1999).

Shallow-water carbonate platforms experienced demise and drowning during OAE2, as witnessed by shallow-water deposits abruptly overlain by pelagic facies with calcispheres and planktic foraminifers (*e.g.,* Jenkyns, 1991; Korbar *et al.*, 2012). Only few carbonate platforms, like the Apennine Platform (Parente *et al.*, 2007, 2008; Frijia & Parente, 2008) and the Mexico Platform (Elrick *et al.*, 2009), recorded a nearly continuous growth. Due to climatic and oceanographic differences, the northern Tethyan carbonate platforms were strongly controlled by the rate of terrigenous input whereas the southern ones were considerably affected by hypersaline events (Philip & Airaud-Crumiere, 1991).
The worldwide synchronous occurrence of microbialitic facies in different shallow-water areas during OAE2 has been interpreted as an episodic eutrophic phase alternating with oligo-mesotrophic conditions and "normal" carbonate production (*see* Frijia *et al.*, 2019). This cyanobacterial proliferation on carbonate platforms was probably directly triggered by the Large Igneous Provinces volcanism (Philip & Airaud-Crumiere, 1991; Erba, 2004; Frijia *et al.*, 2019).
A major crisis and biologic turnover affected the benthic organisms for at least one million years (*e.g.,* Philip & Airaud-Crumiere, 1991; Erba, 2004; Vaziri-Moghaddam & Kalanat, 2020), resulting in a decline in diversity and in partial extinctions. Particularly, rudists underwent a severe extinction event during OAE2: the dominantly aragonite-secreting rudists disappeared, the calcite-dominated forms diversified, and the family Hippuritidae appeared.

1.2. *Chondrodonta* beds in Cretaceous shallow-water carbonate platforms

1.2.1. The bivalves of the genus Chondrodonta

Chondrodonta Stanton, 1901 is an oyster-like bivalve, common in shallow-water carbonates of the Cretaceous Tethyan Realm. It had a discontinuous stratigraphic distribution, with a peak abundance

during the Aptian – Cenomanian period (Posenato *et al.*, 2018, 2020). The oldest reported *Chondrodonta* accumulations may date back to the (?) Berriasian (Masse *et al.*, 2015) as well as the youngest accumulations likely deposited during the (?) Campanian (Freneix & Lefèvre, 1967), although the low biostratigraphic resolution of shallow-water carbonate successions prevents to constrain more precise ages.

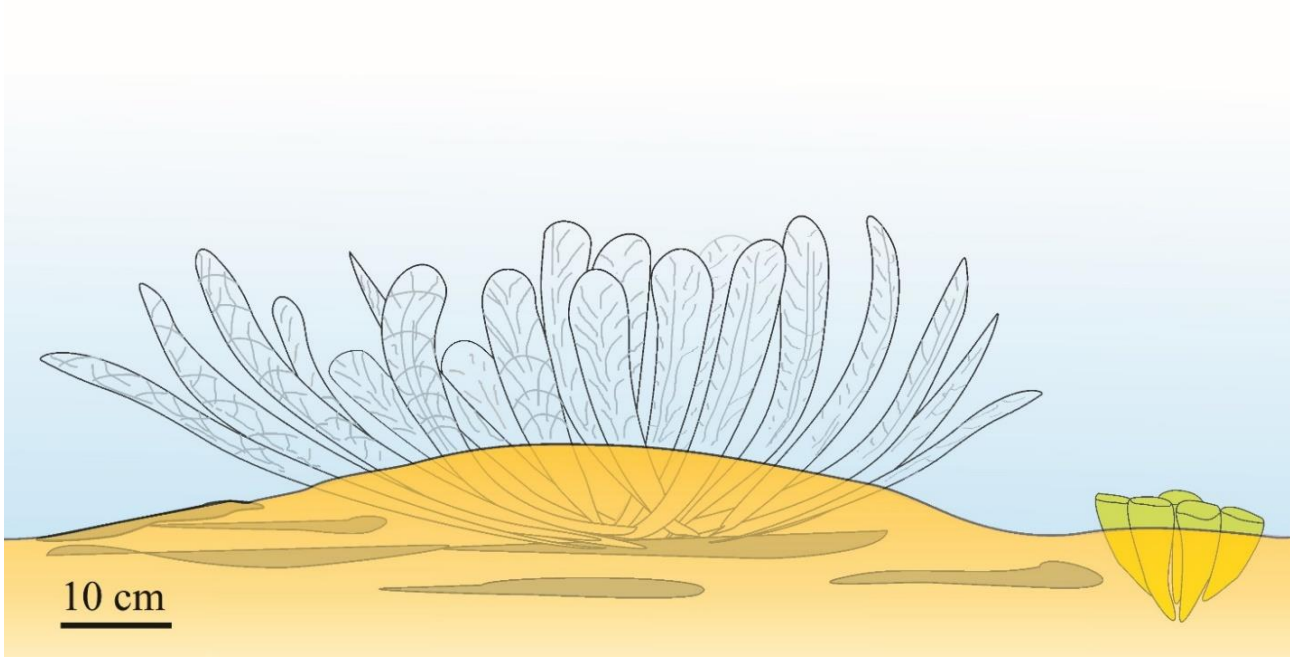

Fig. 1.6. Reconstruction of *Chondrodonta joannae* (Choffat) in life position forming a bouquet-like congregation like low shrub. For comparison, a radiolitid bouquet on the right (Posenato *et al.,* 2020).

Chondrodonta had a predominant calcite, dorso-ventrally elongated and slightly inequivalve shell. It was an epifaunal filter-feeding and represented one of the Mesozoic cementers (*e.g.,* lithiotids, rudists, oysters) with a gregarious life-habit (Fig. 1.6). *Chondrodonta* developed a "mud-sticker" strategy of bottom stabilization (*e.g.,* Ayoub-Hannaa & Fürsich, 2011) like the rudist elevator ecological morphotypes (*i.e.,* radiolitids and hippuritids; *see* Skelton & Gili, 2002) and formed highly dense aggregates (bivalve mounds, reefs, pavements, carpets) which influenced the sedimentation rates and the dynamics of the carbonate platforms (Gili *et al.*, 1995; Riding, 2002; Skelton & Gili, 2012; Harper, 2012; Posenato & Masetti, 2012; Bassi *et al.*, 2017).

Chondrodonta accumulations are reported worldwide (Dhondt & Dieni, 1992, 1993), from Japan and the Middle East to the Caribbean, in a set of marine sub-environments including tidal flats, lagoons, back-reefs and platform margins. The bivalve is documented both in monospecific biostromes (*e.g.,*

Phelps, 2011; Phelps *et al.*, 2014; Posenato *et al.*, 2018) and within rudist facies (*e.g.,* Bover-Arnal *et al.*, 2010; Posenato *et al.*, 2020).

The valves of *Chondrodonta* are often found still articulated due to the dorso-ventrally elongated and tightly interlocked chondrophores, which "*allowed very little motion of valves*" (Stanton, 1901, p. 302). For this reason, the diagnostic taxonomical characters of the inner shell surface are generally not detectable and, therefore, the systematic position of *Chondrodonta* is still debated. A reorganization of the available systematic remarks of the bivalve has been attempted in the studies of Posenato *et al.* (2018, 2020), summarized here below.

1.2.2. Systematic remarks

Chondrodonta was tentatively placed by Stanton (1901, 1947) within the Pectinacea whereas Douvillé (1902), based on a supposed dimyarian condition, suggested a close relation with Pinnidae. Other authors referred it to the Ostreida (*e.g.,* Hoernes, 1902; Schubert, 1903; Nevesskaya *et al.*, 1971; Dhondt & Dieni, 1993; Bieler *et al.*, 2010), or to "*doubtful members*" of Ostreida (Cox & Stenzel, 1971; Carter, 1990). The affinity with oysters proposed by Dhondt & Dieni (1993) was based on the occurrence of chomata in some *Chondrodonta* shells. However, these structures also occur in the Plicatulidae (Carter *et al.*, 2012).

Freneix & Lefévre (1967) proposed a close affinity of the family Chondrodontidae with Plicatulidae and Prospondylidae, due to the same cemented right valve, to the lack of the byssal attachment and to a similar oyster-like morphology. In the most recent classifications of Bivalvia, Carter *et al.* (2011) placed Chondrodontidae within the superfamily Plicatuloidea (Order Pectinida). This classification is supported by recent observations on the shell composition and microstructures (Posenato *et al.*, 2018). The affinities with the living *Plicatula* are (1) the cementation on the right valve, (2) the occurrence of an inner aragonitic layer, replaced in the fossil shells by sparry calcite cement, and (3) an outer layer of simple and irregularly crossed foliated calcite. However, *Plicatula* and *Chondrodonta* also show significant differences, mostly concerning the hinge and ligament morphologies.

The morphology of the hinge plate and of the chondrophores of *Chondrodonta* were used to distinguish three subgenera (Freneix & Lefèvre, 1967). *Chondrodonta* s.s. is characterized by a smooth hinge plate, with *C. munsonii* (Hill) as type-species. This type of hinge plate occurs also in the Aptian *C. glabra* Stanton, documented from both Texas (Stanton, 1901, 1947) and southern Italy (Gargano Promontory; Posenato *et al.*, 2018). *C. glabra* Stanton represents an early evolutionary phase of the bivalve, characterized by a small size and by a prevailing smooth, non-plicate shell with

a short hinge plate. *C. glabra* developed a "mud-sticker" bottom stabilization and produced moderately elongated, stick-like shells (Guerzoni, 2016; Posenato *et al.*, 2018).

Chondrodonta (*Cleidochondrella*) is characterized by a double chondrophore of the attached valve, with *C. elmaliensis* Freneix and Lefèvre as type-species (Santonian – Campanian in age). *Chondrodonta* (*Freneixita*) Stenzel (pro *Chondrella* Freneix and Lefèvre) is, instead, distinguished by a double elongated scar on the hinge plate, formerly considered by Douvillé (1902) as a muscle scar, and reinterpreted by Freneix & Lefèvre (1967) as an internal ligament coupled with the resilium between the chondrophores. Based on the hinge plate morphology, *C. joannae* (Choffat) can be referred to the subgenus *Chondrodonta* (*Freneixita*), characterized by a large shell with considerably morphological variability ranging from elongate-ovate to fan-shaped forms (Dhondt & Dieni, 1993).

1.2.3. Stratigraphic distribution of the Chondrodonta accumulations

Although some authors report *Chondrodonta* in Southern Tethys shallow-water limestones of probable (?) Berriasian – Hauterivian age (*see* Pratt & Smewing, 1990; Zaghbib-Turki, 2003; Masse *et al.*, 2015), the first recognized occurrence of *C. glabra* is documented in the Barremian – early Aptian of the Caribbean Province (Scott & Finch, 1999; Phelps *et al.*, 2014). In the Mediterranean and Middle East Provinces, the first occurrence of *Chondrodonta* is documented in Switzerland (Wissler *et al.*, 2003; Bover-Arnal *et al.*, 2011), in southern France (Masse, 1993; Leonide *et al.*, 2012), in Italy (Graziano *et al.*, 2013; Graziano & Raspini, 2015) and in Oman (Immenhauser *et al.*, 2004), in limestones of Barremian - early Aptian age.

The first *Chondrodonta* species with plicate shells is reported in the Carribean Province and ranges from the early Albian (*C. youngi* Scott) to the middle – late Albian (*C. munsoni* Stanton; Scott, 2007; Scott & Filkorn, 2007; Scott & Hinote, 2007).

Along the Tethyan margins, the better-known plicated *C. joannae* (Choffat) spreads during the Late Cretaceous (*e.g.,* Dhondt & Dieni, 1993; Ayoub-Hannaa & Fürsich, 2011; Ayoub-Hannaa *et al.*, 2014). In the Adriatic Carbonate Platform, for instance, this species produced thick and widespread shell accumulations, formerly used as regional marker beds (*e.g.,* Gušić & Jelaska, 1993; Jurkovšek *et al.*, 1996). In literature, the most recent observations of *Chondrodonta* are in the middle - upper Turonian carbonates of Israel (Bein, 1976; Frank *et al.*, 2010) and in the (?) Santonian – lower Campanian shallow-water limestones of Turkey (Freneix & Lefèvre, 1967).

Although *Chondrodonta* has been reported in several studies on Cretaceous shallow-water limestones, datasets collected in multiple decades of research and with different methods inevitably complicate the assignment of a precise stratigraphic position for these bivalve accumulations.

Moreover, despite its great abundance and wide stratigraphic and geographic distribution, there is a very little available literature focusing on the possible palaeoenvironmental significance of the proliferation of this bivalve, especially with respect to the stratigraphic intervals of Cretaceous OAEs. According to some authors (Graziano, 2013; Posenato *et al.*, 2018, 2020), *Chondrodonta* can be considered as an opportunistic, r-strategist taxon and its proliferation around the times of Cretaceous OAEs could be interpreted as evidence of environmental instability (*e.g.,* nutrient loading) leading to population blooms (Posenato *et al.*, 2020) and predominance over other biota (*e.g.,* rudists).
However, the exact timing between its proliferation and the onset/termination of OAEs as well as the possible factors triggering its flourishing have not been understood yet; therefore, the role of *Chondrodonta* within a context of environmental stress in shallow-water carbonate platforms at the turn of oceanic anoxic events, is today still unclear.

1.3. Aim and general outline of the Thesis

The Thesis aims to define a precise time-relationship between the proliferation of *Chondrodonta* and some of the major Cretaceous OAEs as well as to shed a light on the possible palaeoenvironmental factors triggering the flourishing of this bivalve. The objective is to highlight the stratigraphic occurrence, distribution, and ecological significance of *Chondrodonta* with respect to the palaeoenvironmental changes (*e.g.,* from oligo- to mesotrophic benthic communities) recorded in shallow-water areas during OAEs.
The selected *Chondrodonta* accumulations crop out in shallow-water carbonate platforms of the central Tethys: the Apulia Carbonate Platform (early Aptian) and the Adriatic Carbonate Platform (late Cenomanian). The choice of the abovementioned *Chondrodonta*-bearing stratigraphic successions is mainly linked to the geographical proximity of the outcrops (circum-Mediterranean area). Also, the good exposure of all the studied stratigraphic sections has been deemed essential for more precise and detailed analyses.
To define the precise stratigraphic position of the *Chondrodonta* accumulations with respect to the Oceanic Anoxic Events 1a and 2 time-intervals, sedimentologic-lithostratigraphic, biostratigraphic and chemostratigraphic ($\delta^{13}C$, $\delta^{18}O$ and $^{87}Sr/^{86}Sr$) analyses have been carried out on the selected outcrops. The concentration of major, trace elements and REE has been measured to outline the geochemical pattern of the *Chondrodonta*-bearing outcrops and to help palaeoecological and palaeoenvironmental interpretations.
After this introductory first chapter, the second chapter (2) gives a brief introduction on the methods used. The third chapter (3) focuses on the *Chondrodonta* accumulations of the lower Aptian Apulia

Carbonate Platform (Gargano Promontory, SE Italy) and integrates data of stratigraphic sections spaced ~ 5 km apart. The aim is to determine both the temporal relationship between the *Chondrodonta* beds and the OAE1a interval and the palaeoenvironmental changes triggering the flourishing of the bivalve. Results are then compared to the coeval major environmental perturbations recorded in the adjacent Adriatic/Ionian Basin.

The fourth chapter (4) deals with the stratigraphic interval of proliferation of *Chondrodonta* in the upper Cenomanian Adriatic Carbonate Platform (northwestern Istrian Peninsula, NW Croatia). The aim is to define both its stratigraphic position with respect to OAE2 and the possible palaeoenvironmental changes at the base of its flourishing. Results are correlated to the coeval major perturbations recorded in the nearby basinal settings.

Chapter five (5) presents a literature review on the *Chondrodonta* accumulations worldwide reported, aimed to highlight the precise stratigraphic occurrence and the possible synchronicity of these beds at the turn of the late early Aptian OAE1a and of the late Cenomanian – early Turonian OAE2. The sixth chapter (6) summarizes and draws the conclusions on the results previously presented and discussed.

2. Methods

The following methods have been integrated to define the precise stratigraphic position and the ecological significance of the *Chondrodonta* accumulations investigated in this Thesis. The stratigraphic framework around these bivalve beds was built using biostratigraphic and chemostratigraphic ($\delta^{13}C$, $\delta^{18}O$, $^{87}Sr/^{86}Sr$) data. Sedimentologic and petrographic analyses were coupled with major, trace elements and REE concentrations to infer palaeoenvironmental changes associated with the proliferation of *Chondrodonta*.

2.1. Fieldwork, lithofacies analysis and biostratigraphy

The investigated stratigraphic intervals were sampled at decimetre- to metre- scale and a higher sampling density was applied across the *Chondrodonta* accumulations.

Textures were classified based on Dunham (1962), Embry & Klovan (1971), Insalaco (1998) and Lokier & Al Junaibi (2016). Rock components for lithofacies definition were analysed semi-quantitatively and expressed in terms of relative abundance (abundant, common, rare) with respect to the texture of the rocks.

The biostratigraphic schemes here used are based on the most recent reviews of small benthic foraminifers (Velić, 2007; Schröeder *et al.*, 2010; Chiocchini *et al.*, 2012) and of dasycladales (Carras *et al.*, 2006).

2.2. Geochemical analyses

2.2.1. $\delta^{13}C$ and $\delta^{18}O$ curves

In all the investigated sections, samples were collected at variable spacings, generally between 0.2 – 1 m and analysed for the $\delta^{13}C$ and $\delta^{18}O$ ratios within the purest micritic portion of the rock matrix. To obtain a clear isotope signal free from contamination by bioclasts or by recrystallization, the polished slabs were studied under a binocular microscope and checked with the respective thin sections to identify the most suitable areas to be drilled. The best-preserved *Chondrodonta* and rudist shells were also selected and their grade of preservation was checked under a binocular microscope by analysing visible growth increments, compact fibrous microstructure of the outer shell layers and impacts of bioerosion and fracturing.

About 5 mg of powder was obtained from each sample by micro-drilling polished slabs with a 0.5 – 0.8 mm Tungsten drill-bit and a hand-held drill. The analyses were performed either at the Museum

für Naturkunde of Berlin, Germany or at the School of Earth, Energy and Environmental Sciences of the Stanford University, California, U.S.A.. At the Museum für Naturkunde, approximately 400 µg of sample powder was reacted in 12 ml vacutainer by individual acidic addition (orthophosphoric acid, H_3PO_4 at 98%) at 30°C. The oxygen and carbon isotopic compositions were measured using a Thermo Finnigan GASBENCH II coupled online with a Thermo Finnigan DELTA V isotope ratio mass spectrometer. Pure CO_2 (4.5) was used as reference gas and calibrated against the VPDB standard by using IAEA reference materials (NBS 18, NBS 19). Reproducibility of replicate measurements of lab standards (limestone) is generally better than 0.10‰ (one standard deviation). Some of the samples underwent duplicate analyses to test the reliability of the isotopic signals related to possible micro-variations in the sedimentary textures.

At Stanford, the micritic fraction of the samples was drilled out using a dental micro-drill. Between 50 – 100 µg of sample powder was analysed using a Thermo Finnigan GASBENCH interfaced with a Thermo Finnigan DELTA PLUS XL mass spectrometer via a Thermo Finnigan ConFlo III unit. The weighed-out samples were then placed in sealed vials that were flushed with He gas and reacted with 0.5 ml of phosphoric acid for 1 h at 72°C. The precision obtained from the instrument is 0.021‰ and 0.045‰ (1 σ) for carbon and oxygen, respectively, based on the six measurements of the NBS 19 lab standard.

All results are reported in per mil (‰), in the conventional δ-notation with reference to the Vienna Pee Dee Belemnite (VPDB) standard.

Reliability check. The $\delta^{13}C$ and $\delta^{18}O$ values measured in the studied sections have been interpreted considering the possible issues deriving from the diagenetic alteration of shallow-water carbonates. In the last decades, the high-resolution $\delta^{13}C$ stratigraphy has been successfully applied to the correlation of Cretaceous shallow-water carbonate platforms and hemi-pelagic deposits (*e.g.,* D'Argenio *et al.*, 2004; Wissler *et al.*, 2004; Parente *et al.*, 2007; Burla *et al.*, 2008; Vahrenkamp, 2010; Huck *et al.*, 2011; Di Lucia *et al.*, 2012; Amodio & Weissert, 2017). However, syn- and post-depositional diagenetic alteration (Allan & Matthews, 1982; Lohmann, 1988; Marshall, 1992; Oehlert & Swart, 2014, 2019; Schmitt *et al.*, 2020) as well as biological fractionation and local palaeoceanographic conditions may cause the $\delta^{13}C$ composition of shallow-water carbonates to deviate from the global open ocean value (Patterson & Walter, 1994; Immenhauser *et al.*, 2008; Amodio *et al.*, 2008; Huck *et al.*, 2017). A positive covariance between $\delta^{13}C$ and $\delta^{18}O$ bulk values is often used to infer either decreasing alteration in the freshwater phreatic zone (Swart & Oehlert, 2018) or diagenetic alteration under the meteoric water influx in the mixing zone (Allan & Matthews, 1982). As a result, several studies propose the lack of covariance between $\delta^{13}C$ and $\delta^{18}O$ values as indicative

of the unaltered nature of samples (*e.g.,* Grotzinger *et al.*, 2011 among others). Nevertheless, recent studies point out that a lack of correlation between $\delta^{13}C$ and $\delta^{18}O$ alone cannot be used as proof for sample preservation and that changes in sediment source through time can also produce paired shifts in $\delta^{13}C$ and $\delta^{18}O$ values (Swart & Oehlert, 2018; Oehlert & Swart, 2019).

2.2.2. $^{87}Sr/^{86}Sr$ ratio

About 3 to 10 mg of powder was obtained from each sample by micro-drilling polished surfaces of *Chondrodonta* and rudist shells. A 0.5 mm Tungsten drill-bit with a hand-held drill was used, following the method described in Frijia & Parente (2008). To assess the preservation of the original shell microstructure, shells were screened petrographically using visible light and, where possible, analysed in terms of elemental composition of Mg, Sr, Mn, and Fe (*see* Brand & Veizer, 1980; Steuber *et al.*, 2005; Frijia *et al.*, 2015; Schmitt *et al.*, 2020).

Samples were analysed either at the Institute of Geology, Mineralogy and Geophysics of the Ruhr University Bochum (Germany) or in the class 1000 clean laboratory of the Chemical and Geological Sciences Department at the University of Modena and Reggio Emilia (UNIMORE). At Bochum, after strontium separation by standard ion-exchange methods, strontium-isotope ratios were analysed on a Finnigan MAT 262 thermal-ionization mass spectrometer and normalized to an $^{86}Sr/^{88}Sr$ value of 0.1194 (*see* Huck *et al.*, 2010 and Frijia *et al.*, 2015 for details). At the UNIMORE, about 5 to 10 mg of powder from each sample was cleaned and dissolved, following the procedures described in Li *et al.* (2011) and Vescogni *et al.* (2014). In the dissolution steps, samples were sequentially leached using a solution of 0.3% w/w acetic acid to obtain two solutions with about 30% and then 40% of dissolved material. The second leachate was collected, evaporated to dryness, and dissolved in 3N HNO_3 for the Sr separation. After centrifuging, samples were loaded into Eichrom Sr spec-resin filled columns, washed with 3N HNO_3 and Sr was, finally, eluted with MilliQ(r) water.

The $^{87}Sr/^{86}Sr$ ratio of the samples was determined using a double-focusing MC-ICP-MS with a forward Nier–Johnson geometry (Thermo Fisher Scientific, NeptuneTM) housed at the Centro Interdipartimentale Grandi Strumenti of the UNIMORE (*see* Lugli *et al.,* 2017 for details).
The $^{87}Sr/^{86}Sr$ values were corrected for instrumental bias to a NIST SRM 987 standard value of 0.710248 (McArthur *et al.*, 2001) following the procedure of Howarth & McArthur (1997) and McArthur *et al.* (2001) to derive numerical ages based on the look-up table of McArthur *et al.* (2001) (version 5: 04/2013). The numerical ages were then translated into the chronostratigraphic ages of the Geological Time Scale of McArthur *et al.* (2012, 2020). Minimum and maximum ages were

obtained by combining the statistical uncertainty (2 s. e.) of the mean values of the Sr-isotope ratios with the uncertainty of the seawater curve (*see* Frijia *et al.*, 2015 for details on the procedure).

Concentrations of Ca, Mg, Fe, Sr, and Ba were measured with the Perkin Elmer Optima 4200 DV ICP-OES housed at the UNIMORE. About 2 to 5 mg of powdered samples were repeatedly washed with Milliq water, dried down and dissolved in 1N HNO_3. Samples were then centrifuged, and the supernatant transferred and diluted with Milliq to a 4% nitric acid solution for Mg, Fe, Sr, and Ba analyses. An aliquot of the sample was further diluted to measure Ca. The ICP-OES was externally calibrated with multi-element calibration standards, prepared in a matrix of 4% nitric acid in the concentration range from 1 ppb to 10 ppm for all the elements. Precisions were typically better than 5% RSD (relative standard deviation) for Ca, Mg, Sr, and Fe and better than 20% for Mn and Ba.
In samples with not sufficient material to measure both trace element concentrations and $^{87}Sr/^{86}Sr$, elemental concentrations were measured by the LA-ICP-MS analysis (*see* below).

Reliability check. The $^{87}Sr/^{86}Sr$ ratios measured in the studied samples have been interpreted considering the possible issues deriving from the diagenetic alteration of shells. The outer low-Mg calcite layer of Cretaceous rudist and oyster shells has been widely recognized as a suitable archive for the Sr-isotope composition of ocean waters, allowing to precisely date shallow-water limestones using the Strontium Isotope Stratigraphy (SIS) (*e.g.,* Steuber *et al.*, 2005; Frijia & Parente, 2008; Boix *et al.*, 2011; Huck & Heimhofer, 2015; Frijia *et al.*, 2015; Schmitt *et al.*, 2020). The concentration of strontium, iron and manganese in shells is commonly used for estimating the degree of diagenetic alteration (Ullmann & Korte, 2015). Several elemental threshold values have been suggested for both rudists (Fe < 100 ppm, Mn < 50 ppm, Sr > 700 ppm; Steuber *et al.*, 2005; Frijia *et al.*, 2015) and *Chondrodonta* (Mn < 250 ppm, Sr > 500 ppm; Damas Mollá *et al.*, 2006). Considering that diagenesis is usually associated with a decreased Sr concentration coupled with increased Fe - Mn concentrations and increased $^{87}Sr/^{86}Sr$ ratios, only shells with low iron and manganese concentrations in skeletal calcite and high strontium concentrations are, usually, considered suitable for SIS.

2.2.3. Major, trace elements and REE concentration

2.2.3.1. Geochemistry of carbonates: an overview

In the geochemical study of rocks and sediments, major elements (Ca, Al, Mg, Na, K, Si, Ti, Fe, Mn, and P) are the main rock constituents and are conventionally distinguished from trace elements (*e.g.,* Cr, Zr, Ni) by having a concentration greater than 0.1%.

The concentration of both major and trace elements in stratigraphic sections is considered a useful tool to decipher the geochemical environment associated to the deposition of carbonate rocks (*e.g.,* Frimmel, 2009; Bodin *et al.*, 2013; Westermann *et al.*, 2013; Fantasia *et al.*, 2016; Coimbra *et al.*, 2017; Dickson *et al.*, 2017; Engelke *et al.*, 2018; Özyurt *et al.*, 2020), as it gives information on the detrital input, on the palaeoproductivity conditions and on the seawater oxygenation.

Al and Ti (as well as Si and Zr) are generally derived from crustal rocks and, therefore, their concentration in limestones provides information on the detrital/terrestrial input (Brumsack, 2006). Based on the assumption that Al represents the major clay mineral detrital input (Brumsack, 2006; Pearce *et al.*, 2009), the concentration of many major and trace elements is usually normalized to Aluminum before being interpreted (*see* Calvert & Pedersen, 1993; Morford *et al.*, 2001; Tribovillard *et al.*, 2006; Hetzel *et al.*, 2009; Pearce *et al.*, 2009; Westermann *et al.*, 2013; Sanchez-Hernandez & Maurrasse, 2016; Hueter *et al.*, 2019 among others).
P is considered an important source of nutrients for the ocean, which drives primary productivity on various time scales (*e.g.,* Tyrrell, 1999; Benitez-Nelson, 2000). The flux of dissolved P into the seawater is mainly controlled by continental runoff via river water (Föllmi, 1996; Compton *et al.*, 2000) and an increase in the concentration of P in carbonates is usually interpreted as indicative of higher nutrient levels in the oceans (Föllmi, 1996; Hetzel *et al.*, 2009; Westermann *et al.*, 2013).

Variations in the concentration of Redox-Sensitive Trace Elements (RSTE) in marine sediments are used in geochemical studies to characterize changes in the redox state during the deposition of carbonate rocks (Algeo & Maynard, 2004; Tribovillard *et al.*, 2004, 2006; Brumsack, 2006). Under reducing conditions, RSTE are less soluble in the seawater and are preferentially transferred from the water column into the sediments (Tribovillard *et al.*, 2006). The reducing conditions occurring during OAEs, for instance, enhance the transfer of RSTE into organic-rich sediments (*see* Algeo & Maynard, 2004; Snow *et al.*, 2005; Tribovillard *et al.*, 2006; Pearce *et al.*, 2009; Jenkyns, 2010; Stein *et al.*, 2011, 2012; Owens *et al.*, 2017); the latter become, therefore, richer in RSTE with respect to the average shale values of Wedepohl (1971, 1991). Increased uptake of RSTE during basinal black shale deposition further reduces their concentration in the seawater reservoir of the platform top, resulting in a decrease of the RSTE concentration in shallow-water carbonates (*see* Algeo, 2004; Hueter *et al.*, 2019). Conversely, increases in the concentration of RSTE may represent a shift to more “normal marine” and more oxygenated conditions on the platform top.

To reconstruct the palaeo-redox conditions of sedimentary deposits, a suite of RSTE is generally recommended to be used rather than a single element (Tribovillard *et al.*, 2006). The overall changes

in the RSTE concentrations should be looked at different temporal scales due to their variable residence time in the oceans (from a few kyr to hundreds of kyr; Ku *et al.*, 1977; Sholkovitz & Schneider, 1991; Shields & Stille, 2001; Bodin *et al.*, 2007). Nevertheless, due to their different solubility in waters with variable levels of oxygen, overall decreases in the RSTE concentration in shallow-marine deposits are commonly assigned to an oxygen deficiency phase (Algeo & Maynard, 2004; Tribovillard *et al.*, 2006; Bodin *et al.*, 2007; Hueter *et al.*, 2019).

Rare Earth Elements (REE) are an extremely coherent group in terms of chemical behavior, widely used to trace oceanographic processes and as proxies of water-mass oxygenation (*e.g.,* Webb & Kamber, 2000; Nozaki, 2008; Frimmel, 2009; Liu *et al.*, 2019; Özyurt *et al.*, 2020). Due to their coherent chemical properties in the marine system, REE exhibit systematic changes across their series (from La to Lu), related to the progressive filling of the f-electron shell (Zhang *et al.*, 1994; Zhang & Nozaki, 1996, 1998; Nozaki, 2001; Azmy *et al.*, 2011). Particularly, the Cerium concentration in the seawater shows an anomalous behavior compared to other REE, due to its tetravalent state in oxic environments leading to its enhanced removal from the water column by scavenging processes (Elderfield, 1988; Nozaki, 2008). Cerium, together with Europium which shows a similar behavior, is a redox-sensitive element considered as a natural proxy for revealing interaction processes between particles and solutions, and redox reactions (*e.g.,* Kim *et al.*, 2012). Consequently, the Cerium (Ce) anomaly (Ce/Ce*; *i.e.,* the deviation of the Ce concentration relative to neighboring trivalent REE) can be used to trace seawater redox conditions in sediments where diagenetic alteration and/or a detrital source of REE content can be excluded (*e.g.,* De Baar *et al.*, 1988; Kim *et al.*, 2012; Bodin *et al.*, 2013; Chen *et al.*, 2015; Li *et al.*, 2019; Hueter *et al.*, 2019; Özyurt *et al.*, 2020).

2.2.3.2. The LA-ICP-MS analysis and interpretation of the results

Elemental concentrations in bulk samples were measured by the Laser Ablation Inductively Coupled Plasma Mass Spectrometry (LA-ICP-MS) analysis. The purest micritic fraction of all samples was properly checked under a binocular microscope avoiding shells, bioclasts and cements.

The concentration of a selected group of RSTE (V, As, Mo, U) was measured to assess the oxygenation state of the water as well as the concentration of P was used to estimate the palaeoproductivity conditions. Measured concentrations include Al and Ti, used to approximate the abundance of terrigenous matter, and rare earth elements (REE). Particularly, the cerium anomaly (Ce/Ce* ratio) was used as further proxy for the degree of seawater oxygenation. This set of elements has been commonly used in the geochemical characterization of Cretaceous shallow- and deep-water

limestones (*e.g.,* Hetzel *et al.*, 2009; Pearce *et al.*, 2009; Stein *et al.*, 2011, 2012; Westermann *et al.*, 2013; Sanchez-Hernandez & Maurrasse, 2016; Dickson *et al.*, 2017; Owens *et al.*, 2017; Hueter *et al.*, 2019 among others) and, for the aim of the Thesis, it has been used to evaluate the geochemical concentrations within the intervals of proliferation of *Chondrodonta* with respect to the limestones deposited above and below.

The elemental concentrations were determined using a 213 nm, Q-switched Nd:YAG laser from New Wave connected to a Thermo Finnigan ELEMENT2 sector field ICP-MS, located at the Max Planck Institute for Chemistry of Mainz (Germany) (Jochum *et al.*, 2007). Each sample was measured in three spots in two areas of the thick section. Standard settings of the laser system were (1) an energy density of 7 J cm^{-2}, (2) a pulse rate of 10 Hz, (3) low oxide production rates (ThO/Th < 0.5 %), (4) a laser spot diameter size of 60 – 120 μm, and (5) washout, blank count rate, and ablation times of 45, 20, and 110 s, respectively. NIST-612 and MACS-3 were used as calibration material and ^{43}Ca as an internal standard to calculate absolute element concentrations from signal intensities. Precision (1 relative standard deviation) is about 5 – 10%.
All elemental concentrations in the bulk samples were normalized to Al and plotted as element/Al ratios. This step was aimed to correct the effect of variable dilution by carbonate and biogenic silica as well as to highlight the relative enrichment (or depletion) of elements with respect to clay (*e.g.,* Calvert & Pedersen, 1993; Morford *et al.*, 2001).

REE concentrations were normalized to the Post-Archean Australian Shale (PAAS) standard values given in Taylor & McLennan (1985). After the normalization, the Ce anomaly (Ce/Ce*) was defined following the Nozaki's (2008) calculation:

$$Ce/Ce^* = 2Ce_N / (La_N + Pr_N)$$

where N stands for shale- (*i.e.,* PAAS-) normalized concentrations.

Reliability check of the REE signal. Contamination by terrestrial clays can control the primary REE content of ancient marine carbonates (Nothdurft *et al.*, 2004; Liu *et al.*, 2019). Several lines of evidence can be used in combination to infer a diagnostic seawater REE signature. Beside negative Ce anomalies (0.38 – 0.81; average 0.57), the Y/Ho ratio can be used as tracer to assess whether carbonate particles reflect a primary marine signature or siliciclastic components (Bau, 1991; Nozaki *et al.*, 1997; Nothdurft *et al.*, 2004; Frimmel, 2009; Liu *et al.*, 2019). According to literature, typical Y/Ho ratios in marine carbonates free from terrigenous contamination, generally show a wider range of values (44 – 74, with an average of 45.50) compared to the modern seawater Y/Ho ratio of 60 or

even higher (Bau, 1991, 1996; Nozaki *et al.*, 1997; Liu *et al.*, 2019); Y/Ho ratios with a value of 35 or lower are, instead, more likely to reflect a siliciclastic contamination (Chen *et al.,* 2015). Also, Ling *et al.* (2013) propose high Aluminum (> 3500 ppm) and Scandium (> 2 ppm) concentrations as indexes of terrestrial contamination on both the REE signal and the Ce anomaly.

A small quantity of terrestrial particulate matter (*i.e.,* shale), which has a high REE content, may also deviate the overall REE pattern from the typical seawater-like one (the South Pacific deep-water curve of Zhang & Nozaki, 1996), making it closer the North American Shale Composite of Gromet *et al.* (1984). REE may also take up the 'bell-shaped' pattern, characterized by MREE (*i.e.,* Mid REE; Sm, Eu, Gd, Tb, Dy) enrichments and declining HREE (*i.e.,* Heavy REE; Ho, Er, Tm, Yb, Lu) and LREE (*i.e.,* Light REE; La, Ce, Pr, Nd), typical of limestones contaminated by siliciclastic and/or by riverine influence (Della Porta *et al.*, 2015 and references therein). The terrestrial influence on the REE signal is also supported by a LREE/HREE ratio close or even above 1.
The ratio can be calculated using the following formula (*see* Menendez *et al.*, 2018 and references therein):

$$LREE/HREE = (La_N + 2*Pr_N + Nd_N) / (Er_N + Tm_N + Yb_N + Lu_N)$$

where N stands for shale- (*i.e.,* PAAS-) normalized concentrations.

Furthermore, original REE patterns can be significantly altered during carbonate diagenesis (Azmy *et al.*, 2011; Smrzka *et al.*, 2019; Özyurt *et al.*, 2020 and references therein). Several parameters have been investigated to assess the potential diagenetic influence on the REE signature in limestones (Nothdurft *et al.*, 2004; Frimmel, 2009; Liu *et al.*, 2019). It has been shown that the progressive REE scavenging during post-depositional diagenesis may produce a positive correlation between the Ce anomaly and ΣREE (*i.e.*, summation of REE + Y abundances) as well as between the Eu anomaly and ΣREE (Shields & Stille, 2001; Shields & Webb, 2004). The Eu anomaly, like the Ce anomaly, can be calculated following the definition of Bau & Dulski (1996):

$$Eu/Eu^* = 2Eu_N / (Sm_N + Gd_N).$$

where N stands for shale- (*i.e.,* PAAS-) normalized concentrations.

Similarly, an absence of correlation between Ce/Ce* and Eu/Eu* implies a negligible or absent influence of post-depositional alteration on the measured Ce/Ce* (*e.g.,* Liu *et al.*, 2019).
Given these conditions, the relationship between Ce/Ce* and Pr/Pr* can be used to characterize redox conditions by the La anomaly diagram (Bau & Dulski, 1996).

The La anomaly diagram (Bau & Dulski, 1996; Bodin *et al.*, 2013) is, indeed, used to assess both the genuine/real Ce anomaly and whether the Ce/Ce* ratio could be used to trace the real seawater oxygenation state.

A negative Ce anomaly can also be artificially created by a La enrichment rather than by a Ce depletion and, therefore, Bau & Dulski (1996) proposed to compare the Ce anomaly with the Pr anomaly to trace a potential La anomaly. According to Bau & Dulski (1996), in the La anomaly diagram (*see* an example in Fig. 2.1) field I indicates no anomaly, field IIa indicates a positive La anomaly causing an apparent negative Ce anomaly, field IIb indicates a negative La anomaly causing an apparent positive Ce anomaly, field IIIa indicates a genuine positive Ce anomaly and field IIIb indicates genuine negative Ce anomaly.

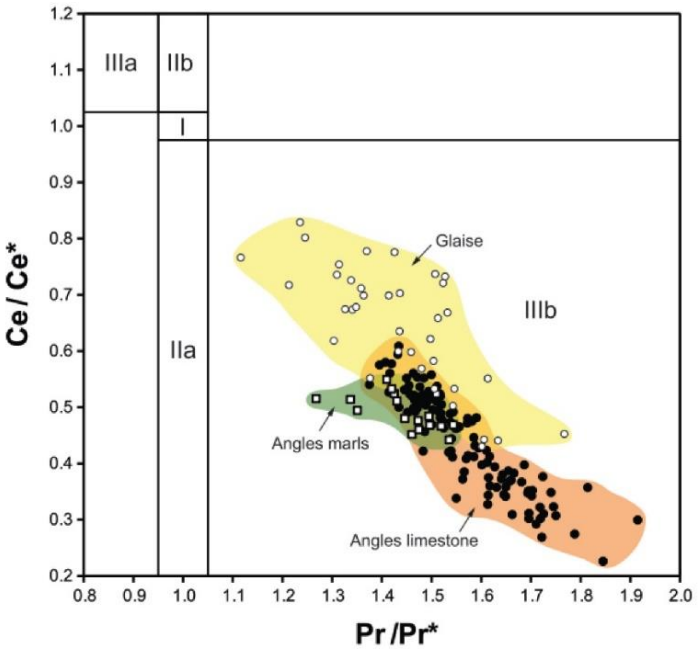

Fig. 2.1. Example of Lanthanum anomaly diagram (from Bodin *et al.*, 2013) in which all samples fall within the IIIb field, indicative of a genuine/real negative Ce anomaly.

The Pr/Pr* anomaly used in the La anomaly diagram is calculated following the definition of Bau & Dulski (1996):

$$Pr/Pr^* = 2Pr_N / (Ce_N + Nd_N)$$

where N stands for shale- (*i.e.,* PAAS-) normalized concentrations.

3. *Chondrodonta* proliferation within the lower Aptian Apulia Carbonate Platform

3.1. Abstract

The lower Aptian *Chondrodonta* bedsets within the inner platform limestones of the Apulia Carbonate Platform (Gargano Promontory, southern Italy) underwent stratigraphic and geochemical analyses to assess the environmental controls on the proliferation of *Chondrodonta* and its timing and causal relationship to OAE1a.

Chondrodonta occurs with sparse to common individuals within requieniid rudist limestones, forms monospecific biostromes during the early phase of environmental stress and then rapidly disappears at the peak of OAE1a. It proliferates in an interval of fluctuating seawater oxygenation with relatively increased trophic sources and correlates also with increasing nutrient levels in the nearby pelagic realm.

These fluctuating and unstable environmental conditions right below the onset of OAE1a created an environmental "window" favourable for *Chondrodonta* to flourish, outplaying the less tolerant benthos (*i.e.,* rudists). Further increase in inhospitable conditions leading to OAE1a, constituted an upper threshold for *Chondrodonta* and allowed mesotrophic taxa like *Bacinella-Lithocodium* and orbitolinids to dominate the benthic community.

3.2. Geological setting

The Apulia Carbonate Platform (ACP) represents a major palaeo-geographic domain in the central - southern margin of the Mesozoic Tethys (Bernoulli, 2001; Bosellini, 2004). During the Cretaceous, it was located at tropical palaeo-latitudes, either in a set of isolated carbonate banks (Eberli *et al.*, 1993; Bosellini *et al.*, 1999a) or as a broad peninsula (Bosellini, 2002).

From a structural point of view, the ACP represents part of the stable and relatively undeformed foreland of the southern Apennine thrust belt (Bosellini *et al.*, 1999a) (Fig. 3.1). The westward margin of the ACP is today buried under the Apennine thrust sheets (Bradanic foredeep) whereas the eastward and northward margins are bounded by the basinal deposits of the Ionian of the Umbria-Marche Basins, respectively. To the southeast, the Jurassic – Early Cretaceous margin of the ACP lies 20 – 30 km offshore the present Apulia coastline (De Dominicis & Mazzoldi 1989; De Alteriis & Aiello, 1993).

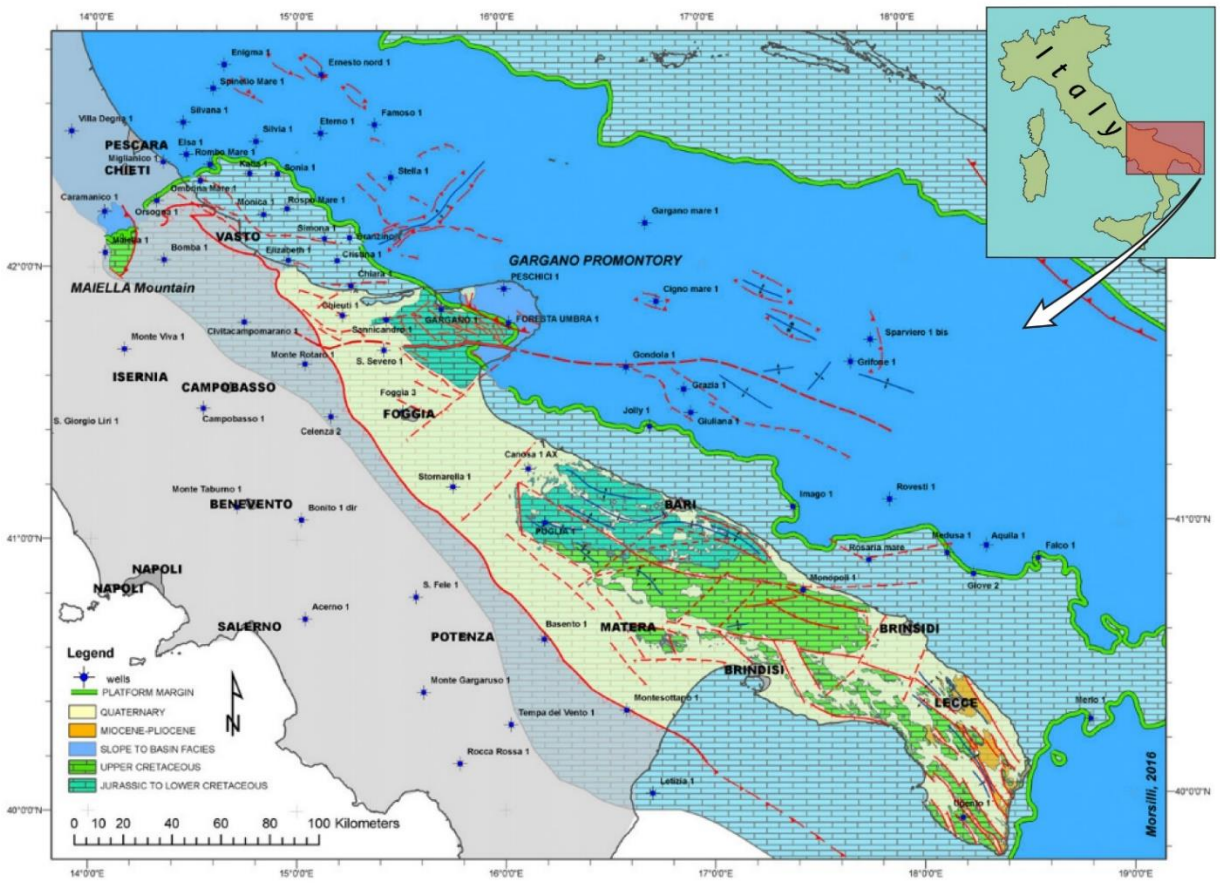

Fig. 3.1. Distribution of Jurassic – Quaternary sedimentary deposits along the Apulia Carbonate Platform (ACP) and the adjacent Adriatic Basin (Morsilli, 2016; Morsilli *et al.*, 2017).

The margin of the ACP is characterized by an overall aggrading architecture with different geometric and depositional features (Bosellini *et al.*, 1999a; Borgomano, 2000; Hairabian *et al.*, 2015). Although Cretaceous inner platform facies extensively crop out in the Apulia region, the ACP margin and its transition to the coeval Ionian/Adriatic basinal succession are exposed only on the Gargano Promontory (from Middle Jurassic to Eocene) and on the Maiella Mountain (from Upper Cretaceous to Miocene) (Morsilli & Bosellini, 1997; Bosellini *et al.*, 1999a). Elsewhere, the platform margin is located offshore in the Adriatic Sea to the east and beneath the Apennines foredeep to the west, covered by Cenozoic successions (Morsilli *et al.*, 2017).

The Gargano Promontory (south-eastern Italy; Fig. 3.2) represents the north-eastern margin of the ACP (Bosellini *et al.*, 1999a; Borgomano, 2000; Morsilli *et al.*, 2017). It was partially involved in the Neogenic southern Apennines and Dinaric thrust belts and is currently interpreted as a deformed foreland. It is folded in a gentle and broad NW-SE anticline, dissected by Miocene – Pliocene reverse and normal faults and by Pleistocene strike-slip faults (Bertotti *et al.*, 1999; Brankman & Aydin, 2004; Billi *et al.*, 2007).

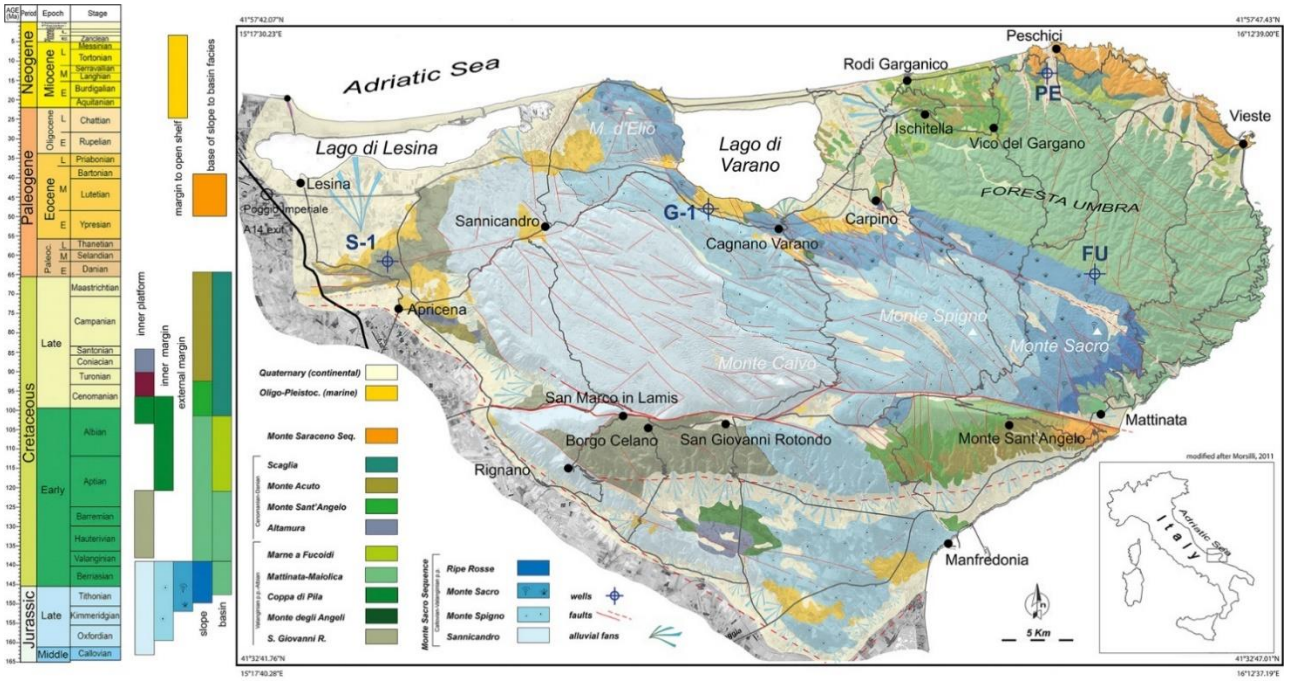

Fig. 3.2. Simplified geological map of the Gargano Promontory (Morsilli, 2011; Morsilli *et al.*, 2017).

The outcropping carbonate succession on the Gargano Promontory records a suite of depositional environments ranging from inner platform-peritidal to relatively deep-water pelagic (Morsilli & Bosellini, 1997; Bosellini *et al.*, 1999a; Borgomano, 2000). The Gargano outcrops are also relevant as potential analogs of the opposite Adriatic Carbonate Platform (AdCP), whose limestones occur from Istria to Greece and in the Adriatic offshore (Bega, 2015).

The backbone of the Gargano Promontory mainly consists of Upper Jurassic to Eocene carbonates of platform-to-basin settings (Martinis & Pavan 1967; Masse & Luperto Sinni, 1989; Bosellini *et al.*, 1993). The only Mesozoic part of the shallow-water succession is estimated to be ~ 5 km thick and 1 - 2 km thick in the coeval basinal area (Morsilli *et al.*, 2017). A small outcrop of upper Triassic evaporites (*i.e.*, Anidriti di Burano; Martinis & Pieri, 1964) occurs on the northern seashore (Fig. 3.2). The exposed succession also comprises Miocene sediments, unconformably overlying the Cretaceous and Jurassic deposits in scattered outcrops throughout the Promontory.

During the Late Jurassic – earliest Cretaceous (Callovian *p.p.* – Valanginian *p.p.*), shallow-water and slope-basin domains were connected by marginal and depositional slope areas (Morsilli & Bosellini, 1997). The geometry of the platform–slope transition is still poorly constrained for the Valanginian *p.p.* - early Aptian interval (Bosellini *et al.*, 1999a). Approximately 500 - 600 m of inner platform deposits are preserved (San Giovanni Rotondo Limestone) and abundant calciturbidites occur in the adjacent slope succession (lower Mattinata formation), gradually passing to basinal deposits (upper

Maiolica formation). Margin-bioconstructed (rudists-sponges) facies occur only at Montagna degli Angeli (Monte degli Angeli Limestone), in the southern part of the Promontory (Fig. 3.2).

The margin and the adjacent slope of the ACP suddenly became inactive during the early Aptian and underwent major physiographic changes during the upper Aptian – Cenomanian interval. In the Albian – Turonian interval, a tectonically-induced relative sea-level lowstand provoked a subaerial exposure of the southern Apennines carbonate platforms and the deposition of diachronous bauxite horizons (considered as ? late Cenomanian – Turonian *p.p.* in age on the Gargano outcrops; Hairabian *et al.*, 2015). A subsequent reflooding of the ACP (Turonian *p.p.* - ? Coniacian) produced several complexes of lobes, mainly composed of bioclastic calcarenites and deposited at the base of the slope up to the Danian *p.p.* (Monte Acuto Limestone). The Paleocene - early Eocene interval records further failures along the platform margin (Bosellini *et al.*, 1999a; Adams *et al.*, 2002), resulted in the deposition of mega-breccias and bioclastic turbidites throughout the entire Gargano Promontory.

3.3. Stratigraphic framework

The San Giovanni Rotondo Limestone (SGRL) (*sensu* Cremonini *et al.*, 1971; Luperto Sinni & Masse, 1986; Claps *et al.*, 1996) here investigated, represents the inner platform deposits of the Lower Cretaceous ACP. The SGRL crops out on the eastern and south-eastern Gargano Promontory (Fig. 3.2, 3.3A) and changes eastwards to the margin facies of the Monte degli Angeli Limestone and to the slope and basin deposits of the Mattinata and Maiolica formations (Bosellini *et al*., 1999a).

The SGRL is a 500 - 600 m-thick shallow-water carbonate succession spanning the upper Valanginian *p.p.* - Aptian *p.p.* (Claps *et al.*, 1996) (Fig. 3.3A). A first sedimentological description was given by Luperto Sinni & Masse (1986), then revised by Claps *et al.* (1996) who divided the stratigraphic succession into three members (Fig. 3.4).

Member 1 (140 m thick, partially equivalent to the Borgo Celano Member of Luperto Sinni & Masse, 1986), late Valanginian – middle Hauterivian *p.p.* in age, consists of a monotonous and non-cyclic subtidal succession of metre-thick mudstones and wackestones beds, and scattered decimetre-thick skeletal or oolitic grainstones to packstones.

Member 2 (~ 310 m thick, partially equivalent to the Loferitic member of Luperto Sinni & Masse, 1986), middle Hauterivian *p.p.* – upper Barremian *p.p.* in age, consists of a cyclic succession characterized by a quasi-periodic alternation of "loferitic" beds with centimetre-thick layers of green shales and stromatolites, commonly with dinosaur footprints on the bed surfaces (Bosellini & Morsilli, 2001; Petti *et al.*, 2008).

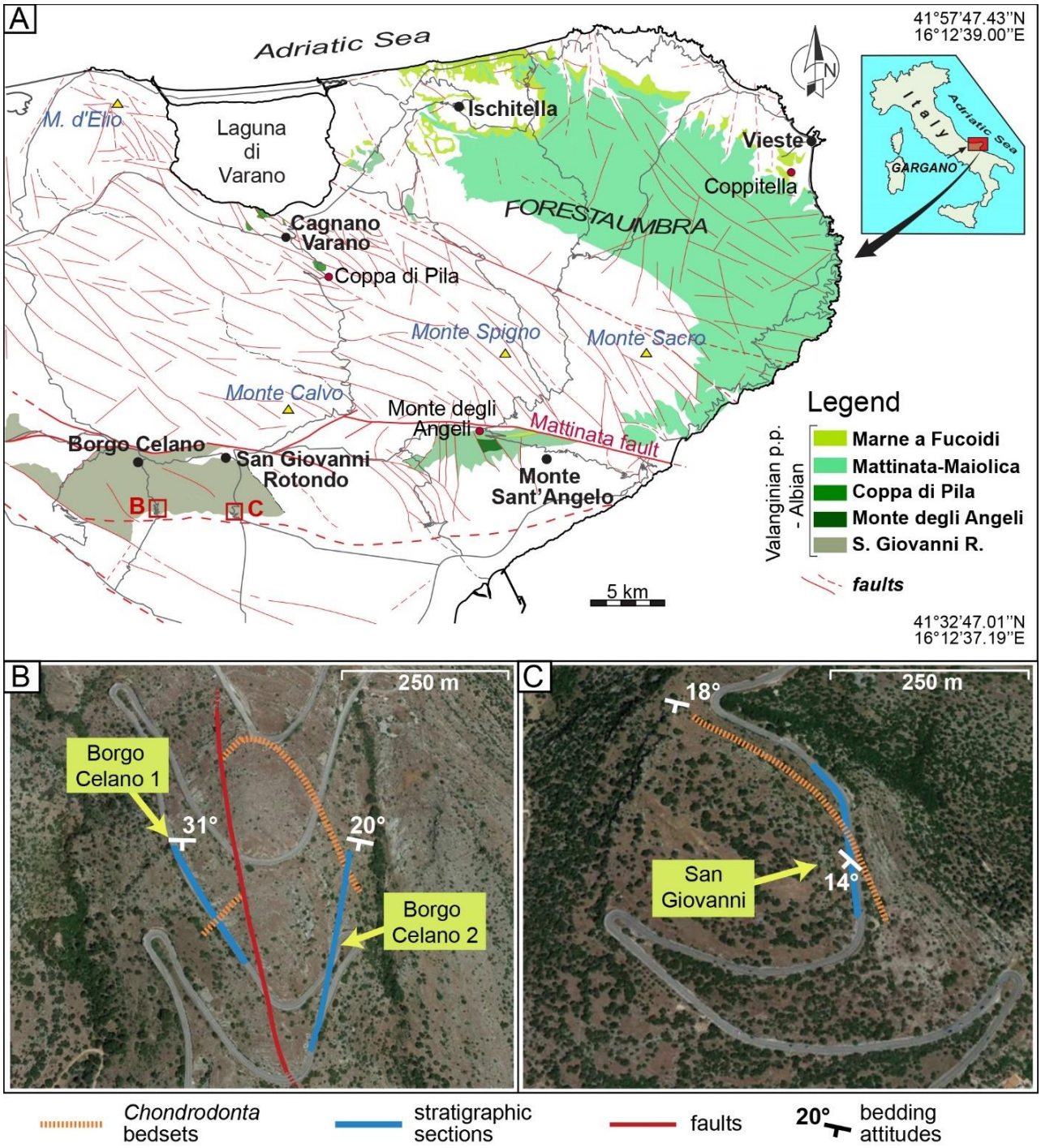

Fig. 3.3. A) simplified geological map of the Gargano Promontory (Morsilli *et al.,* 2017) with location of the studied sections (Borgo Celano and San Giovanni). B) location of the two stratigraphic sections in the Borgo Celano area, sampled on opposite sides of the hill following the bedding dip of the *Chondrodonta* bedset. C) location of the stratigraphic section in the San Giovanni Rotondo area. Orange dotted lines indicate the position of the *Chondrodonta* bedsets according to the bedding dip measurements.

Member 3 (~ 100 m thick, partially equivalent to the Requieniid member of Luperto Sinni & Masse, 1986), upper Barremian *p.p.* – lower Aptian *p.p.* in age, shows a variety of facies ranging from

subtidal high-energy thin-bedded calcarenites to domal stromatolites; *Chondrodonta* (*cfr.* Graziano, 2013) or "ostreids" (*cfr.* Di Palma, 1995; Claps *et al.*, 1996; Spalluto *et al.*, 2005) accumulations mark the base of this member.

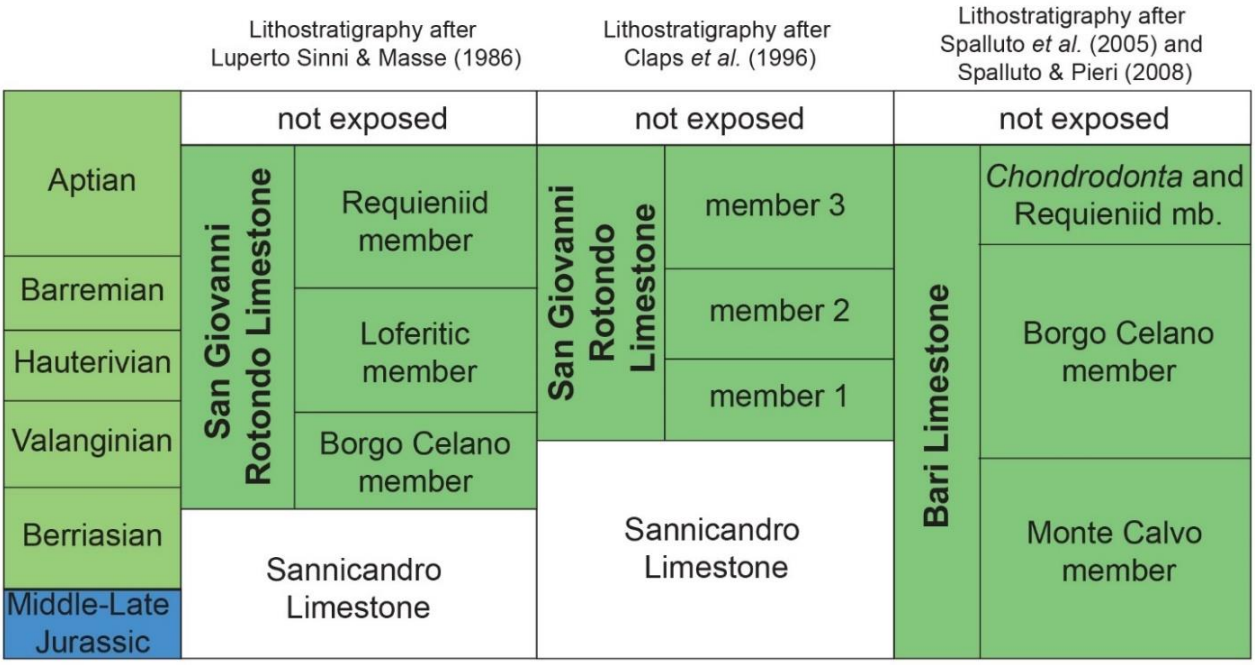

Fig. 3.4. Comparison of the lithostratigraphic frameworks proposed for the inner platform carbonates of the Lower Cretaceous San Giovanni Rotondo Limestone (Luperto Sinni & Masse, 1986; Claps *et al.*, 1996) and of the Upper Jurassic – Lower Cretaceous Bari Limestone (Spalluto *et al.*, 2005; Spalluto & Pieri, 2008). To be noted the difference in nomenclature and age between lithostratigraphic members given by the groups of authors, due to the low stratigraphic resolution.

Spalluto *et al.* (2005) and Spalluto & Pieri (2008) merged the SGRL and the Callovian *p.p.* – Valanginian *p.p.* inner platform Sannicandro Limestone (*sensu* Luperto Sinni & Masse, 1994; Morsilli & Bosellini, 1997) into the Bari Limestone (Fig. 3.4), exposed in the Murge area (central Apulia). The Bari Limestone has been further divided into three stratigraphic members and a fully Aptian *p.p.* age has been proposed for the uppermost *Chondrodonta* and Requieniid member (partially equivalent to member 3 of Claps *et al.,* 1996).

Although the time-discrepancy in the lithostratigraphic frameworks proposed for the Upper Jurassic - Lower Cretaceous inner platform limestones of the Gargano Promontory due to a low stratigraphic resolution (Fig. 3.4), the stratigraphic sections here studied are referred to the uppermost SGRL, according to Claps *et al.* (1996).

In the shallow-water carbonates of the Gargano Promontory, *Chondrodonta*-bearing beds are reported in lagoon to tidal flat settings (Luperto Sinni & Masse, 1986; Claps *et al.*, 1996; Graziano *et al.*, 2013;

Guerzoni, 2016; Posenato *et al.*, 2018) and in a resedimented, tens of metres-long, slab of margin (Guerzoni, 2016; Morsilli *et al.*, 2017). This Thesis focuses on the *Chondrodonta* accumulations of the south-eastern Gargano Promontory (Checchia Rispoli, 1921), belonging to the upper Barremian *p.p.* - lower Aptian SGRL (Di Palma, 1995; Claps *et al.*, 1996; Guerzoni, 2016; Posenato *et al.*, 2018) and equivalent to the lower Aptian *p.p.* Bari Limestone (Spalluto *et al.*, 2005; Spalluto & Pieri, 2008; Graziano *et al.*, 2013).

3.4. Methods

Well-exposed outcrops located along road-cuts (Fig. 3.3B, C) facilitated the identification of textures, sedimentary structures, and fossil content. The stratigraphic sections measured in the Borgo Celano area (Fig. 3.3B) have been analysed by several authors in the last decades (Luperto Sinni & Masse, 1986; Claps *et al.,* 1996; Spalluto *et al.*, 2005; Graziano *et al.*, 2013; Guerzoni, 2016; Posenato *et al.*, 2018); data of the San Giovanni stratigraphic section (Fig. 3.3C) are here presented for the first time.

Thin sections of 176 samples (53 for San Giovanni and 123 for Borgo Celano) were used to integrate field descriptions and to define lithofacies and biostratigraphic constraints. A total of 7 polished slabs of *Chondrodonta*-bearing samples was studied to aid the sedimentological analyses and interpretations. Spectral gamma-ray measurements were made with a hand-held spectrometer (Radiation Solutions model RS-125) to measure relative variations in the concentration of organic matter in the bulk rocks on the lower part of the Borgo Celano outcrop.

The *Chondrodonta* accumulations are here defined as "bedsets" (Campbell, 1967) as they are composed of superimposed levels forming a unique set of *Chondrodonta* beds, about or more than 1 m thick and laterally continuous (*see* Posenato *et al.*, 2018 for the detailed taphonomic description). The classification of oligo-, meso- and eutrophic associations is based on the nutrient gradients in modern low latitude waters reported in milligrams of chlorophyll α per cubic metre of seawater (*see* Fig. 2 in Mutti & Hallock, 2003) and estimated for the Lower Cretaceous dominant benthos (*see* Fig. 10 in Rameil *et al.,* 2010). Rudist limestones are here considered indicative of oligo- to mesotrophic conditions and the replacement of rudists by mesotrophic taxa like orbitolinids and *Bacinella-Lithocodium* is considered indicative of elevated nutrient levels (Vilas *et al.*, 1995; Rameil *et al.*, 2010; Huck *et al.*, 2010; Najarro *et al.*, 2011; Núñez-Useche *et al.*, 2020).

For the $\delta^{13}C$ and $\delta^{18}O$ analyses on the bulk rock, 140 samples (53 for San Giovanni, 32 for Borgo Celano 1 and 55 for Borgo Celano 2) were collected, coupled with the best-preserved shells (7

Chondrodonta and 2 rudist shells in San Giovanni, 1 rudist and 6 *Chondrodonta* shells in Borgo Celano).
Samples from the San Giovanni and the Borgo Celano 2 sections were analysed at the Museum für Naturkunde of Berlin whereas samples from the Borgo Celano 1 section were analysed at the School of Earth, Energy and Environmental Sciences of the Stanford University of California, U.S.A.

A total of 12 shell fragments of *Chondrodonta* (n = 7) and rudists (n = 5) were sampled for Strontium Isotope Stratigraphy (SIS). Five fragments of *Chondrodonta* shells from the *Chondrodonta* bedset (7.1 – 9.25 m) and two well-preserved fragments of requieniids in rudist floatstones (21 – 21.7 m) were chosen for the San Giovanni section. At Borgo Celano, two rudist fragments and one of *Chondrodonta* shell from the *Chondrodonta* bedset (15.5 – 16.1 m) and one fragment of rudist and one of *Chondrodonta* from a bivalve floatstone (placed 4 m below the *Chondrodonta* bedset) were chosen. Ten samples were analysed at the Department of Chemical and Geological Sciences of the UNIMORE and two samples at the Institute of Geology, Mineralogy and Geophysics of the Ruhr University of Bochum (Germany).

A total of 19 samples (13 for San Giovanni and 6 for Borgo Celano) was collected for the measurement of the concentration of major, trace elements and REE by the LA-ICP-MS analysis, performed at the Max Plank Institute for Chemistry of Mainz (Germany).

For details on the sample preparation and on the analytical procedures used for all the geochemical analyses, *see* Chap. 2, par. 2.2.1 – 2.2.3; for the complete geochemical dataset, *see* Appendix I.

3.5. Results

3.5.1. Lithofacies and lithofacies associations

Based on sedimentologic and petrographic analyses of outcrops and thin sections, eleven lithofacies were identified (Tab. 3.1, Fig. 3.5). Textures change from mud- to grain-supported to even bindstones; the benthic fauna is mainly represented by bivalves (requieniids and *Chondrodonta*), foraminifers and dasycladales. Micro-encrusters (*e.g., Bacinella-Lithocodium*) are particularly concentrated in some stratigraphic intervals.

The eleven lithofacies were grouped into three lithofacies associations (LA) and interpreted in terms of depositional environment (Tab. 3.1). Lithofacies association 1 (**LA1**) consists of mud-supported and bioturbated BW and MD facies episodically interbedded with beds of PP and BF (Fig. 3.5).

Microbialites form both stromatolitic bindstones (ST) and discontinuous laminar microstructures in MD, BW and PP.

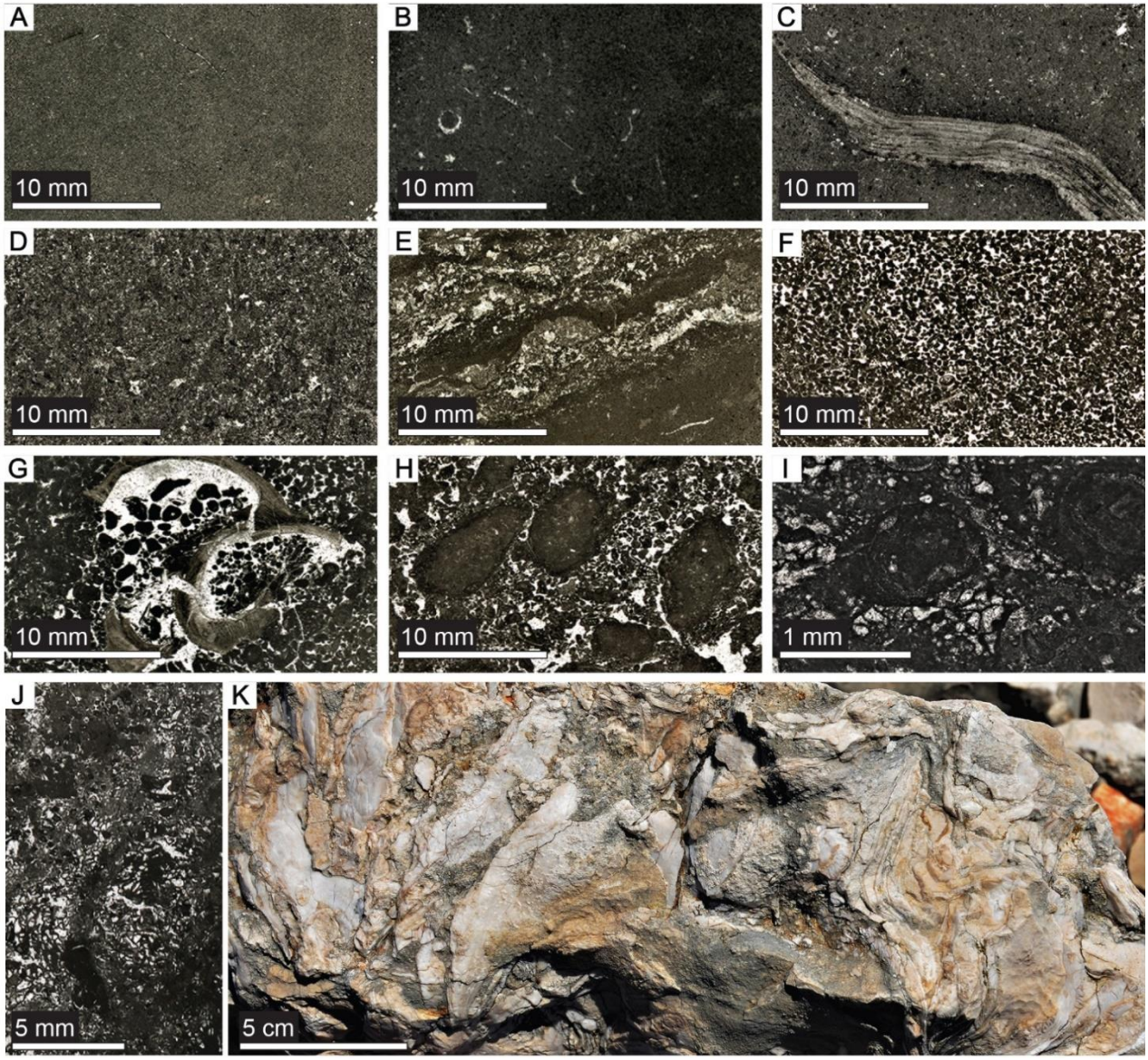

Fig. 3.5. Photographs of the eleven lithofacies in their peculiar characters recognized in the investigated sections. A) bioturbated mudstone (MD). B) bioclastic wackestone (BW). C) bivalve floatstone (BF). D) peloidal-bioclastic wackestone-packstone (PP). E) stromatolite (ST). F) peloidal-foraminiferal packstone-grainstone (PG). G) bivalve floatstone-rudstone (RF). H) oncoid floatstone-rudstone (OF). I) floatstone-rudstone with common *Bacinella-Lithocodium* (LB). J) *Bacinella-Lithocodium* bindstone (BL). K) *Chondrodonta* boundstone (CB), bouquet-like shell aggregates from the upper part of the *Chondrodonta* bedset in the Borgo Celano area.

Chondrodonta boundstones (CB) also occur. The benthic fauna is composed of scattered bivalves (*e.g.,* requieniids, *Chondrodonta*) and of common micro-encrusters like *Thaumatoporella* and *Cayeuxia*.

Lithofacies	**Textures**	**Bed features and thickness**	**Components**	**Sedimentary and diagenetic features**	**Lithofacies association and depositional settings**
MD - Bioturbated mudstone	Mudstone; mudstone-wackestone	Massive and tabular centimetre- to metre-thick beds	*Chondrodonta* and requieniid fragments (r), dasycladales (r), foraminifers (r), small-sized oncoids (r), solitary corals (r), echinoderm spines (r); *Thaumatoporella* (c-r), *Cayeuxia* talli (r); peloids (c-r)	Bioturbation, burrows, discontinuous microbial laminae, peloidal-grainstone pockets	**LA1** Low-energy protected lagoon passing to tidal flat
BW - Bioclastic wackestone	Wackestone	Massive and tabular centimetre- to metre-thick beds	Foraminifers (a-c), *Salpingoporella* sp.(a-c), small-sized oncoids (c-r), solitary corals and echinoderm spines (r), bivalve and gastropod fragments (r), ostracods (r); *Thaumatoporella* (c); peloids (c-r)	Peloidal-grainstone pockets, bioturbation, discontinuous microbial laminae	
PP - Peloidal-bioclastic packstone	Packstone-wackestone	Tabular and thin-layered decimetre- to metre-thick beds	Foraminifers (c-r), ostracods (a-r), dasycladales (r), bivalve fragments (r), solitary corals and echinoderm spines (r); *Thaumatoporella* (c-r); peloids (a)	Horizontal shell layers, rare discontinuous microbial laminae	
BF - Bivalve floatstone	Floatstone; mudstone-wackestone matrix	Massive and tabular decimetre- to metre-thick beds	Requieniids (a), *Chondrodonta* (c), nerineids (c-r), oncoids (c-r), foraminifers (c-r), *Salpingoporella* sp. (c-r), solitary corals and echinoderm spines (r); *Thaumatoporella* (a-r); peloids (c-r)	Breakage of shells, rare micro-encrustations	
ST - Stromatolite	Bindstone	Tabular to domal decimetre- to metre-thick beds or centimetre-thick layers within mud facies	Ostracods (r), bivalve fragments (r), foraminifers (r); *Thaumatoporella* (c), microbialitic laminae (a); peloids (a-c)	Planar, wavy, dome-shaped laminae	
CB - *Chondrodonta* boundstone	Boundstone; mudstone-wackestone or wackestone-packstone matrix	Tabular and nodular decimetre-thick beds forming a unique bedset; shells both horizontally oriented (*i.e.,* toppled) or in life-position	*Chondrodonta* (a), requieniids (r), foraminifers (r), dasycladales (r); *Thaumatoporella* (r), *Cayeuxia* talli (c-r), microbial crusts (c-r); peloids (r)	Horizontal shell layers, microbial crusts	

PG - Peloidal-foraminiferal packstone-grainstone	Packstone-grainstone; grainstone	Thin-layered centimetre-to decimetre-thick beds	Foraminifers (a-c), *Salpingoporella* sp. (c), small-sized oncoids (c-r), undetermined bivalve fragments (c-r), echinoderm spines (r); *Thaumatoporella* (c-r); peloids (a), mudclasts (c), aggregate grains (r)	Micritization, micro-encrustations	**LA2** High-energy open lagoon
RF - Bivalve floatstone-rudstone	Floatstone-rudstone; packstone-grainstone matrix	Massive, tabular, and occasionally lense-shaped centimetre-to metre-thick beds	Requieniids (a-c), *Chondrodonta* (c), nerineids (c), oncoids (c), foraminifers (a-c), dasycladales (c-r), undetermined bivalve fragments (c-r), echinoderm spines (c-r), solitary corals (r); *Thaumatoporella* (r), peloids (a-c), mudclasts (c-r), ooid fragments (r)	Bioerosion, bivalve lenses, breakage of shells, micritization, micro-encrustations	
OF - Oncoid floatstone-rudstone	Floatstone-rudstone; packstone-grainstone matrix	Massive and tabular decimetre-to metre-thick beds	Oncoids (a), nerineids (a-c), foraminifers (a-c), dasycladales (c-r), undetermined bivalve fragments (c-r), solitary corals (r), echinoderm spines (r); *Thaumatoporella* (c-r), *Cayeuxia* talli (r); peloids (a-c), ooids (r), mudclasts (r), aggregate grains (r)	Micritization, micro-encrustations	
LB - Floatstone-rudstone with common *Bacinella-Lithocodium*	Floatstone-rudstone; packstone-grainstone or wackestone matrix	Tabular decimetre-thick beds	Requieniids (a-c), oncoids (a-c), nerineids (c-r), *Chondrodonta* (c-r), solitary corals (c-r), echinoderm spines (r); foraminifers (c), dasycladales (c-r); *Thaumatoporella* (r), *Bacinella-Lithocodium* (c), *Cayeuxia* talli (r); peloids (a), mudclasts (c-r), aggregate grains (r)	Micro-encrustations	**LA3** Moderate-energy lagoon under stressed conditions
BL - *Bacinella-Lithocodium* bindstone	Bindstone	Centimetre-to decimetre-thick nodular beds	*Bacinella-Lithocodium* (a); undetermined bivalve fragments (c-r), foraminifers (r), echinoderm spines (r), solitary corals (r), small-sized oncoids (r); *Thaumatoporella* (r); peloids (c-r)	Laminar to patchy cloudy micro-encrustations	

Tab. 3.1. Summary of the main sedimentological characters of the lithofacies associations and of the 11 lithofacies recognized in the studied sections. Components considered are, in order, skeletals, micro-encrusters and non-skeletal grains. Their relative abundance is expressed as: *a*, abundant, *c*, common, *r*, rare. Laminar and patchy cloudy shapes of *Bacinella-Lithocodium* bindstones are from Huck *et al.* (2010).

This mud-dominated lithofacies association is interpreted to have been deposited in low-energy protected subtidal settings with a mostly restricted marine circulation, as indicated by the poorly differentiated biotic assemblages. Inter-supratidal facies and sedimentary structures (*i.e.,* lithofacies

ST, fenestrae, and exposure surfaces) indicate occasional shifts to tidal-flat settings. Subtidal cycles, with occasional exposure surfaces at the top, prevail whereas peritidal cycles, capped by stromatolites plus subaerial exposures, are less common. Apart from the singular occurrence of CB, all lithofacies of LA1 are typical of the inner platform settings documented in many adjacent Tethyan carbonate platforms (*e.g.,* Husinec & Read, 2011, 2018; Di Lucia *et al.,* 2012; Amodio & Weissert, 2017 among others).

Lithofacies association 2 (**LA2**) consists of grain-supported facies (PG, RF, OF) with high skeletal content and diversity (Fig. 3.5). The benthic fauna is composed of common to abundant bivalves (requieniids, *Chondrodonta*), nerineid gastropods, foraminifers and dasycladales. Based on textures and skeletal components as well as on the absence of exposure surfaces or inter-supratidal sedimentary structures (common in LA1), LA2 can be interpreted as deposited in a typical subtidal environment or open lagoon. The latter is characterized by a more open circulation with bivalve accumulations (RF) and high-energy events (PG, OF). A similar interpretation of this type of lithofacies association has been given for other inner platform settings (*e.g.,* Husinec & Read, 2018).

Lithofacies association 3 (**LA3**) is based on the occurrence of *Bacinella-Lithocodium* both as bindstones (BL) and as micro-encrustations in floatstone-rudstones (LB) (Fig. 3.5). These micro-encrusters are concentrated in specific intervals of the stratigraphic succession, in which they predominate over other biota. BL and LB facies alternate with LA2 grain-supported lagoon facies and, less commonly, with mud-supported beds of LA1. *Bacinella-Lithocodium* facies have been considered as indicative of environmental stress on the platform top (*e.g.,* Immenhauser *et al.*, 2005). LA3 can be therefore interpreted as deposited in moderate-energy lagoon settings under environmentally stressed conditions.

3.5.2. Stratigraphy and geochemistry

3.5.2.1. The San Giovanni section

The San Giovanni stratigraphic section (Fig. 3.3C, 3.6) is 23.8 m thick and records low-skeletal, mud-supported facies gradually passing to grain-supported rudist beds with *Bacinella-Lithocodium* micro-encrustations.

The lower part (0 – 15.9 m, SGRL, uppermost member 2 to lowermost member 3) is mostly composed of LA1 metre-thick massive mudstones (MD), miliolid-algal wackestones (BW) and peloidal packstones - locally wackestones (PP).

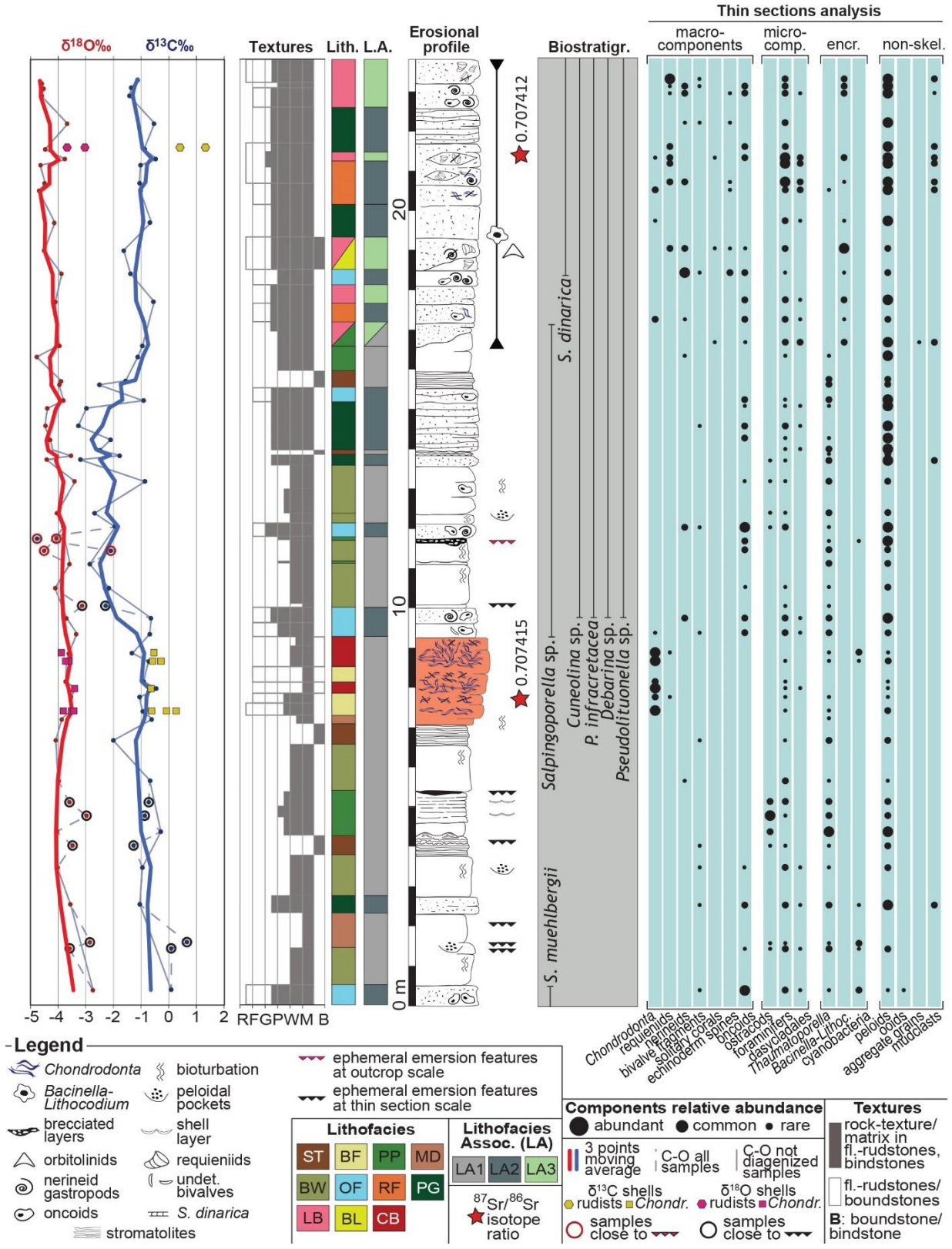

Fig. 3.6. San Giovanni stratigraphic log (base: 41°40'19.90''N, 15°43'44.30''E; top: 41°40'13.85''N, 15°43'46.05''E) including biostratigraphy and stable isotope results ($\delta^{18}O$, $\delta^{13}C$, $^{87}Sr/^{86}Sr$). Rock-components of thin sections are analysed semi-quantitatively and their abundance is expressed relative to the rock texture. The *Chondrodonta* bedset is highlighted in orange; *see* par. 3.5.1 and Tab. 3.1 for the description of lithofacies and lithofacies associations.

Microbial activity generates both decimetre-thick tabular and domal stromatolites (ST) and discontinuous peloidal – microbial laminae in MD, BW and PP. All these beds are abundantly bioturbated and show common ephemeral emersion-related features like breccias, vugs and fenestrae. Less common LA2 thin-bedded peloidal packstone-grainstones (PG) and oncoid floatstone-rudstones (OF) are intercalated and gradually increase upwards in thickness and frequency. *Chondrodonta* and nerineids, oncoids, miliolids and micro-encrusters (*e.g., Cayeuxia, Thaumatoporella*) are common; ostracods are locally abundant and horizontally oriented in thin layers (4 – 5.4 m).

The *Chondrodonta* bedset (base of member 3, CB and locally BF) occurs between 7.1 – 9.25 m, on top of a tabular stromatolite and is overlain by BW, PP and OF beds rich in oncoids and *Thaumatoporella* (10 – 13.5 m). The occurrence of *Salpingoporella muehlbergii* is only at the base of the section and the association of *Cuneolina* sp., *Debarina* sp., *Praechrysalidina infracretacea*, *Pseudolituonella* sp. and *Salpingoporella* sp. occurs above the *Chondrodonta* bedset (~ 10 m from the base).

The upper part of the section (15.9 – 23.8 m, SGRL, member 3) lacks stromatolites and is mainly composed of LA2 and LA3 facies. The base is made of a metre-thick peloidal-packstone (PP) overlain by thin-bedded peloidal-foraminiferal packstone-grainstones (PG) interbedded with centimetre-thick requieniid beds (RF) and metre-thick oncoid floatstone-rudstones (OF).

Requieniids increase upwards in size and abundance and are locally arranged in lenticular accumulations. *Chondrodonta* occurs as common bioclast together with nerineids, dasycladales (*Salpingoporella* sp.) and foraminifers (miliolids, *P. infracretacea*, *Cuneolina* sp.); orbitolinids are scattered within requieniid facies (17.5 – 21 m from the base). *Bacinella-Lithocodium* micro-encrustations (LB) occur commonly across the upper part of the section; a *Bacinella*-bindstone (BL) occurs between 18.5 – 19.3 m in association with requieniid fragments and orbitolinids. The first occurrence of *Salpingoporella dinarica* is at 18.5 m above the base of the section.

The $\delta^{13}C$ curve in the San Giovanni section (Fig. 3.6) records an overall upward decreasing trend from +0.1‰ to -1.1‰ and a range of values between +0.7‰ and –4.8‰, with a mean of -1.3‰. Above the *Chondrodonta* bedset, a sharp negative shift from -0.6‰ to -2.4‰ (9.8 – 10.1 m) marks the onset of a negative plateau that extends up to 15.9 m and contains the most negative values of the entire $\delta^{13}C$ curve. The overall decreasing trend in $\delta^{18}O$ is less marked and does not show abrupt positive or negative shifts; $\delta^{18}O$ values decrease from -2.7‰ to -4.6‰, with an average of -3.9‰.

3.5.2.1.1. Major, trace elements and REE

The concentration of Al in the San Giovanni section ranges between 50 and 1000 ppm for most of the stratigraphic section (Fig. 3.7). An only sharp positive peak, of ~ 3200 ppm, is recorded right above the top of the *Chondrodonta* bedset (at 10 m), in correspondence of an oncoid-floatstone with ephemeral emersion-related features.

The measured P/Al ratio averages around 0.06 with weak increases up to 0.1 within the *Chondrodonta* bedset and a marked decrease in its uppermost part. The Ti/Al ratio oscillates between 0.03 and 0.06 throughout the section and shows a minimum of ~ 0.035 within the *Chondrodonta* bedset (at 8.7 m). The highest values, between 0.05 and 0.06, are instead reached close to the major peak in Al (10.1 - 10.5 m).

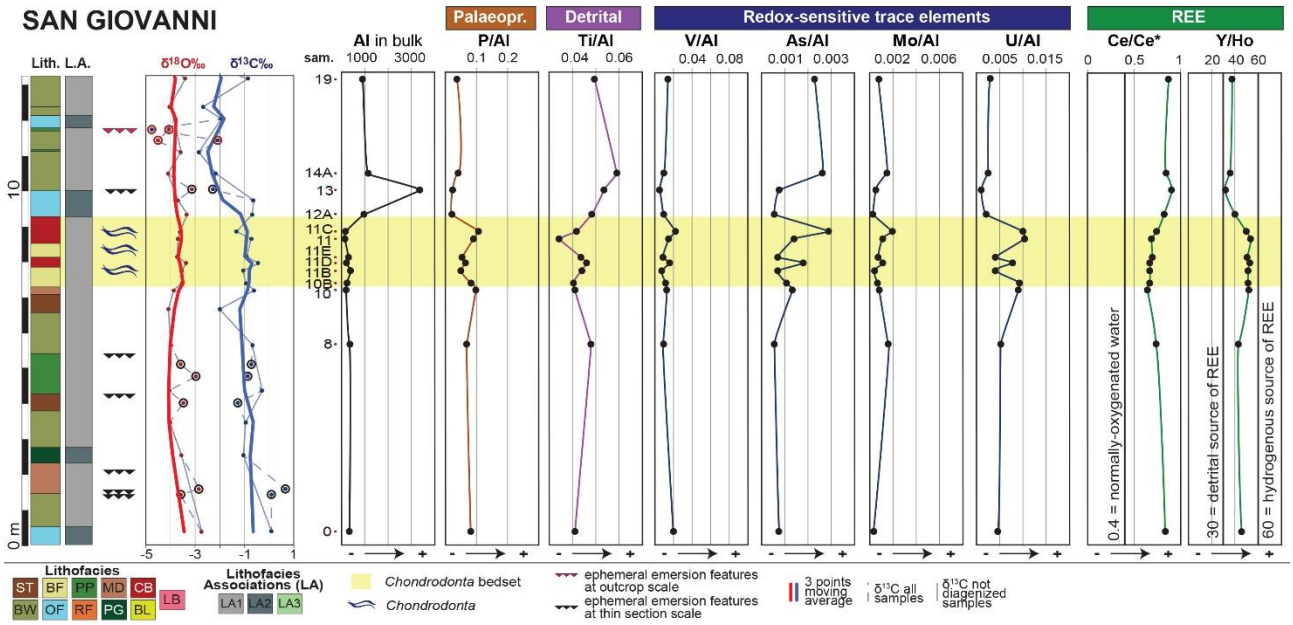

Fig. 3.7. Palaeoproductivity (P/Al), detrital input (Ti/Al and Al) proxies, Redox-Sensitive Trace Elements, Ce anomaly (expressed as Ce/Ce* ratio) and Y/Ho ratio measured for the San Giovanni section. P, Ti, and RSTE concentrations are reported as ratios on the concentration of Al in the bulk rock and plotted against the lithostratigraphic column and the $\delta^{13}C$ and $\delta^{18}O$ curves. For the description of lithofacies and lithofacies associations, *see* par. 3.5.1 and Tab. 3.1. The concentration of Al is reported in ppm.

The Redox-Sensitive Trace Elements (RSTE)/Al ratios are generally low (Fig. 3.7). Within the *Chondrodonta* bedset, both the V/Al and the Mo/Al ratios show short fluctuations, between 0.01 and 0.02 and between 0.001 and 0.002, respectively. The As/Al and the U/Al ratios show sharper positive peaks, up to 0.003 and up to 0.01, respectively. At the top of the bedset (from 9.4 m), all the RSTE/Al ratios abruptly decrease.

A negative Ce anomaly is recorded for the entire section. The highest values of the Ce/Ce* ratio occur above the *Chondrodonta* bedset (from 9.4 m) with peaks of 0.85 to 0.9 whereas, within the bedset, values range around 0.65. The Y/Ho ratio ranges between 35 and 60, with the highest values reached within the bedset and the lowermost ones reached immediately above it, from 10.1 m.

3.5.2.2. The Borgo Celano 1 section

The Borgo Celano 1 stratigraphic section (Fig. 3.3B, 3.8A) is 25.3 m thick (SGRL, members 2 and 3) and consists of lime mud-rich beds interbedded with grain-supported and bioclastic deposits. *Bacinella-Lithocodium* micro-encrustations occur in the uppermost part of the section.

Most of the section consists of alternating LA1 and LA2 facies associations with rare LA3. The lowermost 13.5 m are characterized by metre- and decimetre-thick for-algal-*Thaumatoporella* wackestones (BW), bioturbated mudstones (MD) and molluskan floatstones with common *Chondrodonta*, requieniids and nerineids (BF).

These lithofacies are intercalated with decimetre-thick, thin-bedded peloidal-foraminiferal packstones and grainstones (PP, PG) and bioclastic-oncoid rudstones and floatstones (OF, RF). The abundance of skeletal material is moderate, especially for foraminifers and dasycladales; ostracods are locally common and micro-encrusters, except for scattered *Thaumatoporella*, are rare.

Upwards (13.5 – 22.5 m), the bioclastic content, especially requieniids, decreases gradually. Microbial activity generates discontinuous microbial-peloidal laminae in MD and BW and decimetre-thick domal and tabular stromatolites (ST), interlayered with mudstones and grain-supported facies. Ephemeral emersion-related features like vugs and fenestrae are common. The *Chondrodonta* bedset (15.5 – 16.1 m, SGRL, base of member 3, CB and locally BF) overlies a tabular stromatolite and is followed by ~ 3 m of limestones depleted in mollusks, foraminifers and dasycladales and relatively enriched in *Thaumatoporella* and other micro-encrusters (*e.g., Cayeuxia* thalli). The last occurrence of *S. muehlbergii* is recorded 11 m above the base of the section. *Cuneolina* sp., *P. infracretacea*, *Nezzazzatids*, *Debarina* sp. and *Pseudolituonella* sp. gradually appear upwards; *Mayncina* sp., *Salpingoporella heraldica* and *Actinoporella podolica* occur around the *Chondrodonta* bedset.

The uppermost part of the section (22.5 – 25.3 m) consists of LA2 and LA3 facies associations and starts with a massive peloidal packstone-grainstone (PG) rich in foraminifers (miliolids, *Cuneolina* sp., *P. infracretacea*) and dasycladales (*Salpingoporella* sp.). It is followed by oncoid floatstone-rudstone beds (OF) and bivalve (requieniids, *Chondrodonta*) floatstones with scattered orbitolinids and common *Bacinella-Lithocodium* micro-encrustations (LB).

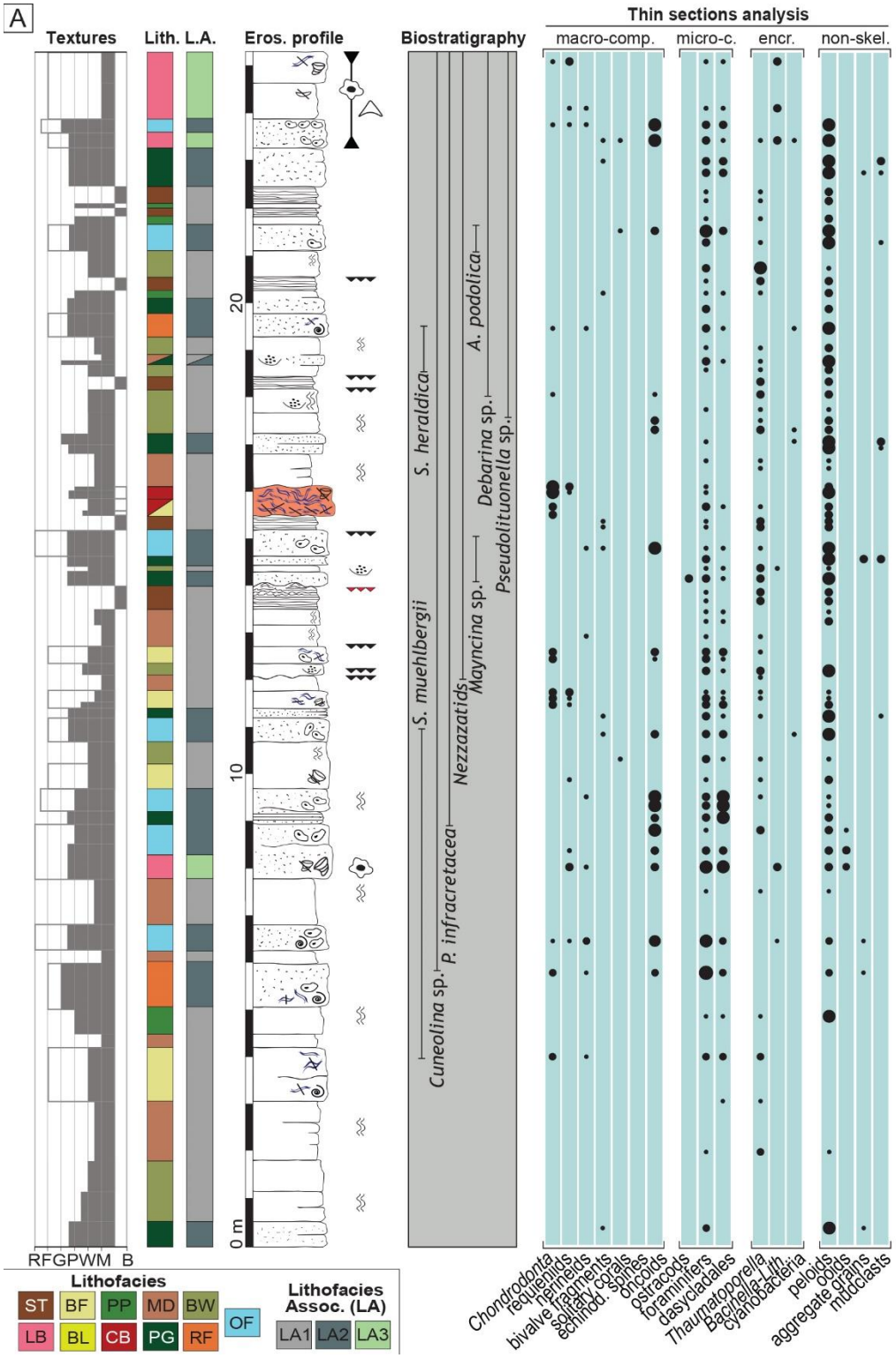

Fig. 3.8A. Borgo Celano 1 stratigraphic log (base: 41°40'31.38''N, 15°39'58.40''E; top: 41°40'27.35''N, 15°40'01.85''E) including biostratigraphy. Rock-components of thin sections are analysed semi-quantitatively and their abundance is expressed relative to the rock texture. The *Chondrodonta* bedset is highlighted in orange; *see* par. 3.5.1 and Tab. 3.1 for the description of lithofacies and lithofacies associations and Fig. 3.6 for the complete legend.

The $\delta^{13}C$ curve in the Borgo Celano 1 section (Fig. 3.8B) records an overall slightly upward increasing trend from -2.1‰ at the base to -0.9‰ at the top, with a mean of -0.9‰. In the lower part of the section, the positive trend is punctuated at 11 m by a negative shift from +0.1‰ (the highest value of the $\delta^{13}C$ curve) to about -3.0‰. This shift marks the base of a negative plateau occurring up

to 18 m, with values averaging around -0.9‰. The $\delta^{18}O$ curve exhibits a similar, slightly increasing trend from -4.6‰ at the base to -3.8‰ at the top, with an average of -3.7‰ and no sharp positive or negative shifts.

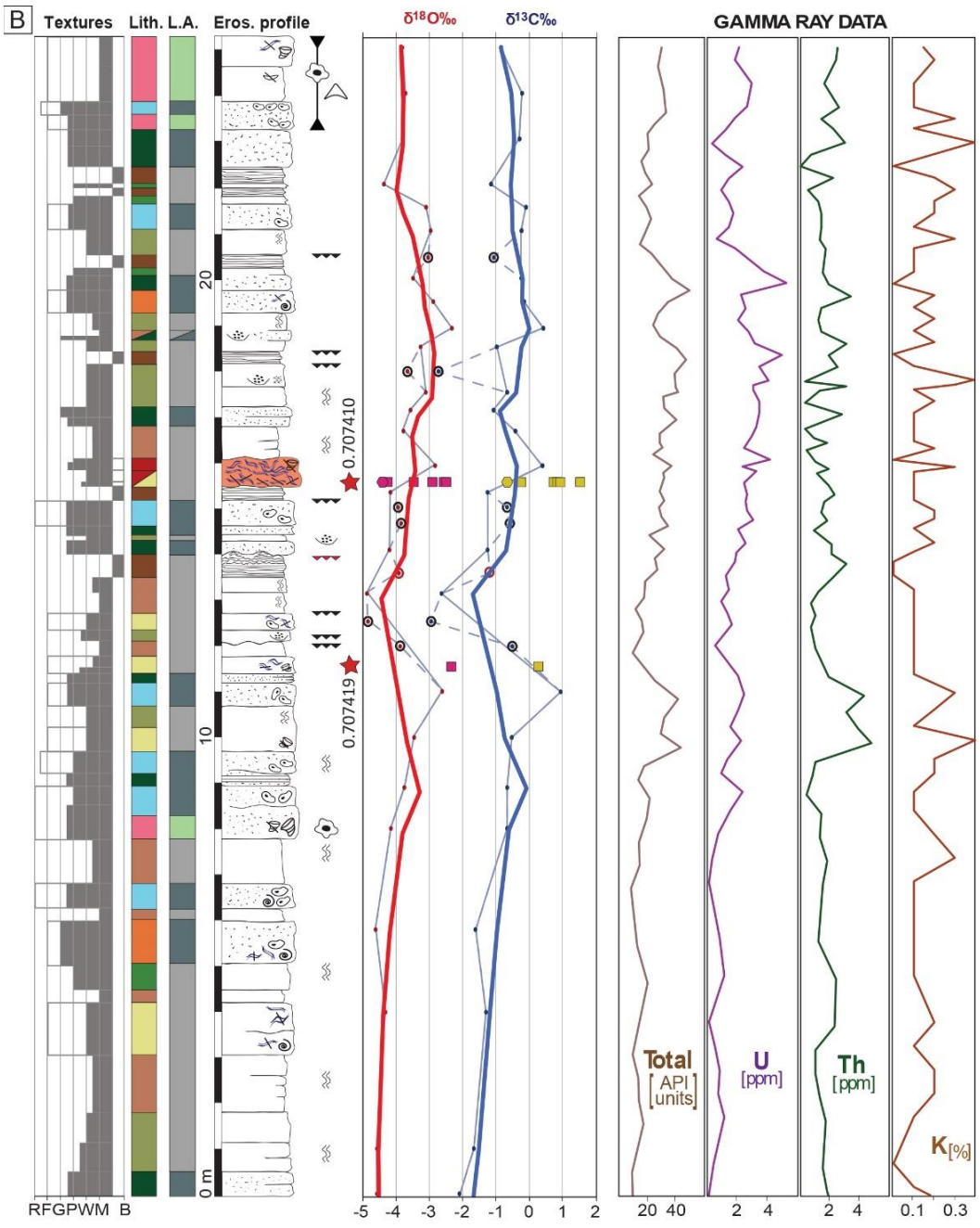

Fig. 3.8B. Borgo Celano 1 stratigraphic log including stable isotope ($\delta^{18}O$, $\delta^{13}C$, $^{87}Sr/^{86}Sr$) results and gamma ray data (Total API, uranium, thorium, and potassium). The *Chondrodonta* bedset is highlighted in orange; *see* par. 3.5.1 and Tab. 3.1 for the description of lithofacies and lithofacies associations and Fig. 3.6 for the legend.

The total gamma ray intensity is generally below 20.0 API units in the first 13 m of the Borgo Celano 1 section (Fig. 3.8B). It shows an overall increase upsection, with peaks up to 40.0 (8 – 11.5 m) and 50.0 API units (at 19.8 m). The concentration of uranium is lower than 2 ppm in the first 13 m and increases upwards with peaks of more than 5 ppm (at 18.4 and 20 m, respectively). Above 20 m,

signals of both total gamma ray and uranium decrease. The concentration of thorium ranges around 2 ppm throughout the section, with peaks of 4 ppm between 8 – 11.5 m. Values decrease to 1 ppm only in the upper part (17 - 20 m from the base). The concentration of potassium varies between 0 and 0.4% throughout the section and shows sharp concentration peaks at 10, 17 and 20 m from the base.

3.5.2.2.1. Major, trace elements and REE

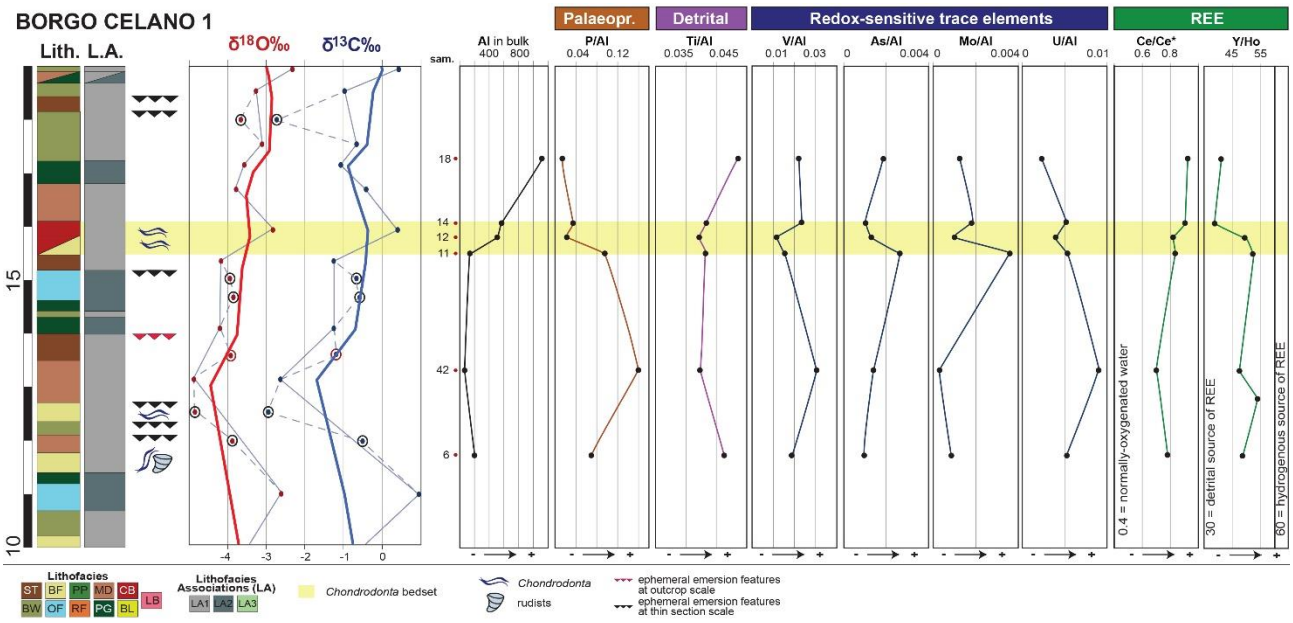

Fig. 3.9. Palaeoproductivity (P/Al), detrital input (Ti/Al and Al) proxies, Redox-Sensitive Trace Elements, Ce anomaly (expressed as Ce/Ce* ratio) and Y/Ho ratio measured for the Borgo Celano 1 section. P, Ti, and RSTE concentrations are reported as ratios on the concentration of Al in the bulk rock and plotted against the lithostratigraphic column and the $\delta^{13}C$ and $\delta^{18}O$ curves. For the description of lithofacies and lithofacies associations, *see* par. 3.5.1 and Tab. 3.1. The concentration of Al is reported in ppm.

In the measured tract (11.7 – 17.2 m from the base) of the Borgo Celano 1 section (Fig. 3.9), the concentration of Al starts increasing within the *Chondrodonta* bedset (15.4 – 16.1 m) from ~ 160 to 500 ppm and reaches a peak of 1100 ppm at ~ 17 m.

The measured P/Al ratio oscillates between 0.02 and 0.14 and decreases within the uppermost part of the *Chondrodonta* bedset, from 0.1 to ~ 0.03. The Ti/Al ratio oscillates between 0.03 and 0.055, and averages around 0.04 within the *Chondrodonta* bedset.

The Redox-Sensitive Trace Elements (RSTE)/Al ratios have generally low values (Fig. 3.9). Both V/Al and U/Al ratios show the highest value (of 0.03 and of 0.009, respectively) at 12.5 m, in correspondence of the lowermost value of Mo/Al. Both Mo/Al and As/Al ratios show the highest value, of ~ 0.004, at the base of the *Chondrodonta* bedset (15.4 m).

A negative Ce anomaly is recorded for the entire Borgo Celano 1 section (Fig. 3.9). The Ce/Ce* ratio ranges between ~ 0.65 and 0.90 in an overall increasing trend. The Y/Ho ratio ranges between 35 and 55, with the lowermost values reached within the *Chondrodonta* bedset.

3.5.2.3. The Borgo Celano 2 section

The Borgo Celano 2 stratigraphic section (Fig. 3.3B, 3.10A, B) is 56.8 m thick (SGRL, member 2 and 3) and shows lime mud-rich facies alternating with grain-supported and bioclastic beds. *Bacinella- Lithocodium* micro-encrustations are common in the lower-middle part of the section and stromatolites predominate in the upper part.

The lowermost 7.6 m are composed of alternating LA1 and LA2 facies successions, with a generally low skeletal abundance. This lower part of the section is marked at the base and at the top by tabular stromatolites (ST) and contains bioturbated mudstones (MD) and *Thaumatoporella*-wackestones and packstones (BW and PP). These are interbedded with massive decimetre-thick peloidal-foraminiferal packstone-grainstones (PG) and molluskan-oncoid floatstone-rudstones (OF, RF) with requieniids and nerineids. The *Chondrodonta* bedset (1.7 – 2 m, base of member 3, CB) occurs within both mud- and grain-supported facies.

In the middle part of the section (7.6 – 31.1 m), stromatolites are absent and the skeletal abundance generally increases. This part consists mostly of interbedded LA2 and LA3 skeletal-rich facies, arranged in massive decimetre- to metre-thick requieniid-oncoid floatstone-rudstones, in both granular and muddy matrices (RF, OF and BF). Requieniids increase upwards in size and abundance. These skeletal-rich facies are interbedded with thin-bedded peloidal-foraminiferal packstones and grainstones (PG, PP) and, commonly, with lithofacies LB. *Bacinella-Lithocodium* micro-encrustations form bindstones (BL) between 9.5 and 14.3 m. Common constituents of this middle part include requieniids, small benthic foraminifers (miliolids, *P. infracretacea*, *Cuneolina* sp., *Debarina* sp.) and dasycladales (*Salpingoporella* sp.). *Thaumatoporella* is locally abundant and orbitolinids occur within rudist and *Bacinella-Lithocodium* facies. *Bacinella-Lithocodium* micro-encrustations (LB) eventually disappear in favour of muddy strata (MD, BW) and, upsection, of grain-supported strata (OF, RF).

The upper part of the section (31.1 – 56.8 m) records the complete disappearance of the LA3 facies association and of rudist limestones. It is composed of LA1 facies with interbedded thin LA2 intervals and is characterized by predominant stromatolites (ST) (Fig. 3.10B). These occur either as centimetre-

thick wavy laminae within MD, as tabular decimetre-thick beds alternating with PP, PG, OF and BW, or as tabular and dome-shaped decimetre- to metre-thick beds (between 46.1 – 56.8 m).

The abundance of macro-fossils, especially requieniids, is generally low in the upper part of the section; exceptions are noted for *S. dinarica*, which reaches its highest concentration between 38.7 – 38.9 m, and for an orbitolinid-rich wackestone (*Mesorbitolina lotzei, Praeorbitolina cormyi*) at 50 – 51.5 m.

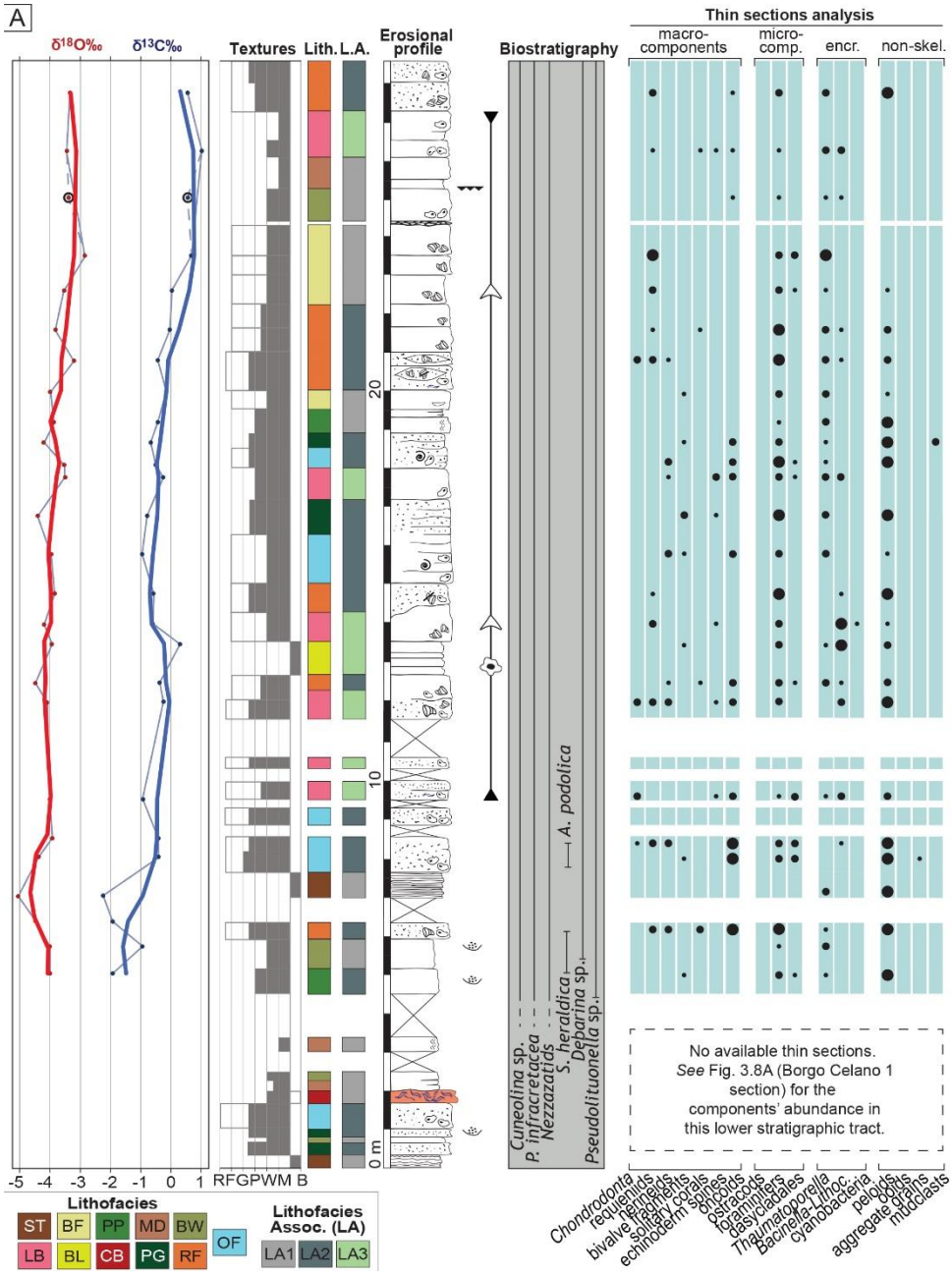

Fig. 3.10A. Borgo Celano 2 stratigraphic log (lower part) (base: 41°40'31.7''N, 15°40'07.55''E; top: 41°40'24.30''N, 15°40'04.70''E) including biostratigraphy and stable isotope results ($\delta^{18}O$, $\delta^{13}C$). Rock-components of thin sections are analysed semi-quantitatively and their abundance is expressed relative to the rock texture. The *Chondrodonta* bedset is highlighted in orange; *see* par. 3.5.1 and Tab. 3.1 for the description of lithofacies and lithofacies associations and Fig. 3.6 for the complete legend.

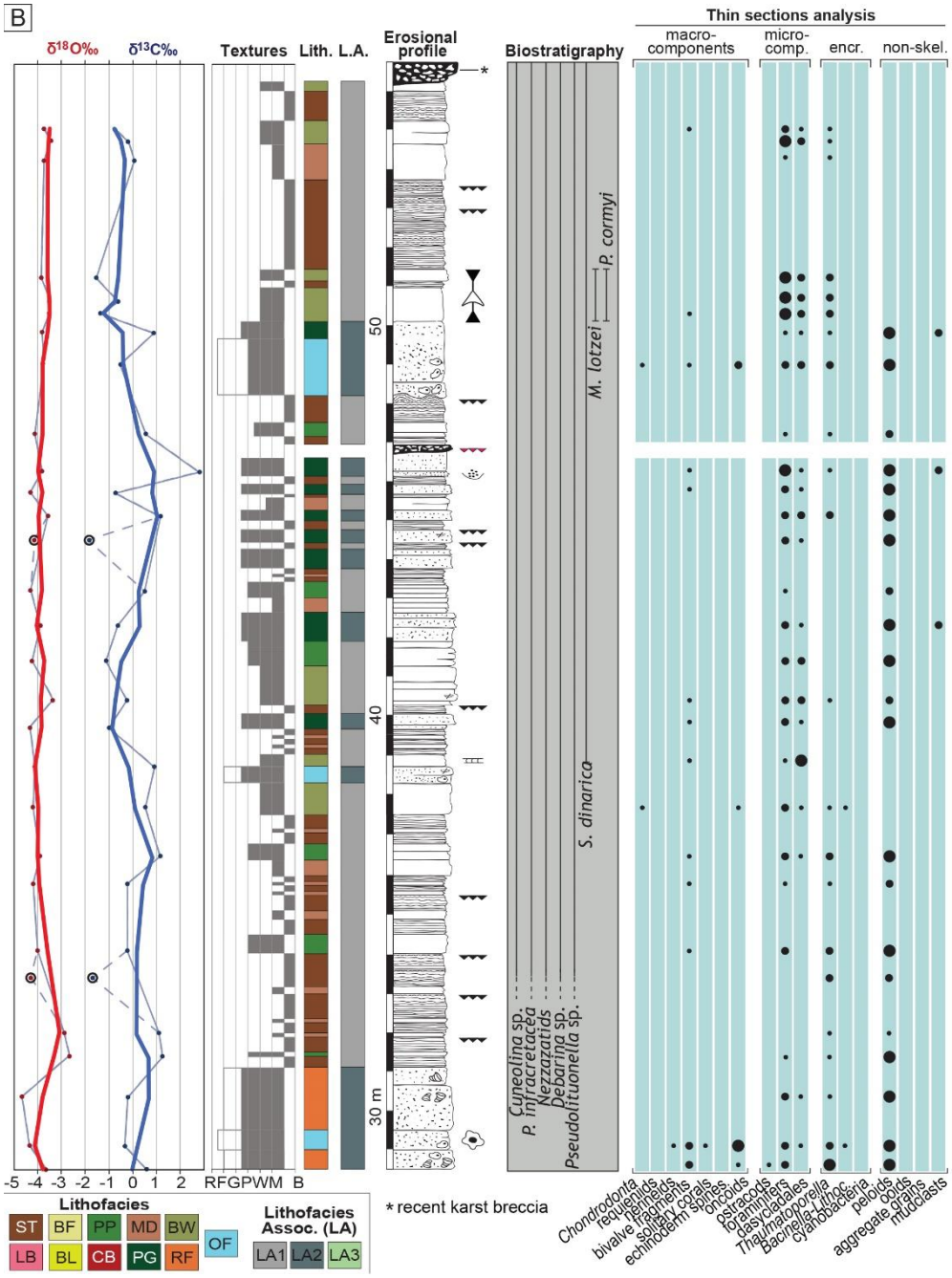

Fig. 3.10B. Borgo Celano 2 stratigraphic log (upper part) (base: 41°40'31.7''N, 15°40'07.55''E; top: 41°40'24.30''N, 15°40'04.70''E) including biostratigraphy and stable isotope results ($\delta^{18}O$, $\delta^{13}C$). Rock-components of thin sections are analysed semi-quantitatively and their abundance is expressed relative to the rock texture; *see* par. 3.5.1 and Tab. 3.1 for the description of lithofacies and lithofacies associations and Fig. 3.6 for the complete legend.

The $\delta^{13}C$ values in the Borgo Celano 2 section (Fig. 3.10A, B) increase up-section from -1.9‰ at the base to -0.7‰ at top, with an average of -0.2‰. The lower part (0 – 7.6 m) contains a negative peak of -2.2‰ (7 m). Values slightly increase in the middle part (7.6 – 31.1 m) and a short negative shift, from +0.3‰ to -0.1‰, occurs around the *Bacinella*-rich level (12 – 15.8 m). In the upper part of the section (31.1 – 56.8 m) two negative peaks, of -1.7‰ and of -1.9‰, occur respectively at 33.4 m and at 44.6 m, in correspondence of beds with ephemeral-emersion related features. The most positive peak of the stratigraphic section, of +2.8‰, occurs at 46.35 m (Fig. 3.10B). The $\delta^{18}O$ curve also increases up-section, rising from -4.0‰ at the base to -3.5‰ at the top.

3.5.3. Chondrodonta bedsets

The *Chondrodonta* bedsets occur in the lower-middle part of the studied sections (*see* Fig. 3.6, 3.8A, 3.10A), interbedded with carbonate mud-rich facies and stromatolites. The bivalves belong to the species *C. glabra* Stanton (Posenato *et al.*, 2018), form para- to autochthonous accumulations and occur in an almost monospecific association with subordinated requieniids. *C. glabra* shells, 8 - 12 cm long on average, are mostly articulated, present a generally low degree of breakage, and show a variable orientation and distribution throughout the bedsets. The outer calcite shell layer is preserved whereas the inner aragonitic one is dissolved (*see* Posenato *et al.*, 2018).

The *Chondrodonta* bedset in the Borgo Celano 1 section (Fig. 3.11A, B), about 60 cm thick and deposited on top of a 40 cm-thick tabular stromatolite, is composed of nodular floatstone-rudstone beds in which chaotically oriented shells and small bouquet-like aggregates (*see* Fig. 3.5K) are scattered between dense sheets of sub-horizontal individuals. The upper surface of the bedset shows three sub-circular knobs (Posenato *et al.*, 2018), about 20 – 30 cm high and 1.5 – 3 m in diameter and characterized by vertical oriented valves often arranged in bouquet-like aggregates (Fig. 3.11A, D). In the flat surfaces among the reliefs, horizontal valves locally micro-bioturbated are frequent (Fig. 3.11C). In the Borgo Celano 2 section, a few hundred metres eastwards, the same *Chondrodonta* bedset is half the thickness and directly overlies subtidal oncoid beds.

Shells occur within a *Chondrodonta* fragments-packstone (Fig. 3.11E) (micro-facies CP in Posenato *et al.*, 2018) or in a peloidal-bioclastic wackestone-packstone matrix (Fig. 3.11F) (micro-facies PWP in Posenato *et al.*, 2018). The *Chondrodonta* fragments-packstone is characterized by large *Chondrodonta* shells often encrusted by microbial crusts, up to 2 mm-thick, and nubeculariid layers (*see* Fig. 9D in Posenato *et al.*, 2018). The peloidal-bioclastic wackestone-packstone is dominated by very fine peloids with a locally faint lamination detected by peloidal accumulations in millimetre-thick laminae. Beside *Chondrodonta*, small benthic foraminifers, dasycladales and *Thaumatoporella* are secondary micro-components.

In the San Giovanni section, the *Chondrodonta* bedset is 170 cm thick (Fig. 3.12A, B), deposited on top of a 60 cm-thick tabular stromatolite. It is composed of a lower sub-set, about 60 - 70 cm thick and arranged in decimetre-thick tabular beds, and of an upper sub-set of nodular and undulated beds, 100 - 120 cm-thick on average. In the tabular sub-set, *Chondrodonta* is absent to locally common, scattered in small patches with shells mostly sub-horizontal or, less commonly, in upright position. In the nodular subset, shells increase considerably in abundance and are arranged in floatstone-rudstones of sub-horizontal shells packed in dense sheets (Fig. 3.12C), interbedded to floatstone

patches (*i.e.*, parautochthonous accumulations) with chaotically oriented individuals beside bouquet-like aggregates; the abundance of both individuals in up-right position and bouquets increases towards the top of the bedset (Fig. 3.12D).

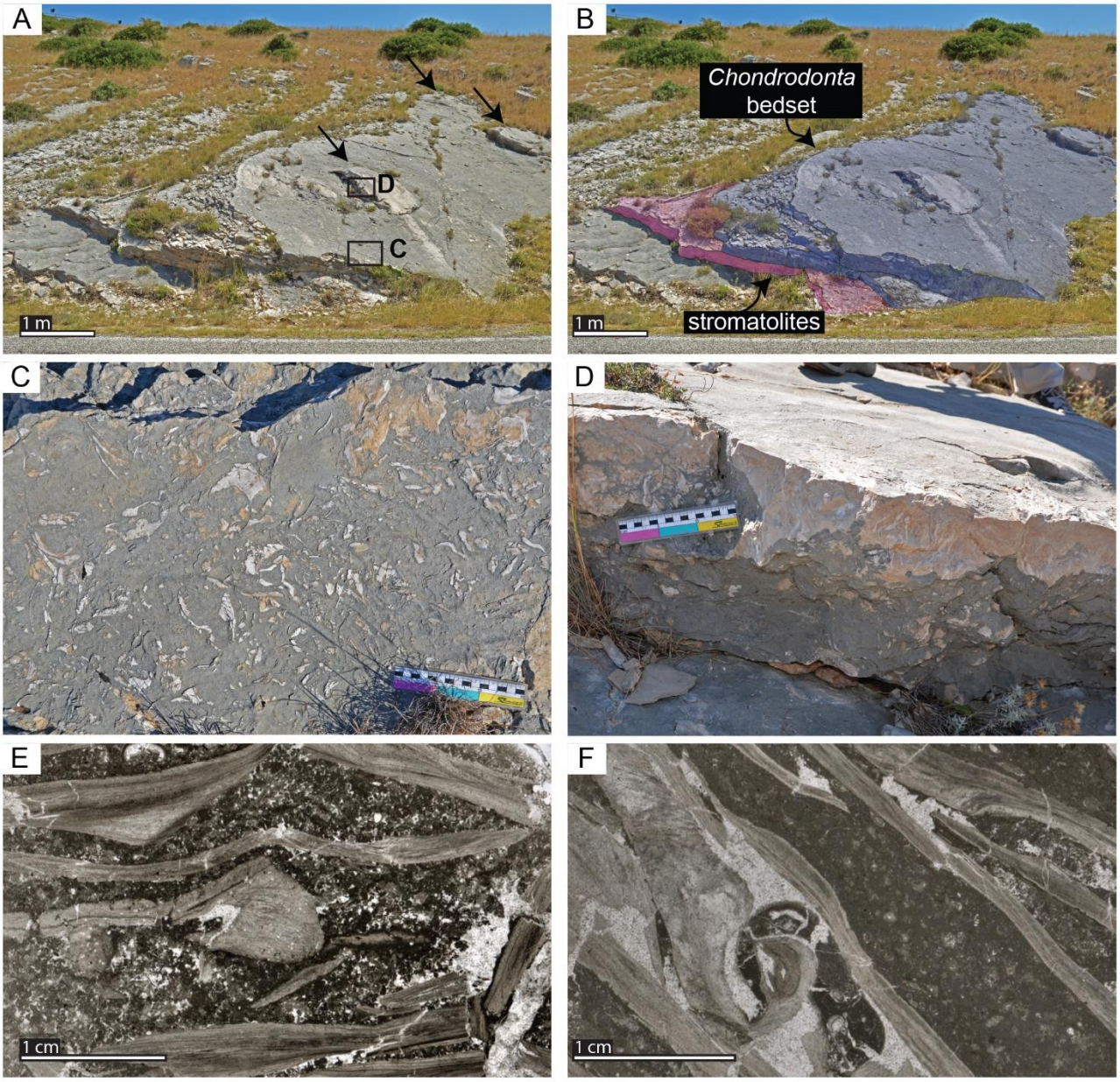

Fig. 3.11. Field photographs of the *Chondrodonta* bedset of the Borgo Celano 1 section. A) roadcut of the bedset; arrows point to the three knobby reliefs recognized in Posenato *et al.* (2018). B) same roadcut on which the bedset and the underlying stromatolites have been highlighted. C) abundant and frequently sub-horizontal shells on the upper surface of the bedset. D) shells in up-right position and arranged in bouquet-like aggregates within the knobby reliefs. E-F) thin sections from the *Chondrodonta* bedset, showing E) sub-horizontal shells bearing in a *Chondrodonta* fragments-packstone matrix and F) sub-vertical shells bearing in a wackestone-packstone matrix.

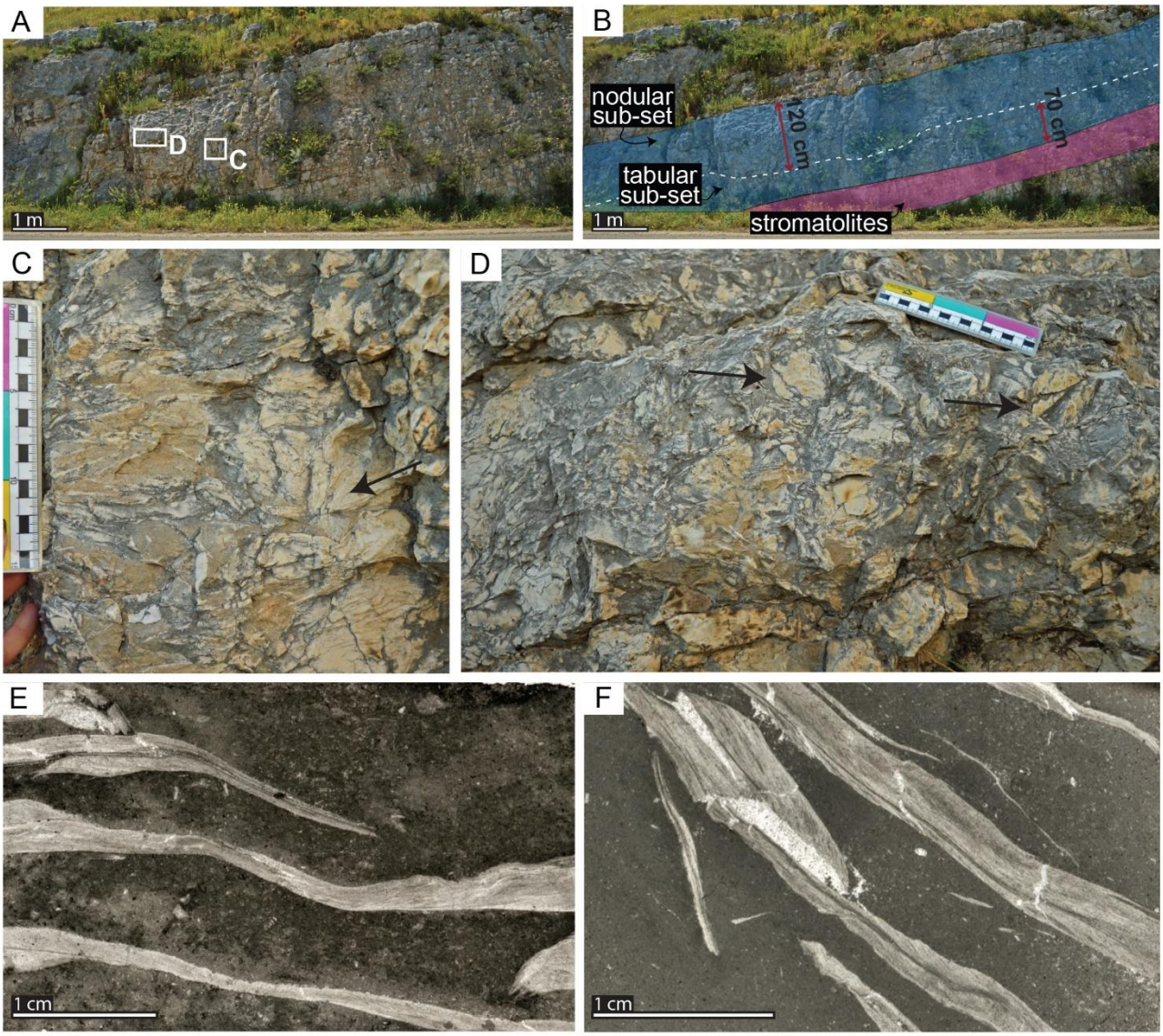

Fig. 3.12. Field photographs of the *Chondrodonta* bedset of the San Giovanni section. A) roadcut of the bedset. B) same roadcut on which the bedset and the underlying stromatolites have been highlighted; the bedset has been divided into a lower tabular sub-set and an upper nodular subset. C) close-up of the densely packed sub-horizontal shells in the lower nodular sub-set; arrows point to scattered individuals with a sub-vertical orientation. D) close-up of the upper nodular sub-set, in which shells are frequently in up-right position (some of these pointed by arrows) and in small-bouquet-like aggregates. E-F) thin sections from the *Chondrodonta* bedset, showing E) sub-horizontal shells bearing in bioclastic wackestone matrix and F) sub-vertical shells bearing in a *Chondrodonta* fragments-wackestone matrix.

The bedset in San Giovanni forms a monospecific association in which requieniids occur only rarely. *Chondrodonta* shells occur either within a peloidal-bioclastic wackestone-packstone (Fig. 3.12E) or in a *Chondrodonta* fragments- and bioclastic-wackestone matrix (Fig. 3.12F), passing to a mudstone in the upper part. Small benthic foraminifers, dasycladales and *Thaumatoporella* are subordinated micro-components; *Cayeuxia* is common in the uppermost part of the bedset.

3.6. Interpretation and discussion

3.6.1. Reliability of the geochemical results

In the studied sections, scatterplots of $\delta^{13}C$ and $\delta^{18}O$ show no significant correlation for individual lithofacies nor for lithofacies associations (Fig. 3.13A, B), suggesting that variations in $\delta^{13}C$ are not the result of facies changes. In the analysed samples, most of the isotope bulk values is coherent with the rudist and *Chondrodonta* shells isotope values (*see* also $\delta^{13}C$ and $\delta^{18}O$ curves in Fig. 3.6 and 3.8B).

The analysed samples partly overlap the Aptian isotopic field of the Apennine Platform shallow-water carbonates (Di Lucia *et al.*, 2012; Schmitt *et al.*, 2020) and plot within the lower range of Barremian - Aptian seawater ("low-latitude") biotic calcite field of Prokoph *et al.* (2008) (Fig. 3.13C). With respect to the field of the Aptian Apennine Platform carbonates, an important tail of more depleted $\delta^{13}C$ and $\delta^{18}O$ values is observed. The moderate inverted "J" stable isotope pattern (more visible for the San Giovanni section; *see* Fig. 3.13A, C) indicates an impact of meteoric diagenesis (Allan & Matthews, 1982; Lohmann, 1988), mainly affecting LA1 and LA2 facies. In the presented dataset, LA1 and, subordinately, LA2 facies, contain frequent exposure-related features like spar-filled fenestrae, micro-vugs and thin intraformational brecciated levels (Fig. 3.13A, C). Despite this evidence of meteoric alteration, not all samples located below emersion surfaces have negative $\delta^{13}C$ values as well as not all samples with negative $\delta^{13}C$ values are associated with exposure surfaces. These findings confirm the complexity of the stable isotopes' behavior in shallow-water carbonates associated to exposures (*e.g.,* Immenhauser *et al.*, 2003; Theiling *et al.*, 2007; Christ *et al.*, 2012) and suggest that some negative excursions may be related to changes in the primary marine carbon isotope signal.

Considering the potential for diagenetic effects, a conservative approach was chosen to use the $\delta^{13}C$ profiles for stratigraphic correlations (*e.g.,* Huck *et al.,* 2017). All samples with evidence of exposure/dissolution features at the outcrop or at the microscope scale were discarded and a smoothing procedure was run to highlight low-order trends and excursions in $\delta^{13}C$ (*see* Fig. 3.6, 3.8B, 3.10A, B). The general trend of $\delta^{13}C$ values is more likely to record the long-term global variations of the open ocean than higher-order fluctuations; the latter are more likely to result from variations in local environmental conditions on the shallow platform (Colombie *et al.,* 2011).

The overall isotope trends and excursions, which extend across multi-metre-thick intervals in both San Giovanni and Borgo Celano, can be traced and correlated across the two sections (*e.g.,* the positive $\delta^{13}C$ peak at the top of the *Chondrodonta* bedsets, which precedes a decreasing trend of the

curve). This evidence suggests that isotopic patterns in the smoothed data are, therefore, significant and reflect a control overriding the local-scale diagenetic processes.

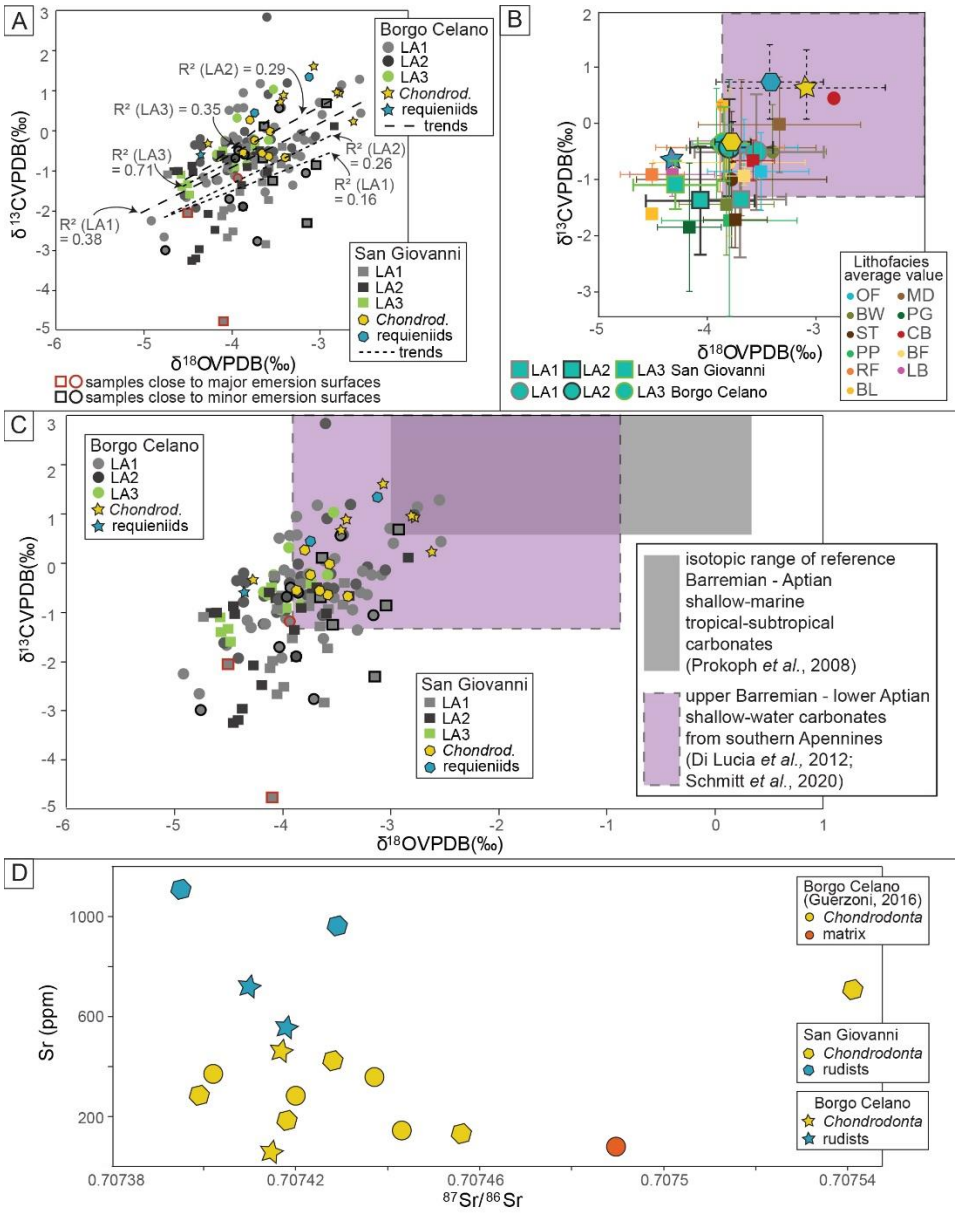

Fig. 3.13.
A) C and O correlation for the bulk of each lithofacies association and for *Chondrodonta* and requieniid shells. B) C and O average correlation for single lithofacies, lithofacies associations and shells. C) scatterplots of the studied sections against the isotopic range of both the Barremian - Aptian shallow-marine tropical-subtropical carbonates of Prokoph *et al.* (2008) and the Barremian – lower Aptian shallow-water carbonates of the Apennine Platform (Di Lucia *et al.*, 2012; Schmitt *et al.*, 2020). D) correlation between the concentration of Sr (ppm) and the $^{87}Sr/^{86}Sr$ value in *Chondrodonta* and requieniid shells, compared to the Borgo Celano shell samples analysed by Guerzoni (2016).

In the presented dataset, all shell samples have Fe and Mn concentrations below the conventional threshold indicative of diagenetic resetting, and they show no covariance with Sr concentrations (Tab. 3.2). The Sr content is higher in rudist shells (558 ppm to 1109 ppm) than in *Chondrodonta* shells (57 to 708 ppm), as also observed by Schmitt *et al.* (2020) in samples from the Apennine Platform. No correlation between decreasing Sr content and increasing/decreasing $^{87}Sr/^{86}Sr$ in rudists and *Chondrodonta* shells (Fig. 3.13D) as well as no covariance of Sr concentration with $\delta^{13}C$ or $\delta^{18}O$

values, were observed. Only one sample from the *Chondrodonta* bedset of San Giovanni, despite its high Sr concentration, yields an $^{87}Sr/^{86}Sr$ value higher than the isotope composition of the sample matrix (sample DPG11-A; *see* Tab. 3.2). On the other hand, a few samples with low Sr concentration also have low $^{87}Sr/^{86}Sr$ values (Tab. 3.2). This evidence indicates that strict thresholds in Fe, Mn and Sr concentrations are not perfect screening mechanisms for identifying samples with primary isotope ratios.

Internal consistency of Sr isotopic values among different components within the same bed or nearby beds is, instead, considered as a strong evidence for preservation of the original signal (McArthur *et al.*, 2004, 2012). Therefore, samples with elemental concentrations below the published elemental threshold values (*e.g.,* Sr > 500 ppm for *Chondrodonta* and Sr > 700 ppm for rudists) were considered for SIS only when their Sr-isotope values were within the analytical error ($8*10^{-6}$ in average), with respect to other shells from the same bed or from the nearby beds. Only one sample (SG14-D; *see* Tab. 3.2), despite its internal consistency of the Sr isotopic value, was discarded for the SIS due to a lower Sr concentration with respect to the one measured in the matrix.

To reveal the possible influence of terrigenous input on the REE signal, several lines of evidence have been used (Nothdurft *et al.*, 2004; Liu *et al.*, 2019; *see* Chap. 2, par. 2.2.3.2 for details). Both stratigraphic sections show a negative Ce anomaly, in a range of 0.64 – 0.9 at San Giovanni (averaging 0.75) and of 0.72 – 0.93 at Borgo Celano 1 (averaging 0.83) (*see* Fig. 3.7 and 3.9). The concentration of Al averages 669 ppm at San Giovanni and 437 ppm at Borgo Celano 1 whereas the concentration of Sc averages 0.17 ppm at San Giovanni and 0.12 ppm at Borgo Celano 1 (*see* Appendix I). In both cases, values are clearly lower with respect to the upper concentration limits (3500 ppm of Al and 2 ppm of Sc) which may exert a terrigenous influence on the Ce anomaly (Ling *et al.,* 2013).

The Y/Ho ratio, used as tracer to assess whether carbonate particles reflect a primary marine signature or siliciclastic components (*e.g.,* Nothdurft *et al.*, 2004; Frimmel, 2009; Liu *et al.*, 2019) averages 46 at San Giovanni and 46.7 at Borgo Celano 1, indicating marine carbonates likely free of contamination from terrigenous material (Bau, 1991, 1996; Nozaki *et al.*, 1997; Liu *et al.*, 2019). However, the uppermost four samples at San Giovanni (DPG12A, 13, 14A and 19; *see* Fig. 3.7) in correspondence of the highest concentration of Aluminum (between 1000 and 3200 ppm) show the lowest Y/Ho ratio, between 31 and 40, indicative of a possible siliciclastic contamination (Chen *et al.*, 2015). At Borgo Celano 1, the lowest Y/Ho ratios, between 39 and 41 (SG14 and 18; *see* Fig. 3.9) correspond to an increased concentration of Al (between 450 and 1150 ppm).

Location	Sample		Component	$^{87}Sr/^{86}Sr$ measured	± 2 s.e. ($*10^{-6}$)	$^{87}Sr/^{86}Sr$ corrected	± 2 s.e. mean ($*10^{-6}$)	Mg (µg/g)	Sr (µg/g)	Fe (µg/g)	Mn (µg/g)	Min	Age (Ma) preferred	Max
San Giovanni	*Chondrodonta* bedset	DPG11-A	*Chondrodonta*	0.707538	19	*0.707541*		1847	708	91.9	4.93			
		DPG10B-E	*Chondrodonta*	0.707453	9	*0.707456*		1266	130	46.5	4.36			
		DPG10B-C	*Chondrodonta*	0.707425	5	0.707428		1670	423	100	2.77			
		DPG10B-F	*Chondrodonta*	0.707415	6	0.707418		1362	181	38.5	2.87			
		DPG11D-B	*Chondrodonta*	0.707396	7	0.707399		1705	283	40	1.76			
					mean	**0.707415**	**21**					125.2	**125.87**	126.35
		DPG11-m	matrix					1351	66	179	5			
		DPG38-A	requieniid	0.707415	5	0.707395		1075	1109	35	0.9			
		DPG37-A	requieniid	0.707426	18	0.707429		1021	963	29.8	1.2			
					mean	**0.707412**	**34**					124.55	**125.75**	126.65
		DPG37-m	matrix					1156	61	128	4			
Borgo Celano	*Chondr.* bedset	BCG3-1	requieniid	0.707404	5	0.707410		1718	720	37	3.46			
		SG14-D	*Chondrodonta*	0.707412	6	*0.707415*		1713	57	42	11.5			
					mean	**0.707410**	**34**					124.48	**125.65**	126.60
		BCG-m	matrix					1949	96	185	10			
		SG6B-A	requieniid	0.707415	4	0.707418		979	558	7.42	5.63			
		SG6B-B	requieniid	0.707419	6	0.707422		na	na	na	na			
		SG6A	*Chondrodonta*	0.707414	5	0.707417		2589	463	34.8	3.54			
					mean	**0.707419**	**3**					125.9	**125.98**	126.08
		SG6-m	matrix					1543	73	136	9			

Tab. 3.2. Elemental concentrations and Sr-isotope ratios of the studied rudist and *Chondrodonta* samples collected from the San Giovanni and the Borgo Celano 1 sections. Sr-isotopes values have been corrected for interlaboratory bias (*see* text for further details). Preferred numerical ages have been derived from the look-up table of McArthur *et al.* (2001, version 5: 04/2013), which is calibrated to the Geological Time Scale of McArthur *et al.* (2012) and Ogg & Hinnov (2012). *See* text for details on the precision estimation and on the calculation of minimum and maximum ages. In italics, samples discharged from the Strontium Isotope Stratigraphy (SIS); in bold, the mean value of the Sr isotope ratio for each sample set and the preferred numerical age derived from it. Minimum and maximum ages were obtained by combining the statistical uncertainty (2 s. e.) of the mean values of the Sr-isotope ratios with the uncertainty of the seawater curve (*see* Frijia *et al.*, 2015 for details on the procedure).

This finding is partly confirmed by the overall PAAS-normalized REE patterns (Fig. 3.14A). The concentration of REE in the San Giovanni and Borgo Celano 1 samples, normalized to the Post-Archean Australian Shale (PAAS) standard values given in Taylor & McLennan (1985), has been plotted against the South Pacific deep-water curve of Zhang & Nozaki (1996) which displays the typical seawater REE signal, and against the North American Shale Composite of Gromet *et al.* (1984). At San Giovanni, a slight enrichment in HREE (*i.e.,* Heavy REE) with respect to LREE (*i.e.,* Light REE) occurs in most samples (Fig. 3.14A). Although the difference in concentration between LREE and HREE is not clearly marked as in the South Pacific deep-water curve, similar overall REE patterns have been formerly interpreted as indicative of a marine signal of REE (*see*, for instance, Fig. 7 in Hueter *et al.*, 2019 and Fig. 6A in Özyurt *et al.*, 2020). However, the uppermost four samples (DPG12A, 13, 14A and 19) show the typical "bell-shaped" pattern, characterized by an MREE (*i.e.,* Mid REE) enrichment and declining LREE and HREE, and interpreted as an indicator for

contamination and/or riverine influence (*see* Della Porta *et al.*, 2015; Hueter *et al.*, 2020). The latter samples also correspond to the lowest Y/Ho ratio measured for the San Giovanni section as well as to a LREE/HREE ratio above 1 (*see* Menendez *et al.*, 2018 and references therein), further supporting a siliciclastic influence limited to the stratigraphic interval between 9.3 – 13.2 m (*see* Fig. 3.7).

The overall PAAS-normalized REE patterns for the Borgo Celano 1 section display a signature closer to the North American Shale Composite with respect to the San Giovanni samples (Fig. 3.14A). REE patterns are almost flat (exception given for sample SG14) and the enrichment in HREE with respect to LREE is neglectable. The typical "bell-shaped" pattern is clearly visible in the uppermost sample (SG18), which also records a low Y/Ho ratio and the highest LREE/HREE ratio (close to 1). These findings suggest a higher siliciclastic input in the uppermost part of Borgo Celano 1 (between 16 and 17 m) as well as an overall more pronounced terrestrial contamination with respect to the San Giovanni section.

All samples, from both San Giovanni and Borgo Celano 1, were further screened for diagenetic alteration, which may exert an influence on both the REE patterns and the Ce anomaly (Nothdurft *et al.*, 2004; Frimmel, 2009; Liu *et al.*, 2019). Positive correlations between the Ce anomaly and ΣREE (*i.e.*, summation of REE + Y abundances), between the Eu anomaly and ΣREE as well as between Ce/Ce* and Eu/Eu* have been formerly used to assess the potential diagenetic effect on the REE signature in limestones (Shields & Stille, 2001; Shields & Webb, 2004; Liu *et al.*, 2019). In the San Giovanni samples, very low or absent positive correlation between the abovementioned parameters is observed (Fig. 3.14B, C, D), suggesting an irrelevant influence of post-depositional alteration on the measured Ce/Ce* and on the general REE signal. In contrast, weak to moderate positive correlations in the same parameters occur in the Borgo Celano 1 samples (Fig. 3.14B, C, D), indicating the possible influence of post-depositional alteration.

Furthermore, the relationship between Ce/Ce* and Pr/Pr* has been used to characterize redox conditions by the La anomaly diagram of Bau & Dulski (1996) (Fig. 3.14E). Most of the San Giovanni samples and half of the Borgo Celano 1 ones fall within the IIIb field, indicative of a genuine negative Ce anomaly due to a real depletion of Ce with respect to the neighboring REE (*i.e.*, La and Pr), and not artificially created by a La enrichment (Bau & Dulski, 1996; Bodin *et al.*, 2013; Hueter *et al.*, 2019). Three samples from San Giovanni and the other half of the Borgo Celano 1 ones (collected in the uppermost part of the section) fall within the IIa field, indicating a slightly over-estimated negative Ce anomaly due to a positive La anomaly.

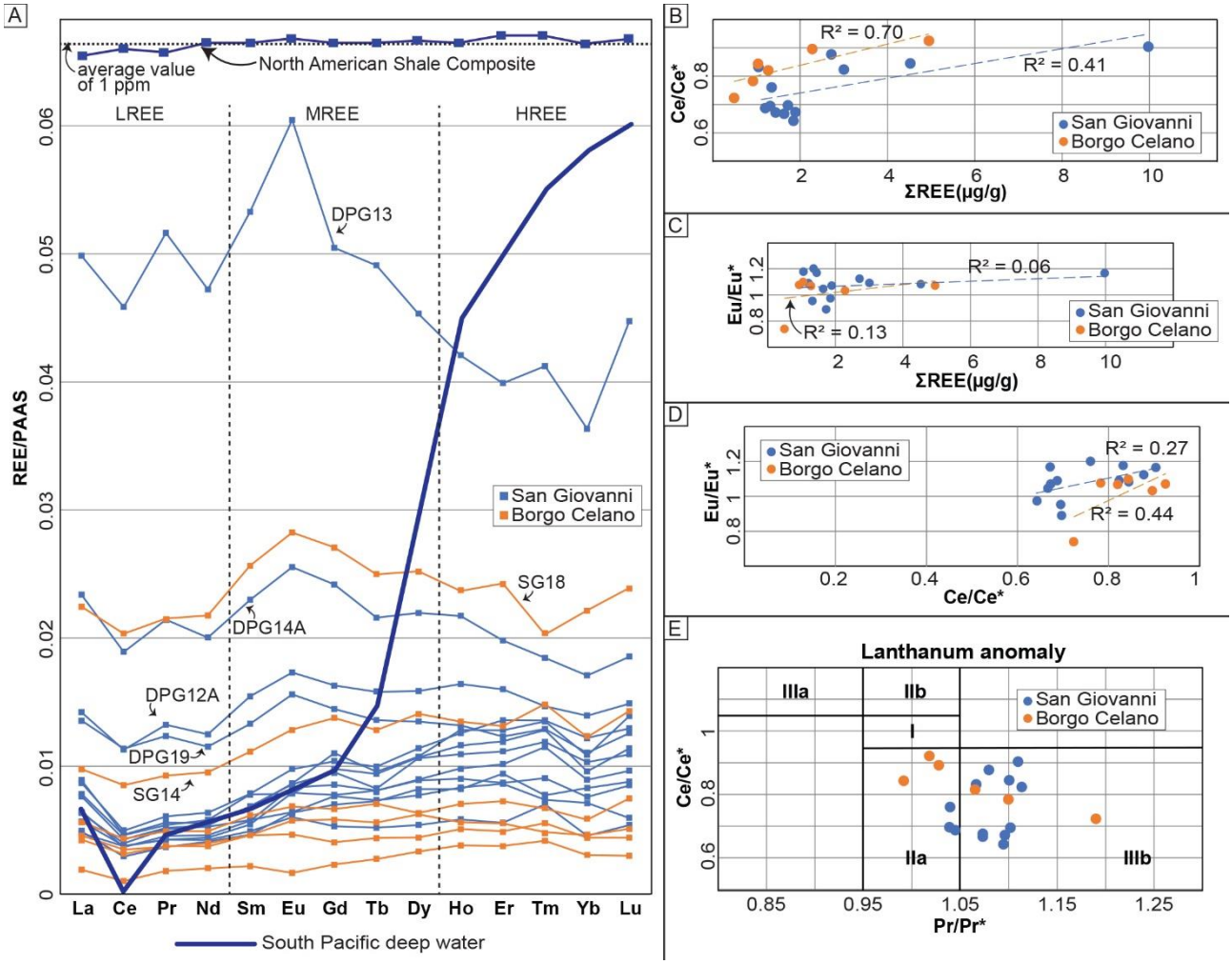

Fig. 3.14. A) the PAAS-normalized REE patterns of the San Giovanni (blue) and Borgo Celano 1 (orange) sections, plotted against the North American Shale Composite of Gromet *et al.* (1984) and against the South Pacific deep-water curve of Zhang & Nozaki (1996). Abbreviations: LREE (*i.e.,* Light REE; La, Ce, Pr, Nd), MREE (*i.e.,* Mid REE; Sm, Eu, Gd, Tb, Dy), HREE (*i.e.,* Heavy REE; Ho, Er, Tm, Yb, Lu). B) correlation between the Ce anomaly (Ce/Ce*) and ΣREE. C) correlation between the Eu anomaly (Eu/Eu*) and ΣREE. D) correlation between Ce/Ce* and Eu/Eu*. E) the lanthanum anomaly diagram, showing samples falling within the IIa and IIIb fields of Bau & Dulski (1996).

To sum up, samples from the San Giovanni section display an overall diagnostic seawater REE signature, with a minimum siliciclastic input (concentrated only between 9.3 – 13.2 m) and a negligible to absent diagenetic overprint.

Samples from the Borgo Celano 1 section must be, in contrast, treated carefully for the interpretation of the redox state. Although some indexes suggest a negligible terrigenous input (high Y/Ho and low LREE/HREE ratios), the shale-like REE pattern as well as the positive covariance between the REE anomalies (*see* above and Fig. 3.14) suggest at least a partial alteration of the REE signal and of the Ce anomaly due to both siliciclastic and diagenetic influences.

Therefore, the negative Ce anomaly recorded at San Giovanni can be considered more reliable in indicating the real seawater signal and can thus be used, coupled with the RSTE/Al ratios, to estimate the redox state during the deposition of the studied limestones.

3.6.2. Correlation of the stratigraphic sections

The integrated high-resolution framework based on biostratigraphy, SIS and C-isotope stratigraphy enables correlation of lithofacies and lithofacies associations.

The benthic foraminiferal assemblage at the base of the three sections (Fig. 3.6, 3.8A, 3.10A), including *Cuneolina* sp., *P. infracretacea*, *Mayncina* sp. and the last occurrence of the dasycladacean alga *S. muehlbergii* (0.5 m at San Giovanni and 11 m at Borgo Celano), indicates a lowermost Aptian age (Chiocchini *et al.*, 2012). Above the *Chondrodonta* bedsets, the co-occurrence of *Debarina* sp., *Pseudolituonella* sp. and *S. dinarica* indicates either an early (Chiocchini *et al.*, 2012) or early - late (Di Lucia *et al*., 2012) Aptian age. The co-occurrence of *M. lotzei* and *P. cormyi* within the uppermost part of the Borgo Celano 2 section (*see* also Claps *et al.*, 1996) suggests a late early Aptian or, possibly, an early late Aptian age, according to the most recent review of Schröeder *et al.* (2010).

The mean $^{87}Sr/^{86}Sr$ from the *Chondrodonta* bedsets at San Giovanni (0.707415) and at Borgo Celano 1 (0.707410) are statistically indistinguishable (*see* Tab. 3.2), suggesting that they are roughly coeval. The first occurrence of *Debarina* sp. a few metres above the top of the *Chondrodonta* bedsets, supports this interpretation. The isotopic values indicate an estimated age of 125.87 ± 0.6 Ma at San Giovanni and of 125.65 ± 1 Ma at Borgo Celano, corresponding to the lower part of the early Aptian, consistent with the biostratigraphic data. Samples of a bivalve floatstone 5 m below the *Chondrodonta* bedset at Borgo Celano 1 have an $^{87}Sr/^{86}Sr$ mean value of 0.707419, calibrated to an age of 125.98 Ma ± 0.1. A rudist floatstone 12 m above the *Chondrodonta* bedset at San Giovanni has a value of 0.707412, calibrated to an age of 125.75 Ma ± 1. The similar $^{87}Sr/^{86}Sr$ values among sections constrain the age of the *Chondrodonta* bedsets within the early Aptian, at the boundary between *Globigerinelloides blowi* and *Leupoldina cabri* planktic foraminiferal zones, according to the GTS2012 (Ogg & Hinnov, 2012).

The negative excursions in $\delta^{13}C$ above the *Chondrodonta* bedsets are interpreted to be correlative, as are the negative excursions around the *Bacinella*-rich interval. The *Chondrodonta* bedsets have therefore been used as stratigraphic *datum* to correlate the stratigraphic sections (Fig. 3.15).

Both stratigraphic sections are characterized by a benthic community dominated by *Chondrodonta* and micro-encrusters in the lower part and by *Bacinella-Lithocodium* in the upper part. These biotic

changes reflect a stressed platform ecosystem during the deposition of the lower Aptian San Giovanni Rotondo Limestone, preventing the thriving of a diversified macro- and micro-benthic fauna. Similar biotic turnovers, indicative of environmental stress, have been documented worldwide during the early Aptian (Rameil *et al.*, 2010; Huck *et al.*, 2010; Skelton & Gili, 2012; Stein *et al.*, 2012; Huck *et al.*, 2014; Núñez-Useche *et al.*, 2020 among others).

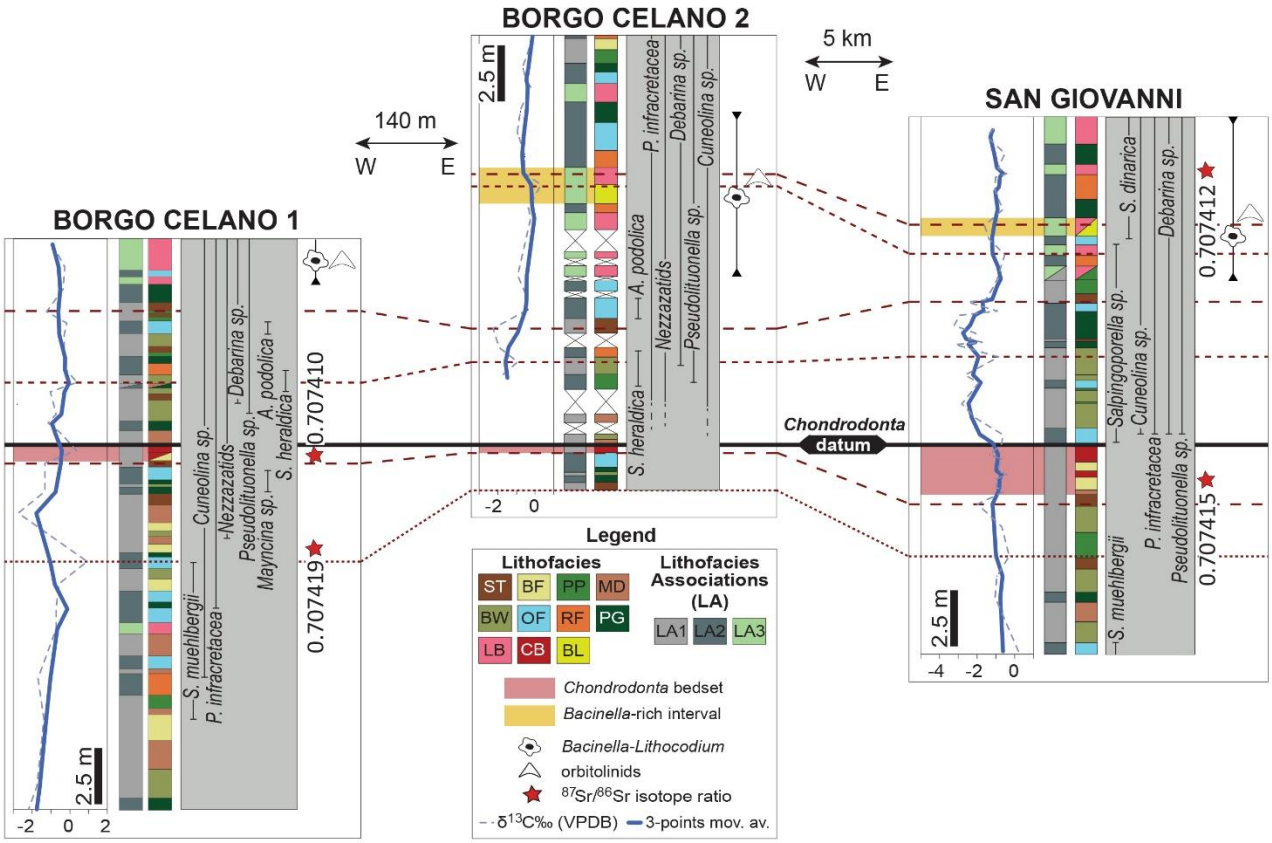

Fig. 3.15. Attempt of correlation between the investigated sections based on SIS, biostratigraphy, $\delta^{13}C$ curves and on the vertical evolution of lithofacies. The *Chondrodonta* bedsets are here used as *datum*. *See* par. 3.5.1 and Tab. 3.1 for the description of lithofacies and lithofacies associations.

Relative sea-level fluctuations in the stratigraphic sections are indicated by both ephemeral emersion-related features in the lower part and by a facies shift towards open shelf deposits in the middle-upper part. These fluctuations can be attributed either to decreased carbonate production or to eustatic changes. Along the margin of the ACP, a pronounced lower Aptian backstepping of at least 5 km landward is indicated by pelagic facies (Marne a Fucoidi formation) overlying the slope and margin succession. This backstepping, interpreted as a drowning unconformity (Bosellini *et al.*, 1999a; Graziano, 2013) or as a partial drowning (Morsilli *et al.*, 2017), is coeval with the drowning phase

documented in many other lower Aptian Tethyan platforms (Husinec *et al.*, 2012; Bover-Arnal *et al.*, 2012; Maurer *et al.*, 2013; Pictet *et al.*, 2015 among others). However, no high-resolution sequence stratigraphic studies of the lower Aptian inner platform facies on the ACP have been carried out to date and the short stratigraphic interval analysed in this study prevents a broader scale comparison to track sea-level changes at a regional or global scale.

3.6.3. Platform-to-basin correlation: the OAE1a interval on the ACP

The $\delta^{13}C$ record of the studied sections can be used in combination with biostratigraphic markers and SIS to achieve a chemostratigraphic correlation with the $\delta^{13}C$ curves of the Cismon Apticore in southern Alps (Menegatti *et al.*, 1998; Erba *et al.*, 1999) and of the Adriatic Basin adjacent to the ACP (Luciani *et al.*, 2001, 2006) (Fig. 3.16).

The beginning of the negative $\delta^{13}C$ trend in the studied sections (1.6 m at San Giovanni and 11.1 m at Borgo Celano) is correlative with the top of the magnetochron M0 of Malinverno *et al.* (2010), right below the onset of the C3 segment in the Cismon section. The C3-C6 chemostratigraphic segments of the Selli Event (Menegatti *et al.*, 1998; Erba *et al.*, 1999; Malinverno *et al.*, 2010) are here placed within the middle-upper part of the San Giovanni section and in the lower part of Borgo Celano composite. The beginning of the C3-C4 segments within the Cismon Apticore is correlated with the negative shift right above the *Chondrodonta* bedsets (Fig. 3.16). The positive shift of the C6 segment in the Cismon Apticore is tentatively correlated with the *Bacinella*-rich level. Higher in the Borgo Celano composite section, the increasing $\delta^{13}C$ values associated with thick stromatolite beds are tentatively correlated to the C7 segment. According to this interpretation, both the San Giovanni and the Borgo Celano $\delta^{13}C$ curves would capture the entire perturbations of the global carbon cycle associated with OAE1a, including their prelude in the upper C2 segment.

This chemostratigraphic correlation places the *Chondrodonta* bedsets within the uppermost C2 segment, making them coeval with the *Chondrodonta* accumulations of the Monte degli Angeli Limestone margin facies (*see* Graziano, 2013; Guerzoni, 2016) exposed along the southern Gargano Promontory (Fig. 3.3A).

The chemostratigraphic C3–C4 segments (Fig. 3.16) correlate in the studied sections with an interval of peloidal packstone-grainstones and lime mud-rich facies with scarce to absent skeletal components like mollusks, foraminifers and dasycladales (*see* Fig. 3.6, 3.8A, 3.10A). This decreased abundance of organisms indicates deposition under stressed conditions during the first part of OAE1a, as also suggested by the trace element concentrations in the San Giovanni section for this tract (between 9.3

and 13.2 m; *see* Fig. 3.7). Decreased RSTE/Al and P/Al ratios occur coupled with an increase in both Al (ppm) and Ti/Al concentrations, which also partly alter the Ce anomaly and the REE signal (*see* par. 3.6.1). Increased Al (ppm) and Ti/Al may indicate short episodes of enhanced weathering of continental rocks. During the OAE1a interval, indeed, weathering was usually triggered by CO_2 pulses from active volcanism that resulted in higher average temperatures (O'Brien *et al.*, 2017) and likely more accentuated precipitation cycles (Tejada *et al.*, 2009). Increased siliciclastics, together with dysaerobic seawaters and lower nutrient levels may explain, therefore, the impoverished fauna in the C3–C4 segments of the ACP.

Stressed conditions on the ACP in the lower part of OAE1a are further suggested by the gamma ray profiles of the Borgo Celano 1 section (*see* Fig. 3.8B). The increase in the total API units and, particularly, in uranium (ppm) across the C3-C4 tract may indicate a progressive enrichment in organic matter. Similar trends, with a marked gamma ray peak caused by an increased concentration of uranium, have been observed in the lower part of the Shu'aiba formation in northern Oman (Vahrenkamp, 2010). The OAE1a interval in the Shu'aiba formation (*cfr.* "Maximum Flooding Interval"; *see* Vahrenkamp, 2010) is marked by a gamma ray peak caused by the uranium, interpreted as indicative of an enrichment in organic matter.

This enrichment in organic matter at Borgo Celano also correlates with a global biocalcification crisis (Weissert & Erba, 2004; Erba *et al.*, 2010; Giraud *et al.*, 2018), carbonate platforms drowning in northern Tethys, and biotic turnover (from rudist- to *Bacinella-Lithocodium*-dominated) on carbonate platforms of the southern Tethys (*e.g.,* Skelton & Gili, 2012; Huck *et al.*, 2014).

The San Giovanni section and the lower part of the Borgo Celano composite have been further correlated to the $\delta^{13}C$ curve of the Coppitella section in the Adriatic Basin. This section is made of the pelagic deposits of the Marne a Fucoidi formation (Fig. 3.3A). Black shales occur only in the C6-C7 segments (*cfr.* "lower" and "upper" black shales in Luciani *et al.*, 2001, 2006), are absent in the C3–C4 segments and not exposed in the C5 (*see* Fig. 3.16). Both the micropaleontological associations and the stratigraphic position of black shales at Coppitella indicate that eutrophication occurred only from the upper part of OAE1a interval in the Adriatic Basin (*i.e.,* from the C6 segment; Luciani *et al.*, 2001).

Moderate and high fertility conditions have been interpreted for the lower (C6 segment) and upper (middle C7 segment) black shales, respectively (*see* Fig. 6 to 9 in Luciani *et al.*, 2001). The same time interval was characterized by biotic turnovers in the shallow-water settings of the ACP. Indeed,

the gradual disappearance of rudists in favour of orbitolinids and *Bacinella-Lithocodium* assemblages is indicative of a gradual shift from oligo- to mesotrophic conditions across OAE1a, according to the nutrient gradients for benthic communities proposed by Mutti & Hallock (2003) and Rameil *et al.* (2010).

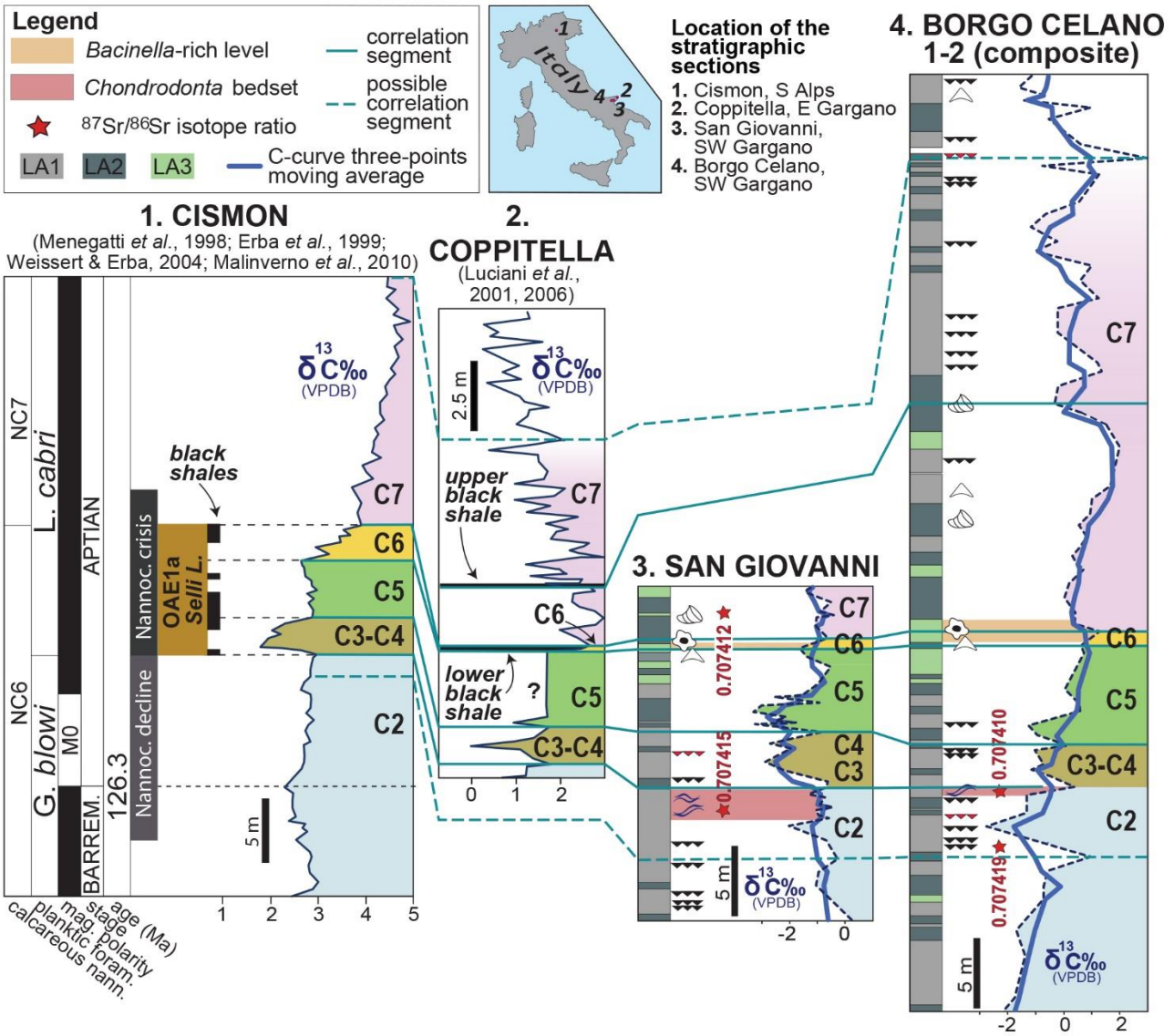

Fig. 3.16. Chemostratigraphic correlation of the studied sections (San Giovanni and Borgo Celano composite) with the reference $\delta^{13}C$ curve of the Cismon Apticore in southern Alps (Menegatti *et al.*, 1998; Erba *et al.*, 1999) and with the $\delta^{13}C$ curve of the pelagic Coppitella section on the Gargano Promontory (Luciani *et al.*, 2001, 2006), representative of the Adriatic Basin adjacent to the ACP. The $\delta^{13}C$ curve of the Cismon Apticore has been taken from Erba *et al.* (1999), the nannofossil and planktic foraminiferal biostratigraphy is from Weissert & Erba (2004); the nomenclature of the C-isotope C2–C7 segments and the black shale levels are from Menegatti *et al.*(1998) and the nannoconid decline and crisis intervals as well as the magnetic polarity are from Malinverno *et al.* (2010); the numerical age of the Barremian – Aptian boundary is after Ogg & Hinnov (2012).

The *Bacinella*-rich level of San Giovanni and Borgo Celano (*i.e.*, chemostratigraphic C6 segment) correlates to the deposition of the "lower" black shale and to moderate fertility conditions in the Adriatic Basin (Fig. 3.16; *see* Luciani *et al.*, 2001). An increased nutrients input on the ACP in this tract is also suggested by the more open-shelf facies of the coeval Coppa di Pila limestones (northern Gargano; Fig. 3.3A). Here, orbitolinid-rich mudstones with subordinate *Bacinella-Lithocodium* micro-encrustations are overlain by foraminifers- and bivalve-rich beds, indicative of restoration of normal-marine conditions at the end of the anoxic event (Guerzoni, 2016).

Transient peaks in the abundance of *Bacinella-Lithocodium*, coeval with black shale deposition during OAE1a, also occur on the Arabian and Adriatic platforms and have been interpreted to reflect meso-eutrophic conditions on the platform top (*e.g.,* Immenhauser *et al.*, 2005; Huck *et al.*, 2010; Rameil *et al.*, 2010; Hueter *et al.*, 2019).
The smaller magnitude bloom of *Bacinella-Lithocodium* on the ACP, with respect to the Arabian and Adriatic platforms, can be attributed to moderate nutrient levels on the platform top, coeval to the only moderate fertility conditions in the Adriatic Basin.
A transgressive and deepening-up trend is further interpreted at the base of the *Bacinella-Lithocodium* interval on the Arabian and Adriatic platforms (Huck *et al.*, 2010). On the ACP, a transgressive episode at the base of the *Bacinella-Lithocodium* facies is suggested by the deepening-up trend interpreted from open shelf LA2 deposits progressively replacing restricted subtidal LA1 facies in the C5-C6 segments (*see* Fig. 3.6, 3.8A and 3.15).

3.6.4. Palaeoenvironmental controls on the proliferation of Chondrodonta

During OAE1a, environmental disturbances triggered by the Barremian - Aptian climate warming (Larson, 1991; Larson & Erba, 1999; Tejada *et al.*, 2009) caused biotic stress in the shallow- and deep-water domains (*e.g.,* Pancost *et al.*, 2004; Dumitrescu *et al.*, 2006; Föllmi *et al.*, 2006; Najarro *et al.*, 2010). Ocean eutrophication (*i.e.,* "nannoconid crisis"; Erba, 1994, 2004) and carbonate platforms demise (Weissert *et al.*, 1998; Wissler *et al.*, 2003) are widely documented. Intensified precipitation and biogeochemical continental weathering triggered by the warmer and more humid climate, increased the nutrient (*e.g.,* phosphorous) input to shallow-water areas (Föllmi, 1996, 2012; Compton *et al.*, 2000). The reinforced upwelling towards coastlines, due to intensified atmospheric and oceanic circulation during greenhouse periods, also resulted in the widespread accumulation of phosphatic sediments in shallow-water areas (Föllmi, 2012). As a result, the higher trophic levels on the platforms top promoted biotic turnover from oligo- to mesotrophic benthic communities during

OAE1a (*e.g.,* Immenhauser *et al.*, 2005; Skelton & Gili, 2012; Huck *et al.*, 2014; Amodio & Weissert, 2017; Hueter *et al.*, 2019). Nevertheless, biotic changes in the shallow-water benthic communities occurred also in the prelude phase of the anoxic event.

Chondrodonta is considered an opportunistic, r-strategist taxon and a relatively high nutrient availability has been suggested as a prerequisite for its thriving (Posenato *et al.*, 2018, 2020). This interpretation is supported by the stratigraphic occurrence of the studied *Chondrodonta* bedsets on the ACP, in an interval of transition from oligo-mesotrophic (*i.e.,* rudists) to fully mesotrophic (*i.e., Bacinella-Lithocodium*, orbitolinids) biotic assemblages (Fig. 3.6, 3.8A, 3.10A).
A relative increase in the P/Al concentration and its trend within the *Chondrodonta* bedset of the San Giovanni section (*see* Fig. 3.7) suggests relatively higher and fluctuating trophic levels during its deposition. These nutrient fluctuations, which occur just below the onset of OAE1a, correlate with an oligo-mesotrophic regime in the Adriatic Basin (*see* par. 3.6.3) and with increasing eutrophication in the nearby pelagic Cismon Apticore (Fig. 3.17; *see* Bottini *et al.*, 2015). The latter correlation further suggests the increase of trophic sources to have occurred at a broader to even regional scale, with respect to the single outcrop scale. However, stratigraphic evidence on the major sources of P on the ACP during the proliferation of *Chondrodonta* still needs to be investigated.

The facies analysis of the *Chondrodonta* bedsets on the lower Aptian ACP indicates a low-energy and restricted subtidal environment during their deposition. The RSTE/Al ratios at San Giovanni (Fig. 3.7) and, in a lesser extent, at Borgo Celano 1 (Fig. 3.9) show fluctuating trends within the *Chondrodonta* bedsets, suggesting that rapid changes in the local redox conditions did not exclude them. The high values of the negative Ce anomaly at San Giovanni further support less oxygenated seawaters during the interval of proliferation of this bivalve. These findings indicate that *Chondrodonta* was resilient to variations in the seawater oxygenation and circulation as confirmed by literature, where most Cretaceous monospecific (or quasi-) *Chondrodonta* biostromes are documented in low-energy, protected areas of the inner platform (Malchus *et al.*, 1995; Leonide *et al.*, 2012; Phelps *et al.*, 2014; Millán *et al.*, 2014; Núñez-Useche *et al.*, 2020 among others).
Although recent studies question anoxia as a driving mechanism for the demise of rudist–coral ecosystems in the prelude of OAE1a (*see* Hueter *et al.*, 2020), fluctuating seawater oxygenation may have represented a stressor for less tolerant benthic communities, enabling the more resilient *Chondrodonta* to outpace them.

The stratigraphic position of the *Chondrodonta* bedsets on the ACP corresponds also to an interval of increasing water temperature in pelagic settings (Fig. 3.17), far below the cooling episodes

recorded within OAE1a (*see* Jenkyns, 2018). Although the bivalve is also documented in cooler-water settings in the Aptian (*e.g.,* Millán *et al.*, 2014), warmer waters could have enhanced its proliferation before the onset of the Selli Event.

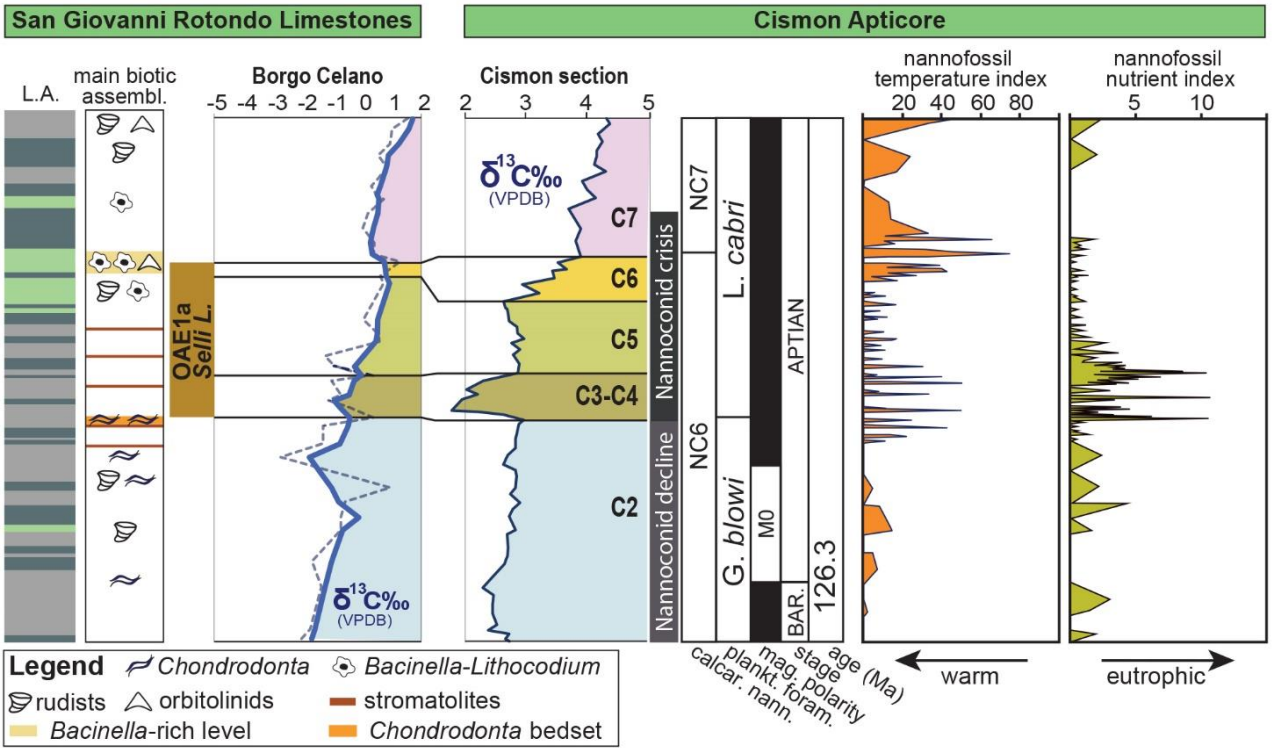

Fig. 3.17. Attempt of reconstruction of the palaeoenvironmental fluctuations influencing the proliferation of *Chondrodonta* within the lower Aptian SGRL. The main biotic events in the studied sections are compared to the temperature and nutrient fluctuations in the nearby pelagic realm of the Cismon section. The $\delta^{13}C$ curve of the Cismon Apticore has been taken from Erba *et al.* (1999), the nannofossil and planktic foraminifers biostratigraphy is from Weissert & Erba (2004); the nomenclature of the C-isotope C2–C7 segments is from Menegatti *et al.* (1998) and the Nannoconid decline and crisis intervals as well as the magnetic polarity are from Malinverno *et al.* (2010); the nannofossil temperature and nutrient indexes are from Bottini *et al.* (2015); the numerical age of the Barremian – Aptian boundary is after Ogg & Hinnov (2012). *See* par. 3.5.1 and Tab. 3.1 for the description of lithofacies associations.

In addition to warmer and more humid conditions of the early Aptian (Erba, 1994; Weissert & Erba, 2004), changes in water chemistry (*e.g.,* salinity and pH) may have facilitated the *Chondrodonta* proliferation by excluding other benthic competitors and potential predators. The early dissolution of the aragonitic inner shell layer in the *Chondrodonta* bedsets of Borgo Celano has been interpreted by Posenato *et al.* (2018) as possible consequence of a different aragonite saturation state related to seawater acidification during OAE1a. Because major changes in CO_2 concentrations did not

apparently result in any prolonged surface ocean acidity below or during OAE1a (*see* Naafs *et al.*, 2016), the seawater acidification as cause co-favoring the flourishing of *Chondrodonta* cannot be determined nor excluded.

The geochemical proxies of the San Giovanni section also show changes towards the top of the *Chondrodonta* bedset (*i.e.,* towards the onset of OAE1a; *see* Fig. 3.7 and 3.16). The relative decrease in the RSTE/Al and in the P/Al ratios, coupled with an increased concentration of Al and Ti/Al indicative of a terrigenous input, may reflect the exacerbation of the environmental stress on the ACP at the onset of the anoxic event, which resulted in conditions that excluded *Chondrodonta*.

It is, therefore, conceivable that the proliferation of this opportunistic bivalve took place in a short and confined environmental "window", triggered by the changing climate peaking with OAE1a and mainly resulting in nutrient pulses on the platforms top. The occurrence and duration of this environmental "window" was also controlled by local palaeogeographic and hydrodynamic settings. Indeed, low-energy, restricted seawaters with fluctuating oxygenation allowed *Chondrodonta* to outplay the less tolerant rudists and to form monospecific biostromes close to the onset of OAE1a. Other environmental fluctuations (*e.g.,* seawater temperature and acidification) may have also contributed to its transient dominance within the benthic community.
This environmental "window", witness of a progressive deterioration of the carbonate platform preluding OAE1a, was also contemporaneous to the biotic crisis in the pelagic environment, as *Chondrodonta* flourished on the ACP within rudist limestones during the nannoconid decline and proliferates (*i.e.*, *Chondrodonta* bedsets) right below the nannoconid crisis interval (*see* Fig. 3.17).
The exacerbation of the environmental fluctuations and the extreme deterioration of the shallow-water carbonate system on the ACP at the onset of OAE1a reached the threshold for *Chondrodonta*, causing its disappearance and its final replacement by fully mesotrophic taxa like *Bacinella-Lithocodium* and orbitolinids. The opportunistic behavior of *Chondrodonta* can be, therefore, considered rather efficient in the transitional context between more stable, stenotopic and eurytopic benthic communities.

3.7. Conclusions

The Cretaceous oyster-like bivalve *Chondrodonta* is commonly found in lower Aptian shallow-water limestones that record considerable climate and environmental changes; despite this, a precise time and causal relationship between the proliferation of this bivalve and the environmental perturbations linked with OAE1a has not emerged yet.

The lower Aptian *Chondrodonta* accumulations within the inner platform facies of the ACP, have been correlated to the uppermost chemostratigraphic C2 segment of C-isotope curve straddling OAE1a. *Chondrodonta* appears on the ACP within rudist limestones and reaches a brief phase of maximum proliferation in monospecific biostromes (*Chondrodonta* bedsets) that terminate abruptly right below the negative $\delta^{13}C$ excursion (C3 segment) of OAE1a.

Increasing nutrient load preluding the onset of OAE1a created an environmental "window" favourable for *Chondrodonta* to proliferate outpacing the less tolerant benthos (*i.e.*, rudists). Low energy, restricted circulation and fluctuating seawater oxygenation controlled the occurrence and duration of this environmental "window" on the ACP. Further increase of inhospitable conditions leading to OAE1a (*i.e.,* terrigenous inputs coupled with decreased nutrients and dysoxic seawaters) inhibited the proliferation of *Chondrodonta*, allowing *Bacinella-Lithocodium* and orbitolinids to dominate within the benthic community.

4. *Chondrodonta* proliferation within the upper Cenomanian Adriatic Carbonate Platform

4.1. Abstract

The upper Cenomanian *Chondrodonta* accumulations within the inner platform limestones of the Adriatic Carbonate Platform (northern Istria, Croatia) underwent stratigraphic and geochemical analyses to assess the timing and causal relationship between the proliferation of this bivalve and OAE2.

Chondrodonta appears on the AdCP within radiolitid rudist limestones and reaches a phase of maximum proliferation and predominance in the benthic community (*i.e., Chondrodonta*-rich interval) in the upper part of the Savudrija section, correlated to the upper Cenomanian $\delta^{13}C$ curve below the onset of OAE2 and to increasing eutrophication in the nearby basin settings.

The changing climate leading to OAE2 created a scenario of environmental stress mainly characterized by increasing nutrient load as well as by intermittent terrigenous inputs and cool seawaters with fluctuating oxygenation and circulation. These environmental changes represented stressors for the rudist community of the AdCP, allowing the opportunistic and more resilient *Chondrodonta* to become the dominant benthos at the prelude phase of OAE2.

4.2. Geological setting

The Adriatic Carbonate Platform (AdCP) represents one of the major Mesozoic carbonate platforms of the peri-Mediterranean area. The whole stratigraphic succession, spanning a Triassic to Eocene age (Velić *et al.*, 2002; Tišljar *et al.*, 2002; Vlahović *et al.*, 2005) widely crops out in several countries bordering the eastern Adriatic Sea, from Italy to Albania (Fig. 4.1) and is estimated to be 8 km thick (Brčić *et al.*, 2017).

The AdCP developed as an isolated platform starting from the Middle Triassic, due to a rifting phase which dismantled and drowned the former carbonate deposits (*e.g.,* Tišljar *et al.*, 2002; Velić *et al.*, 2003; Vlahović *et al.*, 2005; Cazzini *et al.*, 2015). During the Early Jurassic, these rifting processes resulted in the development of the Apulian, Apennine, and Adriatic platforms (Velić *et al.*, 2003; Korbar, 2009). The AdCP then underwent a drifting phase up to the Late Cretaceous (Husinec & Sokač, 2006) when the first collision with Eurasia commenced and led to a compressional phase for the peri-Adriatic domains (*i.e.,* Dinarides, Hellenides and Southern Alps) (Stampfli & Mosar, 1999; Husinec & Sokač, 2006; Korbar, 2009).

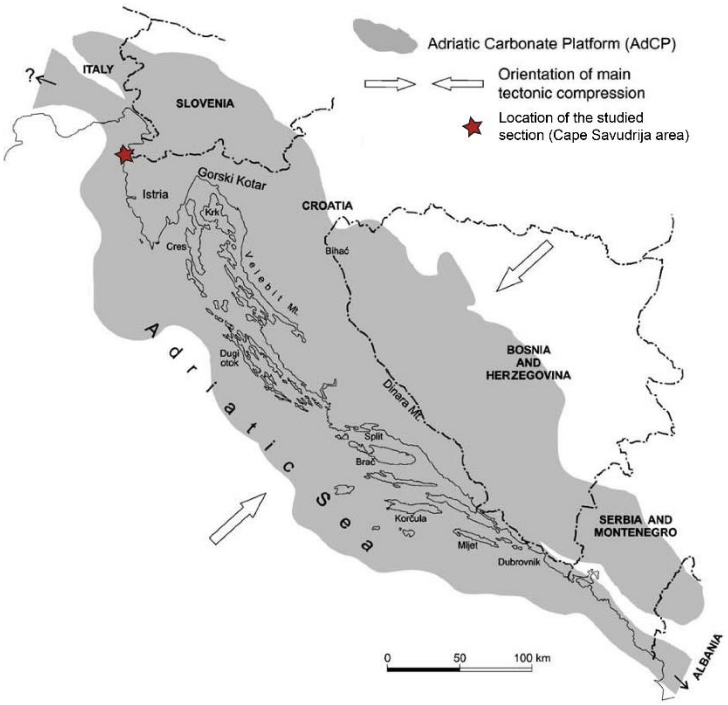

Fig. 4.1. The Adriatic Carbonate Platform (AdCP) deposits (Vlahović *et al.*, 2005). The studied section, in the Cape Savudrija area, is marked by the red star.

Combined synsedimentary tectonics and eustasy interrupted the shallow-water carbonate production on the AdCP several times during the Cretaceous, promoting episodic subaerial exposures and drowning events (Gušić & Jelaska, 1993; Moro, 1997; Moro *et al.*, 2002; Vlahović *et al.*, 2005; Korbar *et al.*, 2012). During the Paleogene, at the beginning of the Alpine collision, part of the AdCP became the foreland of the orogenic system. Regional flexures and uplifts resulted in an emersion and a wide karstification of the platform (Otoničar, 2007). During the Eocene, due to the southwestern migration of Dinaric fold-and-thrust belt, part of the previous foreland started to subside, gradually becoming a foredeep overlain by flysch deposits (Velić *et al.*, 2003; Wrigley *et al.*, 2015).

Compared with other sectors of the AdCP affected by Cenozoic (Paleogene) deformation processes, the Istrian Peninsula remained relatively stable. It represents one of the few areas of the AdCP where a stratigraphic continuity can be observed (Korbar, 2009; Huck *et al.*, 2010) and shows a structural setting resulted from the late Paleogene and Neogene thrust and fold propagations (Márton *et al.*, 2008, 2014; Korbar, 2009) (Fig. 4.1).

The Istrian carbonate succession is composed of shallow-water limestones of Middle Jurassic to Eocene age (Dragičević & Velić, 2002; Tišljar *et al.*, 2002). Velić *et al.* (1995) divided the succession into four transgressive–regressive mega-sequences, all interrupted by major subaerial exposures (Tišljar *et al.*, 1998; Velić *et al.*, 2003; Vlahović *et al.*, 2003). The first mega-sequence spans the upper Bathonian – lower Kimmeridgian, the second one spans the upper Tithonian – Aptian, the third one spans the Aptian – Santonian, the last one spans the Eocene and is mostly irregularly covered by Quaternary deposits (Velić *et al.*, 2003).

The whole Jurassic – Eocene stratigraphic succession crops out in the northwestern Istrian Peninsula (Fig. 4.2). Particularly, Eocene flysch deposits extensively occur in the northern part of the Peninsula

whereas its southern part is characterized by a broad and gentle anticline plunging toward NE (Fig. 4.2B) (*e.g.,* Pleničar *et al.*, 1969; Polšak & Šikić, 1969). The anticline displays Upper Jurassic shallow-water carbonates at its core and Lower Cretaceous to Cenomanian successions on both flanks (Fig. 4.2B). This regional trend is interrupted by an ENE-WSW-oriented thrust (north of Umag area; Fig. 4.2B, C) culminating in a parallel anticline structure (Cape Savudrija promontory).

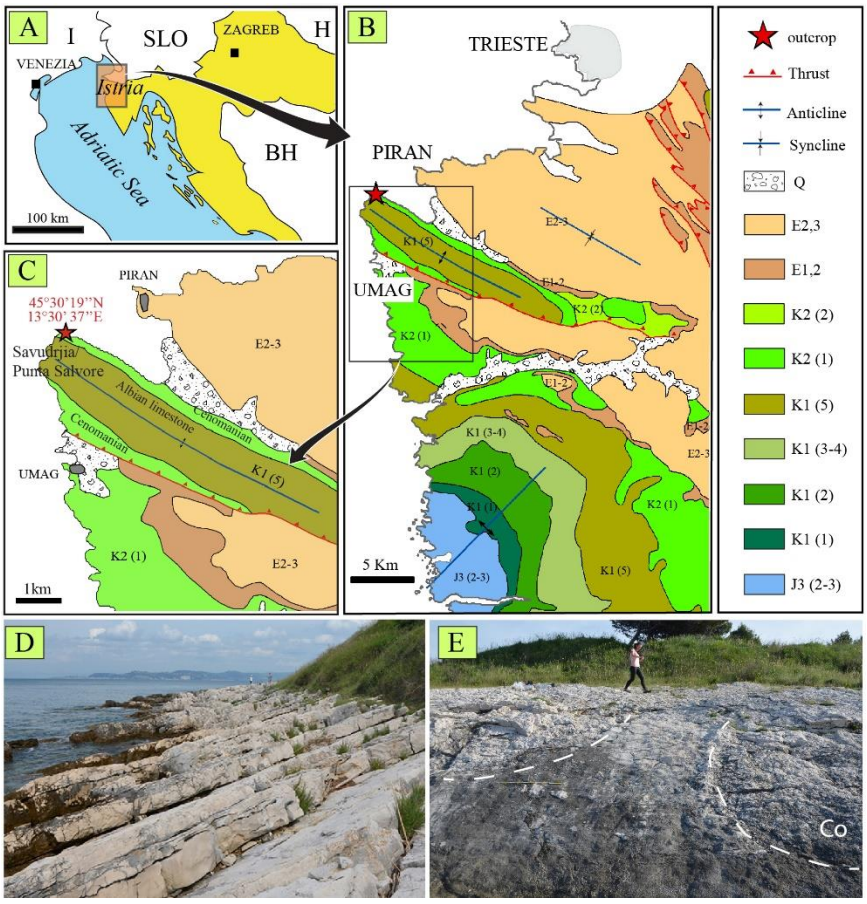

Fig. 4.2. Stratigraphic framework of the studied area, from Posenato *et al.* (2020). A) Geographic location of the Istrian Peninsula (NW Croatia). B) Schematic geological map of NW Istria; legend: J3 (2–3), Kimmeridgian - Tithonian; K1 (1), Valanginian; K1 (2), Hauterivian; K1 (3, 4), Barremian - Aptian; K1 (5), Albian; K2 (1), Cenomanian; K2 (2), Turonian; E1, 2, lower to middle Eocene; E2, 3, middle to upper Eocene; Q, Quaternary. C) Focus on the Cape Savudrija outcrop in the Umag area. D) The lower part of the Cape Savudrija succession and E) the upper part, with two *Chondrodonta* mounds (abbrev. Co) showing a topographic relief of few decimetres.

4.3. Stratigraphic framework

The Cenomanian carbonates of the Istrian Peninsula, extensively cropping out in Croatia, are ascribable to the Milna formation (Gušić & Jelaska, 1990, 1993) equivalent to the Povir formation cropping out in Slovenia (Jurkovšec *et al.*, 1996). The Milna formation represents inner platform shallow-water limestones mainly composed of bivalve biostromes (of mostly para-autochthonous radiolitid and chondrodontid shells) and microbial laminites (Steuber *et al.*, 2005). It is overlain by the uppermost Cenomanian – lower Turonian Sveti Duh formation, composed of fine-grained limestones with planktic foraminifers (Jenkyns, 1991; Gušić & Jelaska, 1993; Davey & Jenkyns,

1999). The latter indicate a pelagic incursion over the platform and mark the initial phase of the Cenomanian – Turonian drowning of the AdCP (Gušić & Jelaska, 1993). This drowning has been formerly interpreted as induced by the global Cenomanian - Turonian eustatic sea-level rise (Gušić & Jelaska, 1993) which also produced, in suitable settings, the Cretaceous OAE2 postulated by Jenkyns (1991).

The stratigraphy of the Savudrija area (Fig. 4.2D, E), focus of this Thesis, is quite simple and consists of inner platform limestones of the Cenomanian Milna formation, conformably overlying Albian limestones and dolomites (Velić & Vlahović, 1994). The coeval platform margin, instead, occurs in offshore seismic profiles, less than 15 km westward the Cape Savudrija tip (Grandić *et al.*, 2013; Velić *et al.*, 2015).

The sampled part of the succession comprises upper Cenomanian peritidal carbonates, mainly consisting of subtidal wackestone-packstones and bivalve floatstone-rudstones alternating with stromatolitic beds (Tišljar *et al.*, 1983; Steuber *et al.*, 2005; Mezga *et al.*, 2006; Moro *et al.*, 2007; Posenato *et al.*, 2020).

Particularly, the lower sampled tract is mostly composed of radiolitid rudists with subordinated monopleurids, either forming biostromes or occurring as scattered individuals in mudstone-wackestones (Polšak, 1967a; Pleničar *et al.*, 1969). A significant change in the bivalve associations is recorded upwards, where the succession becomes *Chondrodonta*-dominated. Such an evident taxonomical change has been formerly used as stratigraphic marker for the upper part of the Cenomanian carbonates of Istria (Polšak, 1967b; Pleničar *et al.*, 1969) as well as for the upper part of the Milna (Gušić & Jelaska, 1990) and the Povir (Jurkovšec *et al.*, 1996) formations.

4.4. Methods

A well-exposed outcrop (Fig. 4.2C), located along the rocky coast in the NW-SE elongated promontory of the Cape Savudrija area (or Punta Salvore in the past geological literature), allowed the identification of textures and sedimentary structures as well as an easy recognition of both the fossil content and the upward changes in the bivalve associations.

Thin sections of 75 samples were used to integrate field descriptions and to define lithofacies and biostratigraphic constraints.

For the $\delta^{13}C$ and $\delta^{18}O$ analyses on the bulk rock, 67 samples were collected together with the 30 best-preserved shells (20 *Chondrodonta* and 8 rudist shells) and analysed at the Museum für Naturkunde of Berlin.

Three shell fragments of *Chondrodonta* (n = 1) and rudists (n = 2), collected between 4.1 and 27.5 m in the stratigraphic section, were sampled for the Strontium Isotope Stratigraphy (SIS). Two samples were analysed at the Department of Chemical and Geological Sciences of the UNIMORE and one sample at the Institute of Geology, Mineralogy and Geophysics of the Ruhr University of Bochum (Germany).

A total of 29 samples has been collected for the measurement of the concentration of major, trace elements and REE by the LA-ICP-MS analysis, performed at the Max Plank Institute for Chemistry of Mainz (Germany).
For details on the sample preparation and on the analytical procedures used for all the geochemical analyses, *see* Chap. 2, par. 2.2.1 – 2.2.3; for the complete geochemical dataset, *see* Appendix I.

4.5. Results

4.5.1. Lithostratigraphy

The Savudrija section (Fig. 4.3A, B) is 42.5 m thick and consists of inner platform limestones with prevailing grain-supported beds (*see* also Moro *et al.*, 2007). Based on the major changes in textures, sedimentary structures and fossil associations, the Savudrija section has been divided into three stratigraphic intervals.

Stratigraphic interval 1 (0 – 13.5 m; Fig. 4.3A) is organized in peritidal cycles. These cycles are mainly composed of massive, decimetre-thick bioclastic (foraminifers, *Thaumatoporella parvoversiculifera*) and often bioturbated wackestones, alternating with decimetre- to metre-thick, thin-bedded peloidal-foraminiferal packstones and, in the upper part of the interval, with decimetre- to metre-thick rudist floatstone-rudstones in a mud-supported matrix. Centimetre-thick beds of mudstones, in some cases bioturbated, are also present. These lithofacies are capped by tabular decimetre-thick inter-supratidal stromatolites composed of planar to wavy laminae or, episodically, by dissolution cavities that usually represent the upper part of the cycles. Grain-supported beds, consisting either of thin-layered centimetre- to metre-thick peloidal-foraminiferal packstone-grainstones or of rudist floatstone-rudstones in a granular matrix, occur in the lower part of the interval. The few macro-fossils of stratigraphic interval 1 are almost totally represented by rudists (radiolitids and rare monopleurids).

Stratigraphic interval 2 (13.5 – 26.3 m; Fig. 4.3A, B) is dominated by metre-thick tabular to lense-shaped rudist floatstones and floatstone-rudstones. Rudist shells occur in an occasionally bioturbated

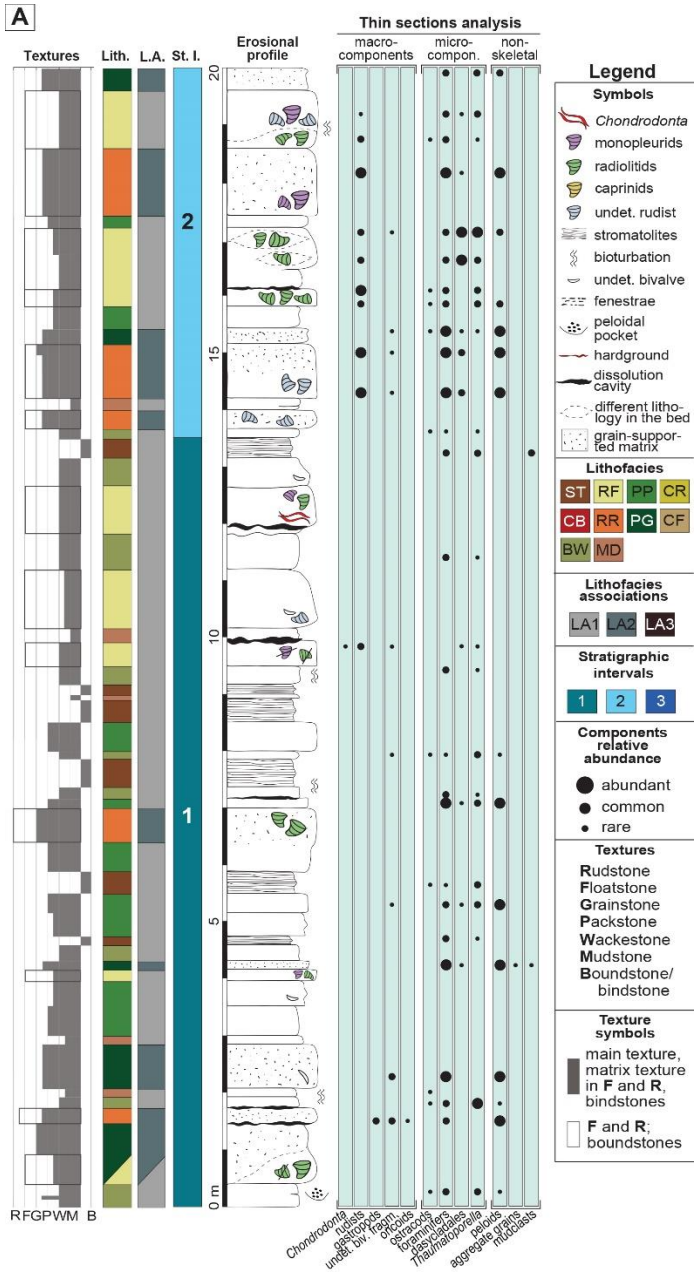

Fig. 4.3A. Savudrija stratigraphic log (lower part) (45°30'19.18''N, 13°30'30''E). Rock-components are analysed semi-quantitatively and their abundance is expressed relative to the rock texture; *see* Tab. 4.1 and Fig. 4.4 for the description of lithofacies. Abbreviations: L. A., lithofacies associations; S. I., stratigraphic intervals.

lime mud-matrix or in a grain-supported matrix with sign of fragmentation, bioerosion and micritization.

These rudist beds are mostly interbedded with centimetre- to decimetre-thick peloidal packstones and packstone-grainstones containing common to abundant foraminifers (*e.g., Chrysalidina gradata*), dasycladales, *T. parvoversiculifera* and rare ostracod shell fragments. Stromatolites, bioturbated bioclastic wackestones and centimetre-thick mudstone-beds occur rarely and are mostly concentrated in the uppermost part of the stratigraphic interval.

The macro-fauna is more abundant with respect to stratigraphic interval 1 and is mainly represented by rudists (radiolitids and subordinated monopleurids and caprinids); *Chondrodonta* appears as a subordinated component in the upper part, associated with rudist beds. The top of the stratigraphic interval is marked by a major exposure surface.

Stratigraphic interval 3 (26.3 – 42.5 m; Fig. 4.3.B) is mainly composed of *Chondrodonta* accumulations with abundant *Chondrodonta* shells, arranged in boundstones and in decimetre- to metre-thick floatstones and floatstone-rudstones, in some cases lense-shaped. These beds mostly alternate with bioturbated foraminifers - *T. parvoversiculifera* wackestones, peloidal-foraminiferal packstone-grainstones and centimetre- to decimetre-thick inter-supratidal stromatolites with fenestral and clotted microfabrics.

Rudist floatstone-rudstones arranged in decimetre- to metre-thick tabular or lense-shaped beds are scattered in the middle - upper part of the interval.

The entire stratigraphic interval 3 is *Chondrodonta*-dominated; radiolitid rudists mostly occur as subordinated components in *Chondrodonta* beds and episodically become major components only at the top of the interval. Beside bivalves, also foraminifers (*e.g.,* miliolids, *C. gradata*), dasycladales and *T. parvoversiculifera* are common micro-components; aggregate grains and micritic intraclasts can also occur within the grain-supported beds.

Based on outcrop and thin sections analyses, ten lithofacies were identified (Fig. 4.4, Tab. 4.1). Textures range from mud to grain-supported to even bindstones and the benthic fauna is mainly represented by bivalves (radiolitids and *Chondrodonta*), foraminifers, dasycladales and micro-encrusters like *T. parvoversiculifera*.

The ten lithofacies have been grouped into three lithofacies associations (LA) and interpreted in terms of depositional environment (Tab. 4.1). The recognized textures, biotic assemblages and interpretations are comparable with those described for the Cenomanian carbonates of Istria (Polšak, 1967a, b; Pleničar *et al.,* 1969; Brčić *et al.*, 2021), as well as with upper Cenomanian inner

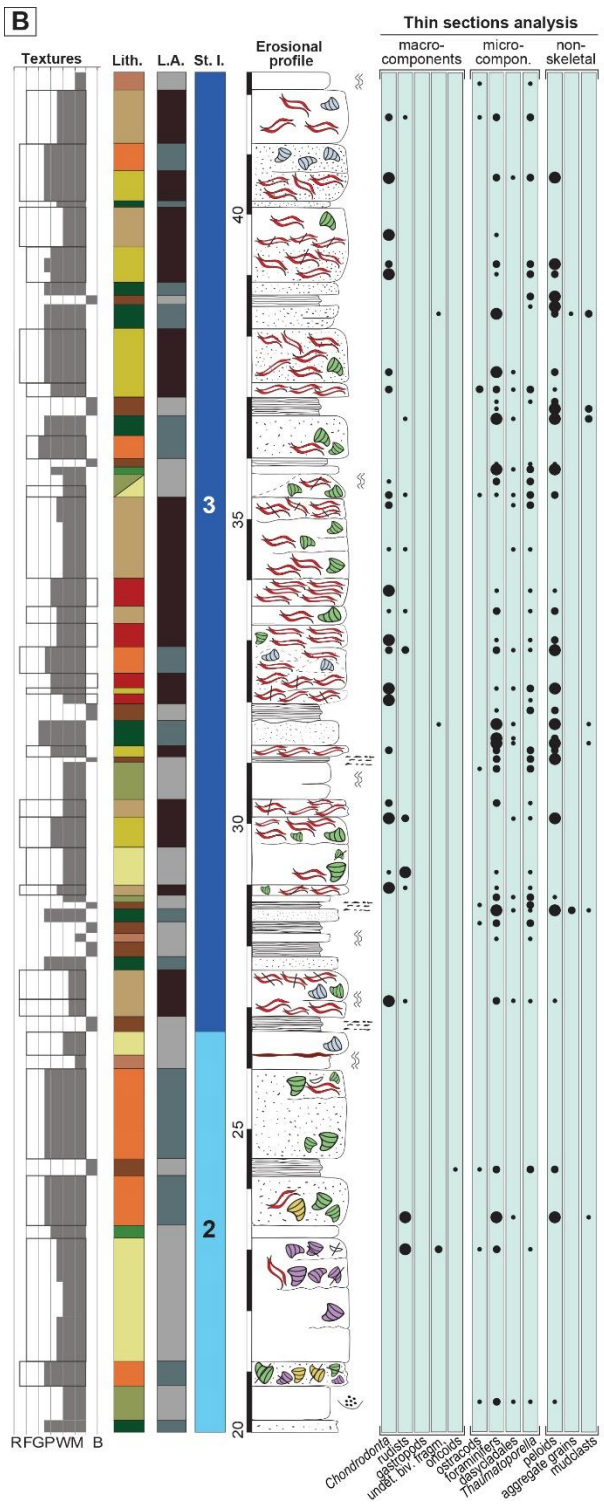

Fig. 4.3B. Savudrija stratigraphic log (upper part) (45°30'19.18''N, 13°30'30''E). Rock-components are analysed semi-quantitatively and their abundance is expressed relative to the rock texture; *see* Tab. 4.1 and Fig. 4.4 for the description of lithofacies and Fig. 4.3A for the legend. Abbreviations: L. A., lithofacies associations; S. I., stratigraphic intervals.

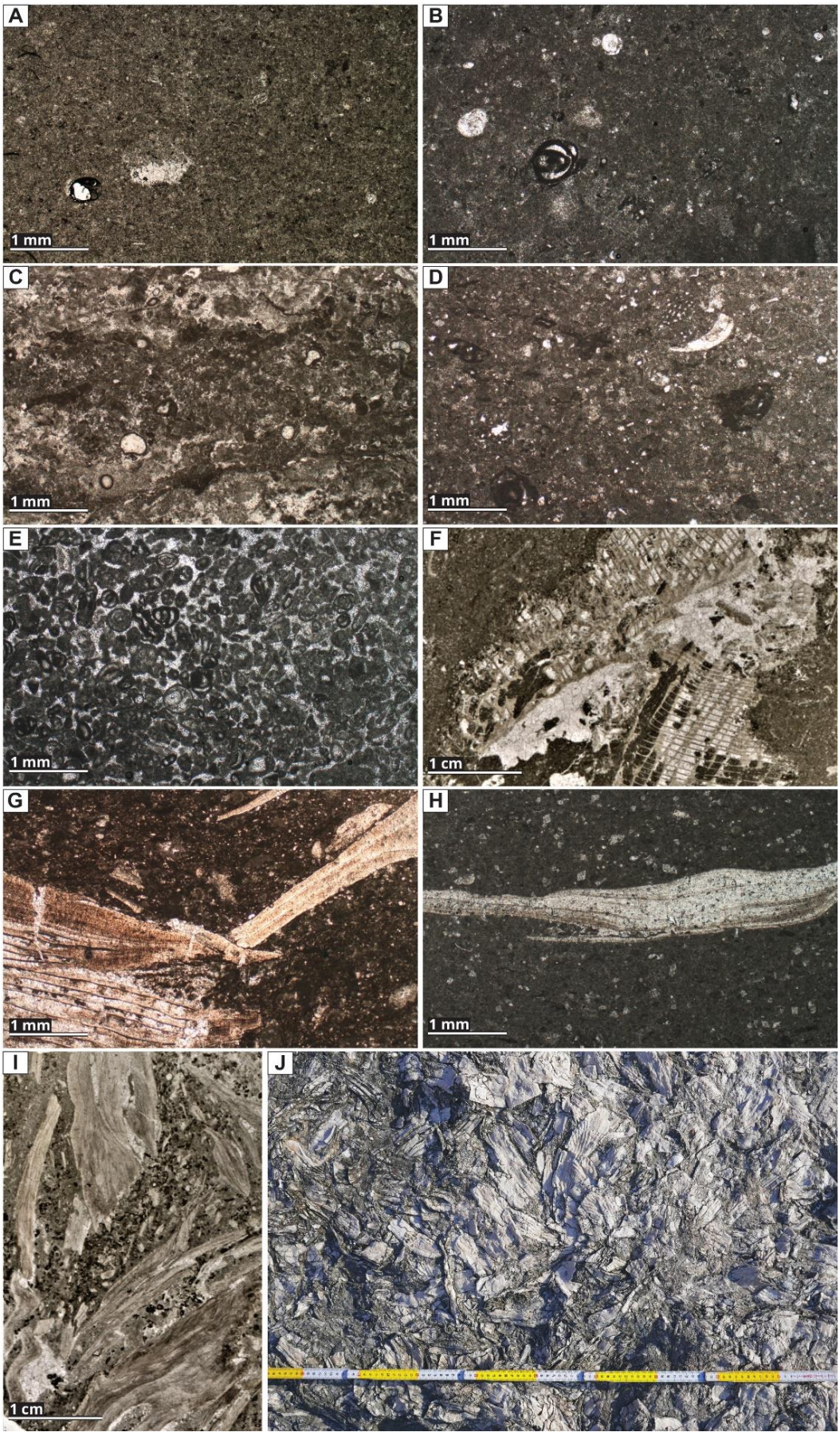

Fig. 4.4. Photographs of the ten lithofacies distinguished within the Savudrija section. A) bioturbated mudstones, MD. B) bioclastic wackestones, BW. C) stromatolites, ST. D) peloidal-bioclastic packstones, PP. E) peloidal-foraminiferal packstone-grainstones, PG. F) rudist floatstones, RF. G) rudist rudstones, RR. H) *Chondrodonta* floatstones, CF. I) C*hondrodonta* rudstones, CR. J) *Chondrodonta* boundstones, CB. *See* Tab. 4.1 for a detailed description.

Lithofacies	**Textures, bed features and thickness**	**Components**	**Sedimentary and diagenetic features**	**Lithofacies association and depositional settings**
MD – Bioturbated mudstones	Mudstone, mudstone-wackestone; tabular centimetre- to decimetre-thick beds	Ostracods (r), foraminifers (r), *T. parvoversiculifera* (r)	Bioturbation	**LA1** Low-energy protected lagoon passing to tidal flat
BW – Bioclastic wackestones	Wackestone; massive and tabular decimetre-thick beds	Undetermined bivalve fragments (r), small-sized oncoids (c-r), ostracods (c-r), foraminifers (a-c), dasycladales fragments (r), *T. parvoversiculifera* (a-c), peloids (c-r)	Bioturbation, peloidal pockets	
ST – Stromatolites	Bindstone; laminated, tabular decimetre-thick beds	Small-sized oncoids (r), ostracods (r), foraminifers (c-r), *T. parvoversiculifera* (c-r), peloids (a-c)	Planar to wavy lamination; fenestral and clotted microfabrics	
PP – Peloidal packstones	Packstone, rarely wackestone-packstone; tabular and thin-layered decimetre- to metre- thick beds	Undetermined bivalve fragments (r), foraminifers (a-c), dasycladales fragments (r), *T. parvoversiculifera* (a-c), peloids (a)	-	
RF – Rudist floatstones in mud-matrix	Floatstone, floatstone-rudstone; mudstone-wackestone to packstone matrix; tabular to occasionally lense-shaped decimetre- to metre-thick beds	Rudists (a-c), *Chondrodonta* (r), undetermined bivalve fragments (r), ostracods (r), foraminifers (c), dasycladales fragments (c-r), *T. parvoversiculifera* (c-r), peloids (c)	Bioturbation, bivalve lenses, dissolution cavities at the top of the beds	
PG – Peloidal-foraminiferal packstone-grainstones	Packstone-grainstone, grainstone; thin-layered centimetre- to decimetre-thick beds	Rudists (r), undetermined bivalve fragments (c), foraminifers (a-c), dasycladales fragments (c), *T. parvoversiculifera* (r), peloids (a), aggregate grains (r), micritic intraclasts (c)	Micritization, bioerosion	**LA2** High-energy open lagoon
RR – Rudist rudstones in granular matrix	Floatstone-rudstone with packstone-grainstone matrix; massive and occasionally lense-shaped decimetre- to metre-thick beds	Rudists (a), *Chondrodonta* (c-r), gastropods (r), undetermined bivalve fragments (c-r), oncoids (r), foraminifers (a-c), dasycladales fragments (c-r), *T. parvoversiculifera* (c-r), peloids (a)	Bioerosion, bivalve lenses, shell fragments, micritization	
CF – *Chondrodonta* floatstones in mud matrix	Floatstone, floatstone-rudstone with mudstone-wackestone to packstone matrix; tabular to slightly lense-shaped decimetre- to metre-thick beds	*Chondrodonta* (a-c), rudists (r), ostracods (r), foraminifers (c-r), dasycladales fragments (r), *T. parvoversiculifera* (c-r), peloids (c-r)	Bivalve lenses, fragmentation of shells	**LA3** Moderate-energy lagoon under stressed conditions
CR – *Chondrodonta* rudstones in granular matrix	Floatstone-rudstone with packstone-grainstone matrix; tabular to slightly lense-shaped	*Chondrodonta* (a-c), rudists (c-r), ostracods (c-r), foraminifers (a-r), dasycladales fragments (r), *T. parvoversiculifera* (c), peloids (a-r)	Bivalve lenses, fragmentation of shells	

	decimetre- to metre-thick beds			
CB – *Chondrodonta* boundstones	Boundstone with wackestone to-grainstone matrix; tabular and nodular decimetre- to metre-thick beds	*Chondrodonta* (a), rudists (c-r), foraminifers (r), dasycladales fragments (r), *T. parvoversiculifera* (c-r), peloids (a)	Horizontally oriented and toppled shells within layers, bivalve lenses	

Tab. 4.1. Summary of the main sedimentological characters of the lithofacies associations and of the 10 lithofacies recognized in the Savudrija section. Components considered are, in order, skeletals, micro-encrusters and non-skeletal grains. Their relative abundance is expressed as: *a*, abundant, *c*, common, *r*, rare.

platform carbonates of Central and Southern Apennines (*e.g.,* Di Stefano & Ruberti, 2000; Parente *et al.*, 2007, 2008; Pandey *et al.*, 2011; Korbar *et al.*, 2012; Frijia *et al.*, 2015, 2019).

Lithofacies association 1 (**LA1**) consists of mud-supported facies like bioturbated mudstones (MD, Fig. 4.4A) and bioclastic wackestones (BW, Fig. 4.4B), episodically interbedded with stromatolites (ST, Fig. 4.4C), peloidal packstones (PP, Fig. 4.4D) and rudist floatstone-rudstones in a mud-supported matrix (RF, Fig. 4.4F). The benthic fauna is mainly composed of rudists (mostly radiolitids), subordinated *Chondrodonta*, foraminifers and micro-encrusters like *T. parvoversiculifera*. This mud-dominated lithofacies association is interpreted to be representative of a low-energy, protected subtidal environment with periodical shifts to tidal-flat settings. The poorly differentiated biotic assemblages indicate a mostly restricted marine circulation. Subtidal facies capped either by stromatolites with occasional fenestrae or by dissolution cavities, can be inferred as peritidal and subtidal cycles, respectively.

Lithofacies association 2 (**LA2**) consists of grain-supported facies like peloidal-foraminiferal packstone-grainstones (PG, Fig. 4.4E) and rudist floatstone-rudstones in a granular matrix (RR, Fig. 4.4G), with a higher skeletal content and diversity. The benthic fauna is mainly composed of rudists (mostly radiolitids, subordinated monopleurids, scattered caprinids), scattered *Chondrodonta*, abundant foraminifers (*e.g., C. gradata*), undetermined bivalves and dasycladales, rare gastropods. Based on textures, skeletal components and on the rare inter-supratidal sedimentary structures, LA2 can be interpreted as deposited in a typical subtidal environment, with a more open circulation.

Lithofacies association 3 (**LA3**) is based on the occurrence of *Chondrodonta*-rich beds, either in the form of lense-shaped boundstones (CB, Fig. 4.4J), or as shell fragments in floatstone-rudstones within a wackestone (CF, Fig. 4.4H) or a packstone-grainstone matrix (CR, Fig. 4.4I). *Chondrodonta* is particularly abundant in the upper part of the stratigraphic succession, where it predominates. Rudists

are only subordinated and foraminifers, *T. parvoversiculifera*, dasycladales and other bioclasts are rare. Coupling the lithofacies textures with the high concentration of *Chondrodonta* with respect to any other benthos, this lithofacies association can be interpreted as deposited in moderate-energy subtidal settings, presumably under stressed environmental conditions, not favourable for the thriving of a diversified benthic fauna.

4.5.2. Biostratigraphy and geochemistry

In the Savudrija stratigraphic section, the biostratigraphic association composed of *Chrysalidina gradata* D'Orbigny, *Pastrikella balcanica* (Cherchi, Radoičić and Schroeder), *Vidalina radoicicae* Cherchi and Schroeder, *Pseudorhapydionina dubia* (De Castro), and *Pseudolituonella reicheli* Marie, has been recognized from the base to the top (Fig. 4.5).

The $\delta^{13}C$ curve in the Savudrija section does not show abrupt shifts. Only a more evident negative trend occurs in the upper part, visible in both single values and in the 3-points moving average (*i.e.,* smoothed) curves. Overall single values range between –2.8‰ and +3.5‰, with a mean of +1.6‰.
In stratigraphic interval 1 (0 – 13.5 m) the $\delta^{13}C$ curve is almost flat; a weakly positive trend is more visible in the smoothed curve, with single values oscillating around +1.9‰. A slightly positive-negative shift occurs in stratigraphic interval 2 (13.5 – 26.3 m), visible in both the single values and the smoothed curve. Here, single values reach a maximum of +3.5‰ (at 15.8 m), followed by a gradual decrease up to +1.4‰. Interval 3 (26.3 – 42.5 m) shows the most negative single values, reaching –0.3‰ at 32 m from the base, right below the interval of maximum proliferation of *Chondrodonta* (*i.e.*, lithofacies CB, *Chondrodonta* boundstone). This negative, although not abrupt, trend is also depicted in the smoothed curve.
The $\delta^{18}O$ curve shows a flatter pattern in both single values and the smoothed curve. Single values slightly decrease up-section, from -2.0‰ at the base to -2.3‰ at the top. The most positive value, of –0.1‰, is reached in stratigraphic interval 1 (0 – 12 m), at 7.5 m from the base. The most negative value, of –3.0‰, is reached in the uppermost part of interval 3 (26.3 – 42.5 m), at 39.6 m from the base of the section.

The concentration of Al in the Savudrija section ranges between 100 and 480 ppm in the lower part (0 – 26.3 m) and is characterized by an almost flat profile with slightly decreasing values (Fig. 4.5). At the base of the *Chondrodonta*-rich interval (26.3 m) the concentration of Al increases, with sharp positive peaks up to ~ 1500 ppm (at ~ 32 m). Above 34.8 m, the concentration abruptly decreases.

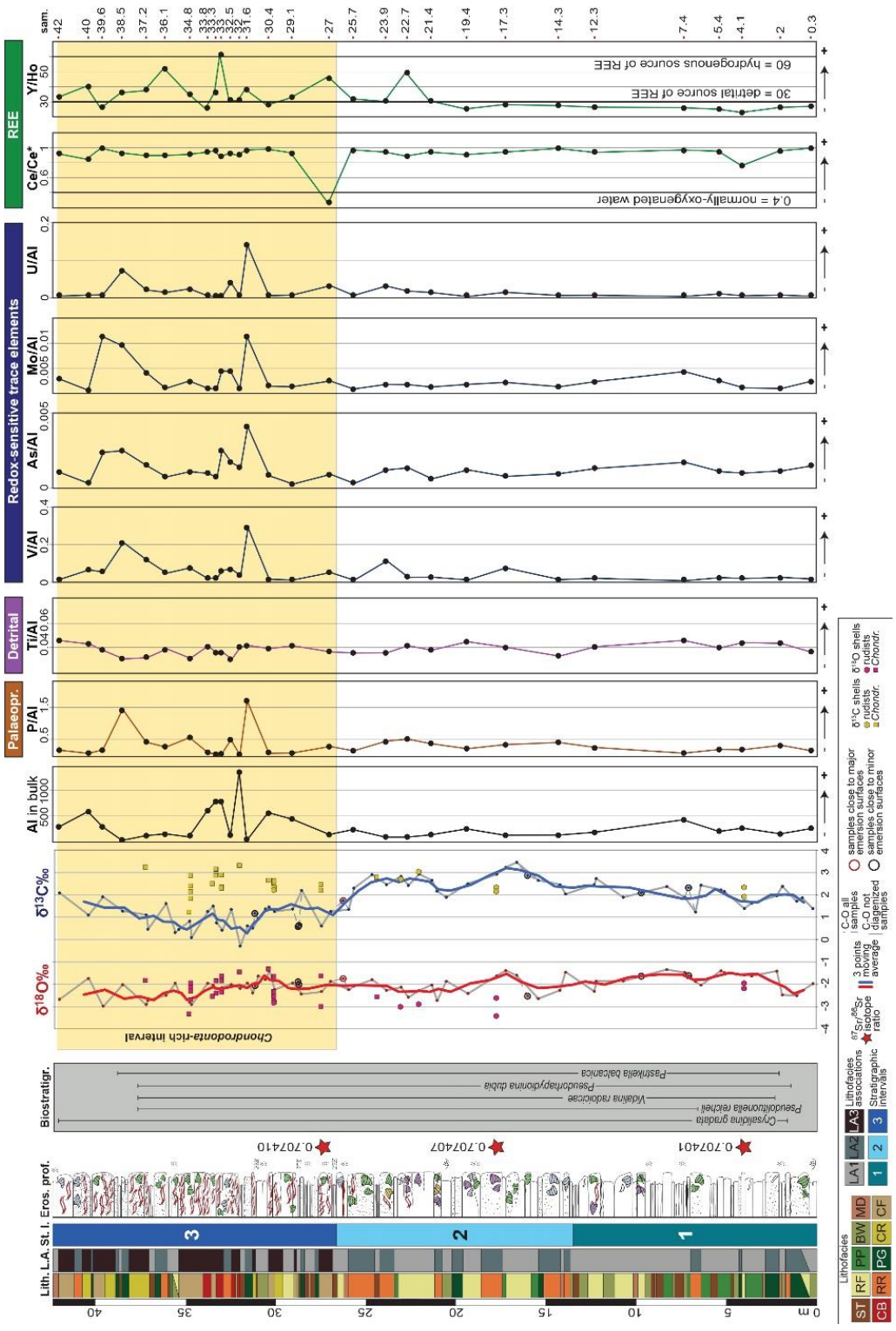

Fig. 4.5. Savudrija stratigraphic section (simplified log) including biostratigraphy, stable isotope results ($\delta^{18}O$, $\delta^{13}C$, $^{87}Sr/^{86}Sr$), palaeoproductivity (P/Al), redox-state (RSTE/Al) and detrital input (Ti/Al and Al) proxies, Ce anomaly (expressed as Ce/Ce* ratio) and Y/Ho ratio. P, Ti, and RSTE concentrations are reported as ratios on the concentration of Al in the bulk rock and plotted against the lithostratigraphic column and the $\delta^{13}C$ and $\delta^{18}O$ curves. *See* text, Tab. 4.1, and Fig. 4.4 for the description of lithofacies, lithofacies associations and stratigraphic intervals and Fig. 4.3A for the complete legend. The concentration of Al is reported in ppm.

The measured P/Al ratio is generally lower than 0.5 for most part of the stratigraphic section. It starts increasing within the *Chondrodonta*-rich interval (from 30.4 m from the base) where sharp positive peaks, of 1.6 (at 31.6 m) and of 1.5 (at 38.5 m), occur. The concentration of Ti/Al ranges around 0.04 for the entire section and shows an almost flat curve. In the *Chondrodonta*-rich interval, no abrupt changes in the concentration of Ti/Al occur.

The Redox Sensitive Trace Elements (RSTE)/Al ratio are generally very low, close to zero for most part of the section (Fig. 4.5). Their curves are almost flat up to ~ 30 m from the base of the section, with only weak concentration peaks. In the *Chondrodonta*-rich interval (from 30.4 m), all RSTE/Al ratios increase and show a fluctuating trend. Sharp positive peaks occur at 31.5 - 32 m and, above them, another major increase in concentration (more visible for the As/Al and Mo/Al ratios) occurs at ~ 38 m.

A slightly negative Ce anomaly is recorded for the entire section, with values of the Ce/Ce* ratio oscillating between 0.9 and 1. A sharp negative peak occurs only at 27 m, where the Ce/Ce* ratio reaches a value of 0.25. The Y/Ho ratio mostly ranges around 30 and shows positive peaks, up to 60, only starting from 22.7 m from the base of the section.

4.5.3. Changes in the biotic associations: the Chondrodonta-rich interval

The macro-fauna of the Savudrija section is mostly composed of rudists and *Chondrodonta*, with subordinated gastropods, pectinoids and undetermined ostreids. Upward changes in the bivalve associations can be traced throughout the fossiliferous beds.

Stratigraphic interval 1 records very few rudist- sparse floatstones with a generally low density of individuals (Fig. 4.6A). Only in the uppermost part of the interval (9.5 – 10 m) rudists and other bivalve fragments are more abundant (Fig. 4.6B). Rudists form either autochthonous accumulations of 5 cm-long shells, or parautochthonous accumulations composed of moderately broken valves.

Within the rudist community, radiolitids prevail and are in some cases arranged in small bouquets; monopleurids are common to rare (*see* Fig. 4.6A, B).

In stratigraphic interval 2, the thickness and the frequency of fossiliferous beds increase. Rudists are more abundant, form autochthonous and parautochthonous accumulations and occasionally occur in 10 cm-thick and 1 m-wide lenticular beds. The orientation of shells is occasionally horizontal and oblique, and the rate of fragmentation is low to moderate. Rudists still predominate in the bivalve community; radiolitids prevail with shells up to 25 cm long (Fig. 4.6C). Subordinated monopleurids and rare caprinids also occur in the uppermost part of the interval. *Chondrodonta* appears in the stratigraphic section as common to rare component in rudist limestones (Fig. 4.6D). Its shells are 7 – 8 cm long on average and mostly still-articulated. Rare undetermined pectinoids and ostreids are also present.

In stratigraphic interval 3, the bivalve community becomes *Chondrodonta*-dominated, whose *Chondrodonta* specimens are ascribable to *C. joannae* (Choffat) (*see* Posenato *et al.*, 2020).

Radiolitids, with less common monopleurids and caprinids, occur either in scattered accumulations alternated to *Chondrodonta* beds or as subordinated components within the latter (Fig. 4.6E, F). *Chondrodonta* reaches a phase of maximum concentration between 32 and 40 m from the base of the section, here defined as *Chondrodonta*-rich interval.

The *Chondrodonta*-rich interval is composed of several beds with densely packed, toppled shells, interbedded with inter-supratidal stromatolites and subtidal lithofacies (Fig. 4.7A).

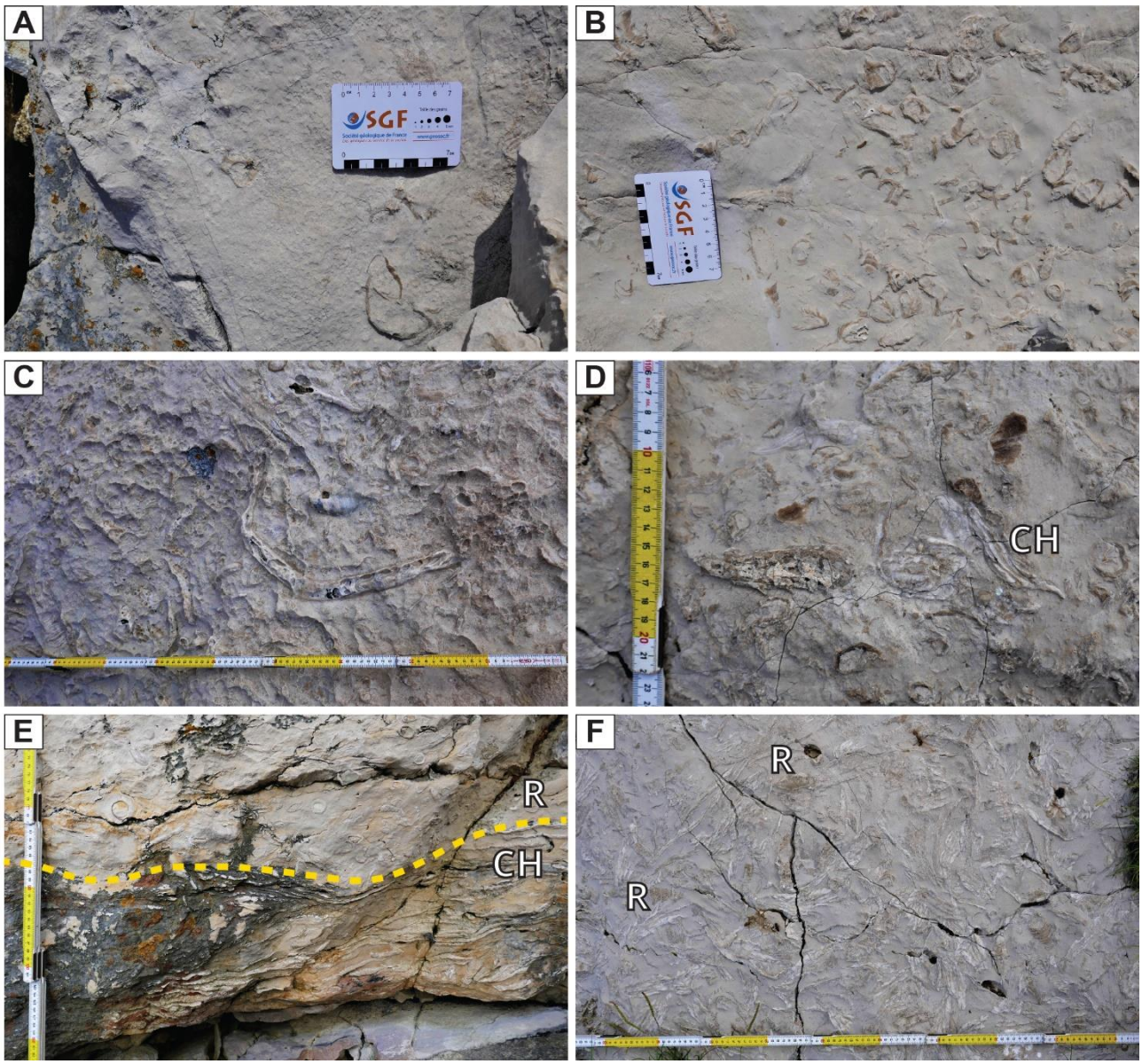

Fig. 4.6. Field photographs of the bivalve associations within the Savudrija section. A) Sparse monopleurid floatstone. B) Dense radiolitid floatstone-rudstone. C) Radiolitid floatstone-rudstone with shells up to 25 cm long. D) Rudist floatstone-rudstone with scattered *Chondrodonta* shells (abbrev. CH). E) *Chondrodonta* (below the yellow line) and rudist (above; abbrev. R) floatstone-rudstone with toppled, horizontally orientated *Chondrodonta* shells. F) *Chondrodonta* floatstone-rudstone with scattered radiolitids. Photograph orientation: F) represents a layer section, A-E) represent layer surfaces.

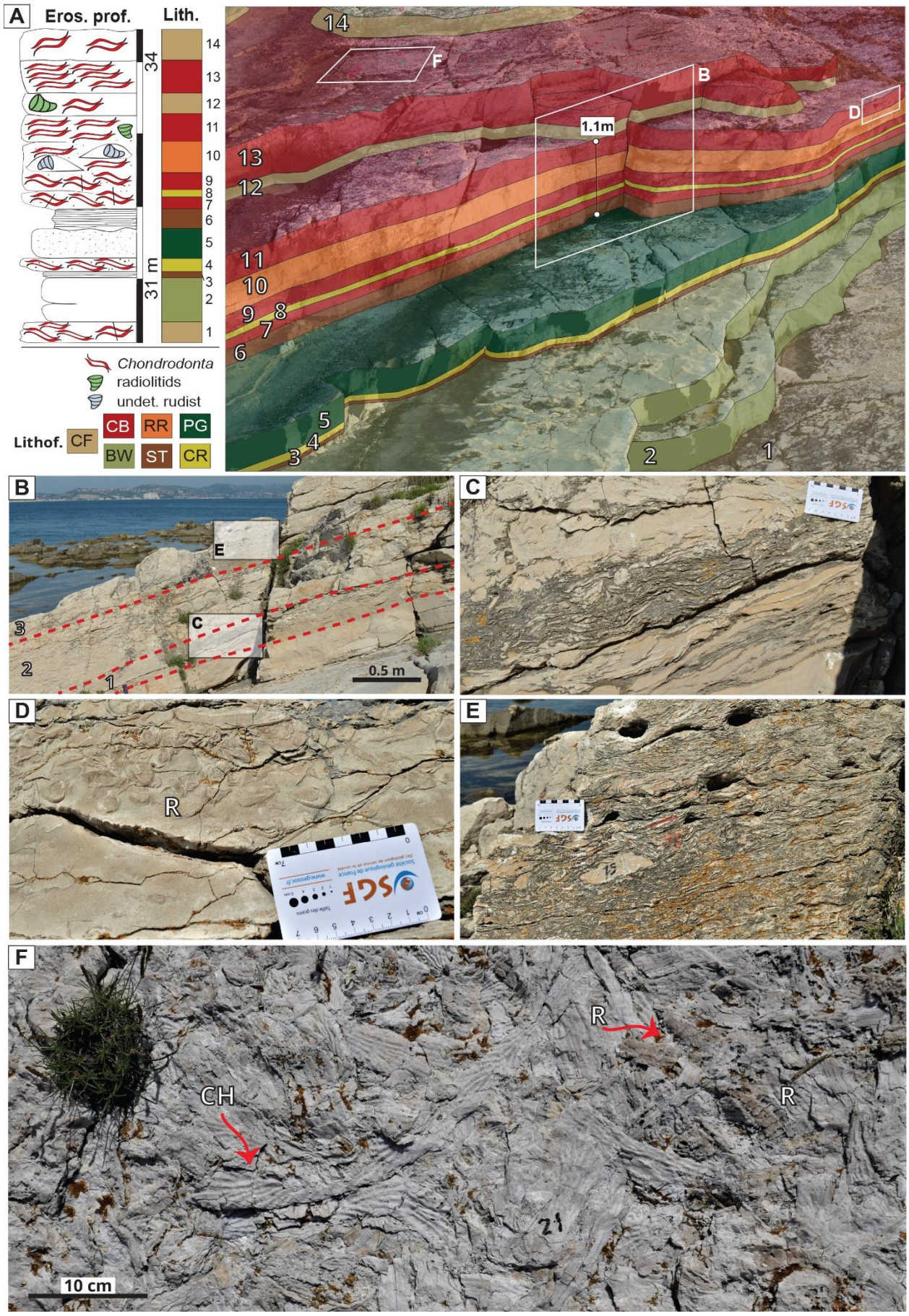
A
Eros. prof.
Lith.
34
31 m
14
13
12
11
10
9
8
7
6
5
4
3
2
1
Chondrodonta
radiolitids
undet. rudist
Lithof.
CF
CB
RR
PG
BW
ST
CR
F
B
D
1.1m
E
C
0.5 m
R
CH
10 cm

Fig. 4.7. Field photographs of the *Chondrodonta*-rich interval in the upper part of the Savudrija section. A) detail of a stratigraphic segment of the upper part of the Savudrija section with repetitive *Chondrodonta* accumulations; a schematic corresponding erosional profile is reported on the left. *See* Fig. 4.3A, B for the complete profile and legend, and Tab. 4.1 for the description of lithofacies and lithofacies associations. B) detail of the thickest *Chondrodonta* accumulation, where three internal beds (*i.e.,* 1, 2, 3) can be recognized. The first internal bed, ~ 30 cm thick, is composed of very abundant, densely packed, and horizontally oriented *Chondrodonta* shells (C). The second internal bed, ~ 50 cm thick, shows prevailing *Chondrodonta* shells less densely packed, moderately fragmented and with a more chaotical distribution of toppled shells. These alternate with small radiolitid lenses approximately 1 m in length, composed of mostly bioeroded and, rarely, in life-position shells (D). The third bed, 40 – 50 cm thick, is similar to the first bed and is composed of densely packed, toppled *Chondrodonta* shells with a higher rate of fragmentation (E). F) a bed-plane surface with *Chondrodonta* shells up to 50 cm long. Abbreviations: CH, *Chondrodonta*; R, radiolitids.

Chondrodonta occurs in both dense floatstone-rudstones (*i.e.,* parautochthonous accumulations) and boundstones (*i.e.,* autochthonous accumulations). The shell completeness is variable without evidence of transport and current orientations. Shells, up to 50 cm long, are mostly horizontally oriented; only small sized *Chondrodonta* shells occur in upright position whereas larger individuals are always toppled. In these beds, *C. joannae* occurs together with pectinoids (*e.g., Neithea*) and with scattered rudist bouquets. The bed-plane surfaces of the *Chondrodonta* beds, often largely exposed, show a very high shell coverage rate (*see* Fig. 4.7F).

The bed with the highest shell concentration is ~ 130 cm thick and occurs between 32 and 33.3 m in the stratigraphic section, above a 30 – 40 cm-thick stromatolitic bed (Fig. 4.7A). The *Chondrodonta* accumulation is mono- to pauci-specific and can be further divided into three beds (Fig. 4.7B, C, E). *Chondrodonta*-rich beds alternate with small radiolitid lenses, about ~ 1 m in diameter, containing mostly bioeroded individuals, rarely in life-position (Fig. 4.7D). Another well-exposed *Chondrodonta* bed-plane surface occurs above, between 33.6 – 34 m from the section base and shows the most spectacular *C. joannae* deposit (Fig. 4.7A, F). This surface, with an exposure of more than 5 m^2, is composed of complete and very large shells of *C. joannae*, up to 50 cm long, prevailing over small sized and fragmented individuals. Shells are generally curved, and no individuals were found in life-position. Rose diagrams of the growth directions of shells, created by Posenato *et al.* (2020) for the whole uppermost surface (Fig. 4.8.1-3) and for separated quadrants (Fig. 4.8.4), show a general random distribution.

The abundance and predominance of *Chondrodonta* over rudists slightly decrease only in the topmost part of the stratigraphic section (40 – 42.3 m) where rudist-dominated assemblages with subordinated *Chondrodonta* shell fragments occur (*see* Fig. 4.3B).

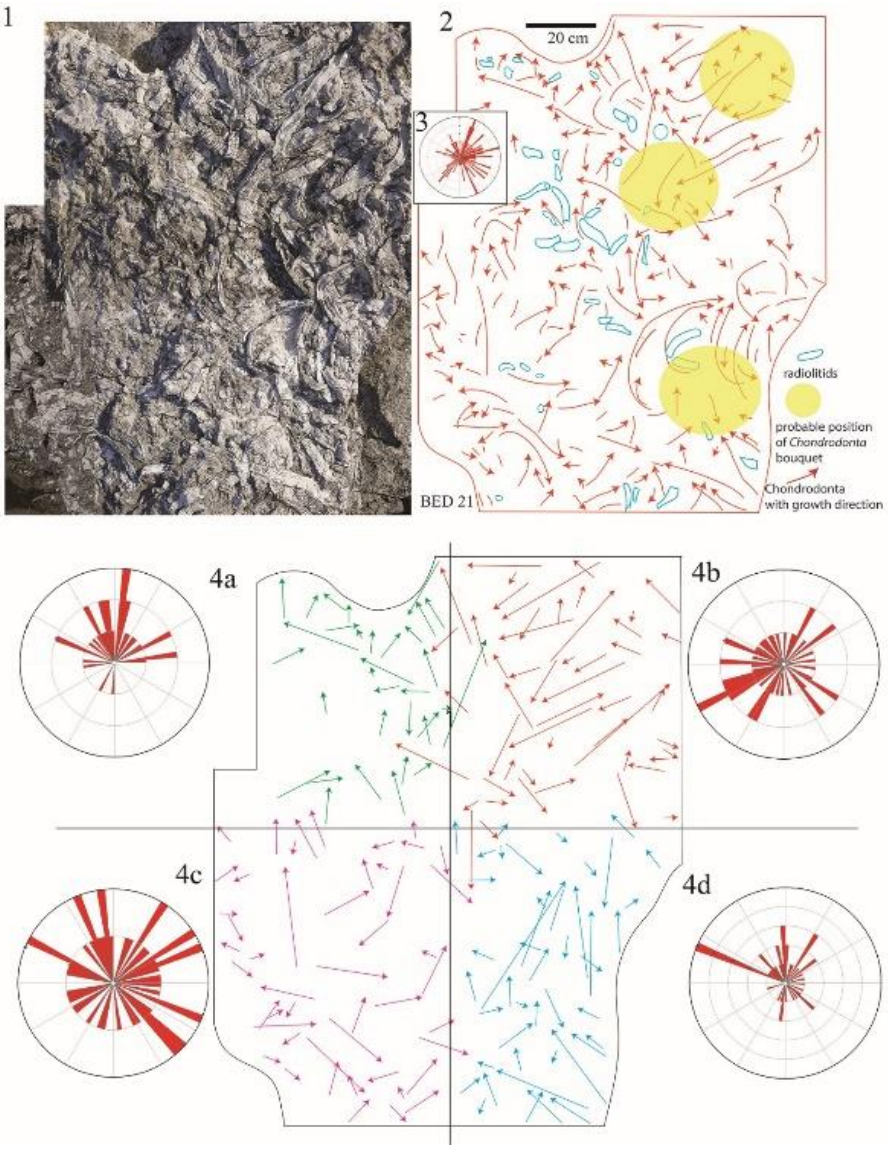

Fig. 4.8.
The bed-plane surface of the *Chondrodonta* interval shown in Fig. 4.7F, taken from Posenato *et al.* (2020) (and labelled as "fossiliferous bed R21"). Panel 1, bedding surface. Panel 2, arrows indicate position, size, and growth direction of *Chondrodonta* shells. Panel 3, the rose diagram indicates the shell growth direction occurring on the whole surface, calculated on straight segment indicated in Panel 4a – d, with no reference to the arrow lengths. Panel 4a – d, rose diagrams plotted for each sector in which the *Chondrodonta*-rich surface has been divided; the straight segments were obtained by joining the apex and the end of each arrow drawn in Panel 2.

4.6. Interpretation and discussion

4.6.1. Reliability of the geochemical results

In the Savudrija section, scatterplots of $\delta^{13}C$ and $\delta^{18}O$ show no significant correlation for individual lithofacies nor for lithofacies associations (Fig. 4.9A, B), suggesting that variations in $\delta^{13}C$ are not the result of facies changes. In the analysed samples, most of the isotope bulk values is coherent with the rudist and *Chondrodonta* shells isotope values, thus suggesting a lack/minimal impact of diagenetic processes on the bulk (Fig. 4.9A; *see* also $\delta^{13}C$ and $\delta^{18}O$ curves in Fig. 4.5).

The analysed samples almost totally plot within the Cenomanian – lower Turonian seawater ("low-latitude") biotic calcite field of Prokoph *et al.* (2008) (Fig. 4.9B) and partly overlap the upper

Cenomanian isotopic field of the Apennine Platform shallow-water carbonates (Frijia & Parente, 2008; Schmitt *et al.*, 2020). The inverted "J" stable isotope pattern, typical of carbonates affected by meteoric diagenesis (Allan & Matthews, 1982; Lohmann, 1988) lacks in the analysed samples, indicating that the isotope patterns are free from meteoric alteration. A weak tail of more depleted $\delta^{13}C$ and $\delta^{18}O$ values is observed only in LA3. Based on facies analysis, LA3 (*see* Fig. 4.3B) indicates deposition in a more restricted environment, more subject to water mass ageing or to short-lasting subaerial exposure episodes.

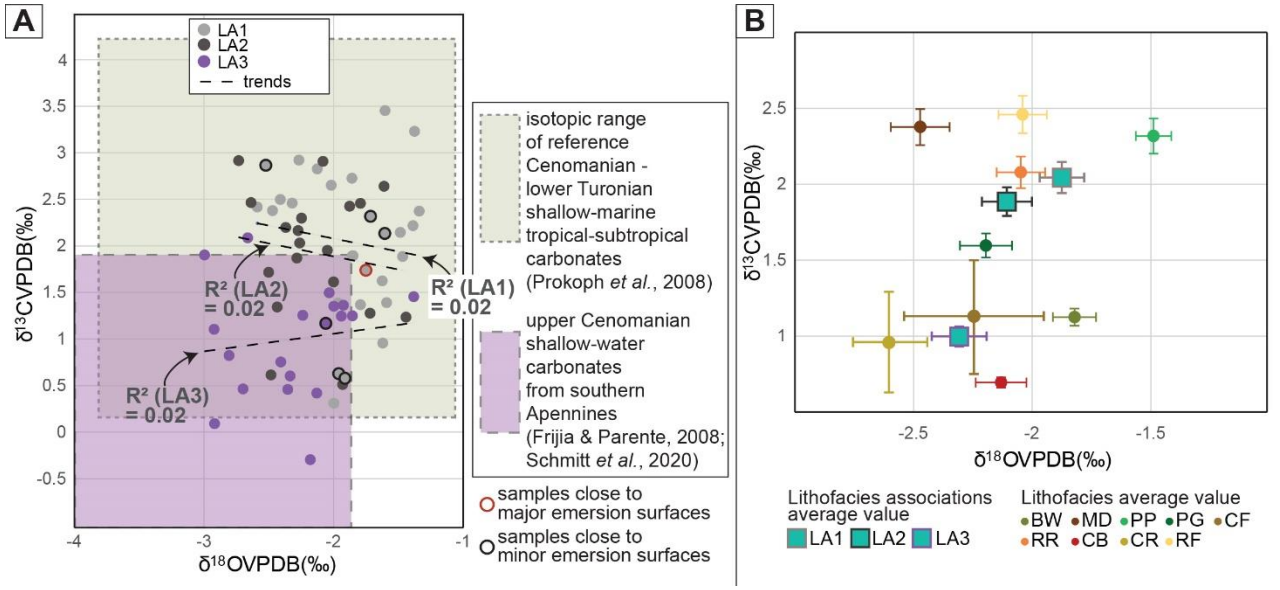

Fig. 4.9. A) C and O correlation for the bulk of each lithofacies association and for *Chondrodonta* and requieniid shells, plotted against the isotopic range of both the Cenomanian – lower Turonian shallow-marine tropical-subtropical carbonates of Prokoph *et al.* (2008) and the upper Cenomanian shallow-water carbonates of the Apennine Platform (Frijia & Parente, 2008; Schmitt *et al.*, 2020). B) C and O average correlation for single lithofacies, lithofacies associations and shells.

Despite this possible evidence of meteoric alteration, not all samples located below emersion surfaces in the Savudrija section have negative $\delta^{13}C$ values as well as not all samples with negative $\delta^{13}C$ values are associated with exposure surfaces. This finding suggests that some negative excursions may be related to changes in the primary marine carbon isotope signal and confirm the complexity of the stable isotopes' behavior in shallow-water carbonates associated to exposures (*e.g.,* Immenhauser *et al.*, 2003; Theiling *et al.*, 2007; Christ *et al.*, 2012).

To exclude any possible diagenetic influence on the samples, a conservative approach was chosen for the use of the $\delta^{13}C$ profile for stratigraphic correlations (Huck *et al.,* 2017). All samples from the entire Savudrija section which showed evidence of exposure/dissolution features at the outcrop or

microscope scale, were discarded and a smoothing procedure was run to highlight low-order trends and excursions in $\delta^{13}C$. The general trend of $\delta^{13}C$ values is, indeed, more likely to record the long-term global variations of the open ocean than higher-order fluctuations; the latter are more likely to result from variations in local environmental conditions on the shallow platform (Colombie *et al.,* 2011).

In the presented dataset, all shell samples (from both rudists and *Chondrodonta*) have not provided enough material for the measurement of the elemental (Fe, Mn, Sr, and Mg) concentrations, thus preventing careful considerations on the degree of alteration on the bivalve shells.

However, during the shell drilling, the areas of most obvious alteration have been avoided and only the pristine portion of the single shell has been considered. *Chondrodonta* and rudist samples here used for the $^{87}Sr/^{86}Sr$ stratigraphy were selected considering both the degree of shell preservation (observed under microscope) and the overall consistency of the Sr-isotopic ratio among shells from the same stratigraphic horizons. Internal consistency of Sr isotopic values among different components within the same bed or nearby beds is considered strong evidence for preservation of the original signal (McArthur *et al.*, 2004, 2012).

The $^{87}Sr/^{86}Sr$ ratios calculated on rudist and *Chondrodonta* shells of the Savudrija section, give absolute values of 0.707401 in the lower part of stratigraphic interval 1 (4.1 m), of 0.707407 in stratigraphic interval 2 (17.8 m) and of 0.707410 in the lowermost part of stratigraphic interval 3 (27.5 m) (*see* Tab. 4.2 and Fig. 4.5).

According to Frijia *et al.* (2015), when samples are collected in a short interval (less than 20 – 30 m) in shallow-water successions with no evidence of intervening stratigraphic gaps, their values can be ascribed as statistically indistinguishable (*see* discussion in Frijia *et al.*, 2015). Therefore, also considering the analytical precision of the measurement (*see* Tab. 4.2), the mean value of 0.707406 given by the three analysed samples has been used for the Strontium Isotope Stratigraphy (SIS).

Sample	**Component**	**$^{87}Sr/^{86}Sr$ measured**	**± 2 s. e. ($*10^{-6}$)**	**$^{87}Sr/^{86}Sr$ corrected**	**± 2 s. e. ($*10^{-6}$)**	**Min**	**Age (Ma) preferred**	**Max**
SA4.1-B	rudist	0.707398	7	0.707401				
SA17.8-A	rudist	0.707404	3	0.707407				
SA27.5-A	*Chondrodonta*	0.707407	7	0.707410				
			mean	0.707406	5	95	**95.25**	95.60

Tab. 4.2. Sr-isotope ratios of the studied rudist and *Chondrodonta* samples collected from the Savudrija section. Sr-isotopes values have been corrected for interlaboratory bias (*see* text for further details). Preferred numerical ages have

been derived from the look-up table of McArthur *et al.* (2012) (LOWESS fit 6), which is calibrated to the Geological Time Scale of McArthur *et al.* (2020). *See* the text for details on the precision estimation. In bold, the mean value of the Sr-isotope ratio set, and the preferred numerical age derived from it. Minimum and maximum ages were obtained by combining the statistical uncertainty (2 s. e.) of the mean values of the Sr-isotope ratios with the uncertainty of the seawater curve (*see* Frijia *et al.*, 2015 for details on the procedure).

To reveal the possible influence of terrigenous input on the REE signal, different lines of evidence have been used (Nothdurft *et al.*, 2004; Liu *et al.*, 2019; *see* Chap. 2, par. 2.2.3.2 for details). The Savudrija stratigraphic section shows an apparent slightly negative Ce anomaly, in a range of 0.25 – 0.99 (averaging 0.9) (*see* Fig. 4.5). The concentration of Al averages 329 ppm and the concentration of Sc averages 0.09 ppm, in both cases clearly lower with respect to the upper concentration limits (3500 ppm of Al and 2 ppm of Sc) which may exert a terrigenous influence on the Ce anomaly (Sholkovitz & Shen, 1995; Ling *et al.,* 2013).

However, the Y/Ho ratio, used as tracer to assess whether carbonate particles reflect a primary marine signature or siliciclastic components (*e.g.,* Nothdurft *et al.*, 2004; Frimmel, 2009; Liu *et al.*, 2019) averages 33.3, indicating marine carbonates likely reflecting a siliciclastic contamination (Chen *et al.*, 2015).

This finding is confirmed by the overall PAAS-normalized REE patterns (Fig. 4.10A). The concentration of REE in the Savudrija samples, normalized to the Post-Archean Australian Shale (PAAS) standard values given in Taylor & McLennan (1985) has been plotted against the South Pacific deep-water curve of Zhang & Nozaki (1996) which displays the typical seawater REE signal, and against the North American Shale Composite of Gromet *et al.* (1984). All REE patterns at Savudrija are way far from the South Pacific deep-water curve. Most samples show the typical "bell-shaped" pattern, characterized by an MREE (*i.e.,* Mid REE) enrichment and declining LREE and HREE, and interpreted as an indicator for contamination and/or riverine influence (*see* Della Porta *et al.*, 2015; Hueter *et al.*, 2020). Few samples show, instead, a flat pattern like the North American Shale Composite indicating, also in this case, a siliciclastic contamination (Gromet *et al.,* 1984). The terrestrial influence on the REE signal is also supported by a LREE/HREE ratio, in all samples close or even above 1 (*see* Menendez *et al.*, 2018).

All Savudrija samples were further screened for diagenetic alteration, which may exert an influence on both the REE patterns and the Ce anomaly (Nothdurft *et al.*, 2004; Frimmel, 2009; Liu *et al.*, 2019). Positive correlations between the Ce anomaly and ΣREE (*i.e.*, summation of REE + Y abundances), between the Eu anomaly and ΣREE as well as between Ce/Ce* and Eu/Eu* have been

formerly used to assess the potential diagenetic effect on the REE signature in limestones (Shields & Stille, 2001; Shields & Webb, 2004; Liu *et al.*, 2019). In the Savudrija samples, very low or absent positive correlation between the abovementioned parameters is observed (Fig. 4.10B, C, D), suggesting an irrelevant influence of post-depositional alteration on the measured Ce/Ce* and on the general REE signal.

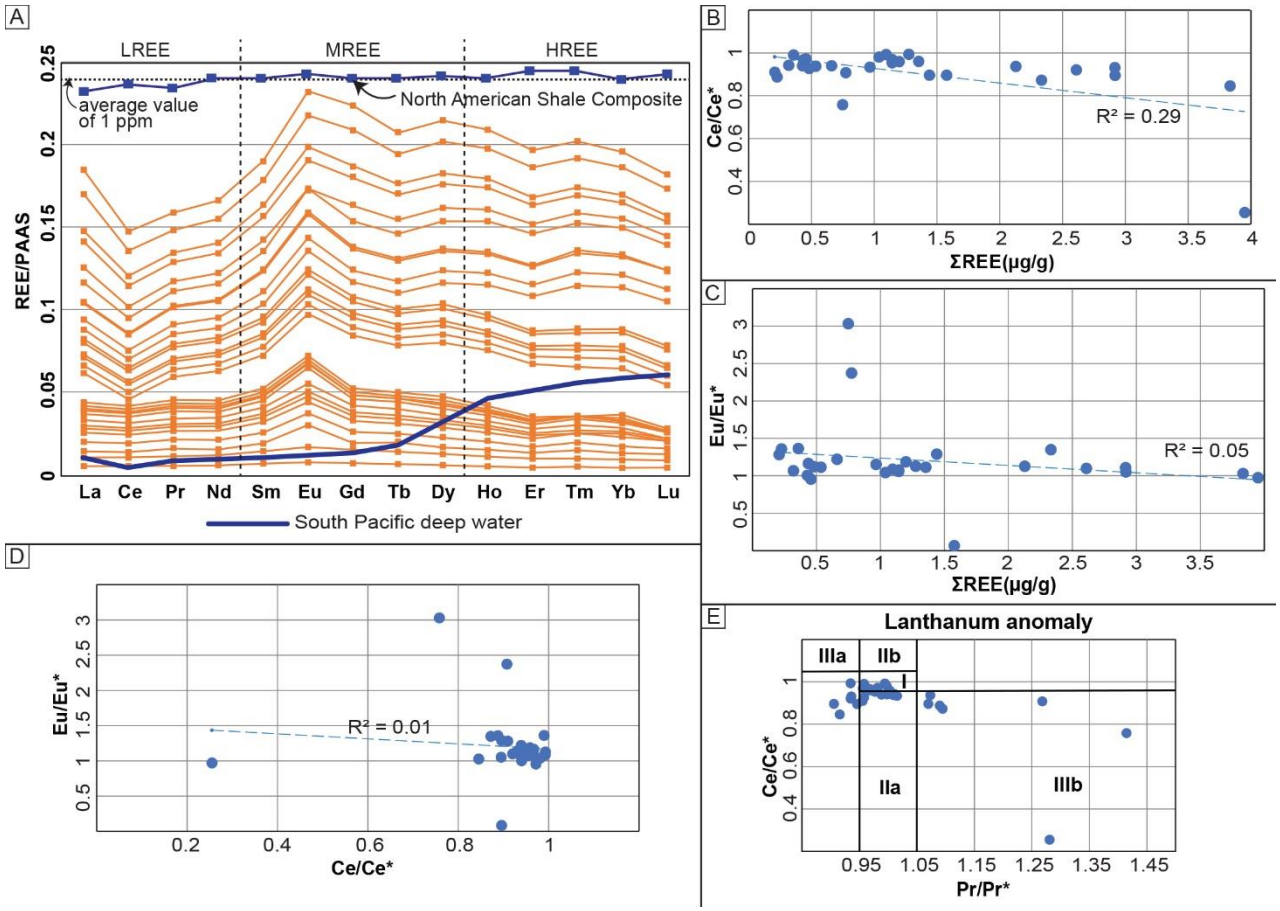

Fig. 4.10. A) the PAAS-normalized REE patterns of the Savudrija section, plotted against the North American Shale Composite of Gromet *et al.* (1984) and against the South Pacific deep-water curve of Zhang & Nozaki (1996). Abbreviations: LREE (*i.e.,* Light REE; La, Ce, Pr, Nd), MREE (*i.e.,* Mid REE; Sm, Eu, Gd, Tb, Dy), HREE (*i.e.,* Heavy REE; Ho, Er, Tm, Yb, Lu). B) correlation between the Ce anomaly (Ce/Ce*) and ΣREE. C) correlation between the Eu anomaly (Eu/Eu*) and ΣREE. D) correlation between Ce/Ce* and Eu/Eu*. E) the lanthanum anomaly diagram, showing samples mostly falling within the I and IIa fields of Bau & Dulski (1996).

Furthermore, the relationship between Ce/Ce* and Pr/Pr* has been used to characterize redox conditions by the La anomaly diagram of Bau & Dulski (1996) (Fig. 4.10E). Only few samples plot within the IIIb field, indicative of a genuine negative Ce anomaly due to a real depletion of Ce with

respect to the neighboring REE (*i.e.*, La and Pr), and not artificially created by a La enrichment (Bau & Dulski, 1996; Bodin *et al.*, 2013; Hueter *et al.*, 2019). Most samples fall within I and IIa fields which indicate, respectively, an absent anomaly and a positive La anomaly causing an apparent negative Ce anomaly (Bau & Dulski, 1996).

To sum up, samples from the Savudrija section display a negligible to absent diagenetic overprint. Nevertheless, the siliciclastic input is considerably high and prevents to use the Ce anomaly, coupled with the RSTE/Al ratios, to delineate the real seawater oxygenation state. For this reason, the redox conditions during the deposition of the *Chondrodonta*-rich interval at Savudrija can be only generally estimated. For the aim of this Thesis, the seawater oxygenation state has been considered only in terms of variations/fluctuations within the *Chondrodonta*-rich beds with respect to the lower stratigraphic interval.

4.6.2. Stratigraphic age attribution

The benthic foraminiferal association recognized within the Savudrija section (Fig. 4.5) is ascribable within the *V. radoicicae* - *C. gradata* concurrent-range zone of Velić (2007) of the Upper Cretaceous deposits of the Adriatic Carbonate Platform as well as within the lower part of the *C. gradata* - *P. reicheli* biozone of Chiocchini *et al.* (2012) for the central Apennine Carbonate Platform. This suggests an upper Cenomanian age for the studied section.

The benthic foraminiferal biozones of Chiocchini *et al.* (2012) have been tied by Frijia *et al.* (2015) on the Upper Cretaceous ammonite zones of Wright & Kennedy (1981, 1984) and Gale (1995, 1996). The *C. gradata* - *P. reicheli* biozone has been found corresponding to the upper part of the *C. guerangeri*, to the entire *M. geslinianum* and to part of the *N. juddii* ammonite zones, confirming an upper Cenomanian age for the Savudrija section. However, the resolution given by biostratigraphy alone is not sufficient to constrain a more precise age for the studied shallow-water limestones.

The most significant tie-point, commonly used for the correlation of upper Cenomanian stratigraphic sections, is the onset of the typical positive excursion in the $\delta^{13}C$ curve characterizing the Cenomanian – Turonian Boundary Event, or Oceanic Anoxic Event 2 (OAE2, Bonarelli Event). The OAE2 represents a major short-term perturbation of the global carbon cycle, which is generally reflected by a prominent positive excursion in $\delta^{13}C$ (2‰ to 4‰) in both marine, terrestrial organic and inorganic carbon (*e.g.,* Schlanger & Jenkyns, 1976; Scholle & Arthur, 1980; Tsikos *et al.*, 2004; Jenkyns, 2010; Jarvis *et al.*, 2006, 2011). The reference $\delta^{13}C$ curve for the English Chalk of Jarvis *et al.* (2006, 2011) is, for instance, marked by a positive excursion of about +3‰ at the onset of OAE2. This excursion

can be equated, according to Tsikos *et al.* (2004) and Gale *et al.* (2005), with the boundary between the *C. guerangeri* and the *M. geslinianum* ammonite zones.

Although the $\delta^{13}C$ composition of shallow-water limestones could deviate from the global open ocean value, due to syn- and post-depositional diagenetic alteration as well as to biological fractionation and local palaeoceanographic conditions (Allan & Matthews, 1982; Marshall, 1992; Immenhauser *et al.*, 2008; Oehlert & Swart, 2014; Huck *et al.*, 2017), the typical positive excursion in absolute values at the onset of OAE2 is well visible also in the $\delta^{13}C$ profiles of Tethyan shallow-water carbonate platforms (*e.g.,* Frijia & Parente, 2008; Korbar *et al.*, 2012; Frijia *et al.*, 2015, 2019; Navarro-Ramirez *et al.*, 2017; Vaziri-Moghaddam & Kalanat, 2020).

The $\delta^{13}C$ pattern in the Savudrija section is almost flat and lacks such a positive shift in absolute values; the deposition of the Savudrija limestones during the OAE2 interval is thus unlikely. Only a slight negative shift occurs in the upper part of the section (*see* Fig. 4.5). A similar flat – slightly negative pattern of the $\delta^{13}C$ curve occurs in upper Cenomanian shallow-water limestones of the Apennine Platform, right before the typical prominent positive excursion recorded at the onset of OAE2 (*see* Frijia & Parente, 2008; Frijia *et al.*, 2015, 2019). These limestones fall within the *C. gradata - P. reicheli* foraminiferal biozone of Chiocchini *et al.* (2012) and within the uppermost part of the upper Cenomanian *C. guerangeri* ammonite zone.

Therefore, considering the information given by both biostratigraphy and carbon-isotope patterns, a correlation between the Savudrija section and the Apennine Platform $\delta^{13}C$ curves of the upper Cenomanian M.te Cerreto (Frijia & Parente, 2008) as well as of the Cenomanian – Turonian M.te Coccovello (Frijia & Parente, 2008; Frijia *et al.*, 2015), has been attempted (Fig. 4.11).

Further, the $\delta^{13}C$ curve of Savudrija has been plotted against the reference curve of the upper Cenomanian – lower Turonian pelagic Eastbourne chalk (Paul *et al.*, 1999; Jarvis *et al.*, 2006, 2011) calibrated on the GTS2020 by Cramer & Jarvis (2020), and against the $\delta^{13}C$ curve of the upper Cenomanian Furlo section in the nearby Umbria - Marche basin (Bottini & Erba, 2018).

In the proposed correlation, the flat – slightly negative pattern characterizing the $\delta^{13}C$ curve of the Savudrija section is found corresponding to the flat – slightly negative pattern occurring in both the lower part of the M.te Cerreto and M.te Coccovello sections and the upper part of the Furlo basinal section. This finding supports the estimated stratigraphic position of the Savudrija section below the onset of OAE2, given by biostratigraphy.

Furthermore, the obtained $^{87}Sr/^{86}Sr$ ratios of the Savudrija section (Tab. 4.2) can be correlated with Sr isotopic values occurring before the onset of OAE2 in the M.te Cerreto section, thus corroborating the stratigraphic correlations via C-isotopes.

These observations confirm an upper Cenomanian age and a stratigraphic position below the OAE2 interval for the here studied Istrian section. Therefore, the *Chondrodonta*-rich interval of Savudrija corresponds to a phase occurred right below the onset of the anoxic event.

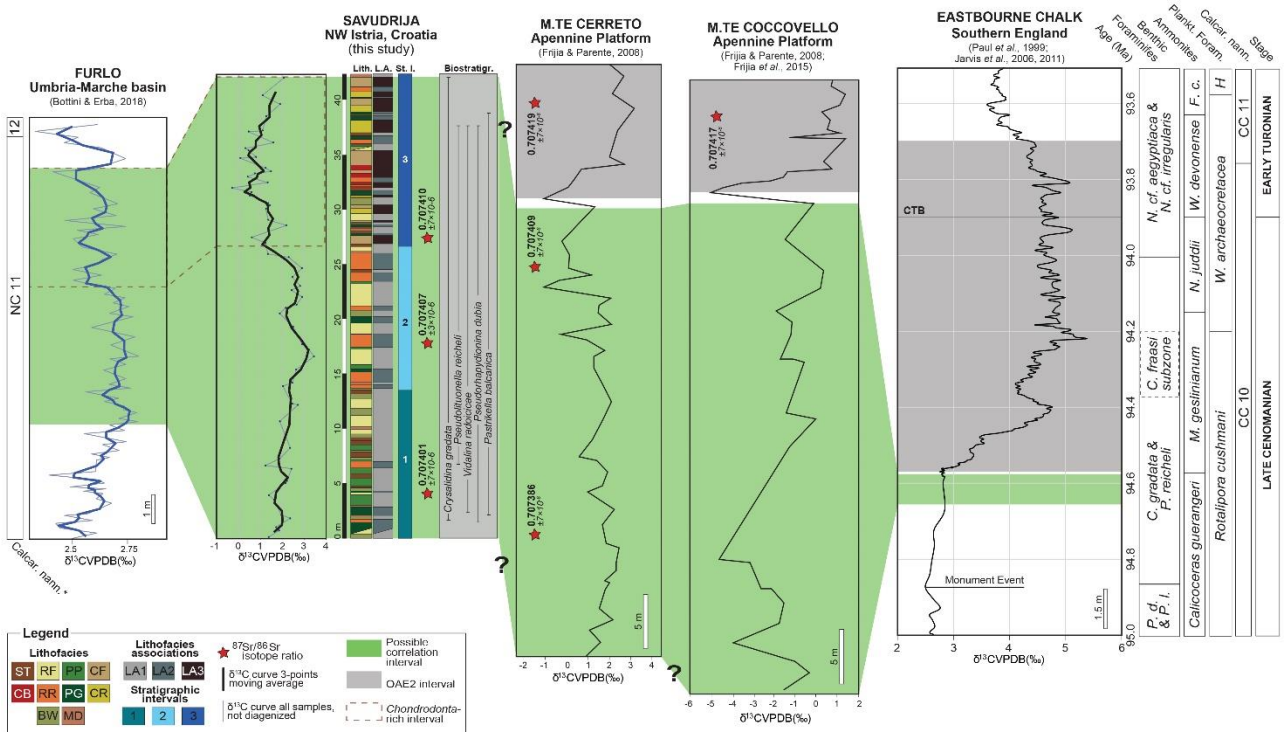

Fig. 4.11. Attempt of stratigraphic correlation between the Savudrija section and the $\delta^{13}C$ curve of the M.te Cerreto section in the Apennine Platform (Frijia & Parente, 2008). The $\delta^{13}C$ curve of Savudrija has also been plotted against the $\delta^{13}C$ profiles of M.te Coccovello (Apennine Platform; Frijia & Parente, 2008; Frijia *et al.*, 2015), of Furlo (Umbria - Marche basin; Bottini & Erba, 2018) and of the reference English Chalk (Paul *et al.*, 1999; Jarvis *et al.*, 2006, 2011), the latter calibrated on the GTS2020. The Cenomanian – Turonian Boundary Event (grey square) is from Jarvis *et al.* (2006). Benthic Foraminiferal Zones are from Chiocchini *et al.* (2012), tied on the Ammonite Zones of Wright & Kennedy (1981, 1984) and Gale (1995, 1996) by Frijia *et al.* (2015). Planktic Foraminiferal Zones are from Coccioni & Premoli Silva (2015), and Calcareous Nannoplankton Zones are from Sissingh (1977), both calibrated on the GTS2020. Calcareous Nannoplankton Zones (*) for the Furlo section are from Roth (1978) and Gambacorta *et al.* (2015). Sr-isotopes for the Apennine Platform are from Frijia & Parente (2008). Abbreviations: P. d. & P. i., P. *dubia* & P. *laurinensis*; F. c., F. *catinus*; H, H. *helvetica*; CTB, Cenomanian – Turonian Boundary. *See* par. 4.5.1 for the description of lithofacies and stratigraphic intervals within the Savudrija section.

4.6.3. Palaeoenvironmental controls on the proliferation of Chondrodonta

During OAE2, environmental disturbances triggered by the mass release of CO_2 associated to the Carribean and High Artic Large Igneous Provinces emplacement (Snow *et al.*, 2005; Kuroda *et al.*,

2007; Jenkyns *et al.*, 2017), caused biotic stress in terrestrial and in both shallow- and deep-marine ecosystems (*e.g.*, Jenkyns *et al.*, 2017; Bottini & Erba, 2018; Frijia *et al.*, 2019; Laurin *et al.*, 2019). Major turnovers and extinctions in the planktic community are widely documented (Leckie *et al.*, 1998, 2002; Huber *et al.*, 1999; Erba, 2004; Turgeon & Brumsack, 2006; Hetzel *et al.*, 2009).
The increase of temperature and precipitation rates enhanced terrestrial weathering which, in turn, resulted in a major nutrient load delivered to oceans and in an increased primary productivity (Leckie *et al.*, 2002; Jenkyns, 2003, 2010; Owens *et al.*, 2013; Jenkyns *et al.*, 2017; Heimhofer *et al.*, 2018). Other possible factors promoting primary productivity were the nitrogen fixation (Junium & Arthur, 2007), the phosphorus regeneration from organic-rich sediments (Mort *et al.*, 2007; Monteiro *et al.*, 2012) as well as the release of great quantities of micro-nutrients like hydrothermal iron coming from the submarine volcanogenic activity (Adams *et al.*, 2010).
Consequently, many shallow-water areas recorded episodic eutrophic phases characterized by synchronous cyanobacterial proliferations (Philip & Airaud-Crumiere, 1991; Erba, 2004; Frijia *et al.*, 2019) which caused a crisis in marine ecosystems and extinctions of some benthic organisms (*e.g.,* Philip & Airaud-Crumiere, 1991; Parente *et al.*, 2008; Vaziri-Moghaddam & Kalanat, 2020). Most shallow-water carbonate platforms experienced demise and drowning or, when resilient, showed a marked biotic turnover and a facies change throughout the event (*e.g.*, Jenkyns, 1991; Parente *et al.*, 2007, 2008; Frijia & Parente, 2008; Korbar *et al.*, 2012; Frijia *et al.*, 2019; Brčić *et al.*, 2021).

However, the time interval preceding the onset of the anoxic event was also characterized by climatic instability with frequent fluctuations in temperature, nutrients, and in other environmental parameters (*e.g.*, Hetzel *et al.*, 2009; Pearce *et al.*, 2009; Jenkyns *et al.*, 2017; O'Brien *et al.*, 2017; Bottini & Erba, 2018; Laurin *et al.*, 2019; Schröder-Adams *et al.*, 2019; Baker *et al.*, 2020).

The proliferation of the opportunistic, oyster-like bivalve *Chondrodonta* has already been suggested as indicator of relatively high nutrient availability in shallow-water areas in time intervals straddling the early Aptian OAE1a (*see* par. 3.6.4 and Posenato *et al.*, 2018; Nuñez-Useche *et al.*, 2020; Del Viscio *et al.*, 2021). This interpretation would support the flourishing of *Chondrodonta joannae* in the studied limestones of the Milna formation in the AdCP. Here, the bivalve gradually blooms within radiolitid rudist limestones and reaches a phase of maximum proliferation (*i.e., Chondrodonta*-rich interval) where it becomes the dominant genera, forming mono- to pauci-specific accumulations (Fig. 4.6, 4.7).
A relative increase in the P/Al concentration and its trend within the *Chondrodonta*-rich interval with respect to the lower stratigraphic tract (Fig. 4.5) suggests relatively higher and fluctuating trophic

levels during its deposition, likely above the threshold for rudist communities (*see* Fig. 10 in Rameil *et al.*, 2010).

By means of both $\delta^{13}C$ chemostratigraphy and biostratigraphy, the Savudrija section has been correlated to the $\delta^{13}C$ curve of the upper Cenomanian Furlo section in the nearby Umbria - Marche basin, located ~ 200 km southwest (Bottini & Erba, 2018). The relatively increased nutrients at Savudrija correlate to a discreetly higher fertility peak in the nannofossil record of the nearby Umbria - Marche basin (Fig. 4.12; Bottini & Erba, 2018). This peak has been translated into a shift from oligo- to mesotrophic conditions occurred at ~ 400 kyr prior to the onset of OAE2 (*see* discussion and Fig. 7 in Bottini & Erba, 2018) and further suggests that the relative nutrient increase occurred not only on the AdCP but probably on a broader geographical scale. However, stratigraphic evidence on the major sources of P on the AdCP during the proliferation of *C. joannae* still needs to be investigated.

The facies and the geochemical analyses of the Savudrija section also highlight a subtidal environment episodically shifting to tidal flat settings during the deposition of the *Chondrodonta*-rich interval (Fig. 4.3B). The increased and fluctuating concentration of Al (ppm) in this stratigraphic tract supports the occurrence of nearby emerged areas (Matičec *et al*., 1996; Moro *et al*., 2008) and further indicates that terrigenous inputs (also supported by the siliciclastic-contaminated REE signal and Ce anomaly; *see* par. 4.6.1) likely exerted an influence on the seawater oxygenation during the proliferation of this bivalve (Fig. 4.5). The latter is also suggested by the RSTE/Al ratios in the *Chondrodonta*-rich interval, showing overall fluctuating patterns compared to the flat curves in lower part of the stratigraphic section.

Quick changes in the seawater circulation and oxygenation as well as in the siliciclastic input, which likely represented stressors for other benthos (*e.g.,* rudists), did not exclude *Chondrodonta*. The resilience of this bivalve to such fluctuations is further supported by the great shell elongation of the Savudrija *C. joannae*, interpreted by Posenato *et al.* (2020) as necessary to avoid the commissure burial and the gill suffocation produced by high carbonate sedimentation rates and fecal products entrapment among shells in low agitated seawaters.

The *Chondrodonta*-rich interval also correlates to a colder seawater temperature phase, indicated by the nannofossil indexes in the Umbria - Marche basin (Fig. 4.12). The positive peaks and the overall increased concentration of the RSTE/Al ratios within the *Chondrodonta*-rich interval of the Savudrija section (*i.e.,* stratigraphic interval 3; *see* Fig. 4.3B), indicate a higher seawater oxygenation which suggests a colder seawater temperature during the proliferation of *Chondrodonta*.

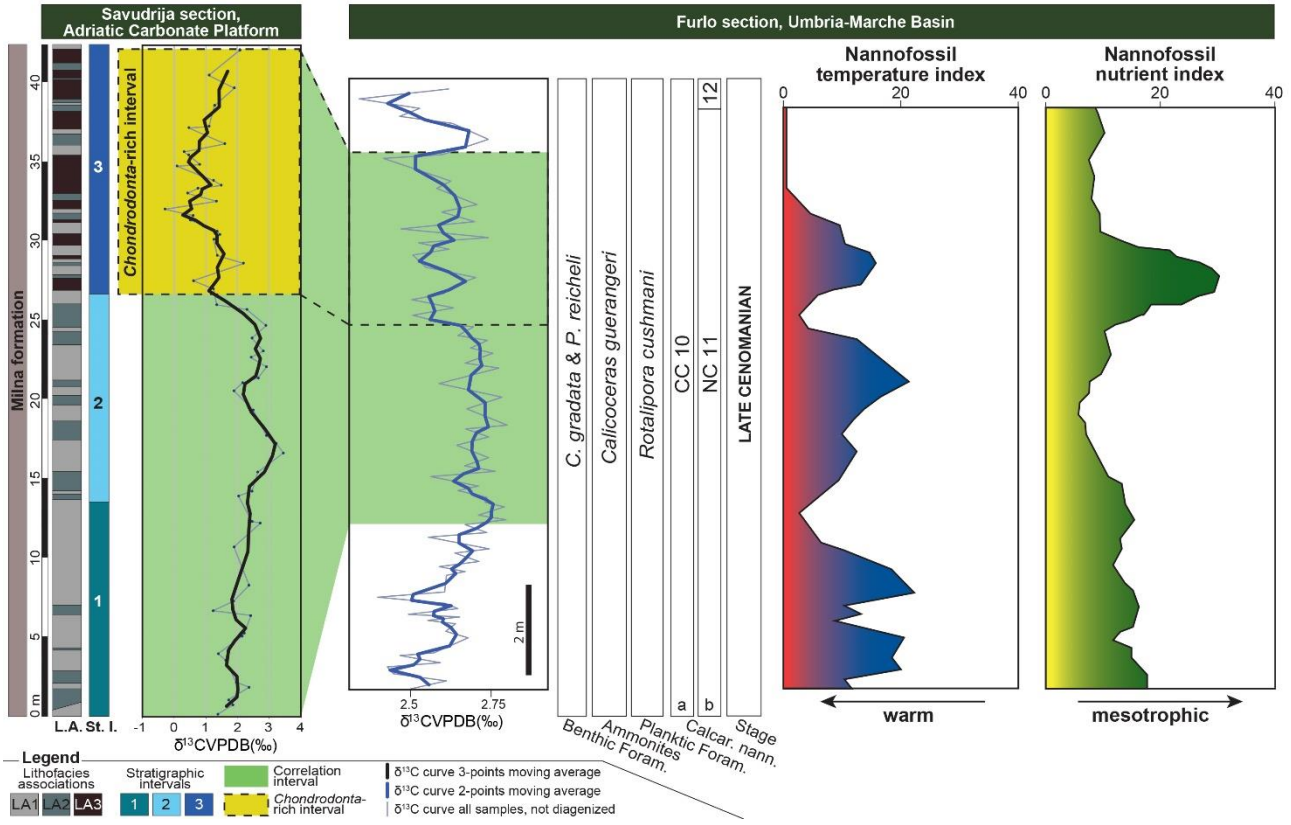

Fig. 4.12. Attempt of reconstruction of the palaeoenvironmental fluctuations possibly influencing the proliferation of *Chondrodonta* within the upper Cenomanian Savudrija section (Milna formation, Adriatic Carbonate Platform). The *Chondrodonta*-rich interval (in yellow) is compared to the temperature and nutrient fluctuations in the nearby pelagic realm of the Furlo section in the Umbria - Marche Basin (Bottini & Erba, 2018). Benthic Foraminiferal Zones are from Chiocchini *et al.* (2012), tied on the Ammonite Zones of Wright & Kennedy (1981, 1984) and Gale (1995, 1996) by Frijia *et al.* (2015). Planktic Foraminiferal Zones are from Coccioni & Premoli Silva (2015), calibrated on the GTS2020. Calcareous Nannoplankton Zones are (a) from Sissingh (1977), calibrated on the GTS2020 and (b) from Roth (1978) and Gambacorta *et al.* (2015). *See* par. 4.5.1 and Tab. 4.1 for the description of lithofacies associations and stratigraphic intervals within the Savudrija section.

Cooler seawaters might have promoted the superstratal mode of life of *Chondrodonta*, enabling this bivalve to filter in a vertical position and at a greater distance from the substrate (10 – 20 cm; Posenato *et al.*, 2020). In contrast, the constratal mode of life of rudists (*see* Chap. 1, Fig. 1.6) was characterized by the bivalve commissure projecting only few centimeters above the sediment-water interface (Gili *et al.*, 1995; Gili & Götz, 2018; Posenato *et al.*, 2020). Beside fluctuations in nutrients, oxygenation and in the siliciclastic contamination, a cooler seawater probably represented another stressor for the rudist community, allowing *Chondrodonta* to proliferate in such a scenario of environmental changes.

All these findings suggest that the proliferation of *Chondrodonta joannae* on the upper Cenomanian AdCP took place during a phase of environmental stress triggered by the changing climate leading to OAE2. A gradual shift from oligo- to mesotrophic conditions, coupled with intermittent terrigenous inputs and with cool seawaters characterized by fluctuating oxygenation and circulation, represented stressing factors for the rudist community of Savudrija but did not prevent the thriving of *Chondrodonta*. The high resilience of this opportunistic bivalve to quick changes in water parameters, allowed it to outplay the less tolerant benthos and to flourish in pauci- to monospecific accumulations at the prelude phase of OAE2.

4.7. Conclusions

Accumulations of the oyster-like bivalve *Chondrodonta* commonly occur in upper Cenomanian shallow-water limestones of the Adriatic Carbonate Platform; despite this, a precise time and causal relationship between the proliferation of this bivalve and the environmental perturbations linked to OAE2 has not emerged yet.

The *Chondrodonta joannae*-rich beds along the rocky coast of the Savudrija area (northern Istria, Croatia), have been correlated to the upper Cenomanian chemostratigraphic C-isotope curve below the onset of OAE2. *Chondrodonta* appears on the AdCP within rudist limestones and reaches a phase of maximum proliferation and predominance over rudists in the uppermost part of the studied section (*i.e., Chondrodonta*-rich interval).

The *Chondrodonta*-rich interval deposited within a scenario of environmental stress triggered by the changing climate leading to OAE2. Increasing nutrient load, intermittent terrigenous inputs, and cool seawaters characterized by fluctuating oxygenation and circulation, represented stressors for the rudist community of Savudrija allowing the opportunistic *Chondrodonta* to become the dominant benthos at the prelude phase of OAE2.

5. Regional occurrence of *Chondrodonta* accumulations

The oyster-like bivalve *Chondrodonta* has been widely documented within and outside the Cretaceous Tethys (*e.g.*, Dhondt & Dieni, 1992, 1993), in a set of shallow-marine sub-environments including tidal flats, lagoons, back-reefs and platform margins. The bivalve has a discontinuous distribution spanning from the (?) Berriasian (Masse *et al.*, 2015) to the (?) Campanian (Freneix & Lefèvre, 1967) but likely shows a peak abundance during the Aptian – Cenomanian period (Posenato *et al.*, 2018, 2020). A literature review of the worldwide *Chondrodonta* accumulations documented at the inner platform scale and spanning the stratigraphic intervals of OAE1a (late Barremian – early Aptian) and OAE2 (late Cenomanian – early Turonian) is here reported. Nevertheless, datasets collected in multiple decades of research and with different methods inevitably complicate the assignment of a precise stratigraphic position to all the documented *Chondrodonta* accumulations, especially with respect to the intervals of Cretaceous OAEs.

5.1. Worldwide *Chondrodonta* accumulations in the late Barremian – early Aptian

Although only few studies on Berriasian – lower Barremian shallow-water carbonates report *Chondrodonta* accumulations in Southern Tethys (*e.g.,* Pratt & Smewing, 1990; Zaghbib-Turki, 2003; Masse *et al.,* 2015) and in the proto-North Atlantic (*e.g.,* Phelps *et al*., 2014), upper Barremian - lower Aptian *Chondrodonta* accumulations have been extensively documented worldwide. With few exceptions (Posenato *et al.*, 2018, 2020), only limited attention has been given to the palaeoecological significance of *Chondrodonta* accumulations. Only a few authors (*e.g.,* Phelps *et al.*, 2015; Posenato *et al.*, 2018; Nuñez-Useche *et al.*, 2020) have interpreted *Chondrodonta* as an indicator of ecological stress in a mesotrophic domain. Other authors (*e.g.,* Leonide *et al.*, 2012; Bonin *et al.*, 2016) consider it as a component of oligotrophic (*cfr.* "Urgonian") communities.
Determining the precise stratigraphic position of every *Chondrodonta* bed reported worldwide for the late Barremian – early Aptian interval, is challenging. Only by integrating recent high-resolution studies on the stratigraphic, environmental, and ecological evolution of worldwide carbonate platform successions spanning OAE1a, a synthesis of the global accumulations was feasible (Fig. 5.1).

In the Helvetic domain (Switzerland) of the Northern Tethys, *Chondrodonta* occurs within oligotrophic coral-rudist limestones (Wissler *et al.*, 2003) of the uppermost Barremian – lower Aptian succession, below the drowning interval associated with mesotrophic associations (Föllmi *et al.*,

2006). *Chondrodonta* also occurs in both rudist limestones and monospecific biostromes in the (?) upper Barremian – lower Aptian carbonates of Hungary (Császár *et al.*, 1994), below an interval with abundant *Bacinella-Lithocodium* and orbitolinids. In the Maestrat Basin (SE Spain), *Chondrodonta* occurs in monospecific biostromes prior to OAE1a (Malchus *et al.*, 1995) but is interpreted as recording "normal marine conditions" (Bonin *et al.,* 2016). In the Vocontian Basin and Provence Platform domains (SE France), stepwise drowning events prior to OAE1a (Masse & Fenerci-Masse, 2013; Giraud *et al.*, 2018) are characterized by Urgonian limestones with episodic orbitolinid levels. Leonide *et al.* (2012) report local chondrodontids in Urgonian rudist facies extending to the uppermost chemostratigraphic C2 segment.

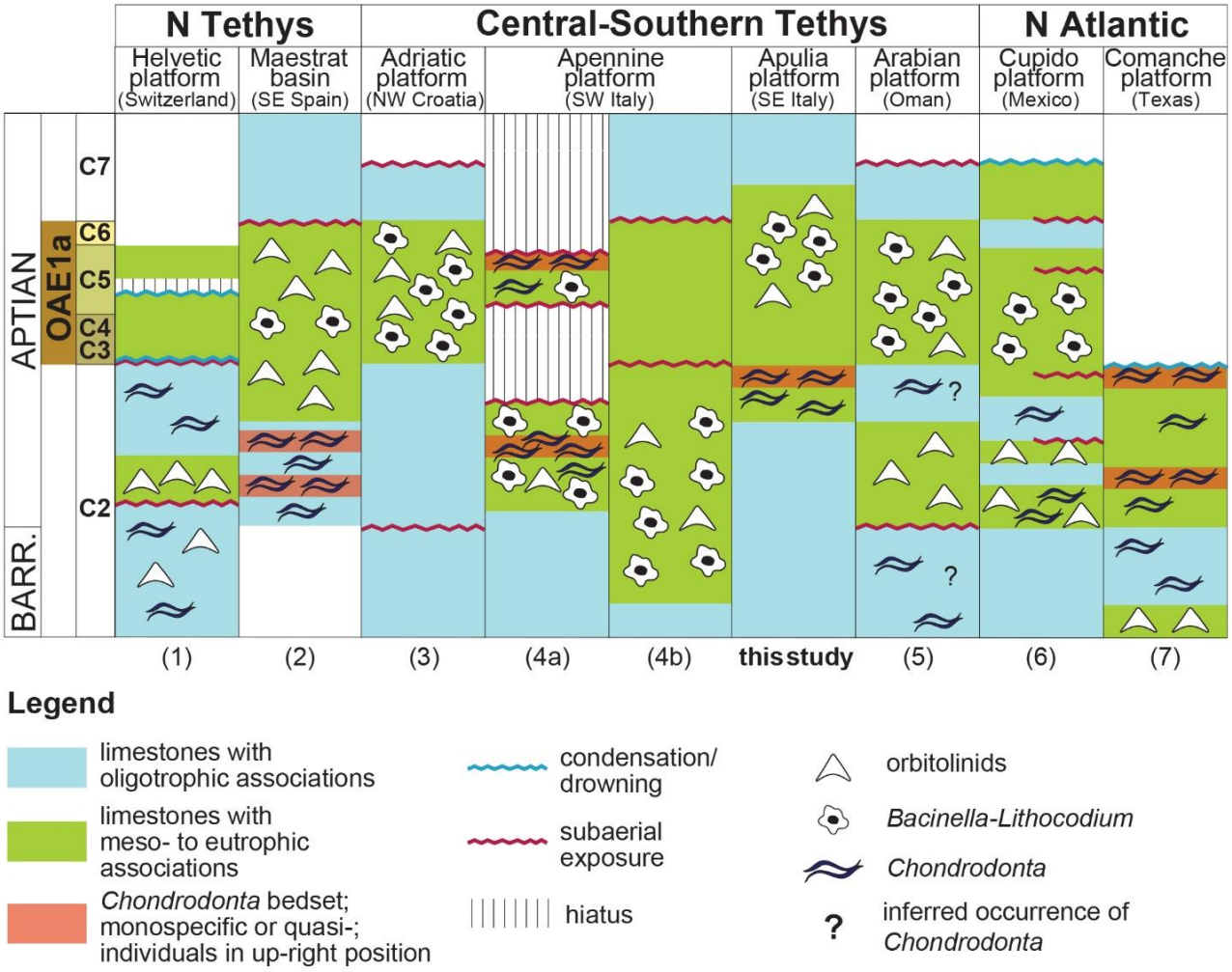

Fig. 5.1. Synthesis of the occurrence of *Chondrodonta* within worldwide inner platform carbonates during the main biotic, environmental, and stratigraphic events spanning the uppermost Barremian – lower Aptian (including OAE1a) interval. The stratigraphic sections (not to scale) have been reported and integrated from (1) Wissler *et al.*, 2003; Föllmi *et al.*, 2006, (2) Malchus *et al.*, 1995; Bonin *et al.*, 2016, (3) Huck *et al.*, 2010, (4a) Graziano & Raspini, 2018, (4b) Amodio &

Weissert, 2017, (5) Pittet *et al.*, 2002; Immenhauser *et al.*, 2004; Rameil *et al.*, 2010; Huck *et al.*, 2010, (6) Nuñez-Useche *et al.*, 2020, (7) Phelps *et al.*, 2014, 2015. Graphics inspired by Amodio & Weissert (2017).

In the Central and Southern Tethyan realm, the upper Barremian – lower Aptian Apennine Platform (Amodio & Weissert, 2017) is characterized by a shift toward mesotrophic conditions with *Bacinella-Lithocodium* and *Palorbitolina lenticularis*. Graziano & Raspini (2018) interpret abundant *Chondrodonta*, in both monospecific biostromes and associated with *Bacinella-Lithocodium* and *P. lenticularis*, as an indication of mesotrophic conditions. Orbitolinid-rich rocks of earliest Aptian age and extensive *Bacinella-Lithocodium* intervals at the turn of OAE1a occur in Oman (Pittet *et al.*, 2002; Rameil *et al.*, 2010; Huck *et al.*, 2010); here *Chondrodonta* floatstones are interpreted as oligotrophic communities proliferating probably up to the uppermost C2 segment, although "abundant oysters" (*cfr.* Immenhauser *et al.*, 2004) are also reported within *Bacinella-Lithocodium* facies. Rudist-*Chondrodonta* limestones interbedded with orbitolinid-rich beds occur in the (?) lower Aptian shallow-water successions of Ethiopia (Bosellini *et al.*, 1999b) and Somalia (Barbieri *et al.*, 1979) and in the (?) Barremian – Aptian limestones of Afghanistan (Abdullah *et al.*, 1980).

In the proto-North Atlantic, Najarro *et al.* (2011) report *Chondrodonta* within oligotrophic assemblages of the Basque-Cantabrian Basin that underlie and overlie OAE1a. Conversely, in the Lusitanian Basin (Portugal), Huck *et al.* (2014) interpret the replacement of oligotrophic rudist-coral limestones by orbitolinid-oyster-rich facies with subordinate *Bacinella-Lithocodium*, as due to paleoenvironmental perturbations and incipient drowning associated with OAE1a. In the Gulf of Mexico, *Chondrodonta* occurs in association with *Bacinella-Lithocodium* in (?) Barremian – lower Aptian limestones of the Atima Platform in Honduras (Scott & Finch, 1999). In the Comanche Platform (Texas) Phelps *et al.* (2014, 2015) report *Chondrodonta* within upper Barremian rudist limestones and as lower Aptian monospecific biostromes (up to the top of the C2 segment) and interpret them as response to increased detrital clay input, preceding sea-level transgression and platform drowning during OAE1a. Similarly, in the Cupido Platform (Mexico) which drowned after OAE1a, Núñez-Useche *et al.* (2020) interpret the occurrence of lowermost Aptian orbitolinid- and *Chondrodonta*-rich beds as a short mesotrophic event caused by both sea-level transgression and increased continental weathering due to a more humid climate. *Chondrodonta* in the Cupido Platform occurs also within oligotrophic assemblages at the onset of OAE1a, below an extensive *Bacinella-Lithocodium* interval recording environmental instability and mesotrophic conditions during the anoxic event.

5.2. Tethyan *Chondrodonta* accumulations in the mid-late Cenomanian – early Turonian

A few studies report *Chondrodonta* accumulations in lower – middle Cenomanian shallow-water carbonates, mostly concentrated in Central (Tišljar *et al.*, 1998, 2002; Di Stefano & Ruberti, 2000; Husinec *et al.*, 2000; Vlahović *et al.*, 2011) and Southern Tethys (Sharp *et al.*, 2010; Razin *et al.*, 2010). In contrast, mid-upper Cenomanian to lower Turonian accumulations have been extensively documented in Tethyan inner platform settings (*e.g.*, Dhondt & Dieni, 1993 and references therein). As for the Barremian – Aptian interval, also in this case only a few authors (*e.g.*, Ayoub-Hannaa & Fürsich, 2012; Posenato *et al.*, 2020) give attention to the palaeoecological significance of the proliferation of this bivalve. Most authors only quote and/or report *Chondrodonta* within rudist limestones or in monospecific biostromes; this datum, coupled with the almost total lack of recent high-resolution studies, prevents a precise definition of the stratigraphic position of all the globally observed *Chondrodonta* accumulations. However, a synthesis of the available literature on the mid-upper Cenomanian – lower Turonian accumulations is here provided.

In the Provence Platform (southern France) of the Northern Tethys, *Chondrodonta* has been reported in association with rudists in upper Cenomanian inner platform limestones (Philip, 1998). In south-central Pyrenees (northern Spain), Drzewiecki & Simo (2000) report chondrodontids in rudist limestones from both lagoon and back-margin facies of the upper Cenomanian Santa Fe formation. *Chondrodonta* is also documented in radiolitid bioherms deposited within upper Cenomanian calcarenite shoals of the western Iberian margin (western – central Portugal) (Berthou *et al.*, 1979; Callapez, 2008).

In Southern Tethys, *Chondrodonta* is observed within the (?) middle – upper Cenomanian rudist limestones of the Yilanli formation in Turkey (Özer *et al.*, 2001) as well as in association with rudists and corals in the upper Cenomanian Zebbag formation of Tunisia (Zaghbib-Turki, 2003). *Chondrodonta* also occurs as subordinated component in rudists communities of the upper Cenomanian shallow-water carbonates of Israel (Bein, 1976; Frank *et al.*, 2010). In the upper Cenomanian – lower Turonian Mishrif formation, widely exposed in the Middle East, *Chondrodonta* occurs as subordinated component in inner platform rudist biostromes from Iraq (Al-Dabbas *et al.*, 2010) and U.A.E. (Burchette & Britton, 1985; Burchette, 1993), where "intact *Chondrodonta*" (*cfr.* Burchette & Britton, 1985) also form ~ 1 m-thick biostromes.

In Egypt, *Chondrodonta* is documented in the inner ramp facies of both the upper Cenomanian Galala formation (Pandey *et al.*, 2011; Saber, 2012; Ayoub-Hannaa & Fürsich, 2012) and the lower Turonian

Abu Qada formation (Ayoub-Hannaa & Fürsich, 2012). Here, the bivalve occurs in rudist limestones together with corals and coralline sponges (Pandey *et al.*, 2011) as well as in quasi-monospecific biostromes ("*C. joannae* association"; *cfr.* Ayoub-Hannaa & Fürsich, 2012), where it is interpreted as indicator of highly stressful environmental conditions. In northern Oman, *Chondrodonta* shells and "large" shells fragments (*cfr.* Adams *et al.*, 2011) are reported as associated components of radiolitid limestones from the upper Cenomanian inner platform Natih formation (Philip *et al.*, 1995; Grélaud *et al.*, 2010; Adams *et al.*, 2011).

In Central Tethys, *Chondrodonta* (*i.e., C. joannae*) accumulations are abundantly documented in shallow-water carbonates from both the Apulia and the Adriatic platforms (*see* Fig. 5.2). In Croatia, for instance, the upper Cenomanian *Chondrodonta* Limestone, widely exposed in Istria and in the Dalmatian islands, is typically represented by alternating stromatolites, *C. joannae* floatstones and (in the top part) pelagic limestones witness of platform drowning (Gušić & Jelaska, 1993; Steuber *et al.*, 2005; Husinec & Jelaska, 2006). The *Chondrodonta* Limestone is also coeval (*see* Steuber *et al.*, 2005) to the *Chondrodonta*-dominated upper part of the Milna formation (Gušić & Jelaska, 1990) analysed in this Thesis (*see* Chap. 4) and has been formerly used as stratigraphic marker for the upper part of the Istrian Cenomanian carbonates (Polšak, 1967b; Pleničar *et al.*, 1969).

In northeastern Italy, several authors report upper Cenomanian *C. joannae* accumulations. In the Karst of Trieste and the Isonzo Karst areas, *Chondrodonta* occurs within the inner platform limestones of the upper Cenomanian Monrupino formation, in association with radiolitid-*Neithea* limestones (Caffau *et al.*, 1995; Pons *et al.*, 2011; Cucchi & Piano, 2014) as well as in decimetre-thick monospecific biostromes (Dhondt & Dieni, 1993; Cestari & Sartorio, 1995; Caffau *et al.*, 1995; Cucchi & Piano, 2014). Particularly, in the lower part of the Monrupino formation, Tentor *et al.* (1994) and Cucchi & Piano (2014) ascribe the *C. joannae* accumulations within the *Chondrodonta* Member (*sensu* Cucchi *et al.*, 1987).

In central Italy, *C. joannae* occurs in lagoon facies associated to caprinid biostromes of the (?) middle - upper Cenomanian Lepini Mountains (Latium region; Carbone & Sirna, 1981). *Chondrodonta* biostromes, up to 60 cm thick and with a variable amount of associated rudists, are also observed within the Maiella Mountains (Abruzzi region; Sanders, 1996; Paris & Sirna, 1996). In southern Italy (Apulia region), *C. joannae* is reported by Spalluto (2012) within the inner platform facies of the (?) middle – upper Cenomanian Bari Limestone (*i.e.*, Sannicandro level *sensu* Azzaroli *et al.*, 1968). Moreover, Le Goff (2016) reports *Chondrodonta*-dominated beds (with shells up to 40 cm long) in the upper Cenomanian Llogara succession (Albania) and infers them a synchronous deposition with

the *C. joannae* accumulations from Croatia and southern Italy (*i.e.*, within the Sannicandro level; *see* Le Goff, 2016).

Fig. 5.2. Summary of the *C. joannae* accumulations reported in literature within mid-upper Cenomanian – lower Turonian shallow-water carbonates of the Tethyan realm. The late Cenomanian palaeomap on the background is from Scotese (2014).

5.3. *Chondrodonta* proliferation: a regional bioevent preluding OAE1a and OAE2

The analysed lower Aptian *Chondrodonta* of the Apulia Carbonate Platform appears as subordinated component in requieniid limestones and then proliferates right below the onset of OAE1a (*i.e.*, *Chondrodonta* bedsets; *see* Chap. 3). The flourishing of this oyster-like bivalve occurs in a scenario of increasing environmental stress on the platform top, coeval to a biotic crisis in the nearby pelagic realm (*i.e.*, nannoconid decline and crisis; Erba, 1994, 2004). The extreme environmental deterioration at the onset of OAE1a reached the threshold for *Chondrodonta* and allowed the mesotrophic *Bacinella-Lithocodium* and orbitolinids to dominate the benthic community.

According to literature, the early Aptian *Chondrodonta* globally thrives both in association with coral-rudist assemblages and in mesotrophic conditions, where it predominates forming monospecific (or quasi-) biostromes before being replaced by fully mesotrophic taxa (Fig. 5.1). Except for the Apennine Platform, these bivalve accumulations globally predate the onset of OAE1a, suggesting the transient dominance of *Chondrodonta* in the benthic community as a precursor of the strong environmental stress and of the fully mesotrophic conditions the worldwide carbonate platforms underwent during the anoxic event.

The analysed upper Cenomanian *Chondrodonta* of the Adriatic Carbonate Platform appears within radiolitid limestones and then proliferates below the onset of OAE2 (*i.e., Chondrodonta*-rich interval; *see* Chap. 4). The bivalve flourishes and becomes the dominant macro-benthos during an environmental stress phase occurred on the platform top at the prelude of the anoxic event and correlates to increasing eutrophication in the nearby basin settings.

In literature, the majority of the *Chondrodonta* accumulations is documented in Tethyan shallow-water carbonates of late Cenomanian age, likely below the onset of OAE2 (Fig. 5.2). Only in few cases (*e.g.*, Al-Dabbas *et al.*, 2010; Ayoub-Hannaa & Fürsich, 2012) the accumulations are dated up to the early Turonian, although the lack of high-resolution studies prevents to verify this stratigraphic position.

A coeval origin for all the *Chondrodonta*-rich stratigraphic intervals deposited on the whole Adriatic Platform has been formerly suggested (Gušić & Jelaska, 1990, 1993; Steuber *et al.*, 2005; Husinec & Jelaska, 2006) and further extended at least to the *Chondrodonta* accumulations of the upper Cenomanian Apulia Carbonate Platform (Le Goff, 2016). The proliferation of *Chondrodonta* in shallow-water carbonates of the Central Tethys as a synchronous late Cenomanian event witness of environmental instability preluding OAE2, is thus likely. Further high-resolution analyses are, however, required to confirm this hypothesis and to eventually extend it to these bivalve accumulations of Northern and Southern Tethys.

6. Conclusions

The oyster-like bivalve *Chondrodonta*, common in Tethyan Cretaceous shallow-water carbonates, shows peaks of concentration during the Aptian – Cenomanian time interval. Despite its abundance and widespread geographic distribution, neither a temporal nor a causal relationship between the flourishing of this bivalve and OAEs has emerged yet.

In this Thesis, the stratigraphic occurrence, distribution, and ecological significance of *Chondrodonta* have been analyzed. The aim was to define the exact timing between the *Chondrodonta* accumulations and some Cretaceous OAEs, as well as the possible OAE-related environmental perturbations (*e.g.,* changes from oligo- to mesotrophic associations) which triggered the proliferation of the bivalve.

The studied *Chondrodonta* accumulations occur in inner platform limestones of the lower Aptian Apulia Carbonate Platform (ACP) straddling OAE1a, and of the upper Cenomanian Adriatic Carbonate Platform (AdCP) straddling OAE2. The stratigraphic framework around the *Chondrodonta* beds was built using biostratigraphic and chemostratigraphic ($\delta^{13}C$, $\delta^{18}O$, $^{87}Sr/^{86}Sr$) data. Sedimentologic-lithostratigraphic and petrographic analyses were coupled with the concentration of major, trace elements and REE measured through the Laser Ablation analysis, to infer palaeoenvironmental changes associated with its proliferation.

- The lower Aptian *Chondrodonta* of the ACP appears within requieniid limestones and reaches a brief phase of maximum proliferation in monospecific biostromes (*i.e.*, *Chondrodonta* bedsets), right below the negative $\delta^{13}C$ excursion marking the onset of OAE1a (*see* Chap. 3). Increasing nutrient load coupled with low-energy, restricted seawaters with fluctuating oxygenation, allowed *Chondrodonta* to proliferate and to outpace the less tolerant rudists. Further increase of inhospitable conditions leading to OAE1a inhibited the proliferation of these oyster-like bivalves, allowing fully mesotrophic taxa like *Bacinella-Lithocodium* and orbitolinids to dominate the benthic community.
- The upper Cenomanian *Chondrodonta* of the AdCP appears within radiolitid limestones and reaches a phase of maximum proliferation and predominance over rudists (*i.e., Chondrodonta*-rich interval) below the onset of OAE2 (*see* Chap. 4). Increasing nutrient load, intermittent terrigenous inputs, fluctuating oxygenation and circulation, represented environmental stressors that allowed *Chondrodonta* to become the dominant macro-benthos and to outpace rudists at the prelude of the anoxic event.

- In literature, most of the worldwide lower Aptian *Chondrodonta* accumulations predate the strong environmental stress that affected the shallow-water carbonate deposition during OAE1a (*see* Chap. 5). Similarly, a synchronous late Cenomanian proliferation of *Chondrodonta* is documented, at least within carbonate platforms of the Central Tethys, below the onset of OAE2.

Combining all these observations and results, mostly based on the chemostratigraphic position of the studied accumulations, it is conceivable that the proliferation of *Chondrodonta* took place in a scenario of increasing environmental deterioration leading to OAE1a and OAE2. The flourishing of this oyster-like bivalve, mostly triggered by nutrient pulses on the platforms top and coeval to increasing fertility in the nearby basins, occurred during an environmental "window" that preludes the early Aptian and the late Cenomanian OAEs.

Chondrodonta benefitted from this environmental instability and occupied a short-lived ecological niche during the shift from oligo- to mesotrophic conditions in shallow-water carbonate areas. The opportunistic behavior of this bivalve was rather efficient in the transitional context between more stable, stenotopic and eurytopic benthic communities. This ecological niche is particularly demonstrated by the widespread lower Aptian *Chondrodonta* beds, which are placed in a transient phase between oligo- and fully mesotrophic assemblages.

Although high nutrient levels mainly triggered the *Chondrodonta* proliferation, the occurrence (or the lack) and the duration of its environmental "window" were also controlled by local limiting environmental factors related to palaeogeography and hydrodynamics as well as by – at least local – quick fluctuations in other seawater parameters. Indeed, as resulted from lithostratigraphic and geochemical analyses on the *Chondrodonta* accumulations of both the ACP and the AdCP, the interval of proliferation occurred in low-energy and restricted seawaters with fluctuating oxygenation and intermittent terrigenous inputs. All these environmental fluctuations represented a hostile threshold for the settlement of the less tolerant rudists, while they promoted the thriving of *Chondrodonta*, which bloomed in monospecific (or quasi-) benthic communities close to the onset of OAEs.

However, the exacerbation of the environmental fluctuations and the extreme deterioration of the shallow-water carbonate system during the anoxic events exceeded the upper threshold for *Chondrodonta*, causing its disappearance and the proliferation of fully mesotrophic taxa, as demonstrated at least by the early Aptian *Chondrodonta* beds.

In conclusion, the proliferation of the opportunistic, r-strategist *Chondrodonta* can be used as stratigraphic marker for an early phase of environmental stress preluding the onset of anoxic events in shallow-water carbonate platforms. The *Chondrodonta*-dominated communities represent a short-living biotic event occurring in the Cretaceous shallow-water carbonate systems as a response to the environmental deterioration before the onset of Oceanic Anoxic Events 1a and 2.

As practice shows in these cases, further analyses would enable to extend this conclusion to other Cretaceous *Chondrodonta* accumulations preluding other major and minor OAEs.

References

Abdullah, S., Chmyriov, V.M. and **Dronov V.I.** (1980) Geology and mineral resources of Afghanistan. *Brit. Geol. Surv. Occas. Publ.*, 1–488.

Adams, E.W., Morsilli, M., Schlager, W., Keim, L. and **van Hoek, T.** (2002) Quantifying the geometry and sediment fabric of linear slopes: examples from the Tertiary of Italy (Southern Alps and Gargano Promontory). *Sed. Geol.*, **154**, 11–30.

Adams, D.D., Hurtgen, M.T. and **Sageman B.B.** (2010) Volcanic triggering of a biogeochemical cascade during Oceanic Anoxic Event 2, *Nat. Geosci.*, **3**, 201–204.

Adams, E.W., Grélaud, C., Pal, M., Csoma, A.É., Al Ja'aidi, O.S. and **Al Hinai, R.** (2011) Improving reservoir models of Cretaceous carbonates with digital outcrop modelling (Jabal Madmar, Oman): static modelling and simulating clinoforms. *Pet. Geosci.*, **17**, 309–332.

Al-Dabbas, M., Al-Jassim, J. and **Al-Jumaily, S.** (2010) Depositional environments and porosity distribution in regressive limestone reservoirs of the Mishrif formation, Southern Iraq. *Arab. J. Geosci.*, **3**, 67–78.

Algeo, T.J. (2004) Can marine anoxic events draw down the trace element inventory of seawater? *Geology*, **32**, 1057– 1060.

Algeo, T.J. and **Maynard, J.B.** (2004) Trace-element behavior and redox facies in core shales of Upper Pennsylvanian Kansas-type cyclothems. *Chem. Geol.*, **206**, 289–318.

Allan, J.R. and **Matthews, R.K.** (1982) Isotope signatures associated with early meteoric diagenesis. *Sedimentology*, **29**, 797–817.

Amodio, S. and **Weissert, H.J.** (2017) Paleoenvironment and palaeoecology before and at the onset of Oceanic Anoxic Event (OAE)1a: Reconstructions from Central Tethyan archives. *Palaeogeogr. Palaeoclimatol. Palaeoecol.*, **479**, 71–89.

Amodio, S., Ferreri, V., D'Argenio, B., Weissert, H. and **Sprovieri, M.** (2008) Carbon-isotope stratigraphy and cyclostratigraphy of shallow-marine carbonates: the case of San Lorenzello, Lower Cretaceous of southern Italy. *Cretaceous Res.*, **29**, 803–813.

Ayoub-Hannaa, W. and **Fürsich, F.T.** (2011) Functional morphology and taphonomy of Cenomanian (Cretaceous) oysters from the eastern Sinai Peninsula, Egypt. *Palaeobiodiv. Palaeoenviron.*, **91**, 197–214.

Ayoub-Hannaa, W. and **Fursich, F.T.** (2012) Palaeoecology and environmental significance of benthic associations from the Cenomanian-Turonian of eastern Sinai, Egypt. *Beringeria*, **43**, 93–138.

Ayoub-Hannaa, W., Fürsich, F.T. and **El Qot, G.M.** (2014) Cenomanian-Turonian bivalves from eastern Sinai, Egypt. *Palaeont. Abt.*, **301**, 63–168.

Azmy, K., Brand, U., Sylvester, P., Gleeson, S.A., Logan, A. and **Bitner, M.A.** (2011) Biogenic and abiogenic low-Mg calcite (bLMC and aLMC): evaluation of seawater REE composition, water masses and carbonate diagenesis. *Chem. Geol.*, **280**, 180–190.

Azzaroli, A., Radina, B., Ricchetti, G. and **Valduga, A.** (1968) Note illustrative della Carta Geologica d'Italia, Foglio 189 "Altamura". *Serv. Geol. Ital.*, 22 pp.

Baker, S.J., Belcher, C.M., Barclay, R.S., Hesselbo, S.P., Laurin, J. and **Sageman, B.B.** (2020) CO_2-induced climate forcing on the fire record during the initiation of Cretaceous oceanic anoxic event 2. *Geol. Soc. Am. Bull.*, **132**, 321–333.

Barbieri, F., Cabdulqaadir, M.M., Di Geronimo, I., Faaduma, C.C., Giulini, P., Maxamuud, M.C.C., Michelini, G. and **Piccoli, G.** (1979) Il Cretaceo della regione di Hiraan in Somalia (valle dello Webi Shabelle) con appendice sulla foresta fossile di Sheekh Guure. *Sci. Geol. Mem.*, **32**, 155–182.

Bassi, D., Posenato, R., Nebelsick, J.H., Owada, M., Domenicali, E. and **Iryu, Y.** (2017) Bivalve borings in Lower Jurassic Lithiotis fauna from northeastern Italy and its palaeoecological interpretation. *Hist. Biol.*, **29**, 937–946.

Bau, M. (1991) Rare-earth element mobility during hydrothermal and metamorphic fluid–rock interaction and the significance of the oxidation state of europium. *Chem. Geol.*, **93**, 219–230.

Bau, M. (1996) Controls on fractionation of isovalent trace elements in magmatic and aqueous systems: evidence from Y/Ho, Zr/Hf, and lanthanide tetrad effect. *Contrib. Mineral. Petrol.*, **123**, 323–333.

Bau, M. and **Dulski, P.** (1996) Distribution of yttrium and rare-earth elements in the Penge and Kuruman iron-formations, Transvaal supergroup, South Africa. *Precambrian Res.*, **79**, 37–55.

Bega, Z. (2015) Hydrocarbon exploration potential of Montenegro – a brief review. *J. Petrol. Geol.*, **38**, 317–330.

Bein, A. (1976) Rudistid fringing reefs of Cretaceous shallow carbonate platform of Israel. *AAPG Bull.*, **60**, 258–272.

Benitez-Nelson, C.R. (2000) The biogeochemical cycling of phosphorus in marine systems. *Earth-Sci. Rev.*, **51**, 109–135.

Bernoulli, D. (2001) Mesozoic-Tertiary carbonate platforms, slopes and basins of the external Apennines and Sicily. In: *Anatomy of an Orogen: the Apennines and Adjacent Mediterranean Basins* (Eds G. B. Vai and I. P. Martini), 307–326.

Berthou, P.Y., **Ferreira Soares, A.** and **Lauverjat, J.** (1979) Mid Cretaceous Events. In: *Cuadernos Geologia Ibérica, Iberian Field Conference 77, Guide I Partie - Portugal*, **5**, 31–124.

Bertotti, G., Casolari, E. and **Picotti, V.** (1999) The Gargano Promontory: a Neogene contractional belt within the Adriatic plate. *Terra Nova*, **11**, 168–173.

Bice, K.L., Birgel, D., Meyers, P.A., Dahl, K.A., Hinrichs, K-U. and **Norris, R.D.** (2006) A multiple proxy and model study of Cretaceous upper ocean temperatures and atmospheric CO_2 concentrations. *Paleoceanography*, **21**, PA2002.

Bieler, R., Carter, J.G. and **Coan, E.V.** (2010) Classification of bivalve families. In: *Nomenclator of bivalve families* (Eds P. Bouchet and J. P. Rocroi). *Malacologia*, **52**, 1–184.

Billi, A., Gambini, R., Nicolai, C. and **Storti, F.** (2007) Neogene-Quaternary intraforeland transpression along a Mesozoic platform-basin margin: the Gargano fault system, Adria, Italy. *Geosphere*, **3**, 1–15.

Bodin, S., Godet, A., Matera, V., Steinmann, P., Vermeulen, J., Gardin, S., Adatte, T., Coccioni, R., and **Föllmi, K.B.** (2007) Enrichment of redox-sensitive trace metals (U, V, Mo, As) associated with the late Hauterivian Faraoni Oceanic Anoxic Event. *Int. J. Earth-Sci.*, **96**, 327–341.

Bodin, S., Godet, A., Westermann, S. and **Föllmi, K.B.** (2013) Secular change in northwestern Tethyan water-mass oxygenation during the late Hauterivian – early Aptian. *Earth Planet. Sci. Lett.*, **374**, 121–131.

Boix, C., Frijia, G., Vicedo, V., Bernaus, J.M., Di Lucia, M., Parente, M. and **Caus, E.** (2011) Larger foraminifera distribution and strontium isotope stratigraphy of the La Cova limestones (Coniacian–Santonian, "Serra del Montsec", Pyrenees, NE Spain). *Cretaceous Res.*, **32**, 806–822.

Bonin, A., Pucéat, E., Vennin, E., Mattioli, E., Aurell, M., Joachimski, M., Barbarin, N. and **Laffont, R.** (2016) Cool episode and platform demise in the Early Aptian: new insights on the links between climate and carbonate production. *Paleoceanography*, **31**, 66–80.

Borgomano, J.R.F. (2000) The Upper Cretaceous carbonates of the Gargano-Murge region, southern Italy: a model of platform-to-basin transition. *AAPG Bull.,* **84**, 1561–1588.

Bosellini, A. (2002) Dinosaurs "re-write" the geodynamics of the eastern Mediterranean and the paleogeography of the Apulia Platform. *Earth-Sci. Rev.*, **59**, 211–234.

Bosellini, A. (2004) The western passive margin of Adria and its carbonate platforms. In: *Geology of Italy.* Florence, 32nd Italian Geological Congress Spec. Vol., 79–92.

Bosellini, A. and **Morsilli, M.** (2001) Il Promontorio del Gargano: cenni di geologia e itinerari geologici. *Quaderni del Parco Nazionale del Gargano* (Ed. C. Grenzi), 48 pp.

Bosellini, A., Neri, C. and **Luciani, V.** (1993) Guida ai carbonati Cretaceo-Eocenici di scarpata e bacino del Gargano (Italia meridionale). *Ann. Univ. Ferrara*, **4**, 77 pp.

Bosellini, A., **Morsilli, M.** and **Neri, C.** (1999a) Long-term event stratigraphy of the Apulia Platform margin (Upper Jurassic to Eocene, Gargano, southern Italy). *J. Sed. Res.*, **69**, 1241–1252.

Bosellini, A., Russo, A. and **Schröeder, R.** (1999b) Stratigraphic evidence for an Early Aptian sea-level fluctuation: the Graua Limestone of south-eastern Ethiopia. *Cretaceous Res.*, **20**, 783–791.

Bottini, C. and **Erba, E.** (2018) Mid-Cretaceous paleoenvironmental changes in the western Tethys. *Clim. Past*, **14**, 1147–1163.

Bottini, C., Erba, E., Tiraboschi, D., Jenkyns, H.C., Schouten, S. and **Sinninghe Damsté, J.S.** (2015) Climate variability and ocean fertility during the Aptian Stage. *Clim. Past*, **11**, 383–402.

BouDagher-Fadel M.K. and **Price G.D.** (2019) Global evolution and palaeogeographic distribution of mid-Cretaceous orbitolinids. *UCL Open Environment,* **1**, 1–21.

Bover-Arnal, T., **Salas, R.**, **Moreno-Bedmar, J.A.** and **Bitzer, K.** (2009) Sequence stratigraphy and architecture of a late Early–Middle Aptian carbonate platform succession from the western Maestrat Basin (Iberian Chain, Spain). *Sed. Geol.*, **219**, 280–301.

Bover-Arnal, T., Moreno-Bedmar, J.A., Salas, R., Skelton, P.W., Bitzer, K. and **Gili, E.** (2010) Sedimentary evolution of an Aptian syn-rift carbonate system (Maestrat Basin, E Spain): effects of accommodation and environmental change. *Geol. Acta*, **8**, 249–280.

Bover-Arnal, T., Salas, R., Martín-Closas, C., Schlagintweit, F. and **Moreno-Bedmar, J.A.** (2011) Expression of an oceanic anoxic event in a neritic setting: lower Aptian coral rubble deposits from the western Maestrat Basin (Iberian Chain, Spain). *Palaios*, **26**, 18–32.

Bover-Arnal, T., Löser, H., Moreno-Bedmar, J.A., Salas, R. and **Strasser, A.** (2012) Corals on the slope (Aptian, Maestrat Basin, Spain). *Cretaceous Res.*, **37**, 43–64.

Bralower, T.J., Cobabe, E., Clement, W., Sliter, W.V., Osburn, C.L. and **Longoria, J.** (1999) The record of global change in mid-Cretaceous (Barremian–Albian) sections from the Sierra Madre, NE Mexico. *J. Foramin. Res.*, **29**, 418–437.

Brand, U. and **Veizer, J.** (1980) Chemical diagenesis of a multicomponent carbonate system-1: trace elements. *J. Sed. Petrol.*, **50**, 1219–1236.

Brankman, C. and **Aydin, A.** (2004) Uplift and contractional deformation along a segmented strike-slip fault system: the Gargano Promontory, southern Italy. *J. Struct. Geol.,* **26**, 807–824.

Brčić, V., Glumac, B., Fuček, L., Grizelj, A., Horvat, M., Posilović, H. and **Mišur, I.** (2017) The Cenomanian–Turonian boundary in the northwestern part of the Adriatic Carbonate Platform (Ćićarija Mtn., Istria, Croatia): characteristics and implications. *Facies*, **63**, 1–20.

Brčić, V., Glumac, B., Brlek, M., Fuček, L. and **Šparika Miko, M.** (2021): Cenomanian – Turonian oceanic anoxic event (OAE2) imprint on the northwestern part of the Adriatic Carbonate Platform and coeval intra-platform basin (Istria and Premuda Island, Croatia). *Cretaceous Res.*, **125**, 104847.

Browning, E.L. and **Watkins, D.K.** (2008) Elevated primary productivity of calcareous nannoplankton associated with ocean anoxic event 1b during the Aptian/Albian transition (Early Cretaceous). *Paleoceanography*, **23**, PA2213.

Brumsack, H.-J. (2006) The trace metal content of recent organic carbon-rich sediments: Implications for Cretaceous black shales formation. *Palaeogeogr. Palaeoclimatol. Palaeoecol.*, **232**, 344–361.

Burchette, T.P. (1993) Mishrif Formation (Cenomanian - Turonian), southern Arabian Gulf: carbonate platform growth along a cratonic basin margin. In: *Cretaceous Carbonate Platforms. AAPG Mem.*, **56**, 185–199.

Burchette, T.P. and **Britton, S.R.** (1985) Carbonate facies analysis in the exploration for hydrocarbons: a case-study from the Cretaceous of the Middle East. *Geol. Soc. London Spec. Publ.*, **18**, 311–338.

Burla, S., Heimhofer, U., Hochuli, P.A., Weissert, H.J. and **Skelton, P.W.** (2008) Changes in sedimentary patterns of coastal and deep-sea successions from the North Atlantic (Portugal) linked to Early Cretaceous environmental change. *Palaeogeogr. Palaeoclimatol. Palaeoecol.*, **257**, 38–57.

Caffau, M., Pugliese, N. and **Pleničar, M.** (1995) The development of the mollusc fauna in the Cenomanian of the stratigraphie sequence of Visogliano (Karst of Trieste, Italy). *Geologija*, **37**, 87–121.

Callapez, P.M. (2008) Palaeogeographic evolution and marine faunas of the mid-Cretaceous Western Portuguese carbonate platform. *Thalassas*, **24**, 29–52.

Calvert, **S.E.** and **Pedersen**, **T.F.** (1996) Sedimentary geochemistry of manganese: implications for the environment of formation of manganiferous black shales. *Econ. Geol.*, **91**, 36–47.

Campbell, C.V. (1967) Lamina, laminaset, bed and bedset. *Sedimentology*, **8**, 7–26.

Carbone, F. and **Sirna, G.** (1981) Upper Cretaceous reef models from Rocca di Cave and adjacent areas in Latium, Central Italy. *SEPM Spec. Publ.*, 427–445.

Carras, N., Conrad, M.A. and **Radoičić, R.** (2006) Salpingoporella, a common genus of Mesozoic Dasycladales (calcareous green algae). *Rev. Paléobiol.,* **25**, 457–517.

Carter, J.G. (1990) Evolutionary significance of shell microstructures in the Palaeotaxodonta, Pteriomorphia and Isofilibranchia (Bivalvia, Mollusca). In: *Skeletal biomineralization: patterns, processes and evolutionary trends* (Ed. J. G. Carter), **1**, 135–301.

Carter, J.G., Altaba, C.R., Anderson, L.C., Araujo, R., Biakov, A.S., Bogan, A.E., Campbell, D.C., Campbell, M., Jin-hua, C., Cope, J.C.W., Delvene, G., Dijkstra, H.H., Zong-jie, F., Gardner, R.N., Gavrilova, V.A., Goncharova, I.A., Harries, P.J., Hartman, J.H., Hautmann, M., Hoeh, W.R., Hylleberg, J., Bao-yu, J., Johnston, P., Kirkendale, L., Kleemann, K., Koppka, J., Kříž, J., Machado, D., Malchus, N., Márquez-Aliaga, A., Masse, J.-P., McRoberts, C.A., Middelfart, P.U., Mitchell, S., Nevesskaja, L.A., Özer, S., Pojeta Jr., J., Polubotko, I.V., Pons, J.M., Popov, S., Sánchez, T., Sartori, A.F., Scott, R.W., Sey, I.I., Signorelli, J.H., Silantiev, V.V., Skelton, P.W., Steuber, T., Waterhouse, J.B., Wingard, G.L. and **Yancey, T.** (2011) A synoptical classification of the Bivalvia (Mollusca). *Paleontol. Contrib.*, **4**, 1–47.

Carter, J.G., Harries, P.J., Malchus, N., Sartori, A.F., Anderson, L.C., Bieler, R., Bogan, A.E., Coan, E.V., Cope, J.C.W., Cragg, S.M., García-March, J.R., Hylleberg, J., Kelley, P., Kleemann, K., Kříž, J., McRoberts, C., Mikkelsen, P.M., Pojeta Jr., J., Tëmkin, I., Yancey, T. and **Zieritz, A.** (2012) Part N, Revised, Volume 1, Chapter 31: Illustrated glossary of the Bivalvia. *Treatise Online*, **48**, 1–209.

Cazzini, F., Zotto, O.D., Fantoni, R., Ghielmi, M., Ronchi, P. and **Scotti, P.** (2015) Oil and gas in the Adriatic foreland, Italy. *J. Pet. Geol.*, **38**, 255–279.

Cestari, R. and **Sartorio, D.** (1995) Rudists and Facies of the Periadriatic Domain. 207 pp.

Checchia Rispoli, G. (1921) Nuove osservazioni geologiche sul Monte Gargano. *Rend. Accad. Linc.*, **28**, 160–166.

Chen, J., Algeo, T.J., Zhao, L., Chen, Z.-Q., Cao, L., Zhang, L. and **Li, Y.** (2015) Diagenetic uptake of rare earth elements by bioapatite, with an example from Lower Triassic conodonts of South China. *Earth-Sci. Rev.*, **149**, 181–202.

Chiocchini, M., Pampaloni, M.L. and **Pichezzi, R.M.** (2012) Microfacies and microfossils of the Mesozoic carbonate successions of Latium and Abruzzi (Central Italy) — Cretaceous. *Car. Geol. Ital. Mem.*, **17**, ISPRA.

Christ, N., Immenhauser, A., Amour, F., Mutti, M., Preston, R., Whitaker, F.F., Peterhänsel, A., Egenhoff, S.O., Dunn, P.A. and **Agar, S.M.** (2012) Triassic Latemar cycle tops - subaerial exposure of platform carbonates under tropical arid climate. *Sed. Geol.*, **265-266**, 1–29.

Claps, M., Parente, M., Neri, C. and **Bosellini, A.** (1996) Facies and cycles of the S. Giovanni Rotondo Limestone (Lower Cretaceous, Gargano Promontory, Southern Italy): the Borgo Celano section. *Ann. Univ. Ferrara*, **7**, 5–35.

Cloetingh, S. and **Haq, B.U.** (2015) Inherited landscapes and sea level change. *Science*, **347**, 1258375.

Coccioni, R. and **Premoli Silva, I.** (2015) Revised Upper Albian–Maastrichtian planktonic foraminiferal biostratigraphy and magneto-stratigraphy of the classical Tethyan Gubbio section (Italy). *Newsl. Stratigr.*, **47**, 47–90.

Coimbra, R., Horikx, M., Huck, S., Heimhofer, U., Immenhauser, A., Rocha, F., Dinis, J. and **Duarte, L.V.** (2017) Statistical evaluation of elemental concentrations in shallow-marine deposits (Cretaceous, Lusitanian Basin). *Mar. Petrol. Geol.*, **86**, 1029–1046.

Colombie, C., Lécuyer, C. and **Strasser, A.** (2011) Carbon- and oxygen isotope records of palaeoenvironmental and carbonate production changes in shallow-marine carbonates (Kimmeridgian, Swiss Jura). *Geol. Mag.*, **148**, 133–153.

Compton, J., Mallinson, D., Glenn, C.R., Filippelli, G., Föllmi, K.B., Shields, G. and **Zanin, Y.** (2000) Variations in the global phosphorus cycle. In: *Marine authigenesis, from global to microbial* (Eds C. R. Glenn, L. Prevot-Lucas and J. Lucas), *SEPM Spec. Publ.*, **66**, 21–33.

Cox, L.R. and **Stenzel, H.B.** (1971) Families doubtfully related to oysters. Family Chondrodontidae Freneix, 1959. In: *Treatise on Invertebrate Paleontology, part N, Bivalvia* (Ed. R. C. Moore), **3**, 1197–1200.

Cramer, B.D. and **Jarvis, I.** (2020) Carbon isotope stratigraphy. In: *The Geologic Time Scale 2020* (Eds F. M. Gradstein, J. G. Ogg, M. D. Schmitz and G. M. Ogg). Elsevier, Amsterdam, 309–343.

Cremonini, G., Elmi, C. and **Selli, R.** (1971) Foglio 156 ‘‘S. Marco in Lamis’’. In: *Note Illustrative della Carta Geologica d’Italia*, *Serv. Geol. Ital.*, Roma, 56 pp.

Császár, G., Mhel, D., Oberhauser, R. and **Lobitzer, H.** (1994) A comparative study of the Urgonian Facies in Vorarlberg (Austria), in Allgäu (Germany) and in the Villány Mountains (Hungary). In: *Jubilaumsschrift 20 J. Geol. Zusammenarbeit* Österr. – *Ungarn (*Eds H. Lobitzer, G. Császár and A. Daurer), Wien, **2**, 145–207.

Cucchi, F. and **Piano, C.** (2014) Brevi note illustrative della carta geologica del carso classico italiano. *GEO-CGT, Cartografia Geologica scala 1:100.000 Regione Autonoma Friuli Venezia-Giulia*, 1–43.

Cucchi F., Pirini Radrizzani C. and **Pugliese N.** (1987) The carbonate stratigraphic sequence of the Karst of Trieste (Italy). *Soc. Geol. Ital. Mem.*, **40**, 35–44.

Damas Mollá, L., Aranburu Artano, A. and **García Garmilla, F.** (2006) Resistencia a la alteración diagenética de conchas de Chondrodonta sp en las calizas rojas del Aptiense–Albiense inferior de Ereño (Bizkaia). *Geogaceta*, **40**, 195–198.

D'Argenio, B., Ferreri, V., Weissert, H.J., Amodio, S., Buonocunto, F.P. and **Wissler, L.** (2004) A multidisciplinary approach to global correlation and geochronology. The Cretaceous shallow-water carbonates of Southern Apennines, Italy. *SEPM Spec. Publ.*, **81**, 103–122.

Davey, S.D. and **Jenkyns, H.C.** (1999) Carbon-isotope stratigraphy of shallow-water limestones and implications for the timing of Late Cretaceous sea-level rise and anoxic events (Cenomanian-Turonian of the peri-Adriatic carbonate platform, Croatia). *Eclogae Geol. Helv.*, **92**, 163–170.

De Alteriis, G. and **Aiello, G.** (1993) Stratigraphy and tectonics offshore of Puglia (Italy, southern Adriatic Sea). *Mar. Geol.*, **113**, 233–253.

De Baar, H.J.W., German, C.R., Elderfield, H. and **Van Gaans, P.** (1988) Rare earth element distributions in anoxic waters of the Cariaco Trench. *Geochim. Cosmochim. Acta*, **52**, 1203–1219.

De Dominicis, A. and **Mazzoldi, G.** (1987) Interpretazione geologico-strutturale del margine orientale della piattaforma Apula. *Soc. Geol. Ital. Mem.*, **38**, 163–176.

Della Porta, G., Webb, G.E. and **McDonald, I.** (2015) REE patterns of microbial carbonate and cements from Sinemurian (Lower Jurassic) siliceous sponge mounds (Djebel Bou Dahar, High Atlas, Morocco). *Chem. Geol.*, **400**, 65–86.

Dhondt, A.V. and **Dieni, I.** (1992) Non-rudistid bivalves from Cretaceous rudist formation. *Geol. Romana*, **28**, 211–218.

Dhondt, A.V. and **Dieni, I.** (1993) Non-rudist bivalves from Late Cretaceous rudist limestones of the NE Italy (Col Dei Schiosi and Lago di S. Croce areas). *Sci. Geol. Mem.*, **45**, 165–241.

Dickson, A.J., Saker-Clark, M., Jenkyns, H.C., Bottini, C., Erba, E., Russo, F., Gorbanenko, O., Naafs, B.D.A., Pancost, R.D., Robinson, S.A., van den Boorn, S.H.J.M. and **Idiz, E.** (2017) A Southern Hemisphere record of global trace-metal drawdown and orbital modulation of organic-matter burial across the Cenomanian–Turonian boundary (Ocean Drilling Program Site 1138, Kerguelen Plateau). *Sedimentology*, **64**, 186–203.

Di Lucia, M., **Trecalli, A.**, **Mutti, M.** and **Parente, M.** (2012) Bio-chemostratigraphy of the Barremian-Aptian shallow-water carbonates of the southern Apennines (Italy): pinpointing the OAE1a in a Tethyan carbonate platform. *Solid Earth*, **3**, 1–28.

Di Palma, V. (1995) Aspetti stratigrafico-sedimentologici dei calcari di piattaforma Cretacico inferiori - Giurassico superiori del Gargano meridionale. *Unpublished Degree Dissertation*, University of Ferrara, Italy, 80 pp.

Di Stefano, P. and **Ruberti, D.** (2000) Cenomanian rudist-dominated shelf-margin limestones from the Panormide carbonate platform (Sicily, Italy): facies analysis and sequence stratigraphy. *Facies*, **42**, 133–160.

Douvillé, H. (1902) Sur le genre Chondrodonta Stanton. *Bull. Soc. Géol. Fr.*, **T2**, 314–318.

Dragičević, I. and **Velić, I.** (2002) The Northeastern margin of the Adriatic Carbonate Platform. *Geol. Croat.*, **55**, 185–232.

Drzewiecki, P.A. and **Simo, J.A.** (2000) Tectonic, eustatic and environmental controls on mid-Cretaceous carbonate platform deposition, south-central Pyrenees, Spain. *Sedimentology*, **47**, 471–495.

Dumitrescu, M., Brassell, S.C., Schouten, S., Hopmans, E.C. and **Sinninghe Damsté, J.S.** (2006) Instability in tropical Pacific sea-surface temperatures during the early Aptian. *Geology*, **34**, 833–836.

Dunham, R.J. (1962) Classification of carbonate rocks according to their depositional texture. In: *Classification of Carbonate Rocks* (Ed. W.E. Ham), *AAPG Mem.*, **1**, 108–121.

Eberli, G.P., Bernoulli, D., Sanders, D. and **Vecsei, A.** (1993) From aggradation to progradation; the Maiella Platform, Abruzzi, Italy. In: *Cretaceous carbonate platforms* (Eds J. A. T. Simo, R. W. Scott and J.-P. Masse), *AAPG Mem.*, **56**, 213–232.

Elderfield, H. (1988) The oceanic chemistry of the rare-earth elements. *Phil. Trans. Roy. Soc. London*, **325**, 105–126.

Elrick, M., Berkyova, S., Klappa, G., Sharp, Z., Joachimski, M. and **Fryda, J.** (2009) Stratigraphic and oxygen isotope evidence for My-scale glaciation driving eustasy in the Early-Middle Devonian greenhouse world. *Paleogeogr. Palaeoclimatol. Paleoecol.*, **276**, 170–181.

Embry, K.O. and **Klovan, J.E.** (1971) A late Devonian reef tract on northeastern Banks Island, Northwestern Territories. *Bull. Can. Petrol. Geol.*, **19**, 730-781.

Engelke, J., Linnert, C., Niebuhr, B., Schnetger, B., Brumsack, H.-J., Mutterlose, J. and **Wilmsen, M.** (2018) Tracking Late Cretaceous environmental change: Geochemical environment of the upper Campanian to lower Maastrichtian chalks at Kronsmoor, northern Germany. *Cretaceous Res.*, **84**, 323–339.

Erba, E. (1994) Nannofossils and superplumes: The Early Aptian “nannoconid crisis”. *Paleoceanography*, **9**, 483–501.

Erba, E. (2004) Calcareous nannofossils and Mesozoic oceanic anoxic events. *Marine Micropaleontology*, **52**, 85–106.

Erba, E. and **Tremolada, F.** (2004) Nannofossil carbonate fluxes during the early Cretaceous: phytoplankton response to nutrification episodes, atmospheric CO_2 and anoxia. *Paleoceanography*, **19**, 1–18.

Erba, E., Channell, J.E.T., Claps, M., Jones, C., Larson, R., Opdyke, B., Premoli Silva, I., Riva, A., Salvini, G. and **Torricelli, S.** (1999) Integrated stratigraphy of the Cismon APTICORE (Southern Alps, Italy): A "Reference section" for the Barremian-Aptian interval at low latitudes. *J. Foramin. Res.*, **29**, 371–391.

Erba, E., Bottini, C., Weissert, H.J. and **Keller, C.E.** (2010) Calcareous Nannoplankton response to surface-water acidification around Oceanic Anoxic Event 1a. *Science*, **329**, 428–432.

Erba, E., Duncan, R.A., Bottini, C., Tiraboschi, D., Weissert, H.J., Jenkyns, H.C. and **Malinverno, A.** (2015) Environmental consequences of Ontong Java Plateau and Kerguelen Plateau volcanism. In: *The Origin, Evolution, and Environmental Impact of Oceanic Large Igneous Provinces* (Eds C. R. Neal, W. W. Sager, T. Sano and E. Erba). *Geol. Soc. Am. Spec. Publ.*, **511**, 271–303.

Erbacher, J., Huber, B.T., Norris, R.D. and **Markey, M.** (2001) Increased thermohaline stratification as a possible cause for an ocean anoxic event in the Cretaceous period. *Nature*, **409**, 325–327.

Fantasia, A., Adatte, T., Spangenberg, J.E. and **Font, E.** (2016) Palaeoenvironmental changes associated with Deccan volcanism, examples from terrestrial deposits from Central India. *Palaeogeogr. Palaeoclimatol. Palaeoecol.*, **441**, 165–180.

Föllmi, K.B. (1996) The phosphorus cycle, phosphogenesis and marine phosphate-rich deposits. *Earth-Sci. Rev.*, **40**, 55–124.

Föllmi, K.B. (2012) Early Cretaceous life, climate and anoxia. *Cretaceous Res.*, **35**, 230–257.

Föllmi, K.B. and **Gainon, F.** (2008) Demise of the northern Tethyan Urgonian carbonate platform and subsequent transition towards pelagic conditions: The sedimentary record of the Col de la Plaine Morte area, central Switzerland. *Sed. Geol.*, **205**, 142–159.

Föllmi, K.B., Weissert, H.J., Bisping, M. and **Funk, H.** (1994) Phosphogenesis, carbon-isotope stratigraphy, and carbonate-platform evolution along the Lower Cretaceous northern Tethyan margin. *Geol. Soc. Am. Bull.*, **106**, 729–746.

Föllmi, K.B., Godet, A., Bodin, S. and **Linder, P.** (2006) Interactions between environmental change and shallow water carbonate buildup along the northern Tethyan margin and their impact on the Early Cretaceous carbon isotope record. *Paleoceanography*, **21**, 1–16.

Frakes, L.A., Francis, J.E. and **Syktus, J.I.** (1992) Climate modes of the Phanerozoic: The history of the Earth's climate over the past 600 million years. *Cambridge University Press, Cambridge, United Kingdom*, 274 pp.

Frank, R., **Buchbinder, B.** and **Benjamini, C.** (2010) The mid-Cretaceous carbonate system of northern Israel: facies evolution, tectono-sedimentary configuration and global control on the central Levant margin of the Arabian Plate. *Geol. Soc. London Spec. Publ.*, **341**, 133–169.

Francis, J.E. and **Frakes, L.A.** (1993) Cretaceous climates. In: *Sedimentology Review* (Ed. V. P. Wright), Blackwell, **1**, 17–30.

Freneix, S. and **Lefèvre, R.** (1967) Deux espèces nouvelles de Chondrodonta et Neithea (Bivalves) du Sénonien du Taurus lycien (Turquie). *Bull. Soc. Géol. Fr.*, **7**, 762–776.

Frijia, G. and **Parente, M.** (2008) Strontium isotope stratigraphy in the upper Cenomanian shallow-water carbonates of the southern Apennines: Short-term perturbations of marine $^{87}Sr/^{86}Sr$ during the oceanic anoxic event 2. *Palaeogeogr. Palaeoclimatol. Palaeoecol.*, **261**, 15–29.

Frijia, G., Parente, M., Di Lucia, M. and **Mutti, M.** (2015) Carbon and strontium isotope stratigraphy of the Upper Cretaceous (Cenomanian-Campanian) shallow-water carbonates of southern Italy: Chronostratigraphic calibration of larger foraminifera biostratigraphy. *Cretaceous Res.*, **53**, 110–139.

Frijia, G., Forkner, R., Minisini, D., Pacton, M., Struck, U. and **Mutti, M.** (2019) Cyanobacteria proliferation in the Cenomanian-Turonian boundary interval of the Apennine carbonate platform: immediate response to the environmental perturbations associated with OAE2? *Geochem. Geophys. Geosyst.*, **20**, 2698–2716.

Frimmel, H.E. (2009) Trace element distribution in Neoproterozoic carbonates as palaeoenvironmental indicator. *Chem. Geol.*, **258**, 338–353.

Gale, A.S. (1995) Cyclostratigraphy and correlation of the Cenomanian stage in Western Europe. In: *Orbital Forcing Timescales and Cyclostratigraphy* (Eds M. R. House and A. S. Gale), *Geol. Soc. London Spec. Publ.*, **85**, 177–97.

Gale, A.S. (1996) Turonian correlation and sequence stratigraphy of the Chalk in southern England. In: Sequence Stratigraphy in British Geology (Eds S. P. Hesselbo and D. N. Parkinson), *Geol. Soc. London Spec. Publ.*, **103**, 177–95.

Gale, A.S., Kennedy, W.J., Voigt, S. and **Walaszczyk, I.** (2005) Stratigraphy of the Upper Cenomanian–Lower Turonian Chalk succession at Eastbourne, Sussex, UK: ammonites, inoceramid bivalves and stable carbon isotopes. *Cretaceous Res.*, **26**, 460–487.

Gambacorta, G., Jenkyns, H.C., Russo, F., Tsikos, H., Wilson, P.A., Faucher, G. and **Erba, E.** (2015) Carbon-and oxygen-isotope records of mid-Cretaceous Tethyan pelagic sequences from the Umbria–Marche and Belluno Basins (Italy). *Newsl. Stratigr.*, **48**, 299–323.

Gibbs, S.J., Robinson, S.A., Bown, P.R., Jones, T.D. and **Henderiks, J.** (2011) Comment on 'Calcareous nannoplankton response to surface-water acidification around oceanic anoxic event 1a'. *Science*, **332**, 175.

Gili, E., Masse, J.-P. and **Skelton, P.W.** (1995) Rudists as gregarious sediment-dwellers, not reef builders, on Cretaceous carbonate platforms. *Palaeogeogr. Palaeoclimatol. Palaeoecol.*, **118**, 245–267.

Giraud, F., Pittet, B., Grosheny, D., Baudin, F., Lécuyer, C. and **Sakamoto, T.** (2018) The palaeoceanographic crisis of the early Aptian (OAE 1a) in the Vocontian Basin (SE France). *Palaeogeogr. Palaeoclimatol. Palaeoecol.*, **511**, 483–505.

Godet, A. (2013) Drowning unconformities: palaeoenvironmental significance and involvement of global processes. *Sed. Geol.*, **293**, 45–66.

Godet, A., Hfaiedh, R., Arnaud-Vanneau, A., Zghal, I., Arnaud, H. and **Ouali, J.** (2014) Aptian palaeoclimate and identification of an OAE1a equivalent in shallow marine environments of the southern Tethyan margin: evidence from southern Tunisia (Bir Oum Ali section, Northern Chott Chain). *Cretaceous Res.*, **48**, 110–129.

Grandić, S., Kratkoviæ, I. and **Baliæ, D.** (2013) Peri-Adriatic platforms proximal talus reservoir potential (part 1). *Nafta*, **64**, 147–160.

Graziano, R. (2013) Sedimentology, biostratigraphy and event stratigraphy of the Early Aptian Oceanic Anoxic Event (OAE1A) in the Apulia Carbonate Platform Margin – Ionian Basin System (Gargano Promontory, southern Italy). *Cretaceous Res.*, **39**, 78–111.

Graziano, R., Raspini, A. and **Spalluto, L.** (2013) High resolution $\delta^{13}C$ stratigraphy through the Selli Oceanic Anoxic Event (OAE1a) in the Apulia carbonate platform: the Borgo Celano section (western Gargano Promontory, Southern Italy). *Ital. J. Geosci.*, **132**, 477–496.

Graziano, R. and **Raspini, A.** (2015) Long- and short-term hydroclimatic variabilities in the Aptian Tethys: Clues from the orbital chronostratigraphy of evaporite-rich beds in the Apennine carbonate platform (Mt. Faito, southern Italy). *Palaeogeogr. Palaeoclimatol. Palaeoecol.*, **418**, 319–343.

Graziano, R. and **Raspini, A.** (2018) High-resolution chronostratigraphy of palaeoecologic and isotopic changes in shallow-marine carbonates: deciphering the completeness of the Aptian record in the Apennine carbonate platform (southern Italy). *Cretaceous Res.*, **86**, 97–128.

Grélaud, C., Razin, P. and **Homewood, P.** (2010) Channelized systems in an inner carbonate platform setting: differentiation between incisions and tidal channels (Natih Formation, Late Cretaceous, Oman). *Geol. Soc. London Spec. Publ.*, **329**, 163–186.

Gromet, L.P., Dymek, R.F., Haskin, L.A. and **Korotev, R.L.** (1984) The "North American shale composite": Its compilation, major and trace element characteristics. *Geochim. Cosmochim. Acta*, **48**, 2469–2482.

Grotzinger, J.P., Fike, D.A. and **Fischer, W.W.** (2011) Enigmatic origin of the largest-known carbon isotope excursion in Earth's history. *Nat. Geosci.*, **4**, 285–291.

Guerzoni, S. (2016) Analisi delle facies di piattaforma interna del Promontorio del Gargano nell'intervallo Barremiano superiore - Aptiano inferiore e confronto con le piattaforme tetidee durante l'Evento Anossico OAE1a. *Ph.D. Thesis*, Università degli Studi di Ferrara, Italy, 294 pp.

Gušić, I. and **Jelaska, V.** (1990) Upper Cretaceous stratigraphy of the Island of Brač within the geodynamic evolution of the Adriatic carbonate platform. *Djela Jugoslavenske akademije znanosti i umjetnosti*, **69**, 160 pp.

Gušic, I. and **Jelaska, V.** (1993) Upper Cenomanian - Lower Turonian sea-level rise and its consequences on the Adriatic-Dinaric carbonate platform. *Geol. Rundsch.*, **82**, 676–686.

Hairabian, A., Borgomano, J., Masse, J.-P. and **Nardon, S.** (2015) 3-D stratigraphic architecture, sedimentary processes and controlling factors of Cretaceous deep-water resedimented carbonates (Gargano Peninsula, SE Italy). *Sed. Geol.*, **317**, 116–136.

Harper, E.M. (2012) Part N, Revised, Volume 1, Chapter 21: Cementing Bivalvia. *Treatise Online*, **45**, 1–12.

Heimhofer, U., Hochuli, P.A., Herrle, J.O., Andersen, N. and **Weissert, H.J.** (2004) Absence of major vegetation and palaeoatmospheric pCO_2 changes associated with oceanic anoxic event 1a (Early Aptian, SE France). *Earth Planet. Sci. Lett.*, **223**, 303–318.

Heimhofer, U., Wucherpfennig, N., Adatte, T., Schouten, S., Schneebeli-Hermann, E., Gardin, S., Keller, G., Kentsch, S. and **Kujau, A.** (2018) Vegetation response to exceptional global warmth during Oceanic Anoxic Event 2. *Nat. Communic.*, **9**, 1–8.

Herrle, J.O., Kössler, P., Friedrich, O., Erlenkeuser, H. and **Hemleben, C.** (2004) High-resolution carbon isotope records of the Aptian to Lower Albian from SE France and the Mazagan Plateau (DSDP Site 545): a stratigraphic tool for paleoceanographic and paleobiologic reconstruction. *Earth Planet. Sci. Lett.*, **218**, 149–161.

Hetzel, A., Böttcher, M.E., Wortmann, U.G. and **Brumsack, H.J.** (2009) Paleo-redox conditions during OAE2 reflected in Demerara Rise sediment geochemistry (ODP Leg 207). *Palaeogeogr. Palaeoclimatol. Palaeoecol.*, **273**, 302–328.

Hochuli, P.A., Menegatti, P., Weissert, H.J., Riva, A., Erba, E. and **Premoli Silva, I.** (1999) Episodes of high productivity and cooling in the early Aptian Alpine Tethys. *Geology*, **27**, 657–660.

Hoernes, R. (1902) Chondrodonta (Ostrea) Joannae Choffat in den Schiosischichten von Görz, Istrien, Dalmatien und der Herzegowina. Sitzungsber. d. kais. Akad. d. Wissensch. *Wien, math.-naturw. Cl.*, **111**, 667–684.

Höfling, R. and **Scott, R.W.** (2002) Early and mid-Cretaceous buildups. *Phanerozoic Reef Patterns, SEPM Spec. Publ.*, **72**, 521–548.

Howarth, R.J. and **McArthur, J.M.** (1997) Statistics for strontium isotope stratigraphy: a robust Lowess fit to the marine Sr-isotope curve for 0 to 206 Ma, with look-up table for derivation of numeric age. *J. Geol.*, **105**, 441–456.

Huber, B.T., Leckie, R.M., Norris, R.D., Bralower, T.J. and **Cobabe, E.** (1999) Foraminiferal assemblage and stable isotopic change across the Cenomanian-Turonian boundary in the subtropical North Atlantic. *J. Foramin. Res.*, **29**, 392–417.

Huck, S. (2011) Understanding the driving factors of the Oceanic Anoxic Event 1a (Early Aptian) - The neritic perspective. *Ph.D. Thesis*, Fakultät für Geowissenschaften der Ruhr-Universität Bochum, 167 pp.

Huck, S. and **Heimhofer, U.** (2015) Improving shallow-water carbonate chemostratigraphy by means of rudist bivalve sclerochemistry. *Geochem. Geophys. Geosyst.*, **16**, 3111–3128.

Huck, S., Rameil, N., Korbar, T., Heimhofer, U., Wieczorek, T.D. and **Immenhauser, A.** (2010) Latitudinally different responses of Tethyan shoal-water carbonate systems to the Early Aptian oceanic anoxic event (OAE 1a). *Sedimentology*, **57**, 1585–1614.

Huck, S., Heimhofer, U., Rameil, N., Bodin, S. and **Immenhauser, A.** (2011) Strontium and carbon-isotope chronostratigraphy of Barremian–Aptian shoal-water carbonates: northern Tethyan platform drowning predates OAE1a. *Earth Planet. Sci. Lett.*, **304**, 547–558.

Huck, S., Heimhofer, U. and **Immenhauser, A.** (2012) Early Aptian algal bloom in a neritic proto-North Atlantic setting: harbinger of global change related to OAE1a? *Geol. Soc. Am. Bull.*, **124**, 1810–1825.

Huck, S., Heimhofer, U., Immenhauser, A. and **Weissert, H.J.** (2013) Carbon-isotope stratigraphy of Early Cretaceous (Urgonian) shoal-water deposits: diachronous changes in carbonate-platform production in the north-western Tethys. *Sed. Geol.*, **290**, 157–174.

Huck, S., Stein, M., Immenhauser, A., Skelton, P.W., Christ, N., Föllmi, K.B. and **Heimhofer, U.** (2014) Response of proto-North Atlantic carbonate-platform ecosystems to OAE1a-related stressors. *Sed. Geol.*, **313**, 15–31.

Huck, S., Wohlwend, S., Coimbra, R., Christ, N. and **Weissert, H.J.** (2017) Disentangling shallow-water bulk carbonate carbon isotope archives with evidence for multi-stage diagenesis: an in-depth component-specific petrographic and geochemical study from Oman (mid-Cretaceous). *The Depositional Record*, **3**, 233–257.

Hueter, A., Huck, S., Bodin, S., Heimhofer, U., Weyer, S., Jochum, K.P. and **Immenhauser, A.** (2019) Central Tethyan platform-top hypoxia during Oceanic Anoxic Event 1a. *Clim. Past Discuss.*, **15**, 1327–1344.

Hueter, A., Huck, S., Heimhofer, U., Bodin, S., Weyer, S., Jochum, K.P., Roebbert, Y. and **Immenhauser, A.** (2020) Evaluating the role of coastal hypoxia on the transient expansion of microencruster intervals during the early Aptian. *Lethaia*, 10.1111/let.12411.

Husinec, A. and **Jelaska, V.** (2006) Relative sea-level changes recorded on an isolated carbonate platform: Tithonian to Cenomanian succession, southern Croatia. *J. Sed. Res.*, **76**, 1120–1136.

Husinec, A. and **Sokač, B.** (2006) Early Cretaceous benthic associations (foraminifera and calcareous algae) of a shallow tropical-water platform environment (Mljet Island, southern Croatia). *Cretaceous Res.*, **27**, 418–441.

Husinec, A. and **Read, J.F.** (2011) Microbial laminite versus rooted and burrowed caps on peritidal cycles: salinity control on parasequence development, Early Cretaceous isolated carbonate platform, Croatia. *Geol. Soc. Am. Bull.*, **123**, 1896–1907.

Husinec, A. and **Read, J.F.** (2018) Cyclostratigraphic and $\delta^{13}C$ record of the Lower Cretaceous Adriatic Platform, Croatia: assessment of Milankovitch-forcing. *Sed. Geol.*, **373**, 11–31.

Husinec, A., Velić, I., Fucek, L., Vlahović, I., Matičec, D., Ostric, N. and **Korbar, T.** (2000) Mid Cretaceous orbitolinid (Foraminiferida) record from the islands of Cres and Losinj (Croatia) and its regional stratigraphic correlation. *Cretaceous Res.*, **21**, 155–171.

Husinec, A., Harman, C.A., Regan, S.P., Mosher, D.A., Sweeney, R.J. and **Read, J.F.** (2012) Sequence development influenced by intermittent cooling events in the Cretaceous Aptian greenhouse, Adriatic platform, Croatia. *AAPG Bull.*, **96**, 2215–2244.

Immenhauser, A., Della Porta, G., Kenter, J.A.M. and **Bahamonde, J.R.** (2003) An alternative model for positive shifts in shallow-marine carbonate $\delta^{13}C$ and $\delta^{18}O$. *Sedimentology*, **50**, 953–959.

Immenhauser, A., Hillgärtner, H., Sattler, U., Bertotti, G., Schoepfer, P., Homewood, P., Vahrenkamp, V., Steuber, T., Masse, J.-P., Droste, H., Taal-van Koppen, J., van der

Kooij, B., van Bentum, E. Van Verwer, K., Strating, E.H., Swinkels, W., Peters, J., Immenhauser-Potthast, I. and **Al Maskery, S.A.J.** (2004) Barremian-lower Aptian Qishn Formation, Haushi-Huqf area, Oman: a new outcrop analogue for the Kharaib/Shu'aiba reservoirs. *GeoArabia*, **9**, 1–42.

Immenhauser, A., Hillgärtner, H. and **Van Bentum, E.** (2005) Microbial-foraminiferal episodes in the Early Aptian of the southern Tethyan margin: ecological significance and possible relation to oceanic anoxic event 1a. *Sedimentology*, **52**, 77–99.

Immenhauser, A., Holmden, C. and **Patterson, W.P.** (2008) Interpreting the carbon-isotope record of ancient shallow epeiric seas: Lessons from the recent. In: *Dynamics of Epeiric Seas* (Eds C. Holmden and B. W. Pratt), *Geol. Assoc. Can. Spec. Publ.*, **48**, 137–174.

Insalaco, E. (1998) The descriptive nomenclature and classification of growth fabrics in fossil scleractinian reefs. *Sed. Geol.*, **118**, 159–186.

Jarvis, I., Gale, A.S., Jenkyns, H.C. and **Pearce, M.A.** (2006) Secular variation in Late Cretaceous carbon isotopes: a new $\delta^{13}C$ carbonate reference curve for the Cenomanian – Campanian (99.6 – 70.6 Ma). *Geol. Mag.*, **143**, 561–608.

Jarvis, I., Lignum, J.S., Gröcke, D.R., Jenkyns, H.C. and **Pearce, M.A.** (2011) Black shale deposition, atmospheric CO_2 drawdown, and cooling during the Cenomanian - Turonian Oceanic Anoxic Event. *Paleoceanography*, **26**, 1–17.

Jenkyns, H.C. (1991) Impact of Cretaceous sea-level rise and anoxic events on the Mesozoic carbonate platform of Yugoslavia. *AAPG Bull.*, **75**, 1007–1017.

Jenkyns, H.C. (1999) Mesozoic Anoxic Events and palaeoclimate. *Zentralblatt für Geologie und Paläontologie, Teil I*, **7**, 943–949.

Jenkyns, H.C. (2003) Evidence for rapid climate change in the Mesozoic-Palaeogene greenhouse world. *Phil. Trans. Roy. Soc. London*, **361**, 1885–1916.

Jenkyns, H.C. (2010) Geochemistry of oceanic anoxic events. *Geochem. Geophys., Geosyst.*, **11**, 1–30.

Jenkyns, H.C. (2018) Transient cooling episodes during Cretaceous Oceanic Anoxic Events with special reference to OAE 1a (Early Aptian). *Phil. Trans. Roy. Soc. London*, **376**, 1–26.

Jenkyns, H.C., Forster, A., Schouten, S. and **Sinninghe Damsté, J.S.** (2004) High temperatures in the Late Cretaceous Arctic Ocean. *Nature*, **432**, 888–892.

Jenkyns, H.C., Dickson, A.J., Ruhl, M. and **van den Boorn, S.H.J.M.** (2017) Basalt-seawater interaction, the Plenus Cold Event, enhanced weathering and geochemical change:

deconstructing Oceanic Anoxic Event 2 (Cenomanian–Turonian, Late Cretaceous). *Sedimentology*, **64**, 16–43.

Jochum, K.P., Stoll, B., Herwig, K. and **Willbold, M. (**2007) Validation of LA-ICP-MS trace element analysis of geological glasses using a new solid-state 193 nm Nd:YAG laser and matrix-matched calibration. *J. Anal. At. Spectrom.,* **22**, 112-121.

Junium, C.K. and **Arthur, M.A.** (2007) Nitrogen cycling during the Cretaceous, Cenomanian-Turonian oceanic anoxic event II. *Geochem. Geophys. Geosyst.*, **8**, Q03002.

Jurkovšek, B., Tolman, M., Ogorelec, B., Šribar, L., Drobne, K., Poljak, M. and **Šribar, L.** (1996) Geological map of the southern part of Trieste - Komen plateau, Cretaceous and Paleogene carbonate rocks. *Inštitut za geologijo, geotehniko in geofiziko*, Ljubljana, 143 pp.

Kerr, A.C., Tarney, J., Kempton, P.D., Pringle, M. and **Nivia, A.** (2004) Mafic pegmatites intruding oceanic plateau gabbros and ultramafic cumulates from Bolivar, Colombia: Evidence for a ‘‘wet’’ mantle plume? *J. Petrol.*, **45**, 1877–1906.

Kim, J., Torres, M.E., Haley, B.A., Kastner, M., Pohlman, J.W., Riedel, M. and **Lee, Y.** (2012) The effect of diagenesis and fluid migration on rare earth element distribution in pore fluids of the northern Cascadia accretionary margin. *Chem. Geol.*, **291**, 152–165.

Korbar, T. (2009) Orogenic evolution of the external Dinarides in the NE Adriatic region: a model constrained by tectonostratigraphy of Upper Cretaceous to Paleogene carbonates. *Earth-Sci. Rev.*, **96**, 296–312.

Korbar, T., Glumac, B., Tesovic, B.C. and **Cadieux, S.B.** (2012) Response of a carbonate platform to the Cenomanian-Turonian drowning and OAE 2: a case study from the Adriatic Platform (Dalmatia, Croatia). *J. Sed. Res.*, **82**, 163–176.

Ku, T.L., Knauss, K.G. and **Mathieu, G.G.** (1977) Uranium in open ocean: concentration and isotopic composition. *Deep-Sea Res.*, **24**, 1005–1017.

Kuroda, J., Ogawa, N.O., Tanimizu, M., Coffin, M.F., Tokuyama, H., Kitazato, H. and **Ohkouchi, N.** (2007) Contemporaneous massive subaerial volcanism and Late Cretaceous oceanic anoxic event 2. *Earth Planet. Sci. Lett.*, **256**, 211–223.

Kuypers, M.M.M., Pancost, R.D., Nijenhuis, I.A. and **Sinninghe Damsté, J.S.** (2002) Enhanced productivity led to increased organic carbon burial in the euxinic North Atlantic basin during the late Cenomanian oceanic anoxic event. *Paleoceanography*, **17-4**, 1–13.

Larson, R.L. (1991) Latest pulse of Earth: Evidence for a mid-Cretaceous superplume. *Geology*, **19**, 547–550.

Larson, R.L. and **Erba, E.** (1999) Onset of the mid-Cretaceous greenhouse in the Barremian- Aptian: Igneous events and the biological, sedimentary, and geochemical responses. *Paleoceanography*, **14**, 663–678.

Laurin, J., Barclay, R.S., Sageman, B.B., Dawson, R.R., Pagani, M., Schmitz, M., Eaton, J., McInerney, F.A. and **McElwain, J.C.** (2019) Terrestrial and marginal-marine record of the mid-cretaceous Oceanic Anoxic Event 2 (OAE 2): High-resolution framework, carbon isotopes, CO_2 and sea-level change. *Palaeogeogr. Palaeoclimatol. Palaeoecol.*, **524**, 118–136.

Leckie, R.M., Yuretich, R.F., West, O.L.O., Finkelstein, D. and **Schmidt M.** (1998) Paleoceanography of the southwestern Western Interior Sea during the time of the Cenomanian-Turonian boundary, Late Cretaceous. In: *Stratigraphy and Paleoenvironments of the Cretaceous Western Interior Seaway, USA* (Eds W. E. Dean and M. A. Arthur), *SEPM Concepts Sedimentol. Paleontol.*, **6**, 101–126.

Leckie, R.M., Bralower, T.J. and **Cashman, R.** (2002) Oceanic Anoxic Events and plankton evolution: biotic response to tectonic forcing during the mid-Cretaceous. *Paleoceanography*, **17-3**, 1–29.

Le Goff, J. (2016) Evolution tectono-sédimentaire du système carbonaté ”Plateforme Apulienne - Bassin Ionien” au Crétacé supérieur dans le sud de l’Albanie: faciès, géométries, diagénèse et propriétés réservoirs associées. *Ph.D. Thesis*, Sciences de la Terre, Université Michel de Montaigne – Bordeaux.

Leonide, P., Borgomano, J., Masse, J.-P. and **Doublet, S.** (2012) Relation between stratigraphic architecture and multi-scale heterogeneities in carbonate platforms: the Barremian–lower Aptian of the Monts de Vaucluse, SE France. *Sed. Geol.*, **265**, 87–109.

Li, D., Shields-Zhou, G.A., Ling, H.F. and **Thirlwall, M.** (2011) Dissolution methods for strontium isotope stratigraphy: Guidelines for the use of bulk carbonate and phosphorite rocks. *Chem. Geol.*, **290**, 133–144.

Li, F., Webb, G.E., Algeo, T.J., Kershaw, S., Lu, C., Oehlert, A.M., Gong, Q., Pourmand, A. and **Tan, X.** (2019) Modern carbonate ooids preserve ambient aqueous REE signature. *Chem. Geol.*, **509**, 163–177.

Ling, H., Chen, X., Li, D., Wang, D., Shields-Zhou, G.A. and **Zhu, M.** (2013) Cerium anomaly variations in Ediacaran - earliest Cambrian carbonates from the Yangtze Gorges area, South China: Implications for oxygenation of coeval shallow seawater. *Precambrian Res.*, **225**, 110–127.

Liu, J., Song, J., Yuan, H., Li, X., Li, N. and **Duan, L.** (2019) Rare earth element and yttrium geochemistry in sinking particles and sediments of the Jiaozhou Bay, North China: Potential proxy assessment for sediment resuspension. *Mar. Pollut. Bull.*, **144**, 79–91.

Lohmann, K.C. (1988) Geochemical patterns of meteoric diagenetic systems and their application to studies of paleokarst. In: *Paleokarst* (Eds N. P. James and P. W. Choquette), Springer Verlag, New York, 58–80.

Lokier, S.W. and **Al Junaibi, M.** (2016) The petrographic description of carbonate facies: are we all speaking the same language? *Sedimentology*, **63**, 1843–1885.

Luciani, V., Cobianchi, M. and **Jenkyns, H.C.** (2001) Biotic and geochemical response to anoxic events: the Aptian pelagic succession of the Gargano Promontory (southern Italy). *Geol. Mag.*, **138**, 277–298.

Luciani, V., Cobianchi, M. and **Lupi, C.** (2006) Regional record of a global oceanic anoxic event: OAE1a on the Apulia Platform margin, Gargano Promontory, southern Italy. *Cretaceous Res.*, **27**, 754–772.

Lugli, F., Cipriani, A., Peretto, C., Mazzucchelli, M. and **Brunelli, D.** (2017) In situ high spatial resolution $^{87}Sr/^{86}Sr$ ratio determination of two Middle Pleistocene (c.a. 580 ka) *Stephanorhinus hundsheimensis* teeth by LA–MC–ICP–MS. *Int. J. Mass Spectrom.*, **412**, 38–48.

Luperto Sinni, E. and **Masse, J.-P.** (1986) Données nouvelles sur la stratigraphie del calcaires de plate-forme du Crétacé inférieur du Gargano (Italie méridionale). *Riv. Ital. Paleontol. Stratigr.*, **92**, 33–66.

Malchus, N., Pons, J.M. and **Salas, R.** (1995) Rudist distribution in the Lower Aptian shallow platform of La Mola de Xert, eastern Iberian Range, NE Spain. *Rev. Mex. Ci. Geol.*, **12**, 224–235.

Malinverno, A., Erba, E. and **Herbert, T.D.** (2010) Orbital tuning as an inverse problem: Chronology of the early Aptian oceanic anoxic event 1a (Selli Level) in the Cismon APTICORE. *Paleoceanography*, **25**, 1–16.

Marshall, J.D. (1992) Climatic and oceanographic isotopic signals from the carbonate rock record and their preservation. *Geol. Mag.*, **129**, 143–160.

Martinis, B. and **Pieri, P.** (1964) Alcune notizie sulla formazione evaporitica del Triassico superiore nell'Italia centrale e meridionale. *Soc. Geol. Ital. Mem.*, **4**, 649–678.

Martinis, B. and **Pavan, G.** (1967) Foglio 157 Monte S. Angelo. In: *Note Illustrative della Carta Geologica d'Italia, Scala 1:100.000*, Roma, *Serv. Geol. Ital.*, 55 pp.

Márton, E., Ćosović, V., Moro, A. and **Zvocak, S.** (2008) The motion of Adria during the Late Jurassic and Cretaceous: new paleomagnetic results from stable Istria. *Tectonophysics*, **454**, 44–53.

Márton, E., Ćosović, V. and **Moro, A** (2014) New stepping stones, Dugi otok and Vis islands, in the systematic paleomagnetic study of the Adriatic region and their significance in evaluations of existing tectonic models. *Tectonophysics*, **611**, 141–154.

Masse, J.-P. (1992) The Lower Cretaceous Mesogean benthic ecosystems: palaeoecologic aspects and palaeo-biogeographic implications. *Palaeogeogr. Palaeoclimatol. Palaeoecol.*, **91**, 331–345.

Masse, J.-P. (1993) Valanginian-Early Aptian carbonate platforms from Provence (SE France). In: *Cretaceous Carbonate Platforms* (Eds A. Simo, R. W. Scott and J.-P. Masse), *AAPG Mem.*, **5**, 363–374.

Masse J.-P. and **Luperto Sinni E.** (1989) A platform to basin transitional model: the lower Cretaceous carbonates of the Gargano Massif. *Soc. Geol. Ital. Mem.*, **40**, 99–108.

Masse, J.-P. and **Steuber, T.** (2007) Strontium isotope stratigraphy of Early Cretaceous rudist bivalves. In: *Cretaceous rudists and carbonate platforms: Environmental feedback* (Ed. R. W. Scott). *SEPM Spec. Publ.*, **87**, 159–165.

Masse, J.-P. and **Fenerci-Masse, M.** (2013) Drowning events, development and demise of carbonate platforms and controlling factors: the Late Barremian–Early Aptian record of southeast France. *Sed. Geol.*, **298**, 28–52.

Masse, J.-P., Fenerci-Masse, M., Özer, S., Güngör, T. and **Akal, C.** (2015) Berriasian rudist faunas and micropalaeontology of Stramberk type carbonate exotics from the Lycian nappes, Bodrum Peninsula, southwest Turkey. *Cretaceous Res.*, **56**, 76–92.

Matičec, D., Vlahović, I., Velić, I. and **Tišljar, J.** (1996) Eocene Limestones Overlying Lower Cretaceous Deposits of Western lstria (Croatia): Did Some Parts of Present lstria Form Land During the Cretaceous?. Geologia Croatica, **49/1**, 117-127.

Maurer, F., van Buchem, F.S.P., Eberli, G.P., Pierson, B.J., Raven, M.J., Larsen, P.-H., Al-Husseini, M.I. and **Vincent, B.** (2013) Late Aptian long-lived glacio-eustatic lowstand recorded on the Arabian Plate. *Terra Nova*, **25**, 87-94.

McArthur, J.M., Howarth, R.J. and **Bailey, T.R.** (2001) Strontium Isotope Stratigraphy: Lowess version 3: best fit to the marine Sr-isotope curve for 0–509 Ma and accompanying look-up table for deriving numerical age. *J. Geol.*, **109**, 155–170.

McArthur, J.M., Mutterlose, J., Price, G.D., Rawson, P.F., Ruffell, A. and **Thirwall, M.F.** (2004) Belemnites of Valanginian, Hauterivian and Barremian age: Sr-isotope stratigraphy,

composition ($^{87}Sr/^{86}Sr$, $\delta^{13}C$, $\delta^{18}O$, Na, Sr, Mg) and palaeo-oceanography. *Palaeogeogr. Palaeoclimatol. Palaeoecol.*, **202**, 253–272.

McArthur, J.M., Howarth, R.J. and **Shields, G.A.** (2012) Strontium isotope stratigraphy. In: *The Geologic Time Scale 2012* (Eds F. M. Gradstein, J. G. Ogg, M. Schmitz and G. Ogg), Elsevier, Amsterdam, 127–144.

McArthur, J.M., Howarth, R.J., Shields, G.A. and **Zhou, Y.** (2020) Strontium stratigraphy. In: *The Geologic Time Scale 2020* (Eds F. M. Gradstein, J. G. Ogg, M. D. Schmitz and G. M. Ogg). Elsevier, Amsterdam, 211–238.

Méhay, S., Keller, C.E., Bernasconi, S.M., Weissert, H.J., Erba, E., Bottini, C. and **Hochuli, P.A.** (2009) A volcanic CO_2 pulse triggered the Cretaceous Oceanic Anoxic Event 1a and a biocalcification crisis. *Geology*, **37**, 819–822.

Menegatti, A.P., Weissert, H.J., Brown, R.S., Tyson, R.V., Farrimond, P., Strasser, A. and **Caron, M.** (1998) High-resolution $\delta^{13}C$ stratigraphy through the Early Aptian "Livello Selli" of the Alpine Tethys. *Paleoceanography*, **13**, 530–545.

Menendez, A., **James, R., Shulga, N., Connelly, D.** and **Roberts, S.** (2018): Linkages between the Genesis and Resource Potential of Ferromanganese Deposits in the Atlantic, Pacific, and Arctic Oceans. *Minerals*, **8**, 1–31.

Mezga, A., Tunis, G., Moro, A., Tarlao, A., Ćosović, V. and **Bucković, D.** (2006) A new dinosaur tracksite in the Cenomanian of Istria, Croatia. *Riv. Ital. Paleontol. Stratigr.*, **112**, 435–445.

Millán, M.I., **Weissert, H.J.**, **Fernández-Mendiola, P.A.** and **García-Mondéjar, J.** (2009) Impact of Early Aptian carbon cycle perturbations on evolution of a marine shelf system in the Basque-Cantabrian Basin (Aralar, N Spain). *Earth Planet. Sci. Lett.*, **287**, 392–401.

Millán, M.I., **Weissert, H.J.**, **Owen, H.**, **Fernández-Mendiola, P.A.** and **García-Mondéjar, J.** (2011) The Madotz Urgonian platform (Aralar, northern Spain): Paleoecological changes in response to Early Aptian global environmental events. *Palaeogeogr. Palaeoclimatol. Palaeoecol.*, **312**, 167–180.

Millán, M.I., **Weissert, H.J.** and **López-Horgue, M.A.** (2014) Expression of the late Aptian cold snaps and the OAE1b in a highly subsiding carbonate platform (Aralar, northern Spain). *Palaeogeogr. Palaeoclimatol. Palaeoecol.*, **411**, 167–179.

Miller, K.G., Kominz, M.A., Browning, J.V., Wright, J.D., Mountain, G.S., Katz, M.E., Sugarman, P.J., Cramer, B.S., Christie-Blick, N. and **Pekar, S.F.** (2005) The Phanerozoic record of global sea-level change. *Science*, **310**, 1293–1298.

Monteiro, F.M., Pancost, R.D., Ridgwell, A. and **Donnadieu, Y.** (2012) Nutrients as the dominant control on the spread of anoxia and euxinia across the Cenomanian-Turonian oceanic anoxic event (OAE2): model-data comparison. *Paleoceanography*, **27**, PA4209.

Morford, J.L., Ruffell, A.D. and **Emerson, S.R.** (2001) Trace metal evidence for changes in the redox environment associated with the transition from terrigenous clay to diatomaceous sediment, Saanich Inlet, BC. *Mar. Geol.*, **174**, 355–369.

Moro, A. (1997) Stratigraphy and paleoenvironments of rudist biostromes in the Upper Cretaceous (Turonian - upper Santonian) limestones of southern Istria, Croatia. *Palaeogeogr. Palaeoclimatol. Palaeoecol.*, **131**, 113–131.

Moro, A., Skelton, P.W. and **Ćosović, V.** (2002) Palaeoenvironmental setting of rudists in the Upper Cretaceous (Turonian – Maastrichtian) Adriatic Carbonate Platform (Croatia), based on sequence stratigraphy. *Cretaceous Res.*, **23**, 489–508.

Moro, A., Tunis, G., Mezga, A., Tarlao, A. and **Ćosović, V.** (2007) Depositional environments of the Upper Cenomanian limestones with rudists and dinosaur footprints, Istria, Croatia. In: *Cretaceous Rudists and Carbonate Platforms: Environmental Feedback* (Ed. R. W. Scott), *SEPM Spec. Publ.*, **87**, 37–44.

Moro, A., Mezga, A., Ćosović, V., Tunis, G. and **Tarlao, A.** (2008) Rudists and dinosaur footprints - mutual relationship within mud-supported Upper Cenomanian peritidal limestones of Istria, Croatia. *Boll. Soc. Geol. Ital.*, **127**/2, 423–428.

Morsilli, M. (2011) Introduzione alla geologia del Gargano. In: *Le miniere di selce del Gargano, VI-III Millennio a.C., alle origini della storia mineraria Europea* (Eds M. Tarantini and A. Galiberti), Florence, Italy, All'Insegna del Giglio, 17–27.

Morsilli, M. (2016) Sintesi delle conoscenze geologiche e stratigrafiche del Promontorio del Gargano. *Geol. e Territ. Ordine Reg. dei Geol. - Puglia*, 15–30.

Morsilli, M. and **Bosellini, A.** (1997) Carbonate facies zonation of the Upper Jurassic-Lower Cretaceous Apulia platform margin (Gargano Promontory, Southern Italy). *Riv. Ital. Paleontol. Stratigr.*, **103**, 193–206.

Morsilli, M., Hairabian, A., Borgomano, J., Nardon, S., Adams, E. and **Gartner, G.B.** (2017) The Apulia Carbonate Platform - Gargano Promontory, Italy (Upper Jurassic–Eocene). *AAPG Bull.*, **101**, 523–531.

Mort, H., Jacquat, O., Adatte, T., Steinmann, P., Föllmi, K.B., Matera, V., Berner, Z. and **Stüben D.** (2007) The Cenomanian/Turonian anoxic event at the Bonarelli Level in Italy and Spain: Enhanced productivity and/or better preservation? *Cretaceous Res.*, **28**, 597–612.

Mutti, M. and **Hallock, P.** (2003) Carbonate systems along nutrient and temperature gradients: some sedimentological and geochemical constraints. *Int. J. Earth Sci.*, **92**, 465–475.

Naafs, B.D.A., Castro, J.M., De Gea, G.A., Quijano, M.L., Schmidt, D.N. and **Pancost, R.D.** (2016) Gradual and sustained carbon dioxide release during Aptian Oceanic Anoxic Event 1a. *Nat. Geosci.*, **9**, 135–142.

Najarro, M., Rosales, I., Moreno-Bedmar, J.A., de Gea, G.A., Barrón, E. and **Delanoy, G.** (2010) High-resolution chemo-and biostratigraphic records of the Early Aptian oceanic anoxic event in Cantabria (N Spain): palaeoceanographic and palaeoclimatic implications. *Palaeogeogr. Palaeoclimatol. Palaeoecol.*, **299**, 137–158.

Najarro, M., Rosales, I. and **Martín-Chivelet, J.** (2011) Major palaeoenvironmental perturbation in an Early Aptian carbonate platform: Prelude of the Oceanic Anoxic Event 1a? *Sed. Geol.*, **235**, 50–71.

Navarro-Ramirez, J.P., Bodin, S., Consorti, L. and **Immenhauser, A.** (2017) Response of western South American epeiric-neritic ecosystem to middle Cretaceous Oceanic Anoxic Events. *Cretaceous Res.*, **75**, 61–80.

Nevesskaja, L.A., Skarlato, O.A., Starobogatov, Y. I. and **Eberzin, A.G.** (1971) A new concept of the bivalve system. *Paleontol. Zh.*, **2**, 3–20.

Norris, R.D., Bice, K.L., Mango, E.A. and **Wilson, P.A.** (2002) Jiggling the tropical thermostat in the Cretaceous hothouse. *Geology*, **30**, 299–302.

Nothdurft, L.D., Webb, G.E. and **Kamber, B.S.** (2004) Rare earth element geochemistry of Late Devonian reefal carbonates, Canning Basin, Western Australia: confirmation of a seawater REE proxy in ancient limestones. *Geochim. Cosmochim. Acta*, **68**, 263–283.

Nozaki, Y. (2001) Rare Earth Elements and their isotopes in the ocean. In: *Encyclopedia of Ocean Sciences* (Eds J. H. Steele, K. K. Turekian and S. A. Thorpe), 2354–2366.

Nozaki, Y. (2008) Rare Earth Elements and their isotopes in the Ocean. In: *Encyclopedia of Ocean Sciences, Second Edition* (Eds J. H. Steele, K. K. Turekian and S. A. Thorpe), 653–665.

Nozaki, Y., Zhang, J. and **Amakawa, H.** (1997) The fractionation between Y and Ho in the marine environment. *Earth Planet. Sci. Lett.*, **148**, 329–340.

Núñez-Useche, F., Barragán, R., Torres-Martínez, M.A., López-Zúñiga, P.A., Moreno-Bedmar, J.A., Chávez-Cabello, G., Canet, C. and **Chacon-Baca, E.** (2020) Response of the western proto-North Atlantic margin to the early Aptian oceanic anoxic event (OAE) 1a: an example from the Cupido platform margin-Gulf of Mexico, NE Mexico. *Cretaceous Res.*, **113**, 104488.

O'Brien, C.L., Robinson, S.A., Pancost, R.D., Damsté, J.S.S., Schouten, S., Lunt, D.J., Alsenz, H., Bornemann, A., Bottini, C., Brassell, S.C., Farnsworth, A., Forster, A., Huber, B.T.,

Inglis, G.N., Jenkyns, H.C., Linnert, C., Littler, K., Markwick, P., McAnena, A., Mutterlose, J., Naafs, B.D.A., Püttmann, W., Sluijs, A., van Helmond, A.G.M., Vellecoop, J., Wagner, T. and **Wrobel, N. E.** (2017) Cretaceous sea-surface temperature evolution: Constraints from TEX86 and planktonic foraminiferal oxygen isotopes. *Earth-Sci. Rev.*, **172**, 224–247.

Oehlert, A.M. and **Swart, P.K.** (2014) Interpreting carbonate and organic carbon isotope covariance in the sedimentary record. *Nat. Commun.*, **5**, 1–7.

Oehlert, A.M. and **Swart, P.K.** (2019) Rolling window regression of $\delta^{13}C$ and $\delta^{18}O$ values in carbonate sediments: Implications for source and diagenesis. *The Depositional Record*, **5**, 613-630.

Ogg, J.G. and **Hinnov, L.A.** (2012). Cretaceous. In: *The Geologic Time Scale 2012* (Eds F. M. Gradstein, J. G. Ogg, M. Schmitz and G. Ogg). Elsevier, Amsterdam, 793–853.

Ohkouchi, N., Kashiyama, Y., Kuroda, J., Ogawa, N.O. and **Kitazato, H.** (2006) The importance of diazotrophic cyanobacteria as primary producers during Cretaceous oceanic anoxic event 2. *Biogeosciences*, **3**, 467–478.

Otoničar, B. (2007) Upper Cretaceous to paleogene forbulge unconformity associated with foreland basin evolution (Kras, Matarsko Podolje and Istria; SW Slovenia and NW Croatia). *Acta Carsolog.*, **36**, 101–120.

Owens, J.D., Gill, B.C., Jenkyns, H.C., Bates, S.M., Severmann, S., Kuypers, M.M.M., Woodfine, R.G. and **Lyons, T.W.** (2013) Sulfur isotopes track the global extent and dynamics of euxinia during Cretaceous Oceanic Anoxic Event 2. *Proc. Nat. Acad. Sci. USA*, **110**, 18407–18412.

Owens, J.D., Lyons, T.W., Hardisty, D.S., Lowery, C.M., Lu, Z., Lee, B. and **Jenkyns, H.C.** (2017) Patterns of local and global redox variability during the Cenomanian–Turonian Boundary Event (Oceanic Anoxic Event 2) recorded in carbonates and shales from central Italy. *Sedimentology*, **64**, 168–185.

Özer, S., Sözbilir, H., Özkar, I., Toker, V. and **Sari, B.** (2001) Stratigraphy of Upper Cretaceous-Palaeogene sequences in the southern and eastern Menderes Massif (western Turkey). *Int. J. Earth Sci.*, **89**, 852–866.

Özyurt, M., Kırmacı, M.Z., Al-Aasm, I.S., Hollis, C., Tash, K. and **Kandemir, R.** (2020) REE characteristics of Lower Cretaceous limestone succession in Gümüshane, NE Turkey: Implications for ocean paleoredox conditions and diagenetic alteration. *Minerals*, **10**, 1–25.

Pancost, R.D., Crawford, N., Magness, S., Turner, A., Jenkyns, H.C. and **Maxwell, J.R.** (2004) Further evidence for the development of photic-zone euxinic conditions during Mesozoic Oceanic Anoxic Events. *J. Geol. Soc. London*, **161**, 353–364.

Pandey, D.K., Fürsich, F.T., Gameil, M. and **Ayoub-Hannaa, W.S.** (2011) Aspidiscus cristatus (Lamarck) from the Cenomanian sediments of Wadi Quseib, East Sinai, Egypt. *J. Palaeontol. Soc. India*, **56**, 29–37.

Parente, M., Frijia, G. and **Di Lucia, M.** (2007) Carbon-isotope stratigraphy of Cenomanian–Turonian platform carbonates from the southern Apennines (Italy): a chemostratigraphic approach to the problem of correlation between shallow-water and deep-water successions. *J. Geol. Soc. London.*, **164**, 609–620.

Parente, M., Frijia, G., Di Lucia, M., Jenkyns, H.C., Woodfine, R.G. and **Baroncini, F.** (2008) Stepwise extinction of larger foraminifers at the Cenomanian-Turonian boundary: A shallow-water perspective on nutrient fluctuations during oceanic anoxic event 2 (Bonarelli event). *Geology*, **36**, 715–718.

Paris, A. and **Sirna, M.** (1996) Geology and paleontology of the south-western carbonate edge of Fucino plain (Abruzzi, central Apennines). *Geol. Romana*, **32**, 183–209.

Patterson, W.P. and **Walter, L.M.** (1994) Depletion in ^{13}C in seawater $\sum CO_2$ on modern carbonate platforms: significance for the carbon isotopic record of carbonate. *Geology*, **22**, 885–888.

Paul, C.R.C., Lamolda, M.A., Mitchell, S.F., Vaziri, M.R., Gorostidi, A. and **Marshall, J.D.** (1999) The Cenomanian – Turonian boundary at Eastbourne (Sussex, UK): a proposed European reference section. *Palaeogeogr. Palaeoclimatol. Palaeoecol.*, **150**, 83–121.

Pearce, M.A., Jarvis, I. and **Tocher, B.A.** (2009) The Cenomanian – Turonian boundary event, OAE2 and palaeoenvironmental change in epicontinental seas: New insights from the dinocyst and geochemical records. *Palaeogeogr. Palaeoclimatol. Palaeoecol.*, **280**, 207–234.

Petti, F.M., Conti, M.A., D'Orazi Porchetti, S., Morsilli, M., Nicosia, U. and **Gianolla, P.** (2008) A theropod dominated ichnocoenosis from late Hauterivian-early Barremian of Borgo Celano (Gargano Promontory, Apulia, southern Italy). *Riv. Ital. Paleontol. Stratigr.*, **114**, 3–17.

Phelps, R.M. (2011) Middle-Hauterivian to Lower-Campanian sequence stratigraphy and stable isotope geochemistry of the Comanche Platform, south Texas. *Ph.D. Thesis*, University of Texas, Austin, 243 pp.

Phelps, R.M., Kerans, C., Loucks, R.G., Da-Gama, R.O.B.P., Jeremiah, J. and **Hull, D.** (2014) Oceanographic and eustatic control of carbonate platform evolution and sequence stratigraphy on the Cretaceous (Valanginian – Campanian) passive margin, northern Gulf of Mexico. *Sedimentology*, **61**, 461–496.

Phelps, R.M., Kerans, C., Da-Gama, R.O.B.P., Jeremiah, J., Hull, D. and **Loucks, R.G.** (2015) Response and recovery of the Comanche carbonate platform surrounding multiple Cretaceous oceanic anoxic events, northern Gulf of Mexico. *Cretaceous Res.*, **54**, 117–144.

Philip, J. (1998) Sequences and systems tracts of mixed carbonate-siliciclastic platform-basin settings: the Cenomanian-Turonian stages of Provence (southeastern France). *Mesozoic Cenozoic Seq. Stratigr. Eur. Basins, SEPM Spec. Publ.*, **60**, 387–395.

Philip, J. and **Airaud-Crumiere, C.** (1991) The demise of the rudist-bearing carbonate platforms at the Cenomanian/Turonian boundary: a global control. *Coral Reefs*, **10**, 115–125.

Philip, J., Borgomano, J. and **Al-Maskiry, S.** (1995) Cenomanian - Early Turonian carbonate platform of Northern Oman: stratigraphy and palaeo-environments. *Palaeogeogr. Palaeoclimatol. Palaeoecol.*, **119**, 77–92.

Pictet, A., Delanoy, G., Adatte, T., Spangenberg, J.E., Baudouin, C., Boselli, P., Boselli, M., Kindler, P. and **Föllmi, K.B.** (2015) Three successive phases of platform demise during the early Aptian and their association with the oceanic anoxic Selli episode (Ardèche, France). *Palaeogeogr. Palaeoclimatol. Palaeoecol.*, **418**, 101–125.

Pittet, B., Van Buchem, F.S.P., Hillgärtner, H., Razin, P., Grötsch, J. and **Droste, H.** (2002) Ecological succession, palaeoenvironmental change, and depositional sequences of Barremian-Aptian shallow-water carbonates in northern Oman. *Sedimentology*, **49**, 555–581.

Pleničar, M., Polšak, A. and **Šikić, D.** (1969) Basic geological map of SFRY 1:100000, sheet Trieste L33-88. In: *Geološki zavod*, Ljubljana, Institut za geološka istraživanja Zagreb.

Polšak, A. (1967a) Macrofaune crétacée de l'Istrie méridionale, Yugoslavie. *Palaeontol. Jugoslav.*, **8**, 1–219.

Polšak, A. (1967b) Basic geological map of SFRY 1:100000, sheet Pula L33–112. In: *Geološki zavod*, Ljubljana, Institut za geološka istraživanja, Zagreb.

Polšak, A. and **Šikić, D.** (1969) Basic geological map of SFRY 1:100000, sheet Rovinj L33-100j. In: *Geološki zavod*, Ljubljana, Institut za geološka istraživanja, Zagreb.

Pomar, L. and **Hallock, P.** (2008) Carbonate factories: A conundrum in sedimentary geology. *Earth-Sci. Rev.*, **87**, 134–169.

Pons, J.M., Vicens, E. and **Tarlao, A.** (2011) Cenomanian radiolitid bivalves from Malchina, Karst of Trieste, Italy. *Cretaceous Res.*, **32**, 1–12.

Posenato, R. and **Masetti, D.** (2012) Environmental control and dynamics of Lower Jurassic bivalve build-ups in the Trento Platform (Southern Alps, Italy). *Palaeogeogr. Palaeoclimatol. Palaeoecol.*, **361**, 1–13.

Posenato, R., Morsilli, M., Guerzoni, S. and **Bassi, D.** (2018) Palaeoecology of Chondrodonta (Bivalvia) from the lower Aptian (Cretaceous) Apulia Carbonate Platform (Gargano Promontory, southern Italy). *Palaeogeogr. Palaeoclimatol. Palaeoecol.*, **508**, 188–201.

Posenato, R., Frijia, G., Morsilli, M., Moro, A., Del Viscio, G. and **Mezga, A.** (2020) Paleoecology and proliferation of the bivalve Chondrodonta joannae (Choffat) in the upper Cenomanian (Upper Cretaceous) Adriatic Carbonate Platform of Istria (Croatia). *Palaeogeogr. Palaeoclimatol. Palaeoecol.*, **548**, 109703.

Poulsen, C.J., Gendaszek, A.S. and **Jacob, R.L.** (2003) Did the rifting of the Atlantic Ocean cause the Cretaceous thermal maximum? *Geology*, **31**, 115–118.

Pratt, B.R. and **Smewing, J.D.** (1990) Jurassic and Early Cretaceous platform margin configuration and evolution, central Oman Mountains. *Geol. Soc. London Spec. Publ.*, **49**, 69–88.

Prokoph, A., Shields, G.A. and **Veizer, J.** (2008) Compilation and time-series analysis of a marine carbonate $\delta^{18}O$, $\delta^{13}C$, $^{87}Sr/^{86}Sr$ and $\delta^{34}S$ database through Earth history. *Earth-Sci. Rev.*, **87**, 113–133.

Pucéat, E., Lécuyer, C., Donnadieu, Y., Naveau, P., Cappetta, H., Ramstein, G., Huber, B.T. and **Kriwet, J.** (2007) Fish tooth $\delta^{18}O$ revising Late Cretaceous meridional upper ocean water temperature gradients. *Geology*, **35**, 107–110.

Rameil, N., Immenhauser, A., Warrlich, G., Hillgärtner, H. and **Droste, H.** (2010) Morphological patterns of Aptian Lithocodium-Bacinella geobodies: relation to environment and scale. *Sedimentology*, **57**, 883–911.

Randall, D.A., Wood, R.A., Bony, S., Colman, R., Fichefet, T., Fyfe, J., Kattsov, V., Pitman, A., Shukla, J., Srinivasan, J., Stouffer, R.J., Sumi, A. and **Taylor, K.E.** (2007) Climate models and their evaluation. In: *Climate Change 2007: The physical science basis*. Contribution of Working Group I to the 4th Assessment Report of the Intergovernmental Panel on Climate Change (Eds S. Solomon *et al.*). *Cambridge University Press, Cambridge, United Kingdom and New York, NY, USA*.

Raup, D.M. and **Sepkoski, J.J.** (1986) Periodic extinction of Families and Genera. *Science*, **231**, 833–836.

Razin, P., Taati, F. and **Van Buchem, F.S.P.** (2010) Sequence stratigraphy of Cenomanian - Turonian carbonate platform margins (Sarvak Formation) in the High Zagros, SW Iran: an outcrop reference model for the Arabian Plate. *Geol. Soc. London Spec. Publ.*, **329**, 187–218.

Riding, R. (2002) Structure and composition of organic reefs and carbonate mud mounds: concepts and categories. *Earth-Sci. Rev.*, **58**, 163–231.

Ries, J.B. (2009) Effects of secular variation in seawater Mg/Ca ratio (calcite-aragonite seas) on $CaCO_3$ sediment production by the calcareous algae Halimeda, Penicillus and Udotea - Evidence from recent experiments and the geological record. *Terra Nova*, **21**, 323–339.

Ross, D.J. and **Skelton, P.W.** (1993) Rudist formations of the Cretaceous: a palaeoecological, sedimentological and stratigraphical review. *Sedimentol. Rev.*, **1**, 73–91.

Roth, P.H. (1978) Calcareous nannoplankton biostratigraphy and oceanography of the northwestern Atlantic Ocean. *Init. Rep. Deep Sea Drilling Proj.*, **44**, 731–759.

Saber, S.G. (2012) Depositional framework and sequence stratigraphy of the Cenomanian-Turonian rocks on the western side of the Gulf of Suez, Egypt. *Cretaceous Res.*, **37**, 300–318.

Sanchez-Hernandez, Y. and **Maurrasse, F.J.-M.R.** (2016) The influence of regional factors in the expression of oceanic anoxic event 1a (OAE1a) in the semi-restricted Organyà Basin, south-central Pyrenees, Spain. *Palaeogeogr. Palaeoclimatol. Palaeoecol.*, **441**, 582–598.

Sanders, D. (1996) Rudist biostromes on the margin of an isolated carbonate platform: the Upper Cretaceous of Montagna della Maiella, Italy. *Eclogae Geol. Helv.*, **89**, 845–871.

Schlanger, S.O. and **Jenkyns, H.C.** (1976) Cretaceous Oceanic Anoxic Events: causes and consequences. *Geol. Mijnbouw*, **55**, 179–184.

Schmitt, K., Heimhofer, U., Frijia, G., Di Lucia, M. and **Huck, S.** (2020) Deciphering the fragmentary nature of Cretaceous shallow-water limestone archives: A case study from the subtropical Apennine carbonate platform. *Newsl. Stratigr.*, 20097.

Scholle, P.A. and **Arthur, M.A.** (1980) Carbon isotope fluctuation in Cretaceous pelagic limestones: potential stratigraphic and petroleum exploration tool. *AAPG Bulletin*, **64**, 67–87.

Schröder-Adams, C.J., Herrle, J.O., Selby, D., Quesnel, A. and **Froude, G.** (2019) Influence of the High Arctic Igneous Province on the Cenomanian/Turonian boundary interval, Sverdrup Basin, High Canadian Arctic. *Earth Planet. Sci. Lett.*, **511**, 76–88.

Schröeder, R., van Buchem, F.S.P., Cherchi, A., Baghbani, D., Vincent, B., Immenhauser, A. and **Granier, B.** (2010) Revised orbitolinid biostratigraphic zonation for the Barremian-Aptian of the eastern Arabian Plate and implications for regional stratigraphic correlations. *GeoArabia Spec. Publ.,* **4**, 49–96.

Schubert, R.J. (1903) Ueber einige Bivalven des istrodalmatinischen Rudistenkalkes. *Jahr. d. k. k. geol. Reich.*, **52**, 265–276.

Scotese, C.R. (2014) Atlas of Late Cretaceous Paleogeographic Maps. *Paleomap Atlas for ArcGIS*, **2**, 1–16.

Scott, R.W. (1995) Cretaceous rudists of Guatemala. *Rev. Mex. Ci. Geol.*, **12**, 294–306.

Scott, R.W. (2007) Key bivalves of the lower Albian Glen Rose Formation, Texas, U.S.A. In: *Cretaceous Rudists and Carbonate Platforms: Environmental Feedback* (Ed. R. W. Scott), *SEPM Spec. Publ.*, **87**, 247–252.

Scott, R.W. and **Finch, R.C.** (1999) Cretaceous carbonate biostratigraphy and environments in Honduras. In: *Sedimentary Basins of the World* (Ed. P. Mann), **4**, 151–165.

Scott, R.W. and **Filkorn, H.F.** (2007) Barremian-Albian rudist zones, U.S. Gulf Coast. In: *Cretaceous Rudists and Carbonate Platforms: Environmental Feedback* (Ed. R. W. Scott), *SEPM Spec. Publ.*, **87**, 167–180.

Scott, R.W. and **Hinote, R.E.** (2007) Barremian-Early Aptian Rudists, Sligo Formation, Texas, U.S.A. In: *Cretaceous Rudists and Carbonate Platforms: Environmental Feedback* (Ed. R. W. Scott), *SEPM Spec. Publ.*, **87**, 237–246.

Sharp, I., Gillespie, P., Morsalnezhad, D., Taberner, C., Karpuz, R., Vergés, J., Horbury, A., Pickard, N., Garland, J. and **Hunt, D.** (2010) Stratigraphic architecture and fracture-controlled dolomitization of the Cretaceous Khami and Bangestan groups: an outcrop case study, Zagros Mountains, Iran. In: *Carbonate Systems of the Mediterranean and the Middle East: Stratigraphic and Diagenetic Reference Models* (Eds F. S. P. Van Buchem, K. D. Gerdes and M. Esteban), *Mesozoic and Cenozoic. Geol. Soc. London Spec. Publ.*, **329**, 343–396.

Shields, G.A. and **Stille, P.** (2001) Diagenetic constraints on the use of cerium anomalies as palaeoseawater redox proxies: an isotopic and REE study of Cambrian phosphorites. *Chem. Geol.*, **175**, 29– 48.

Shields, G.A. and **Webb, G.E.** (2004). Has the REE composition of seawater changed over geological time? *Chem. Geol.*, **204**, 103–107.

Sholkovitz, E.R. and **Schneider, D.L.** (1991) Cerium redox cycles and rare earth elements in the Sargasso Sea. *Geochim. Cosmochim. Acta*, **55**, 2737–2743.

Sissingh, W. (1977) Biostratigraphy of Cretaceous calcareous nannoplankton. *Geol. Mijnbouw*, **56**, 37–65.

Skelton, P.W. (2018) Part N, Volume 1, Chapter 26A: Introduction to the Hippuritida (rudists) - Shell structure, anatomy, and evolution. *Treatise Online*, **104**, 1–37.

Skelton, P.W. and **Gili, E.** (2002) Paleoecological classification of rudist morphotypes. In: *Rudists* (Ed. M. S. Trifunović), *Proceedings First International Conference on Rudists*. Union of Geological Societies of Yugoslavia, Memorial Publication, Beograd, 265–285.

Skelton, P.W. and **Gili, E.** (2012) Rudists and carbonate platforms in the Aptian: a case study on biotic interactions with ocean chemistry and climate. *Sedimentology*, **59**, 81–117.

Skelton, P.W., Spicer, R.A., Kelley, S.P. and **Gilmour, I.** (2003) The Cretaceous World (Ed. P. W. Skelton). *Cambridge University Press, Cambridge, United Kingdom*, 360 pp.

Smrzka, D., Zwicker, J., Bach, W., Feng, D., Himmler, T., Chen, D. and **Peckmann, J.** (2019) The behavior of trace elements in seawater, sedimentary pore water, and their incorporation into carbonate minerals: A review. *Facies*, **65**, 1–47.

Snow, L.J., Duncan, R.A. and **Bralower, T.J.** (2005) Trace element abundances in the Rock Canyon Anticline, Pueblo, Colorado, marine sedimentary section and their relationship to Caribbean plateau construction and oxygen anoxic event 2. *Paleoceanography*, **20**, 1–14.

Spalluto, L. (2012) Facies evolution and sequence chronostratigraphy of a "mid"-Cretaceous shallow-water carbonate succession of the Apulia Carbonate Platform from the northern Murge area (Apulia, southern Italy). *Facies*, **58**, 17–36.

Spalluto, L. and **Pieri, P.** (2008) Carta geologica delle unità carbonatiche mesozoiche e cenozoiche del Gargano sud-occidentale: nuovi vincoli stratigrafici per l'evoluzione tettonica dell'area. *Carta Geol. Ital. Mem. Descr.,* **77**, 147–176.

Spalluto, L., Pieri, P. and **Ricchetti, G.** (2005) Le facies carbonatiche di piattaforma interna del Promontorio del Gargano: implicazioni paleoambientali e correlazioni con la coeva successione delle Murge (Italia meridionale, Puglia). *Boll. Soc. Geol. Ital.*, **124**, 1–16.

Stampfli, G.M. and **Mosar, J.** (1999) The making and becoming of Apulia. *Sci. Geol. Mem.*, **51**, 141–154.

Stanton, T.W. (1901) Chondrodonta, a new genus of ostreiform mollusks from the Cretaceous, with descriptions of the genotype and a new species. In: *Nat. Mus. Proc. Smithson. Inst. US*, **24**, 301–307.

Stanton, T.W. (1947) Studies of some Comanche pelecypods and gastropods. In: *USGS Prof. Pap.*, **221**, 1–256.

Stein, M., Föllmi, K.B., Westermann, S., Godet, A., Adatte, T., Matera, V., Fleitmann, D. and **Berner, Z.** (2011) Progressive palaeoenvironmental change during the Late Barremian – Early Aptian as prelude to Oceanic Anoxic Event 1a: evidence from the Gorgo a Cerbara section (Umbria-Marche basin, central Italy). *Palaeogeogr. Palaeoclimatol. Palaeoecol.*, **302**, 396–406.

Stein, M., Westermann, S., Adatte, T., Matera, V., Fleitmann, D., Spangenberg, J.E. and **Föllmi, K.B.** (2012) Late Barremian–Early Aptian palaeoenvironmental change: The Cassis-La Bédoule section, southeast France. *Cretaceous Res.*, **37**, 209–222.

Steuber, T. (2002) Plate tectonic control on the evolution of Cretaceous platform-carbonate production. *Geology*, **30**, 259–262.

Steuber, T., Korbar, T., Jelaska, V. and **Gušić, I.** (2005) Strontium-isotope stratigraphy of Upper Cretaceous platform carbonates of the island of Brać (Adriatic Sea, Croatia): implications for global correlation of platform evolution and biostratigraphy. *Cretaceous Res.*, **26**, 741–756.

Steuber, T., Scott, R.W., Mitchell, S.F. and **Skelton, P.W.** (2016) Part N, Revised, Volume 1, Chapter 26C: Stratigraphy and diversity dynamics of Jurassic–Cretaceous Hippuritida (rudist bivalves). *Treatise Online*, **81**, 1–17.

Swart, P.K. and **Oehlert, A.M.** (2018) Revised interpretations of stable C and O patterns in carbonate rocks resulting from meteoric diagenesis. *Sed. Geol.*, **364**, 14-23.

Takashima, R., Nishi, H., Huber, B.T. and **Leckie, M.** (2006) Greenhouse worlds and the Mesozoic ocean. *Oceanography*, **19**, 82–92.

Tarduno, J.A., Brinkman, D.B., Renne, P.R., Cottrell, R.D., Scher, H. and **Castillo, P.** (1998) Evidence for extreme climatic warmth from Late Cretaceous arctic vertebrates. *Science*, **282**, 2241–2244.

Taylor, S.R. and **McLennan, S.M.** (1985) The continental crust: Its composition and evolution. Blackwell, Oxford, 312 pp.

Tejada, M.L.G., Suzuki, K., Kuroda, J., Coccioni, R., Mahoney, J.J., Ohkouchi, N., Sakamoto, T. and **Tatsumi, Y.** (2009) Ontong Java Plateau eruption as a trigger for the early Aptian oceanic anoxic event. *Geology*, **37**, 855–858.

Tentor, M., Tunis, G. and **Venturini, S.** (1994) Schema stratigrafico e tettonico del Carso Isontino. *Natura Nascosta*, **9**, 1–32.

Theiling, B.P., Railsback, L.B., Holland, S.M. and **Crowe, D.E.** (2007) Heterogeneity in geochemical expression of subaerial exposure in limestones, and its implications for sampling to detect exposure surfaces. *J. Sed. Res.*, **77**, 159–169.

Tišljar, J., Velić, I., Radovčić, J., Crnković, B., Babić, Lj. and **Jelaska, V.** (1983) Upper Jurassic and Cretaceous peritidal, lagoonal, shallow marine and perireefal carbonate sediments of Istria. In: *Contributions to Sedimentology of Some Carbonate and Clastic Units of the Coastal Dinarides*, Split, *4th IAS Regional Meeting Excursion Guidebook*, 13–35.

Tišljar, J., Vlahović, I., Velić, I., Matičec, D. and **Robson, J.Z.** (1998) Carbonate facies evolution from the Late Albian to Middle Cenomanian in southern Istria (Croatia): influence of synsedimentary tectonics and extensive organic carbonate production. *Facies*, **38**, 137–152.

Tišljar, J., Vlahović, I., Velić, I. and **Sokač, B.** (2002) Carbonate platform megafacies of the Jurassic and Cretaceous deposits of the Karst Dinarides. *Geol. Croat.*, **55**, 139–170.

Tribovillard, N., Riboulleau, A., Lyons, T. and **Baudin, F.** (2004) Enhanced trapping of molybdenum by sulfurized organic matter of marine origin as recorded by various Mesozoic

formations. *Chem. Geol.*, **213**, 385–401.

Tribovillard, N., Algeo, T.J., Lyons, T. and **Riboulleau, A.** (2006) Trace metals as paleoredox and paleoproductivity proxies: An update. *Chem. Geol.*, **232**, 12–32.

Tsikos, H., Jenkyns, H.C., Walsworth-Bell, B., Petrizzo, M.R., Forster, A., Kolonik, S., Erba, E., Premoli Silva, I., Baas, M., Wagner, T. and **Sinninghe Damsté, J.S.** (2004) Carbon-isotope stratigraphy recorded by the Cenomanian–Turonian Oceanic Anoxic Event: correlation and implications based on three key localities. *J. Geol. Soc. London*, **161**, 711–719.

Turgeon, S. and **Brumsack, H.J.** (2006) Anoxic vs dysoxic events reflected in sediment geochemistry during the Cenomanian-Turonian Boundary Event (Cretaceous) in the Umbria-Marche Basin of central Italy. *Chem. Geol.*, **234**, 321–339.

Tyrrell, T. (1999) The relative influences of nitrogen and phosphorus on oceanic primary production. *Nature*, **400**, 525–531.

Ullmann, C.V. and **Korte, C.** (2015) Diagenetic alteration in low-Mg calcite from macrofossils: a review. *Geol. Quarterly*, **59**, 3-20.

Vahrenkamp, V.C. (2010) Chemostratigraphy of the Lower Cretaceous Shu'aiba Formation: a $\delta^{13}C$ reference profile for the Aptian Stage from the southern Neo-Tethys Ocean. In: *Barremian – Aptian stratigraphy and hydrocarbon habitat of the eastern Arabian Plate* (Eds F. S. P. van Buchem, M. I. Al-Husseini, F. Maurer and H. J. Droste), *GeoArabia Spec. Publ.,* **4**, 107–138.

Vaziri-Moghaddam, H. and **Kalanat, B.** (2020) Oxygen level, primary productivity, and water turbulence during the OAE2 interval of Zagros Basin (SW Iran): benthic foraminiferal variations in the carbonate microfacies. *Gondwana Res.*, **83**, 1–15.

Velić, I. (2007) Stratigraphy and palaeo-biogeography of Mesozoic benthic foraminifera of the Karst Dinarides (SE Europa). *Geol. Croat.*, **60**, 1–113.

Velić, I. and **Vlahović, I.** (1994) Foraminiferal Assemblages in the Cenomanian of the Buzet-Savudrija Area (Northwestern Istria, Croatia). *Geol. Croat.*, **47**, 25–43.

Velić, I., Vlahović, I. and **Matičec, D.** (2002) Depositional sequences and palaeogeography of the Adriatic carbonate platform. *Soc. Geol. Ital. Mem.*, **57**, 141–151.

Velić, I., Tišljar, J., Matičec, D. and **Vlahović, I.** (1995) A review of the geology of Istria. In: *First Croatian Geological Congress, excursion guidebook* (Eds I. Vlahović and I. Velić), 21–30.

Velić, I., Tišljar, J., Vlahović, I., Matičec, D. and **Bergant, S.** (2003) Evolution of the Istrian part of the Adriatic carbonate platform from the middle Jurassic to the Santonian and formation of the Flysch Basin during the Eocene: main events and regional comparison. In: *22nd IAS Meeting of Sedimentology - Opatija 2003*, *Field Trip Guidebook*, 3–17.

Velić, I., Malvić, T. and **Cvetković, M.** (2015) Stratigraphy and petroleum geology of the Croatian part of the Adriatic Basin. *J. Petrol. Geol.*, **38**, 281–300.

Vescogni, A., Bosellini, F.R., Cipriani, A., Gürler, G., Ilgar, A. and **Paganelli, E.** (2014) The Dağpazarı carbonate platform (Mut Basin, Southern Turkey): Facies and environmental reconstruction of a coral reef system during the Middle Miocene Climatic Optimum. *Palaeogeogr. Palaeoclimatol. Palaeoecol.*, **410**, 213–232.

Vilas, L., Masse, J.-P. and **Arias, C.** (1995) Orbitolina episodes in carbonate platform evolution: the early Aptian model from SE Spain. *Palaeogeogr. Palaeoclimatol. Palaeoecol.*, **119**, 35–45.

Vlahović, I., Tišljar, J., Velić, I., Matičec, D., Skelton, P.W., Korbar, T. and **Fuček, L.** (2003) Main events recorded in the sedimentary succession of the Adriatic Carbonate Platform from the Oxfordian to the Upper Santonian in Istria (Croatia). In: *22nd IAS Meeting of Sedimentology - Opatija 2003, Field Trip Guidebook*, 19–56.

Vlahović, I., Tišljar, J., Velić, I. and **Matičec, D.** (2005) Evolution of the Adriatic Carbonate Platform: palaeogeography, main events and depositional dynamics. *Palaeogeogr. Palaeoclimatol. Palaeoecol.*, **220**, 333–360.

Vlahović, I., Miksa, G., Mrinjek, E., Hasiotis, S. T., Velić, I., Tišljar, J. and **Matičec, D.** (2011) Response of tracemakers to temporary platform drowning: Lower Cenomanian of southern Istria (Western Croatia). *Palaios*, **26**, 567–577.

Webb, G.E. and **Kamber, B.S.** (2000) Rare earth elements in Holocene reefal microbialites: A new shallow seawater proxy. *Geochim. Cosmochim. Acta*, **64**, 1557–1565.

Wedepohl, K.H. (1971) Environmental influences on the chemical composition of shales and clays. *Phys. Chem. Earth*, **8**, 307–333.

Wedepohl, K.H. (1991) Chemical composition and fractionation of the continental crust. *Geol. Rundsch.*, **80**, 207–223.

Weissert, H.J. and **Erba, E.** (2004) Volcanism, CO_2 and palaeoclimate: a Late Jurassic - Early Cretaceous carbon and oxygen isotope record. *J. Geol. Soc. London*, **161**, 1–8.

Weissert, H.J., McKenzie, J.A. and **Channell, J.E.T.** (1985) Natural variations in the carbon cycle during the Early Cretaceous. In: *The carbon cycle and atmospheric CO_2: Natural Variations Archean to the Present* (Eds E. T. Sundquist and W. S. Broeker). *Am. Geophys. Union Monogr.*, **32**, 531–545.

Weissert, H.J., Lini, A., Föllmi, K.B. and **Kuhn, O.** (1998) Correlation of Early Cretaceous carbon isotope stratigraphy and platform drowning events: a possible link? *Palaeogeogr. Palaeoclimatol. Palaeoecol.*, **137**, 189–203.

Westermann, S., Stein, M., Matera, V., Fiet, N., Fleitmann, D., Adatte, T. and **Föllmi, K.B.** (2013) Rapid changes in the redox conditions of the western Tethys Ocean during the early Aptian oceanic anoxic event. *Geochim. Cosmochim. Acta*, **121**, 467–486.

Wissler, L., Funk, H. and **Weissert, H.J.** (2003) Response of Early Cretaceous carbonate platforms to changes in atmospheric carbon dioxide levels. *Palaeogeogr. Palaeoclimatol. Palaeoecol.*, **200**, 187–205.

Wissler, L., Weissert, H., Buonocunto, F.P., Ferreri, V. and **D'Argenio, B.** (2004) Calibration of the Early Cretaceous time scale: a combined chemostratigraphic and cyclostratigraphic approach to the Barremian-Aptian interval, Campania Apennines and Southern Alps (Italy). In: (Eds.), Cyclostratigraphy: Approaches and Case Histories (Eds B. D'Argenio, A. G. Fischer, I. Premoli Silva, H. Weissert and V. Ferreri). *SEPM Spec. Publ.*, **81**, 123–133.

Wright, C.W. and **Kennedy, W.J.** (1981) The Ammonoidea of the Plenus Marls and the Middle Chalk. *Monograph of the Palaeontographical Society of London*, 134, 148 pp.

Wright, C.W. and **Kennedy, W.J.** (1984) The Ammonoidea of the Lower Chalk, Part 1. *Palaeontograph. Soc. London Monogr.*, **137**, 1–126.

Wrigley, R., Hodgson, N. and **Esestime, P.** (2015) Petroleum geology and hydrocarbon potential of the Adriatic Basin, offshore Croatia. *J. Petrol. Geol.*, **38**, 301–316.

Zaghbib-Turki, D. (2003) Cretaceous coral-rudist formations in Tunisia. In: *North African Cretaceous Carbonate Platform Systems* (Eds E. Gili *et al.*), 83–110.

Zhang, J. and **Nozaki, Y.** (1996) Rare earth elements and yttrium in seawater: ICP-MS determinations in the East Caroline, Coral Sea, and South Fiji basins of the western South Pacific Ocean. *Geochim. Cosmochim. Acta*, **60**, 4631–4644.

Zhang J. and **Nozaki Y.** (1998) Behavior of rare earth elements in seawater at the ocean margin: A study along the slopes of the Sagami and Nankai troughs near Japan. *Geochim. Cosmochim. Acta*, **62**, 1307–1317.

Zhang J., Amakawa H. and **Nozaki Y.** (1994) The comparative behaviors of yttrium and lanthanides in the seawater of the North Pacific. *Geophys. Res. Lett.*, **21**, 2677–2680.

Appendix I - Geochemical dataset

Chapter 3 - *Chondrodonta* within the lower Aptian Apulia Carbonate Platform

C- and O-isotope data

San Giovanni section, $\delta^{13}C$ and $\delta^{18}O$ in bulk samples					
Sample	**Height (m)**	**$\delta^{13}C_{VPDB}$**	**$\delta^{18}O_{VPDB}$**	**3-points mov. average $\delta^{13}C_{VPDB}$**	**3-points mov. average $\delta^{18}O_{VPDB}$**
DPG42	23.4	-1.12	-4.65	-1.12	-4.65
DPG41	23.2	-1.35	-4.57	-1.23	-4.61
DPG40	23	-1.42	-4.64	-1.29	-4.62
DPG39	22.3	-0.50	-3.65	-1.09	-4.29
DPG38	21.65	-0.89	-4.51	-0.94	-4.27
DPG36	21.4	-0.42	-3.71	-0.60	-3.96
DPG37	21.25	-1.01	-4.69	-0.77	-4.31
DPG35	20.8	-1.05	-4.50	-0.83	-4.30
DPG34	20.6	-1.03	-4.74	-1.03	-4.65
DPG33	19.8	-0.62	-4.14	-0.9	-4.46
DPG32	19.1	-1.61	-4.54	-1.09	-4.47
DPG31	18.5	-1.38	-3.88	-1.20	-4.19
DPG30	17.8	-0.52	-4.12	-1.17	-4.18
DPG29C	17.25	-0.73	-4.07	-0.88	-4.02
DPG29B	16.7	-0.93	-3.97	-0.73	-4.05
DPG29	16.4	-1.11	-4.82	-0.92	-4.29
DPG28	15.8	-1.54	-3.90	-1.19	-4.23
DPG27	15.7	-2.53	-3.98	-1.73	-4.24
DPG26	15.3	-0.93	-3.81	-1.67	-3.90
DPG25	15.1	-2.98	-4.42	-2.15	-4.07
DPG24	14.65	-3.26	-4.51	-2.39	-4.25
DPG23	14.3	-2.10	-4.30	-2.78	-4.41
DPG22	14.05	-2.49	-4.22	-2.62	-4.34
DPG21	13.9	-1.75	-3.53	-2.11	-4.02
DPG20	13.8	-3.20	-4.46	-2.48	-4.07
DPG19	13.25	-0.85	-3.38	-1.93	-3.79
DPG18	12.45	-2.68	-4.06	-2.24	-3.97
DPG17	12.1	-1.92	-3.86	-1.82	-3.76
DPG16	11.8	-4.76	-4.11	-	-
DPG15	11.5	-2.07	-4.57	-	-
DPG14B	11.17	-2.85	-3.57	-2.48	-3.83
DPG14A	10.55	-2.15	-4.13	-2.31	-3.85
DPG13	10.1	-2.28	-3.13	-	-
DPG12	9.8	-0.63	-3.69	-1.87	-3.80

DPG12A	9.4	-0.69	-3.31	-1.15	-3.71
DPG11C	8.9	-1.30	-3.61	-0.87	-3.54
DPG11	8.7	-0.73	-3.70	-0.91	-3.54
DPG11E	8.2	-0.90	-3.73	-0.98	-3.68
DPG11D	8	-0.43	-3.36	-0.68	-3.60
DPG11B	7.8	-1.05	-3.56	-0.79	-3.55
DPG10B	7.45	-0.95	-3.53	-0.81	-3.48
DPG10	7.25	-0.59	-3.87	-0.86	-3.65
DPG9	6.7	-2.00	-4.10	-1.18	-3.83
DPG8	5.7	-0.68	-4.02	-1.09	-3.10
DPG5.1	5.15	-0.71	-3.60	-	-
DPG7	4.8	-0.87	-2.93	-	-
DPG6	4.4	-0.28	-4.08	-0.98	-4.07
DPG5	4.05	-1.28	-3.48		
DPG4	3.5	-0.95	-4.05	-0.63	-4.05
DPG3	2.55	-1.04	-3.55	-0.75	-3.89
DPG2	1.6	0.66	-2.79	-	-
DPG1*	1.45	0.10	-3.59	-	-
DPG0	0.4	0.09	-2.70	-0.63	-3.43

*Diagenized samples are marked in red.

San Giovanni section, $\delta^{13}C$ and $\delta^{18}O$ in shell samples				
Sample	**Shell**	**(m)**	**$\delta^{13}C_{VPDB}$**	**$\delta^{18}O_{VPDB}$**
DPG38-B	Rudist	21.65	1.33	-3.07
DPG38-A	Rudist	21.65	0.43	-3.77
DPG11C-A	*Chondrodonta*	8.9	-0.56	-3.92
DPG11-B	*Chondrodonta*	8.7	-0.58	-3.67
DPG11-A	*Chondrodonta*	8.7	-0.25	-3.77
DPG11D-A	*Chondrodonta*	8	-0.69	-3.38
DPG10B-C	*Chondrodonta*	7.45	-0.04	-3.57
DPG10B-B	*Chondrodonta*	7.45	-0.66	-3.59
DPG10B-A	*Chondrodonta*	7.45	0.25	-3.83

Borgo Celano 1 section, $\delta^{13}C$ and $\delta^{18}O$ in bulk samples					
Sample	**Height (m)**	**$\delta^{13}C_{VPDB}$**	**$\delta^{18}O_{VPDB}$**	**3-points mov. average $\delta^{13}C_{VPDB}$**	**3-points mov. average $\delta^{18}O_{VPDB}$**
GPBC13	25.1	-0.85	-3.81	-0.85	-3.81
GPBC12	24.1	-0.21	-3.72	-0.53	-3.77
GPBC11	23.1	-0.29	-3.81	-0.45	-3.78
GPBC10	22.1	-1.16	-4.37	-0.55	-3.97
GPBC9.5	21.6	-0.09	-3.11	-0.51	-3.76

GPBC9	21.1	-0.25	-2.97	-0.50	-3.48
GPBC8.45	20.5	-1.06	-3.05	-	-
GPBC8	20.05	-0.23	-3.50	-0.19	-3.19
GPBC7.5	19.55	-0.15	-2.93	-0.21	-3.13
GPBC6.9	18.95	0.42	-2.35	0.02	-2.92
GPBC6.5	18.55	-0.95	-3.27	-0.23	-2.85
GPBC5.9	18	-2.75	-3.67	-	-
GPBC5.5	17.55	-0.65	-3.12	-0.39	-2.91
GPBC5.1	17.15	-1.07	-3.58	-0.89	-3.32
GPBC4.66	16.71	-0.43	-3.80	-0.71	-3.50
GPBC3.9	15.95	0.39	-2.84	-0.37	-3.41
GPBC3.5	15.35	-1.24	-4.18	-0.43	-3.61
GPBC3.1	15.05	-0.69	-3.96	-	-
GPBC2.65	14.7	-0.61	-3.84	-	-
GPBC2.05	14.1	-1.24	-4.20	-0.70	-3.74
GPBC1.55	13.6	-1.19	-3.92	-	-
GPBC1.05	13.15	-2.64	-4.87	-1.71	-4.41
GPBC0.5	12.55	-2.97	-4.85	-	-
GPBC26.0A*	12	-0.51	-3.92	-	-
GPBC25.0A	11	0.96	-2.62	-0.97	-3.90
GPBC24.0A	10	-0.53	-3.47	-0.74	-3.65
GPBC22.9A	8.9	-0.65	-3.74	-0.07	-3.28
GPBC22.0A	8	-0.65	-4.15	-0.61	-3.79
GPBC19.8A	5.8	-1.62	-4.61	-0.97	-4.17
GPBC18.0A	4	-1.31	-4.33	-1.19	-4.36
GPBC15.0A	1	-1.66	-4.58	-1.53	-4.51
GPBC14.0A	0	-2.09	-4.57	-1.69	-4.49

*Diagenized samples are marked in red.

Borgo Celano 1 section, $\delta^{13}C$ and $\delta^{18}O$ in shell samples				
Sample	**Shell**	**(m)**	**$\delta^{13}C_{VPDB}$**	**$\delta^{18}O_{VPDB}$**
BCG3-A	Rudist	16	-0.71	-4.36
BCG2-A	*Chondrodonta*	16	-0.26	-4.29
BCG1-A	*Chondrodonta*	16	0.89	-3.46
SG14-C	*Chondrodonta*	16	1.60	-2.94
SG14-B	*Chondrodonta*	16	0.96	-2.53
SG-14A	*Chondrodonta*	16	0.93	-2.50
SG6-A	*Chondrodonta*	11.75	0.23	-2.25

Borgo Celano 2 section, $\delta^{13}C$ and $\delta^{18}O$ in bulk samples					
Sample	**Height (m)**	**$\delta^{13}C_{VPDB}$**	**$\delta^{18}O_{VPDB}$**	**3-points mov. average $\delta^{13}C_{VPDB}$**	**3-points mov. average $\delta^{18}O_{VPDB}$**
DG59	55.1	-0.71	-3.46	-0.71	-3.46

DG58	54.8	-0.17	-3.16	-0.44	-3.31
DG57	54.3	0.08	-3.45	-0.27	-3.36
DG56	51.3	-1.53	-3.57	-0.54	-3.40
DG55	50.7	-0.60	-3.19	-0.68	-3.40
DG54	50.4	-1.36	-3.22	-1.16	-3.33
DG53	49.9	0.89	-3.53	-0.36	-3.31
DG52	49.1	-0.52	-3.46	-0.33	-3.41
DG51	47.3	0.56	-3.85	0.31	-3.62
DG50	46.35	2.80	-3.55	0.95	-3.62
DG49	45.8	-0.75	-4.04	0.87	-3.81
DG48	45.2	1.17	-3.29	1.08	-3.63
DG47	44.6	-1.89	-3.86	-	-
DG46	43.3	0.49	-4.03	0.31	-3.79
DG45	42.4	-0.63	-3.62	0.35	-3.65
DG44	41.5	-1.13	-3.96	-0.42	-3.87
DG43	40.5	-0.25	-3.07	-0.67	-3.55
DG42	39.8	-1.00	-4.06	-0.79	-3.70
DG41	38.8	0.93	-3.85	-0.11	-3.66
DG40	37.75	0.54	-3.92	0.16	-3.95
DG36.5	36.5	1.15	-3.63	0.87	-3.80
DG35.8	35.8	-0.23	-3.92	0.49	-3.83
DG34.1	34.1	-0.23	-3.73	0.23	-3.76
DG33.4	33.4	-1.70	-4.03	-	-
DG32	32	1.12	-2.59	0.22	-3.41
DG31.4	31.4	1.26	-2.36	0.72	-2.90
DG30.35	30.35	-0.21	-4.40	0.72	-3.12
DG29.1	29.1	-0.32	-4.08	0.24	-3.62
DG28.5	28.5	0.59	-3.38	0.02	-3.96
DG27.7	27.7	0.56	-3.37	0.28	-3.61
DG26.2	26.2	1.01	-3.47	0.72	-3.40
DG25*	25	0.55	-3.39	-	-
DG23.5	23.5	0.69	-2.88	0.75	-3.24
DG22.6	22.6	0.04	-3.56	0.58	-3.30
DG21.6	21.6	-0.03	-3.84	0.23	-3.42
DG20.8	20.8	-0.44	-3.23	-0.14	-3.54
DG20	20	-0.15	-3.98	-0.21	-3.68
DG19.2	19.2	-0.44	-3.88	-0.34	-3.70
DG18.7	18.7	-0.68	-4.19	-0.42	-4.02
DG18.1	18.1	-0.51	-3.53	-0.54	-3.87
DG17.8	17.8	-0.25	-3.53	-0.48	-3.75
DG16.8	16.8	-0.79	-4.41	-0.52	-3.82
DG15.8	15.8	-0.96	-3.97	-0.67	-3.97
DG14.8	14.8	-0.58	-3.86	-0.78	-4.08
DG14	14	-0.59	-4.20	-0.71	-4.01
DG13.5	13.5	0.30	-3.93	-0.29	-4.00
DG12.5	12.5	-0.37	-4.48	-0.22	-4.20

DG12	12	-0.25	-4.09	-0.10	-4.17
DG9.5	9.5	-0.94	-4.02	-0.52	-4.20
DG8.5	8.5	-0.41	-3.93	-0.54	-4.01
DG8	8	-0.40	-4.39	-0.59	-4.11
DG7	7	-2.24	-5.03	-1.02	-4.45
DG6.35	6.35	-1.93	-4.46	-1.52	-4.63
DG5.7	5.7	-0.93	-4.01	-1.70	-4.50
DG5.0	5	-1.92	-4.01	-1.59	-4.16

*Diagenized samples are marked in red.

Major, trace elements and REE concentrations

San Giovanni section, major and trace elements concentration in bulk samples								
Sample	**(m)**	**Al (ppm)**	**P (ppm)**	**P/Al**	**Ti (ppm)**	**Ti/Al**	**Sc (ppm)**	**V (ppm)**
DPG19	13.25	941.26	33.45	0.036	46.91	0.0498	0.2022	13.44
DPG14A	10.55	1171.61	49.22	0.042	69.79	0.0596	0.2772	9.27
DPG13	10.1	3358.22	69.30	0.021	177.83	0.0530	0.8272	16.78
DPG12A	9.4	955.08	19.17	0.020	46.20	0.0484	0.2193	7.65
DPG11C	8.9	160.53	16.81	0.105	6.73	0.0420	0.0690	3.60
DPG11	8.7	148.54	13.70	0.092	5.07	0.0342	0.0537	2.21
DPG11E	8.2	290.14	15.49	0.053	12.67	0.0437	0.0842	2.24
DPG11D	8	210.81	13.71	0.065	9.68	0.0460	0.0837	3.44
DPG11B	7.8	382.08	18.96	0.05	16.65	0.0436	0.1160	2.85
DPG10B	7.45	223.24	16.01	0.072	9.00	0.0404	0.0820	2.50
DPG10	7.25	197.90	19.56	0.099	8.10	0.0409	0.0750	2.55
DPG8	5.7	320.81	22.25	0.069	15.43	0.0481	0.0773	2.72
DPG0	0.4	336.98	27.29	0.081	13.86	0.0411	0.1023	6.64
		669.01*					0.175	

*The average value is marked in blue.

San Giovanni section, trace elements concentration in bulk samples									
Sample	**(m)**	**V/Al**	**As (ppm)**	**As/Al**	**Mo (ppm)**	**Mo/Al**	**U (ppm)**	**U/Al**	**Y (ppm)**
DPG19	13.25	0.0143	2.15	0.0023	0.66	0.0007	2.31	0.0025	0.49
DPG14A	10.55	0.0079	3.15	0.0027	1.95	0.0017	3.06	0.0026	0.76
DPG13	10.1	0.0050	2.32	0.0007	1.77	0.0005	3.37	0.0010	1.30
DPG12A	9.4	0.0080	0.52	0.0005	0.24	0.0003	1.75	0.0018	0.66

DPG11C	8.9	0.0224	0.47	0.0029	0.31	0.0019	1.59	0.0099	0.46
DPG11	8.7	0.0149	0.21	0.0014	0.17	0.0011	1.54	0.0104	0.44
DPG11E	8.2	0.0077	0.19	0.0007	0.21	0.0007	1.14	0.0039	0.58
DPG11D	8	0.0163	0.39	0.0018	0.24	0.0011	1.68	0.0080	0.51
DPG11B	7.8	0.0075	0.27	0.0007	0.16	0.0004	1.55	0.0041	0.64
DPG10B	7.45	0.0112	0.23	0.0010	0.14	0.0006	2.10	0.0094	0.56
DPG10	7.25	0.0129	0.26	0.0013	0.16	0.0008	1.76	0.0089	0.66
DPG8	5.7	0.0084	0.20	0.0006	0.51	0.0016	1.67	0.0052	0.37
DPG0	0.4	0.0197	0.25	0.0007	0.11	0.0003	1.57	0.0047	0.26

San Giovanni section, REE concentration in bulk samples								
Sample	**(m)**	**La (ppm)**	**Ce (ppm)**	**Pr (ppm)**	**Nd (ppm)**	**Sm (ppm)**	**Eu (ppm)**	**Gd (ppm)**
DPG19	13.25	0.5151	0.909	0.1099	0.3685	0.0745	0.0172	0.068
DPG14A	10.55	0.8882	1.5136	0.1908	0.6414	0.1287	0.0281	0.1137
DPG13	10.1	1.8938	3.6676	0.4595	1.511	0.2983	0.0665	0.2372
DPG12A	9.4	0.5397	0.9034	0.1178	0.3994	0.0865	0.019	0.0766
DPG11C	8.9	0.216	0.3023	0.0379	0.1412	0.0305	0.0087	0.0364
DPG11	8.7	0.1862	0.2362	0.0329	0.1318	0.0261	0.007	0.0329
DPG11E	8.2	0.2976	0.3691	0.0482	0.1858	0.0437	0.0086	0.046
DPG11D	8	0.2452	0.2956	0.0405	0.1476	0.0321	0.0092	0.0402
DPG11B	7.8	0.3301	0.3972	0.0541	0.2034	0.0439	0.0107	0.0488
DPG10B	7.45	0.2903	0.3418	0.0461	0.1719	0.0385	0.0094	0.0448
DPG10	7.25	0.3382	0.3724	0.0498	0.1779	0.0378	0.0095	0.0518
DPG8	5.7	0.2407	0.3176	0.0454	0.169	0.0324	0.0071	0.036
DPG0	0.4	0.1808	0.3003	0.038	0.1359	0.0275	0.0066	0.025
Sample	**(m)**	**Tb (ppm)**	**Dy (ppm)**	**Ho (ppm)**	**Er (ppm)**	**Tm (ppm)**	**Yb (ppm)**	**Lu (ppm)**
DPG19	13.25	0.0105	0.0593	0.0132	0.0357	0.0052	0.0309	0.0054
DPG14A	10.55	0.0166	0.0967	0.0217	0.0575	0.0074	0.0478	0.008
DPG13	10.1	0.0378	0.1994	0.0421	0.1157	0.0165	0.1017	0.0192
DPG12A	9.4	0.0122	0.0698	0.0164	0.0464	0.0059	0.039	0.0064
DPG11C	8.9	0.0062	0.0391	0.009	0.0252	0.0036	0.0213	0.0037
DPG11	8.7	0.0056	0.0361	0.0082	0.0273	0.0031	0.0232	0.0038
DPG11E	8.2	0.0072	0.047	0.0116	0.0346	0.0051	0.0268	0.0049

DPG11D	8	0.0062	0.0394	0.0098	0.0294	0.0046	0.025	0.0041
DPG11B	7.8	0.0077	0.0501	0.0126	0.0394	0.0054	0.0342	0.0056
DPG10B	7.45	0.0064	0.0467	0.0109	0.0323	0.0048	0.0289	0.0047
DPG10	7.25	0.0074	0.0473	0.0128	0.0371	0.0054	0.0303	0.006
DPG8	5.7	0.0056	0.034	0.0083	0.025	0.0029	0.02	0.0026
DPG0	0.4	0.004	0.0237	0.0058	0.0162	0.0028	0.0128	0.0023

San Giovanni section, PAAS-normalized REE concentration in bulk samples								
		La	**Ce**	**Pr**	**Nd**	**Sm**	**Eu**	**Gd**
Sample	**(m)**	**38***	**80**	**8.9**	**32**	**5.6**	**1.1**	**4.7**
DPG19	13.25	0.014	0.0114	0.0123	0.0115	0.0133	0.0156	0.0145
DPG14A	10.55	0.023	0.0189	0.0214	0.02	0.023	0.0255	0.0242
DPG13	10.1	0.05	0.0458	0.0516	0.0472	0.0533	0.0605	0.0505
DPG12A	9.4	0.014	0.0113	0.0132	0.0125	0.0154	0.0173	0.0163
DPG11C	8.9	0.006	0.0038	0.0043	0.0044	0.0054	0.0079	0.0078
DPG11	8.7	0.005	0.003	0.0037	0.0041	0.0047	0.0064	0.007
DPG11E	8.2	0.008	0.0046	0.0054	0.0058	0.0078	0.0078	0.0098
DPG11D	8	0.006	0.0037	0.0046	0.0046	0.0057	0.0083	0.0085
DPG11B	7.8	0.009	0.005	0.0061	0.0064	0.0078	0.0098	0.0104
DPG10B	7.45	0.008	0.0043	0.0052	0.0054	0.0069	0.0086	0.0095
DPG10	7.25	0.009	0.0047	0.0056	0.0056	0.0068	0.0087	0.011
DPG8	5.7	0.006	0.004	0.0051	0.0053	0.0058	0.0064	0.0077
DPG0	0.4	0.005	0.0038	0.0043	0.0042	0.0049	0.006	0.0053
		Tb	**Dy**	**Ho**	**Er**	**Tm**	**Yb**	**Lu**
Sample	**(m)**	**0.77**	**4.4**	**1**	**2.9**	**0.4**	**2.8**	**0.43**
DPG19	13.25	0.0136	0.0135	0.0132	0.0123	0.0129	0.011	0.0126
DPG14A	10.55	0.0216	0.022	0.0217	0.0198	0.0185	0.0171	0.0186
DPG13	10.1	0.0491	0.0453	0.0421	0.0399	0.0412	0.0363	0.0447
DPG12A	9.4	0.0158	0.0159	0.0164	0.016	0.0147	0.0139	0.0149
DPG11C	8.9	0.0081	0.0089	0.009	0.0087	0.0091	0.0076	0.0085
DPG11	8.7	0.0073	0.0082	0.0082	0.0094	0.0077	0.0083	0.0088
DPG11E	8.2	0.0094	0.0107	0.0116	0.0119	0.0128	0.0096	0.0114
DPG11D	8	0.0081	0.009	0.0098	0.0101	0.0115	0.0089	0.0096
DPG11B	7.8	0.01	0.0114	0.0126	0.0136	0.0136	0.0122	0.013
DPG10B	7.45	0.0083	0.0106	0.0109	0.0111	0.0119	0.0103	0.0109

DPG10	7.25	0.0096	0.0107	0.0128	0.0128	0.0135	0.0108	0.0139
DPG8	5.7	0.0073	0.0077	0.0083	0.0086	0.0074	0.0071	0.006
DPG0	0.4	0.0052	0.0054	0.0058	0.0056	0.007	0.0046	0.0054

*Post-Archean Australian Shale (PAAS) REE standard values given in Taylor & McLennan (1985) are marked in green.

San Giovanni section, REE proxies in bulk samples							
Sample	**(m)**	**Ce/Ce***	**Y/Ho**	**Eu/Eu***	**Pr/Pr***	**ΣREE**	**LREE/ HREE**
DPG19	13.25	0.877	37.35	1.124	1.079	2.715	1.018
DPG14A	10.55	0.844	35.28	1.082	1.100	4.526	1.167
DPG13	10.1	0.903	31.05	1.165	1.109	9.972	1.234
DPG12A	9.4	0.823	40.56	1.090	1.113	3.004	0.893
DPG11C	8.9	0.760	52.13	1.201	1.039	1.351	0.549
DPG11	8.7	0.687	53.90	1.090	1.044	1.203	0.479
DPG11E	8.2	0.696	50.55	0.890	1.038	1.722	0.534
DPG11D	8	0.671	52.35	1.168	1.095	1.443	0.501
DPG11B	7.8	0.672	51.56	1.071	1.073	1.891	0.519
DPG10B	7.45	0.666	51.21	1.046	1.073	1.637	0.527
DPG10	7.25	0.642	51.90	0.974	1.094	1.850	0.502
DPG8	5.7	0.694	44.44	0.953	1.101	1.317	0.749
DPG0	0.4	0.832	45.86	1.177	1.066	1.05	0.776
		0.751*	46.01				

*The average value is marked in blue.

The formulas used for the calculation of the above parameters are reported in Chap. 2, par. 2.2.3.2.

Borgo Celano 1 section, major and trace elements concentration in bulk samples								
Sample	**(m)**	**Al (ppm)**	**P (ppm)**	**P/Al**	**Ti (ppm)**	**Ti/Al**	**Sc (ppm)**	**V (ppm)**
SG18	17.27	1120.33	14.09	0.013	58.46	0.052	0.2871	24.77
SG14	16.1	566.29	16.58	0.029	23.54	0.042	0.1616	13.04
SG12	15.66	484.59	11.14	0.023	19.01	0.039	0.0990	5.45
SG11	15.5	176.98	15.43	0.087	7.65	0.043	0.0666	5.03
SG42	13.3	73.47	11.75	0.160	2.86	0.039	0.0326	2.23
SG6	11.75	204.55	14.18	0.069	9.71	0.048	0.0764	3.78
		437.7*					0.12	

*The average value is marked in blue.

Borgo Celano 1 section, trace elements concentration in bulk samples									
Sample	**(m)**	**V/Al**	**As (ppm)**	**As/Al**	**Mo (ppm)**	**Mo/Al**	**U (ppm)**	**U/Al**	**Y (ppm)**
SG18	17.27	0.022	2.07	0.0019	1.35	0.0012	2.55	0.0023	0.97
SG14	16.1	0.023	0.68	0.0012	1.12	0.0020	2.93	0.0052	0.52
SG12	15.66	0.011	0.71	0.0015	0.45	0.0009	1.86	0.0038	0.35
SG11	15.5	0.016	1.03	0.0033	1.17	0.0037	1.69	0.0053	0.29
SG42	13.3	0.030	0.11	0.0015	0.02	0.0003	0.65	0.0089	0.18
SG6	11.75	0.019	0.19	0.0010	0.17	0.0009	1.06	0.0052	0.24

Borgo Celano 1 section, REE concentration in bulk samples								
Sample	**(m)**	**La (ppm)**	**Ce (ppm)**	**Pr (ppm)**	**Nd (ppm)**	**Sm (ppm)**	**Eu (ppm)**	**Gd (ppm)**
SG18	17.27	0.8531	1.6277	0.1917	0.6966	0.1436	0.0311	0.1273
SG14	16.1	0.3712	0.6822	0.0825	0.3048	0.0624	0.0141	0.0647
SG12	15.66	0.2149	0.3467	0.0438	0.1574	0.0344	0.0075	0.0313
SG11	15.5	0.1741	0.28	0.0331	0.1273	0.0258	0.0063	0.0275
SG42	13.3	0.0725	0.0836	0.0163	0.0651	0.0123	0.0018	0.0109
SG6	11.75	0.162	0.2518	0.0336	0.1192	0.0259	0.0051	0.0191
Sample	**(m)**	**Tb (ppm)**	**Dy (ppm)**	**Ho (ppm)**	**Er (ppm)**	**Tm (ppm)**	**Yb (ppm)**	**Lu (ppm)**
SG18	17.27	0.0192	0.111	0.0237	0.0704	0.0081	0.0621	0.0103
SG14	16.1	0.0099	0.062	0.0135	0.0381	0.0059	0.0343	0.0062
SG12	15.66	0.0054	0.0279	0.0071	0.0211	0.0027	0.0163	0.0032
SG11	15.5	0.0043	0.0274	0.0056	0.0161	0.0019	0.0129	0.0022
SG42	13.3	0.0021	0.0147	0.0038	0.0109	0.0017	0.0085	0.0013
SG6	11.75	0.0034	0.0195	0.0051	0.0142	0.0022	0.0124	0.0019

Borgo Celano 1 section, PAAS-normalized REE concentration in bulk samples								
		La	**Ce**	**Pr**	**Nd**	**Sm**	**Eu**	**Gd**
Sample	**(m)**	**38***	**80**	**8.9**	**32**	**5.6**	**1.1**	**4.7**
SG18	17.27	0.022	0.0203	0.0215	0.0218	0.0256	0.0282	0.0271

SG14	16.1	0.01	0.0085	0.0093	0.0095	0.0111	0.0129	0.0138
SG12	15.66	0.006	0.0043	0.0049	0.0049	0.0061	0.0068	0.0067
SG11	15.5	0.005	0.0035	0.0037	0.004	0.0046	0.0057	0.0059
SG42	13.3	0.002	0.001	0.0018	0.002	0.0022	0.0017	0.0023
SG6	11.75	0.004	0.0031	0.0038	0.0037	0.0046	0.0047	0.0041
		Tb	**Dy**	**Ho**	**Er**	**Tm**	**Yb**	**Lu**
Sample	**(m)**	**0.77**	**4.4**	**1**	**2.9**	**0.4**	**2.8**	**0.43**
SG18	17.27	0.025	0.0252	0.0237	0.0243	0.0203	0.0222	0.0239
SG14	16.1	0.0128	0.0141	0.0135	0.0131	0.0149	0.0123	0.0143
SG12	15.66	0.0071	0.0063	0.0071	0.0073	0.0067	0.0058	0.0075
SG11	15.5	0.0056	0.0062	0.0056	0.0055	0.0049	0.0046	0.0051
SG42	13.3	0.0028	0.0033	0.0038	0.0038	0.0042	0.003	0.003
SG6	11.75	0.0044	0.0044	0.0051	0.0049	0.0056	0.0044	0.0044

*Post-Archean Australian Shale (PAAS) REE standard values given in Taylor & McLennan (1985) are marked in green.

Borgo Celano 1 section, REE proxies in bulk samples							
Sample	**(m)**	**Ce/Ce***	**Y/Ho**	**Eu/Eu***	**Pr/Pr***	**ΣREE**	**LREE/ HREE**
SG18	17.27	0.925	41.17	1.071	1.022	4.950	0.962
SG14	16.1	0.896	39.19	1.032	1.026	2.28	0.693
SG12	15.66	0.819	50.27	1.068	1.063	1.274	0.747
SG11	15.5	0.843	52.72	1.099	0.994	1.040	0.794
SG42	13.3	0.723	48.12	0.739	1.189	0.489	0.542
SG6	11.75	0.782	48.81	1.076	1.100	0.924	0.805
		0.831*	46.71				

*The average value is marked in blue.

The formulas used for the calculation of the above parameters are reported in Chap. 2, par. 2.2.3.2.

Chapter 4 - *Chondrodonta* within the upper Cenomanian Adriatic Carbonate Platform

C- and O-isotope data

Savudrija section, $\delta^{13}C$ and $\delta^{18}O$ in bulk samples					
Sample	**Height (m)**	**$\delta^{13}C_{VPDB}$**	**$\delta^{18}O_{VPDB}$**	**3-points mov. average $\delta^{13}C_{VPDB}$**	**3-points mov. average $\delta^{18}O_{VPDB}$**
SA42	42	2.08	-2.66	1.74	-2.46
SA40	40.4	1.10	-1.72	1.53	-2.21
SA39.6	39.6	1.90	-3.00	1.69	-2.46
SA38.5	38.5	1.28	-2.00	1.42	-2.24
SA37.2	37.2	1.10	-2.92	1.43	-2.64
SA37.1	37.1	0.46	-2.70	0.95	-2.54
SA36.1	36.1	1.61	-2.48	1.06	-2.70
SA35.6	35.6	0.31	-2.00	0.79	-2.39
SA35.4A	35.4	0.46	-2.35	0.79	-2.28
SA34.8	34.8	0.82	-2.81	0.53	-2.39
SA34.7A	34.7	0.10	-2.92	0.46	-2.69
SA33.8	33.8	1.25	-1.94	0.72	-2.55
SA33.5	33.5	1.49	-2.03	0.94	-2.30
SA33.3	33.3	0.75	-2.41	1.16	-2.13
SA33	33	0.42	-2.13	0.89	-2.19
SA32.5	32.5	1.35	-2.00	0.84	-2.18
SA32	32	-0.30	-2.18	0.49	-2.10
SA31.6	31.6	0.61	-1.93	0.56	-2.04
SA31.3	31.3	0.51	-2.37	0.28	-2.16
SA31.2	31.2	1.17	-2.06	-	-
SA31	31	0.95	-1.62	0.69	-1.97
SA30.6	30.6	1.37	-1.79	0.94	-1.93
SA30.4	30.4	1.45	-1.38	1.26	-1.60
SA30.1A	30.1	1.25	-2.24	1.36	-1.80
SA29.1	29.1	1.36	-1.93	1.36	-1.85
SA28.8	28.8	0.58	-1.91	1.06	-2.03
SA28.75	28.75	0.63	-1.96	0.86	-1.93
SA28.6	28.6	2.20	-2.44	-	-
SA27.5	27.5	0.60	-2.34	-	-
SA27	27	1.25	-1.86	0.82	-1.91
SA26.3	26.3	1.74	-1.75	-	-
SA26	26	1.34	-2.25	1.07	-2.02
SA25.7	25.7	2.30	-2.08	1.63	-2.06
SA24.7	24.7	2.91	-1.79	2.18	-2.04
SA23.9	23.9	2.46	-2.27	2.55	-2.05
SA23.1	23.1	2.83	-2.13	2.73	-2.06
SA22.7A	22.7	2.42	-2.59	2.57	-2.33

SA22.1	22.1	2.92	-2.27	2.72	-2.33
SA21.4	21.4	2.65	-2.02	2.66	-2.29
SA21.1	21.1	2.16	-2.73	2.58	-2.34
SA20.6	20.6	1.89	-1.85	2.24	-2.20
SA19.4	19.4	2.50	-2.41	2.19	-2.33
SA17.8	17.8	2.91	-1.61	2.44	-1.96
SA17.3	17.3	3.23	-1.38	2.88	-1.80
SA16.7	16.7	3.45	-1.60	3.20	-1.53
SA16.1A	16.1	2.86	-2.52	-	-
SA15.5	15.5	2.64	-2.64	3.11	-1.87
SA14.3	14.3	2.47	-2.26	2.85	-2.17
SA14	14	2.03	-1.44	2.38	-2.11
SA12.4	12.4	2.46	-2.32	2.32	-2.01
SA12.3	12.3	2.73	-1.86	2.40	-1.87
SA10.8	10.8	1.90	-1.86	2.36	-2.01
SA9.8	9.8	2.13	-1.61	-	-
SA8.4	8.4	2.37	-1.34	2.33	-1.69
SA7.4	7.4	1.89	-1.47	2.05	-1.56
SA7.2*	7.2	2.32	-1.72	-	-
SA6.8A	6.8	1.23	-1.88	1.83	-1.56
SA6.5	6.5	2.43	-2.05	1.85	-1.80
SA5.4	5.4	2.22	-1.39	1.96	-1.77
SA5.2	5.2	2.14	-1.49	2.26	-1.64
SA4.1	4.1	1.39	-1.59	1.92	-1.49
SA3.7	3.7	1.62	-1.63	1.72	-1.57
SA2.3	2.3	1.95	-1.40	1.65	-1.54
SA2	2	2.38	-2.47	1.98	-1.83
SA1.2	1.2	1.71	-2.50	2.01	-2.13
SA0.9	0.9	1.87	-2.28	1.99	-2.42
SA0.3	0.3	1.38	-1.97	1.66	-2.25

*Diagenized samples are marked in red.

Savudrija section, $\delta^{13}C$ and $\delta^{18}O$ in shell samples				
Sample	**Shell**	**(m)**	**$\delta^{13}C_{VPDB}$**	**$\delta^{18}O_{VPDB}$**
SA37.2-A	*Chondrodonta*	37.2	3.24	-1.80
SA34.8-A	*Chondrodonta*	34.8	1.23	-3.30
SA34.7-D	*Chondrodonta*	34.7	2.86	-2.10
SA34.7-C	*Chondrodonta*	34.7	1.84	-2.29
SA34.7-B	*Chondrodonta*	34.7	2.41	-1.92
SA34.7-A	*Chondrodonta*	34.7	2.15	-2.68
SA33.5-A	*Chondrodonta*	33.5	2.51	-2.53
SA33.3-B	*Chondrodonta*	33.3	2.88	-1.84
SA33.3-A	*Chondrodonta*	33.3	3.15	-2.38
SA33-C	*Chondrodonta*	33	2.90	-2.35
SA33-B	*Chondrodonta*	33	2.36	-1.83

SA33-A	*Chondrodonta*	33	2.30	-1.62
SA32-A	*Chondrodonta*	32	3.32	-1.43
SA30.4-A	*Chondrodonta*	30.4	2.65	-1.31
SA30.1-E	*Chondrodonta*	30.1	2.65	-1.64
SA30.1-D	Rudist	30.1	2.22	-2.80
SA30.1-C	*Chondrodonta*	30.1	2.64	-2.53
SA30.1-B	*Chondrodonta*	30.1	2.54	-2.31
SA30.1-A	Rudist	30.1	2.34	-2.74
SA27.5-B	*Chondrodonta*	27.5	2.46	-2.98
SA27.5-A	*Chondrodonta*	27.5	2.20	-1.61
SA24.4-A	*Chondrodonta*	24.4	2.79	-2.54
SA23.1-A	Rudist	23.1	2.70	-2.99
SA22.1-A	Rudist	22.1	3.04	-2.87
SA17.8-B	Rudist	17.8	2.34	-3.41
SA17.8-A	Rudist	17.8	2.16	-2.60
SA4.1-B	Rudist	4.1	2.34	-2.18
SA4.1-A	Rudist	4.1	1.92	-1.94

Major, trace elements and REE concentrations

Savudrija section, major and trace elements concentration in bulk samples								
Sample	**(m)**	**Al (ppm)**	**P (ppm)**	**P/Al**	**Ti (ppm)**	**Ti/Al**	**Sc (ppm)**	**V (ppm)**
SA42	42	305.41	61.78	0.202	13.79	0.0451	0.1082	4.85
SA40	40.4	614.50	62.23	0.101	25.94	0.0422	0.1527	40.35
SA39.6	39.6	311.54	66.23	0.212	11.35	0.0364	0.1008	16.97
SA38.5A	38.5	35.95	52.65	1.464	1.08	0.0302	0.0625	7.61
SA37.2	37.2	131.51	58.96	0.448	4.12	0.0313	0.0497	15.45
SA36.1	36.1	167.57	49.70	0.296	6.36	0.0379	0.1004	8.14
SA34.8	34.8	107.10	63.47	0.592	3.184	0.0297	0.0402	8.18
SA33.8	33.8	698.97	60.03	0.085	25.61	0.0366	0.1836	13.98
SA33.3	33.3	824.31	54.32	0.065	28.82	0.0349	0.1434	19.04
SA33	33	815.14	73.74	0.090	29.59	0.0363	0.2699	51.06
SA32.5	32.5	124.26	64.99	0.523	3.59	0.0289	0.0453	8.99
SA32	32	1415.10	65.39	0.046	56.33	0.0398	0.2201	45.81
SA31.6	31.6	30.30	52.67	1.738	1.25	0.0415	0.0315	8.80
SA30.4	30.4	597.20	60.84	0.101	23.62	0.0395	0.1106	9.45
SA29.1	29.1	461.91	52.19	0.113	19.07	0.0412	0.1039	5.31
SA27	27	154.11	48.67	0.315	5.44	0.0353	0.1860	8.02
SA25.7	25.7	254.93	45.93	0.180	9.07	0.0355	0.0464	2.72
SA23.9	23.9	101.71	49.18	0.483	3.56	0.0350	0.0329	11.56
SA22.7B	22.7	102.13	55.42	0.542	4.16	0.0407	0.0300	2.58
SA21.4	21.4	147.36	58.97	0.400	5.61	0.0381	0.0346	3.99
SA19.4	19.4	266.35	65.70	0.246	11.78	0.0442	0.0787	3.25
SA17.3	17.3	141.69	52.43	0.370	5.56	0.0392	0.0418	10.79

SA14.3	14.3	142.71	62.62	0.438	4.67	0.0327	0.0339	2.03
SA12.3	12.3	199.59	57.04	0.285	7.96	0.0398	0.0618	4.14
SA7.4	7.4	448.23	48.41	0.108	20.33	0.0453	0.1211	3.47
SA5.4	5.4	214.64	48.43	0.225	8.31	0.0387	0.0648	5.33
SA4.1	4.1	282.15	61.18	0.216	12.27	0.0434	0.0742	5.59
SA2	2	168.02	59.34	0.353	7.19	0.0428	0.0720	4.39
SA0.3	0.3	278.26	49.91	0.179	9.72	0.0349	0.0816	4.66
		329.06*					0.0925	

*The average value is marked in blue.

Savudrija section, trace elements concentration in bulk samples									
Sample	**(m)**	**V/Al**	**As (ppm)**	**As/Al**	**Mo (ppm)**	**Mo/Al**	**U (ppm)**	**U/Al**	**Y (ppm)**
SA42	42	0.015	0.32	0.0010	0.890	0.0029	1.44	0.0047	0.373
SA40	40.4	0.065	0.19	0.0003	0.397	0.0006	4.56	0.0074	0.741
SA39.6	39.6	0.054	0.74	0.0023	3.525	0.0113	2.61	0.0083	0.138
SA38.5A	38.5	0.211	0.08	0.0025	0.340	0.0094	2.65	0.0739	0.478
SA37.2	37.2	0.117	0.19	0.0015	0.556	0.0042	2.76	0.0210	0.266
SA36.1	36.1	0.048	0.12	0.0007	0.168	0.0010	2.41	0.0144	0.974
SA34.8	34.8	0.076	0.11	0.0011	0.267	0.0024	2.57	0.0240	0.044
SA33.8	33.8	0.020	0.69	0.0009	0.745	0.0010	3.95	0.0056	0.296
SA33.3	33.3	0.023	0.60	0.0007	0.702	0.0008	3.02	0.0036	0.256
SA33	33	0.062	2.09	0.0025	3.673	0.0045	2.98	0.0036	1.120
SA32.5	32.5	0.072	0.21	0.0017	0.544	0.0043	5.08	0.0409	0.077
SA32	32	0.032	1.93	0.0013	1.287	0.0009	5.21	0.0036	0.221
SA31.6	31.6	0.290	0.12	0.0041	0.343	0.0113	4.27	0.1408	0.089
SA30.4	30.4	0.015	0.49	0.0008	0.865	0.0014	3.56	0.0059	0.133
SA29.1	29.1	0.011	0.13	0.0002	0.620	0.0013	3.49	0.0075	0.147
SA27	27	0.052	0.14	0.0009	0.383	0.0024	4.98	0.0323	1.575
SA25.7	25.7	0.010	0.08	0.0003	0.227	0.0008	1.61	0.0063	0.062
SA23.9	23.9	0.113	0.12	0.0012	0.185	0.0018	3.19	0.0314	0.038
SA22.7B	22.7	0.025	0.13	0.0013	0.180	0.0017	1.83	0.0180	0.037
SA21.4	21.4	0.027	0.09	0.0006	0.190	0.0012	2.10	0.0142	0.055
SA19.4	19.4	0.012	0.32	0.0012	0.482	0.0018	0.94	0.0035	0.085
SA17.3	17.3	0.076	0.11	0.0007	0.313	0.0022	2.09	0.0148	0.076
SA14.3	14.3	0.014	0.14	0.0009	0.190	0.0013	0.92	0.0065	0.045
SA12.3	12.3	0.020	0.26	0.0013	0.472	0.0023	1.38	0.0069	0.068
SA7.4	7.4	0.007	0.77	0.0017	1.963	0.0043	1.79	0.0039	0.142
SA5.4	5.4	0.024	0.23	0.0011	0.523	0.0024	2.31	0.0107	0.122
SA4.1	4.1	0.019	0.28	0.0010	0.315	0.0011	1.58	0.0056	0.094
SA2	2	0.026	0.19	0.0011	0.169	0.0010	1.25	0.0074	0.160
SA0.3	0.3	0.016	0.41	0.0015	0.698	0.0025	1.16	0.0041	0.130

Savudrija section, REE concentration in bulk samples								
Sample	**(m)**	**La (ppm)**	**Ce (ppm)**	**Pr (ppm)**	**Nd (ppm)**	**Sm (ppm)**	**Eu (ppm)**	**Gd (ppm)**
SA42	42	0.5576	0.9326	0.0948	0.3566	0.0670	0.0161	0.0693
SA40	40.4	0.8493	1.2163	0.1212	0.4653	0.0851	0.0209	0.1024
SA39.6	39.6	0.2469	0.4863	0.0511	0.1991	0.0396	0.0090	0.0350
SA38.5A	38.5	0.5959	1.0167	0.1034	0.3881	0.0790	0.0188	0.0787
SA37.2	37.2	0.3448	0.5380	0.0528	0.2045	0.0386	0	0.0443
SA36.1	36.1	0.4470	0.7411	0.0795	0.3085	0.0610	0.0152	0.0726
SA34.8	34.8	0.0336	0.0616	0.0072	0.0295	0.0065	0.0018	0.0066
SA33.8	33.8	0.3701	0.7552	0.0927	0.3192	0.0697	0.0157	0.0608
SA33.3	33.3	0.2239	0.4462	0.0510	0.2001	0.0412	0.0087	0.0328
SA33	33	0.2238	0.4153	0.0535	0.1855	0.0436	0.0123	0.0418
SA32.5	32.5	0.0864	0.1611	0.0184	0.0741	0.0144	0.0035	0.0147
SA32	32	0.2715	0.5004	0.0607	0.2077	0.0404	0.0098	0.0313
SA31.6	31.6	0.0666	0.1373	0.0159	0.0639	0.0124	0.0033	0.0141
SA30.4	30.4	0.1873	0.3857	0.0436	0.1604	0.0320	0.0065	0.0268
SA29.1	29.1	0.1728	0.3357	0.0395	0.1459	0.0272	0.0062	0.0235
SA27	27	0.6725	0.3227	0.1244	0.5698	0.1133	0.0279	0.1501
SA25.7	25.7	0.0852	0.1687	0.0186	0.0693	0.0139	0.0025	0.0106
SA23.9	23.9	0.0606	0.1188	0.0138	0.0511	0.0092	0.0020	0.0086
SA22.7B	22.7	0.0439	0.0823	0.0103	0.0353	0.0058	0.0007	0
SA21.4	21.4	0.0819	0.1578	0.0181	0.0676	0.0130	0.0026	0.0112
SA19.4	19.4	0.1395	0.2995	0.0407	0.1111	0.0237	0.0107	0.0186
SA17.3	17.3	0.1241	0.2429	0.0284	0.1100	0.0205	0.0051	0.0185
SA14.3	14.3	0.0661	0.1322	0.0142	0.0539	0.0111	0.0031	0.0106
SA12.3	12.3	0.0991	0.1944	0.0229	0.0858	0.0171	0.0037	0.0147
SA7.4	7.4	0.2115	0.4157	0.0459	0.1792	0.0361	0.0075	0.0309
SA5.4	5.4	0.2203	0.4287	0.0484	0.1854	0.0359	0.0078	0.0320
SA4.1	4.1	0.1365	0.2512	0.0417	0.1119	0.0268	0.0147	0.0189
SA2	2	0.2013	0.4230	0.0510	0.1968	0.0419	0.0101	0.0381
SA0.3	0.3	0.1910	0.4096	0.0471	0.1768	0.0372	0.0080	0.0321
Sample	**(m)**	**Tb (ppm)**	**Dy (ppm)**	**Ho (ppm)**	**Er (ppm)**	**Tm (ppm)**	**Yb (ppm)**	**Lu (ppm)**
SA42	42	0.0098	0.0558	0.0113	0.0302	0.0040	0.0261	0.0037
SA40	40.4	0.0140	0.0850	0.0184	0.0527	0.0070	0.0466	0.0069
SA39.6	39.6	0.0049	0.0278	0.0054	0.0135	0.0019	0.0131	0.0016
SA38.5A	38.5	0.0117	0.0640	0.0132	0.0333	0.0043	0.0268	0.0036
SA37.2	37.2	0.0064	0.0357	0.0071	0.0168	0.0023	0.0160	0.0023
SA36.1	36.1	0.0116	0.0734	0.0186	0.0557	0.0066	0.0456	0.0066
SA34.8	34.8	0.0010	0.0059	0.0012	0.0025	0.0007	0.0034	0
SA33.8	33.8	0.0095	0.0528	0.0115	0.0316	0.0046	0.0309	0.0049
SA33.3	33.3	0.0055	0.0324	0.0070	0.0201	0.0031	0.0211	0.0031
SA33	33	0.0073	0.0561	0.0182	0.0611	0.0105	0.0706	0.0115

SA32.5	32.5	0.0021	0.0120	0.0024	0.0053	0.0009	0.0059	0.0009
SA32	32	0.0052	0.0322	0.0071	0.0204	0.0029	0.0240	0.0040
SA31.6	31.6	0.0021	0.0126	0.0023	0.0061	0.0010	0.0064	0.0009
SA30.4	30.4	0.0039	0.0232	0.0048	0.0127	0.0018	0.0138	0.0018
SA29.1	29.1	0.0035	0.0225	0.0045	0.0130	0.0022	0.0166	0.0023
SA27	27	0.0219	0.1435	0.0337	0.0938	0.0119	0.0784	0.0113
SA25.7	25.7	0.0016	0.0104	0.0019	0.0043	0	0.0055	0.0006
SA23.9	23.9	0.0011	0.0076	0.0012	0.0028	0	0.004	0
SA22.7B	22.7	0	0.0059	0.0007	0.0012	0	0.0012	0
SA21.4	21.4	0.0015	0.0087	0.0017	0.0042	0.0006	0.0031	0.0004
SA19.4	19.4	0.0034	0.0174	0.0033	0.0078	0.0015	0.0081	0.0015
SA17.3	17.3	0.0029	0.0132	0.0027	0.0072	0.0012	0.0063	0
SA14.3	14.3	0.0016	0.0078	0.0016	0.0039	0.0007	0.0031	0.0005
SA12.3	12.3	0.0021	0.0117	0.0025	0.0056	0	0.0061	0
SA7.4	7.4	0.0046	0.0275	0.0054	0.0143	0.0022	0.0156	0.0020
SA5.4	5.4	0.0041	0.0257	0.0048	0.0105	0.0018	0.0117	0.0014
SA4.1	4.1	0.0043	0.0169	0.0041	0.0100	0.0020	0.0107	0.0015
SA2	2	0.0057	0.0301	0.0061	0.0155	0.0019	0.0137	0.0019
SA0.3	0.3	0.0048	0.0248	0.0048	0.0124	0.0018	0.0114	0.0017

Savudrija section, PAAS-normalized REE concentration in bulk samples								
Sample	**(m)**	**La**	**Ce**	**Pr**	**Nd**	**Sm**	**Eu**	**Gd**
		38*	**80**	**8.9**	**32**	**5.6**	**1.1**	**4.7**
SA42	42	0.0146	0.0116	0.0106	0.0111	0.0119	0.0146	0.0147
SA40	40.4	0.0223	0.0152	0.0136	0.0145	0.0152	0.0190	0.0217
SA39.6	39.6	0.0064	0.0060	0.0057	0.0062	0.0070	0.0081	0.0074
SA38.5A	38.5	0.0156	0.0127	0.0116	0.0121	0.0141	0.0171	0.0167
SA37.2	37.2	0.0090	0.0067	0.0059	0.0063	0.0068	0	0.0094
SA36.1	36.1	0.0117	0.0092	0.0089	0.0096	0.0109	0.0138	0.0154
SA34.8	34.8	0.0008	0.0007	0.0008	0.0009	0.0011	0.0016	0.0014
SA33.8	33.8	0.0097	0.0094	0.0104	0.0099	0.0124	0.0143	0.0129
SA33.3	33.3	0.0058	0.0055	0.0057	0.0062	0.0073	0.0079	0.0069
SA33	33	0.0058	0.0051	0.0060	0.0057	0.0077	0.0112	0.0089
SA32.5	32.5	0.0022	0.0020	0.0020	0.0023	0.0025	0.0032	0.0031
SA32	32	0.0071	0.0062	0.0068	0.0064	0.0072	0.0089	0.0066
SA31.6	31.6	0.0017	0.0017	0.0017	0.0019	0.0022	0.0030	0.0030
SA30.4	30.4	0.0049	0.0048	0.0049	0.0050	0.0057	0.0059	0.0057
SA29.1	29.1	0.0045	0.0041	0.0044	0.0045	0.0048	0.0056	0.0050
SA27	27	0.0176	0.0040	0.0139	0.0178	0.0202	0.0253	0.0319
SA25.7	25.7	0.0022	0.0021	0.0020	0.0021	0.0024	0.0022	0.0022
SA23.9	23.9	0.0015	0.0014	0.0015	0.0015	0.0016	0.0018	0.0018
SA22.7B	22.7	0.0011	0.0010	0.0011	0.0011	0.0010	0.0007	0
SA21.4	21.4	0.0021	0.0019	0.0020	0.0021	0.0023	0.0023	0.0024
SA19.4	19.4	0.0036	0.0037	0.0045	0.0034	0.0042	0.0097	0.0039
SA17.3	17.3	0.0032	0.0030	0.0032	0.0034	0.0036	0.0046	0.0039

SA14.3	14.3	0.0017	0.0016	0.0016	0.0016	0.0019	0.0029	0.0022
SA12.3	12.3	0.0026	0.0024	0.0025	0.0026	0.0030	0.0034	0.0031
SA7.4	7.4	0.0055	0.0051	0.0051	0.0056	0.0064	0.0069	0.0065
SA5.4	5.4	0.0057	0.0053	0.0054	0.0057	0.0064	0.0071	0.0068
SA4.1	4.1	0.0035	0.0031	0.0046	0.0034	0.0048	0.0133	0.0040
SA2	2	0.0052	0.0052	0.0057	0.0061	0.0074	0.0092	0.0081
SA0.3	0.3	0.0050	0.0051	0.0052	0.0055	0.0066	0.0073	0.0068
		Tb	**Dy**	**Ho**	**Er**	**Tm**	**Yb**	**Lu**
Sample	**(m)**	**0.77**	**4.4**	**1**	**2.9**	**0.4**	**2.8**	**0.43**
SA42	42	0.0128	0.0126	0.0113	0.0104	0.0102	0.0093	0.0086
SA40	40.4	0.0182	0.0193	0.0184	0.0181	0.0177	0.0166	0.0161
SA39.6	39.6	0.0064	0.0063	0.0054	0.0046	0.0048	0.0047	0.0037
SA38.5A	38.5	0.0152	0.0145	0.0132	0.0115	0.0107	0.0095	0.0085
SA37.2	37.2	0.0084	0.0081	0.0071	0.0058	0.0059	0.0057	0.0053
SA36.1	36.1	0.0150	0.0166	0.0186	0.0192	0.0165	0.0163	0.0154
SA34.8	34.8	0.0013	0.0013	0.0012	0.0008	0.0019	0.0012	0
SA33.8	33.8	0.0123	0.0120	0.0115	0.0109	0.0115	0.0110	0.0115
SA33.3	33.3	0.0072	0.0073	0.0070	0.0069	0.0079	0.0075	0.0073
SA33	33	0.0095	0.0127	0.0182	0.0210	0.0264	0.0252	0.0267
SA32.5	32.5	0.0028	0.0027	0.0024	0.0018	0.0023	0.0021	0.0022
SA32	32	0.0067	0.0073	0.0071	0.0070	0.0074	0.0085	0.0094
SA31.6	31.6	0.0027	0.0028	0.0023	0.0021	0.0027	0.0023	0.0022
SA30.4	30.4	0.0051	0.0052	0.0048	0.0043	0.0046	0.0049	0.0042
SA29.1	29.1	0.0046	0.0051	0.0045	0.0045	0.0055	0.0059	0.0055
SA27	27	0.0284	0.0326	0.0337	0.0323	0.0299	0.0280	0.0264
SA25.7	25.7	0.0021	0.0023	0.0019	0.0015	0	0.0019	0.0013
SA23.9	23.9	0.0014	0.0017	0.0012	0.0009	0	0.0014	0
SA22.7B	22.7	0	0.0013	0.0007	0.0004	0	0.0004	0
SA21.4	21.4	0.0019	0.0019	0.0017	0.0014	0.0015	0.0011	0.0010
SA19.4	19.4	0.0044	0.0039	0.0033	0.0027	0.0037	0.0029	0.0036
SA17.3	17.3	0.0038	0.003	0.0027	0.0025	0.0031	0.0022	0
SA14.3	14.3	0.0021	0.0017	0.0016	0.0013	0.0019	0.0011	0.0013
SA12.3	12.3	0.0027	0.0026	0.0025	0.0019	0	0.0021	0
SA7.4	7.4	0.0060	0.0062	0.0054	0.0049	0.0055	0.0056	0.0047
SA5.4	5.4	0.0053	0.0058	0.0048	0.0036	0.0045	0.0042	0.0033
SA4.1	4.1	0.0056	0.0038	0.0041	0.0034	0.0051	0.0038	0.0036
SA2	2	0.0075	0.0068	0.0061	0.0053	0.0049	0.0048	0.0044
SA0.3	0.3	0.0063	0.0056	0.0048	0.0043	0.0047	0.0041	0.0041

*Post-Archean Australian Shale (PAAS) REE standard values given in Taylor & McLennan (1985) are marked in green.

Savudrija section, REE proxies in bulk samples							
Sample	**(m)**	**Ce/Ce***	**Y/Ho**	**Eu/Eu***	**Pr/Pr***	**ΣREE**	**LREE/ HREE**
SA42	42	0.920	32.84	1.098	0.934	2.608	1.219

SA40	40.4	0.845	40.29	1.028	0.916	3.833	0.933
SA39.6	39.6	0.992	25.68	1.126	0.934	1.274	1.350
SA38.5A	38.5	0.930	35.99	1.107	0.936	2.916	1.264
SA37.2	37.2	0.895	37.32	0	0.905	1.576	1.199
SA36.1	36.1	0.894	52.25	1.051	0.946	2.918	0.582
SA34.8	34.8	0.909	35.89	1.281	0.955	0.206	0.857
SA33.8	33.8	0.936	25.60	1.127	1.073	2.126	0.900
SA33.3	33.3	0.959	36.22	1.115	0.968	1.352	0.793
SA33	33	0.872	61.30	1.349	1.094	2.332	0.238
SA32.5	32.5	0.926	31.03	1.120	0.958	0.480	1.019
SA32	32	0.895	30.78	1.289	1.069	1.439	0.838
SA31.6	31.6	0.966	38.41	1.164	0.967	0.435	0.780
SA30.4	30.4	0.980	27.78	1.040	0.997	1.038	1.082
SA29.1	29.1	0.932	32.55	1.151	1.015	0.964	0.837
SA27	27	0.254	46.67	0.973	1.280	3.951	0.543
SA25.7	25.7	0.971	32.01	0.955	0.981	0.456	1.759
SA23.9	23.9	0.941	30.23	1.067	1.011	0.319	2.618
SA22.7B	22.7	0.887	49.60	1.358	1.089	0.225	5.248
SA21.4	21.4	0.939	30.70	1.003	0.998	0.428	1.613
SA19.4	19.4	0.907	25.30	2.373	1.268	0.772	1.247
SA17.3	17.3	0.939	28.12	1.220	0.988	0.659	1.661
SA14.3	14.3	0.989	27.48	1.363	0.958	0.356	1.127
SA12.3	12.3	0.937	26.49	1.114	1.008	0.534	2.512
SA7.4	7.4	0.968	26.14	1.058	0.956	1.141	1.033
SA5.4	5.4	0.953	25.14	1.077	0.976	1.142	1.428
SA4.1	4.1	0.757	22.93	3.029	1.414	0.746	1.022
SA2	2	0.958	26.28	1.186	1.002	1.198	1.167
SA0.3	0.3	0.992	26.99	1.085	0.994	1.094	1.222
		0.905*	33.38				

*The average value is marked in blue.

The formulas used for the calculation of the above parameters are reported in Chap. 2, par. 2.2.3.2.